

## ABSTRACT

Title of Document:

**CHARACTERIZATION AND MODELING  
OF THE MAGNETOMECHANICAL  
BEHAVIOR OF IRON-GALLIUM ALLOYS**

Jayasimha Atulasimha, Doctor of Philosophy,  
2006

Directed By:

Professor Alison Flatau,  
Department of Aerospace Engineering

Magnetostrictive Iron-Gallium alloys (Galfenol) demonstrate moderate magnetostriction (~350 ppm) under very low magnetic fields (~100 Oe), have very low hysteresis, high tensile strength (~500 MPa), high Curie temperature (~675°C), and in general are machinable, ductile and corrosion resistant. Therefore, they hold great promise for use in active vibration control, actuation, stress and torque sensing applications in helicopters, aircrafts and automobiles. Comprehensive characterization and modeling of the magnetomechanical behavior of these alloys will facilitate design of magnetostrictive actuators and sensors using this material, as well as aid in making it commercially viable.

This dissertation addresses some of these issues, focusing primarily on quasi-static characterization and modeling of the magnetomechanical behavior of single-crystal FeGa alloys with varying gallium content and along different crystallographic directions, and studying the effect of texture on the magnetomechanical behavior of polycrystals. Additionally, improved testing and modeling paradigms for magnetostrictive materials are developed to contribute to a better understanding and prediction of actuation and sensing behavior of FeGa alloys.

In particular, the actuation behavior ( $\lambda$ -H and B-H curves) for 19, 24.7 and 29 at. % Ga  $\langle 100 \rangle$  oriented single crystal FeGa samples are characterized and the strikingly different characteristics are simulated and explained using an energy based model. Actuation and sensing (B- $\sigma$  and  $\epsilon$ - $\sigma$  curves) behavior of  $\langle 100 \rangle$  oriented 19 at. % Ga and  $\langle 110 \rangle$  oriented 18 at. % Ga single crystal samples are characterized. It is demonstrated that the sensing behavior can be predicted by the model, using parameters obtained from the actuation behavior. The actuation and sensing behavior of 18.4 at. % Ga polycrystalline FeGa samples are predicted from the volume fraction of grains close to the [100], [110], [210], [310], [111], [211] and [311] orientations (obtained from cross-section texture analysis). The predictions are benchmarked against experimental actuator and sensor characteristics of a typical polycrystalline sample.

CHARACTERIZATION AND MODELING OF THE MAGNETOMECHANICAL  
BEHAVIOR OF IRON-GALLIUM ALLOYS

By

Jayasimha Atulasimha

Dissertation submitted to the Faculty of the Graduate School of the  
University of Maryland, College Park, in partial fulfillment  
of the requirements for the degree of  
DOCTOR OF PHILOSOPHY

2006

Advisory Committee:  
Professor Alison Flatau, Chair  
Professor Inderjit Chopra  
Dr. Arthur E. Clark  
Professor Michael Coplan  
Professor Norman Wereley  
Professor Manfred Wuttig

© Copyright by  
Jayasimha Atulasimha  
2006

# Dedication

To the memory of my late

Grandparents T.S. Padmanabhan and Chandramma

and

Great-grandfather Nittor Srinivasa Rao

## Acknowledgements

First and foremost, I would like to express my gratitude to my doctoral committee: Dr. Alison Flatau, Dr. Inderjit Chopra, Dr. Arthur Clark, Dr. Manfred Wuttig, Dr. Michael Coplan, and Dr. Norman Wereley for their keen interest and guidance with my research work. I would like to thank Dr. Alison Flatau, my PhD advisor, for her firm support and confidence in my academic work and encouraging me to pursue a wide range of research problems, while helping me to stay focused on my thesis. I am particularly grateful for her support and patient guidance throughout my doctoral research. I would like to thank Dr. Inderjit Chopra, who was my MS advisor, for taking a keen interest in my doctoral work. I greatly appreciate his advice and support through the years. I was indeed privileged to have had stimulating discussions, advice and insights on magnetostrictive materials of both Dr. Arthur Clark and Dr. Manfred Wuttig. I would also like to specially acknowledge the many discussions I had with Dr. James Cullen on the modeling of magnetostrictive materials and his insights on this subject.

I would like to acknowledge the support of DARPA and WPAFB in funding this research with Dr. John Main and Dr. Brian Sanders respectively serving as the technical monitors. I would like to thank Ertema Products Inc. and Dr. Eric Summers in particular for providing the polycrystalline samples and EBSD analysis of the sample cross-sections. I would like to acknowledge the help of Dr. Thomas Lograsso, Ames Lab from whom we procured the Iron-Gallium single-crystal samples, Dr. Kellogg who designed the water-cooled transducer and the magnetostrictive-group at NSWC, Carderock Division for loaning us the  $\text{Fe}_{75.3}\text{Ga}_{24.7}$  sample.

I would like to acknowledge the help of undergrads Sarah, Luke and Baran, for help with initial set-up and later on in testing of FeGa samples. I would like to thank all my fellow graduate students at the magnetostrictive group, particularly Supratik Datta, for their help. Many visiting faculty, research scientists and graduate students at the Smart Structures Lab, Alfred Gessow Rotorcraft Center and faculty

and staff of Aerospace Engineering contributed towards making my graduate work a great and enjoyable experience. In particular I would like to thank Dr. Nagaraj, Dr. Sirohi, and Dr. Couch for their advice and help during these years.

Last but not the least, I would like to thank my family, friends and teachers and in particular my parents Jayasimha and Anupama and sister Nirupama for their innumerable help and moral support over the years without which this accomplishment would not have been possible.

# Table of Contents

<b>Dedication .....</b>	<b>ii</b>
<b>Acknowledgements .....</b>	<b>iii</b>
<b>Table of Contents .....</b>	<b>v</b>
<b>List of Conventions .....</b>	<b>viii</b>
<b>Chapter 1: Introduction .....</b>	<b>1</b>
1.1 Overview of Magnetostrictive FeGa Alloys .....	3
1.1.1 Historical Development of Magnetostrictive Materials.....	3
1.1.2 Comparison of Properties of Smart Materials: Promises of FeGa Alloys ...	4
1.1.3 Actuator and Sensing Application of Magnetostrictive FeGa .....	6
1.2 Basic Principle of Actuation and Sensing with Magnetostrictive Materials ....	10
1.2.1 Actuation Under Constant Pre-load .....	12
1.2.2 Sensing Behavior .....	14
1.3 Physics of Ferromagnetic and Magnetostrictive Materials.....	15
1.3.1 Atomic Magnetism.....	15
1.3.2 Paramagnetism and Ferromagnetism: Role of Exchange Coupling .....	17
1.3.3 Magnetocrystalline Anisotropy and Magnetostriction.....	17
1.3.4 Domains in Ferromagnetic Materials.....	20
<i>Formation of domains: micro-magnetics</i> .....	20
<i>Domain walls and domain wall motion</i> .....	22
1.4 Survey of Constitutive Models for Magnetomechanical Behavior.....	22
1.4.1 Preisach Model: Hysteresis Operators .....	23
1.4.2 Linear Constitutive Equations.....	23
1.4.3 Non-linear Constitutive Equations.....	25
1.5 Background on Metallurgy and Crystal Structure of Iron Gallium Alloys: .....	27
1.6 Organization and Contributions of this Dissertation .....	31
<b>Chapter 2: Magnetic Issues.....</b>	<b>36</b>
2.1 Introduction.....	36
2.1.1 Potential Formulation of the Magnetostatic Problem .....	37
2.1.2 Demagnetization Effect and its Influence on the Magnetization Curve ....	38
2.2 Developing and Benchmarking a FEM Module .....	40
2.2.1 Development of FEM Model .....	40
2.2.2 Benchmarking the 2-D Axisymmetric FEM Model by Studying De-	
magnetization in an Ellipsoidal Shaped Object	41
2.3 Insights from Finite-Element Model of Iron-Gallium Cylinder Samples with	
End Caps .....	46
2.4. Experimental Results with Hall-Chips and Sense Coils Located at Various	
Places .....	52
2.5 Conclusions.....	56

2.6 Summary .....	58
<b>Chapter 3: Experimental Single-crystal Actuation and Sensing Behavior .....</b>	<b>59</b>
3.1 Magnetic Transducer .....	60
3.1.1 Description of Magnetic Transducer .....	61
3.1.2 Sample Preparation and Mounting.....	62
3.1.3 Instrumentation .....	62
3.2 Actuator Behavior .....	65
3.2.1 Actuation Characterization Procedure .....	65
3.2.2 Effect of Gallium Content on Actuator Characteristics .....	66
3.2.4 Repeatability of Data .....	71
3.2.5 Effect of Crystallographic Direction on Actuator Characteristics .....	73
3.3 Sensing Behavior .....	76
3.3.1 Sensing Characterization Procedure .....	76
3.3.2 Constant Drive Current vs. Constant Field Characteristics .....	78
3.3.3 Effect of Crystallographic Direction on Sensing Characteristics .....	80
3.4 Summary of Actuation and Sensing Behavior of Single Crystals .....	83
<b>Chapter 4: Energy-based Model for Single-Crystal Quasi-static Actuation Behavior .....</b>	<b>85</b>
4.1 Modeling Objectives, Literature Survey and Background .....	86
4.1.1 Modeling Objectives .....	86
4.1.2 Literature Survey .....	86
4.1.3 Background: Energy Terms and Thermodynamic Concepts .....	88
4.2 Model Formulation .....	93
4.2.1 Armstrong Model for Cooperative Movement of Moments:.....	94
Domain Movement .....	94
4.2.2 Temperature Effects on Alignment of Moments within a Domain .....	98
4.3 Model Simulation of Thermal Effects .....	101
4.4 Simulation of FeGa Single-Crystal Actuator Behavior with Varied Ga Content .....	103
4.4.1 Magneto Mechanical Behavior of 19 at. % Ga Sample.....	103
4.4.2 Magnetomechanical Behavior of 24.7 at. % Ga Sample .....	106
4.4.3 Magnetomechanical Behavior of 29 at. %Ga Sample .....	109
4.4.4 Discussion of Effect of Ga Content .....	111
4.4.5 Analysis of Sensitivity to Model Parameters: Introduction of a Non-Dimensional Parameter for Smoothing.....	114
4.5 Simulation of Actuator Behavior in Various Crystallographic Directions.....	118
4.5.1 Magnetomechanical Behavior in <110> Direction.....	118
4.5.2 Predicted Behavior in <111> Direction .....	121
4.6 Predicted Behavior Under Tension.....	122
4.7 Summary .....	123
<b>Chapter 5: Modeling the Sensing Behavior (Villari-Effect) &amp; Interaction with Magnetic Circuit .....</b>	<b>126</b>
5.1 Energy Model Application to Sensing Behavior .....	127
5.1.1 Formulation.....	128

5.1.2 Simulation of Behavior Along $\langle 100 \rangle$ .....	129
5.1.3 Simulation of Behavior Along $\langle 110 \rangle$ .....	132
5.1.4 Prediction of Behavior Along $\langle 111 \rangle$ .....	135
5.1.5 Prediction of Behavior of 24.7 and 29 % at. % Ga $\langle 100 \rangle$ FeGa Samples .....	136
5.2 Coupling Magnetic Energy-based Model with Lumped Parameter Model for Interaction with Magnetic Circuit.....	138
5.2.1 Formulation of Coupled Model .....	138
5.2.2 Comparison of Coupled Model with Experimental Data .....	141
5.3 Conclusions.....	144
<b>Chapter 6: Characterization and Analysis of Actuation and Sensing Behavior of Polycrystals.....</b>	<b>146</b>
6.1 Experimental Characterization.....	149
6.1.1 Test Set-up and Procedure .....	150
6.1.2 Manufacturing Process and Variability in Actuator Behavior:.....	151
6.1.3 Final Actuator and Sensor Data and Discussion.....	152
6.2 Texture Analysis .....	155
6.3 Simple Rule of Mixture Model for Polycrystals.....	157
6.4 Model Predictions and Comparison with Experimental Data.....	160
6.4.1 Methodology of Choosing Model Parameters .....	160
6.4.2 Simulation Results for Various Crystallographic Directions.....	161
6.4.3 Simulation of Polycrystalline Behavior and Benchmarking.....	166
6.5 Discussion of $\mu_r$ , $d_{33}$ , $d_{33}^*$ and $E^H$ Estimated by the Model.....	169
6.6 Possible Cause of Variation in Data .....	171
6.6 Conclusions.....	173
<b>Chapter 7: Summary and Conclusions.....</b>	<b>174</b>
7.1 Summary of Research.....	174
7.2 Important Contributions from this Research.....	182
7.3 Future Research Directions.....	184

## List of Conventions

1.  $\langle \ \rangle$  indicates a family of crystallographic directions.
2.  $[ \ ]$  represents a particular crystallographic directions.  
For example, in a cubic crystal  $\langle 100 \rangle$  represents  $[100]$ ,  $[-100]$ ,  $[010]$ ,  $[0-10]$ ,  $[001]$  and  $[00-1]$ .
3.  $\text{Fe}_{81}\text{Ga}_{19}$  also written as 19 at. % Ga, FeGa alloy is used to indicate that the FeGa alloy contains 19 atoms of Gallium for every 81 atoms of Iron, i.e. the Ga content is denoted by percentage of atoms and NOT by percentage mass of Ga.

### COMMONLY USED SYMBOLS

H : Magnetic field

B : Magnetic induction

D: Electric Displacement

M : Magnetization

P: Electric Polarization

$\lambda$  : Magnetostriction

$\sigma$  : Stress

$\epsilon$  : Strain

$\mu_R$  : Relative permeability

$\mu_0$  : Permeability of free-space

E : Young's Modulus (also used for Electric Field)  $E_{\text{subscript}}$  : Energy terms

S : Compliance

$d_{33}$ : Piezo-magnetic coefficient

$d_{33}^*$ : Inverse Piezo-magnetic coefficient, sensitivity

Note: All direction cosines are with respect to the  $\langle 100 \rangle$  directions of a cubic crystal

$(\alpha_1, \alpha_2, \alpha_3)$  : Direction cosines for orientation of magnetic moment

$(\beta_{1F}, \beta_{2F}, \beta_{3F})$  : Direction cosines of magnetic field

$(\beta_{1s}, \beta_{2s}, \beta_{3s})$  : Direction cosines of stress

## Chapter 1: Introduction

Smart materials display a large coupling of thermal, electrical or magnetic properties with mechanical properties enabling them to directly transduce energy from one form to another in an efficient manner. These properties have made them promising materials for actuation and sensing applications.

Over the past two decades various smart materials, viz. shape memory alloys, piezo-electrics and magnetostrictive materials, which respectively transduce thermal, electrical and magnetic energy to mechanical energy, have been used as actuators and sensors in a wide range of fields: medicine, micro-positioning, atomic force microscopes, torque sensing and fuel injection systems in automobiles, sonar transducers for the Navy and control surfaces of helicopters and aircrafts.

Traditionally, shape memory alloy (SMA) and piezo-electric materials have been studied for their application in control and actuation of aerospace structures and some of these technologies are being tested for in-flight applications [**Kennedy2002, Kudva1996**]. Shape memory alloy actuators are well suited to high stroke low bandwidth applications such as for in-flight tracking of rotor blades. On the other hand, piezo-electric materials have found direct application in low stroke, high bandwidth applications such as actuation of trailing edge-flaps in helicopters for reduction of higher harmonic vibrations [**Chopra2002**].

Magnetostrictive materials, which have conventionally been restricted to application in sonars, appear poised to play an increasingly important role in other applications such as active vibration control, actuating control surfaces and stress and torque sensing in helicopters, aircrafts and automobiles. One of the reasons for the promise of these materials in a host of applications is the development of a new class of magnetostrictive alloy, Iron-Gallium alloys (Galfenol), by researchers at the Naval Surface Warfare Center [**Clark2001a**]. These alloys exhibit moderate magnetostriction (~350 ppm) under very low magnetic fields (~100 Oe), have very

low hysteresis, demonstrate high tensile strength (~500 MPa) and limited variation in magnetomechanical properties for temperatures between  $-20^{\circ}\text{C}$  and  $80^{\circ}\text{C}$  [Kellogg2003b]. These materials are in general (for Ga content less than 20 at. %), machinable, ductile and can be welded. Thus they can be easily threaded, attached to existing structures and can be used as load bearing members. They have a high Curie temperature ( $675^{\circ}\text{C}$ ) [Kellogg2003b] and preliminary studies at the Naval Surface Warfare Center and Defense Research and Development Canada, indicate they are corrosion resistant and their properties do not degrade over time. The raw material cost to produce FeGa is about \$0.08/g compared to \$0.50/g for Terfenol-D [Kellogg2003b]. All these factors demonstrate that FeGa has great promise as an engineering material for actuation and sensing applications.

A comprehensive understanding of the magnetomechanical behavior of these alloys will facilitate the optimized design and control of actuators and sensors. With this objective, the dissertation focuses primarily on characterization and modeling of the magnetomechanical behavior of single crystal FeGa alloys with varying gallium content and along different crystallographic directions, and studying the effect of cross-section texture on magnetomechanical behavior of polycrystals. Improved generic testing and modeling paradigms for magnetostrictive materials that could contribute to a better understanding of actuation and sensing behavior of the FeGa alloy are developed. A material characteristics database of FeGa alloy properties is presented that should prove useful in the design of smart actuators and sensors based on this material.

This introductory chapter starts with an overview of the role of magnetostrictive materials, particularly FeGa, in smart structures (Section 1.1). This is followed by a description of the general principles of actuation and sensing with magnetostrictive materials (Section 1.2), physics of magnetostrictive materials (Section 1.3) and current state of the art in modeling magnetostrictive materials (Section 1.4). Section 1.5 provides a background on metallurgical aspects of FeGa alloys, while Section 1.6 highlights the contribution of this thesis toward a better

understanding of the magnetomechanical behavior of single crystal and polycrystalline FeGa alloys.

### **1.1 Overview of Magnetostrictive FeGa Alloys**

This section starts with a brief history of the development of magnetostrictive materials. This is followed by a comparison of the properties of various smart materials, viz. shape memory alloys, piezoelectric and magnetostrictive materials; highlighting the promises of magnetostrictive FeGa alloys. Finally, various applications for different configurations of magnetostrictive actuators and sensors are discussed with an emphasis on utilizing some of the novel properties of FeGa alloys to enhance these applications.

#### **1.1.1 Historical Development of Magnetostrictive Materials**

Magnetostrictive nickel-based alloys (magnetostriction ~50 ppm) were employed in building transducers for SONAR applications in World War II. In the 1960's, it was observed that rare-earths such as Terbium and Dysprosium exhibited large magnetostriction (~10,000 ppm) at low temperature but did not produce significant magnetostriction at room temperature due of their low Curie temperature. This led to attempts in alloying the rare-earths with 3-d transition elements that exhibit higher Curie temperatures, such as iron, to produce alloys that would exhibit large magnetostriction at room temperatures. For example, at room temperature TbFe<sub>2</sub> and DyFe<sub>2</sub> exhibit  $3/2(\lambda_s)$  of 2630 ppm and 650 ppm respectively [Engdahl 2000]. Both these alloys have large magnetocrystalline anisotropies and require large magnetic fields to drive them to saturation. However, the magnetocrystalline anisotropy can be considerably reduced by adding both Tb and Dy in the correct proportion. This lead to the development of the alloy Tb<sub>.27</sub>Dy<sub>.73</sub>Fe<sub>1.95</sub> (commercially known as Terfenol-D) which exhibits large magnetostriction (~2000 ppm) at room temperatures and has considerably lower magnetocrystalline anisotropy than either TbFe<sub>2</sub> or DyFe<sub>2</sub>. One of the drawbacks of Terfenol-D is that it is brittle, which limits its ability to withstand shock loads or operate in tension.

Iron-Gallium alloys developed at the Naval Surface Warfare Center by Clark *et al.* [Clark 2001 a, b Cullen 2002] appear to be promising materials for a variety of actuator and sensing applications. They exhibit moderate magnetostriction (~350 ppm) under very low magnetic fields (~100 Oe) and have very low hysteresis, while demonstrating high tensile strength (~500 MPa) and limited dependence of magnetomechanical properties on temperatures between -20°C and 80°C [Kellogg 2002, 2003b, 2004]. Furthermore, the ability of these alloys to withstand shock loads and harsh operating environments and to operate in tension is likely to significantly expand the design-space for use of magnetostrictive materials in the field of smart structures.

The effect of alloying iron with other 3<sup>rd</sup> group elements, Aluminum and Beryllium, has also been investigated [Cullen 2002, Clark2004]. While both FeGa and FeAl alloys exhibit similar trends upto 25 at. % of Ga or Al, magnetostriction ( $\lambda_{100}$ ) of FeGa is more than twice that of FeAl at the first peak which occurs at ~19 at. % Ga or Al. FeBe alloys, investigated upto 11 at. % Be, show magnetostriction similar to FeGa, but the high toxicity of Be makes FeBe alloys difficult to obtain. Furthermore limited studies to date have shown that ternary alloys of Fe and Ga with nickel, molybdenum, tin, aluminum and cobalt at best do not significantly improve its magnetostrictive properties and have a detrimental effect at some critical compositions [Restorff2002, Dai2003]. Thus, this thesis focuses on the characterization and modeling of the magnetomechanical behavior of binary single crystal and polycrystalline FeGa alloys.

### 1.1.2 Comparison of Properties of Smart Materials: Promises of FeGa Alloys

The properties of a typical shape memory (Nickel Titanium alloy), piezoelectric (Lead Zirconium Titanate) and magnetostrictive material (Terfenol-D) used in engineering applications as well as 19 at. % Ga single-crystal FeGa alloy are discussed and compared (Table 1.1). Shape memory alloys demonstrate upto 6% recoverable strain, nearly two orders of magnitude higher than other materials, making them well suited to applications that require large stroke or deformations.

However, they have a very low bandwidth as they are thermally actuated. The response time could take as long as a few minutes in large structures, such as morphing wings, due to the large time involved in cooling a moderately large embedded thermal mass.

**Table 1.1** Comparison of material properties of various smart materials.

Compiled from [Chopra2002], [Dapino1999] and [Kellogg2003b].

<b>Materials Property</b>	<b>NiTi</b> (Shape memory alloy)	<b>PZT-5H</b> (Piezo-ceramic)	<b>Terfenol-D</b> (Magneto-strictive)	<b>Galfenol</b> (Magneto-strictive)
<b>Free Strain/</b> Magnetostriction (ppm)	60,000	1000	1600-2400	300-400
<b>Modulus</b> E (GPa)	~20(martensite) ~50 (austenite)	~60	25-35	~60
<b>Tensile Strength</b> <b>(Ductile/Brittle)</b>	High (Ductile)	27.6 MPa (Brittle)	28 MPa (Brittle)	500 MPa (Ductile)
<b>Actuation requirement</b>	Heating through ~60°C	~5kV/cm Electric field	~1000 Oe Magnetic field	~100 Oe Magnetic field
<b>Bandwidth</b>	0-1Hz	0.1Hz- ~1MHz	0Hz- ~1MHz	0Hz- ~1MHz
<b>Linearity</b> Strain-voltage OR (Strain-temp for SMA)	Highly non-linear (large hysteresis)	First Order Linear (small hysteresis)	Non-linear (moderate hysteresis)	Non-linear (low hysteresis)

In contrast, piezo-electric and magnetostrictive materials demonstrate very high bandwidth (~100 KHz) but maximum strains of the order of 0.1% making them well suited to low stroke and high frequency applications such as vibration control and production of sonars. However, a suitable stroke amplification

mechanism can be used to convert the high frequency, low stroke to a low frequency high stroke output. Between piezo-electric and magnetostrictive materials, the former require very large electric fields ( $\sim 5$  kV/cm) and may suffer from self-heating problems while the latter require current carrying coils to produce varying magnetic fields, which can make the actuator bulky. Magnetostrictive FeGa alloys have certain unique properties, which may make them better suited than either piezo-electrics or Terfenol-D in certain actuation and sensing applications. For example, the high tensile strength (20 times that of typical piezo-electric and Terfenol-D) may enable the use of these alloys as actuators and sensors in harsh and shock prone environments, such as torque sensors in rotor and automobile transmission shafts, sensors for detection in the presence of underwater explosions, as actuators under tension or tensile/bending sensors, etc. Since, the bias field required is low ( $\sim 10$  times smaller than Terfenol-D), and may be achieved with a small permanent magnet, they show promise for compact and rugged devices.

Additionally, FeGa being ductile and easy to deposit epitaxially on a silicon substrate [Weston2002] makes it well suited for sensing applications on the micro-scale, while FeGa nano-wires [Stadler2005] may hold promise in miniaturized acoustic and tactile sensors.

### **1.1.3 Actuator and Sensing Application of Magnetostrictive FeGa**

This subsection explores various possible applications for magnetostrictive materials as actuators and sensors with an emphasis on utilizing some of the novel properties of FeGa alloys to enhance these applications.

#### *Actuator applications*

Magnetostrictive materials are capable of actuation at very large frequencies ( $\sim 20,000$  Hz) but the strain produced ( $\leq 1500$  ppm) and consequently stroke generated is extremely small. This may be overcome using a bi-directional hybrid pump [Sirohi2003] driven by the magnetostrictive material as shown in Figure 1.1. Such a configuration can rectify the output of the piston driven by a laminated

magnetostrictive material at  $\sim 5000$  Hz and drive the output cylinder at  $\sim 5$  Hz. This corresponds to the rotational speed of a typical helicopter rotor and thus the  $\sim 5$  Hz output can be used for primary rotor control. A 1000 fold decrease in output frequency and the same order of magnitude increase in stroke may be obtained. Such a device has promise in actuating the pitch-link of a helicopter at 1/rev for the purpose of primary rotor control.

Another application of magnetostrictive materials is in the production of sonar devices (Figure 1.2). This is a direct application of magnetostrictive actuation without any necessity for stroke amplification and has been popular with the Navy for the past 4-5 decades. Sonars made from FeGa alloys have the potential advantage of being able to withstand underwater shocks and explosions.

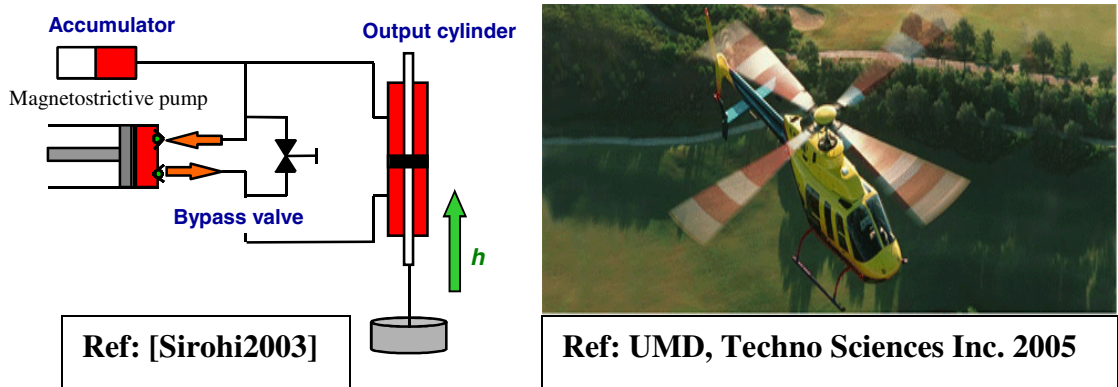


**Figure 1.1** Stroke amplification using a bi-directional hybrid pump (left). Possible use in active pitch control (right).

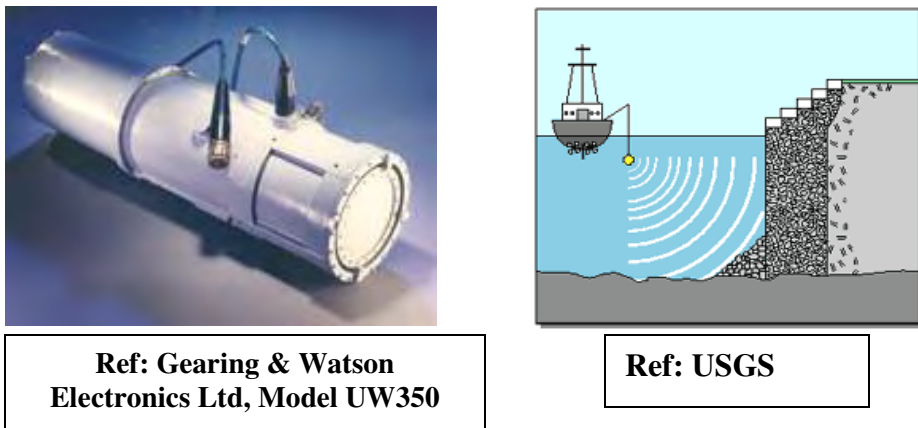


**Figure 1.2** direct applications of magnetostrictive materials in sonar.

*Sensing applications*

A magnetostrictive rod can be used as a macroscopic force or pressure sensor as illustrated in Figure 1.3(a). The rod is magnetized by a DC-bias field which is applied by the drive coil through the ferrite core (magnetic circuit). On application of a force or vibrations, the magnetization of the magnetostrictive sample undergoes a change which can be detected by the change in flux through a sensing coil wound around the sample. An example of a non-contact torque sensor based on an active magnetostrictive magnetic circuit is shown in Figure 1.3(b), where two magnetostrictive strips are bonded to the shaft under torsion load at  $\pm 45^\circ$ . The torque on the shaft produces a tension in one strip and compression in the other, leading to a change in magnetization of both the strips. Furthermore, the reluctance of these strips changes, leading to a difference in the longitudinal field in them. Both these effects can be employed in sensing torque as the shaft rotates relative to a stationary magnetic sensor. FeGa alloys are particularly well suited to this application as they can withstand tensile loads and can operate in harsh environments.

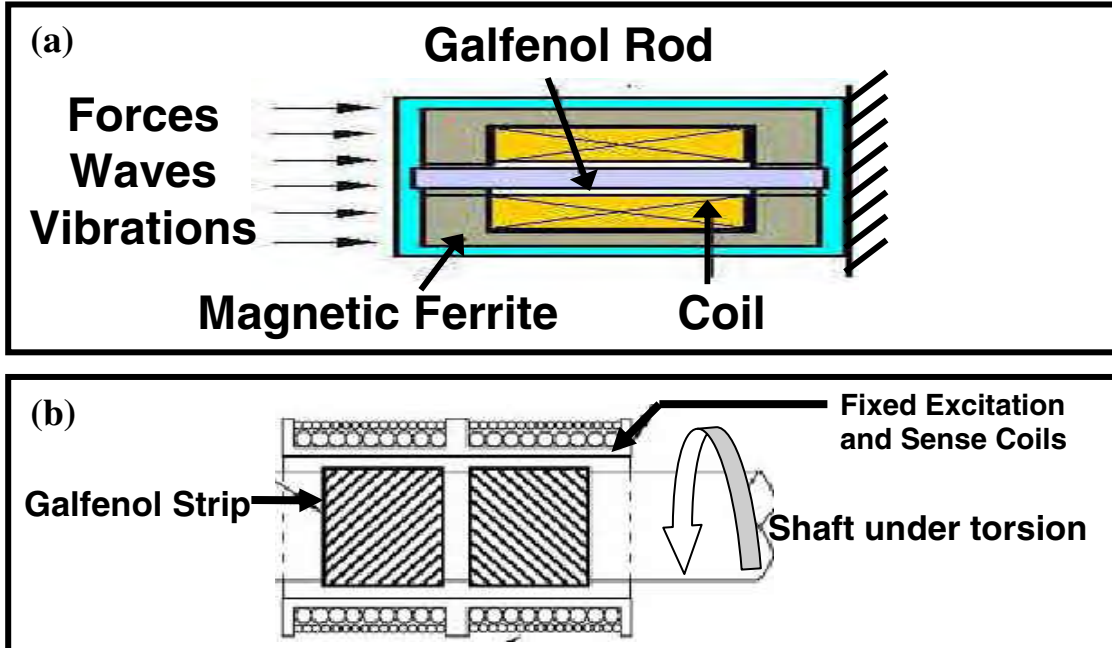


**Figure 1.3** (a) Magnetostrictive force sensor.

(b) Magnetostrictive torque sensor.

Various other configurations for torque sensors as well as position, motion and force sensors are discussed by Calkins *et al.* [Calkins 1999]. Innovative designs for magnetostrictive torque sensors, such as magnetostrictive rings with oppositely polarized circumferential regions [Garshelis1996], have improved the reliability and robustness of this technology.

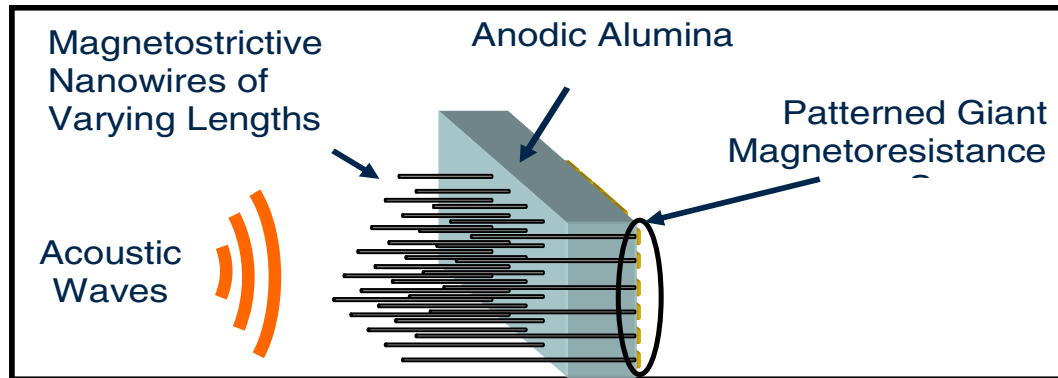


**Figure 1.4** Illustration for application of magnetostrictive nanowires as acoustic sensors [Stadler2005].

At the micro-scale, thin film and MEMS fabrication technologies offer drastic size reduction, cost effectiveness and increased sensitivity and robustness of magnetostrictive sensors. In particular, the fact that FeGa is ductile and can be deposited epitaxially on a silicon substrate makes it well suited to sensing applications on the micro-scale [Weston2002]. Magnetostrictive FeGa nano-wires also appear to hold great promise in miniaturized acoustic sensors as illustrated in Figure 1.4, capable of spatially resolving a large spectrum of acoustic signals by growing nano-wires of different aspect ratios, each sensitive to a small band of frequencies [Stadler2005].

#### *Promises of FeGa Alloys*

In summary, machinability, ductility, weldability, high Curie temperature (675°C) and low raw-material cost [Kellogg2003b] make FeGa an attractive low-cost actuator and sensor material well suited to applications in harsh environments, capable of being easily integrated with a structure and functioning as a load bearing

member. Its corrosion resistance, fatigue properties and stability of properties over time are likely to make it a reliable engineering material. Furthermore, FeGa demonstrates potential for micro-scale actuation and sensing applications as discussed in the previous subsection.

### **1.2 Basic Principle of Actuation and Sensing with Magnetostrictive Materials**

This section describes the basic principle of actuation and sensing with magnetostrictive materials using a simplified description of the underlying process. A more detailed description of the physics of magnetostrictive materials is dealt with in Section 1.3 and serves as a background for the energy-based modeling in this dissertation.

Magnetostrictive materials are a special subset of ferromagnetic materials that exhibit a strong coupling between the direction of the magnetization and length of the sample. Therefore the length of the sample can be changed by magnetizing it along a particular direction and conversely its magnetization can be changed by applying a stress. The principle behind this coupling can be explained with the example of Fe and some of its magnetostrictive alloys, such as FeGa. At room temperatures, these materials have a tetragonal structure with one of the  $\langle 100 \rangle$  directions longer than the other two. The elongated side is known as the long axis and the magnetization or magnetic moment of the material points in this direction.

Figures 1.5 and 1.6 illustrate the magnetization and magnetostriction process in a typical cubic magnetostrictive material on the application of a magnetic field. In the zero-field case (A), the magnetic moments are equally distributed between all six  $\langle 100 \rangle$  directions with the net magnetization along any direction equal to zero. As a magnetic field is applied in one of these directions, for example  $[001]$  direction, all the moments reorient towards this direction. This produces large magnetization in this direction and the sample also elongates in this direction while shortening in the directions perpendicular to it. At sufficiently high fields the material reaches a state of saturation magnetization and magnetostriction, case B, where all moments are

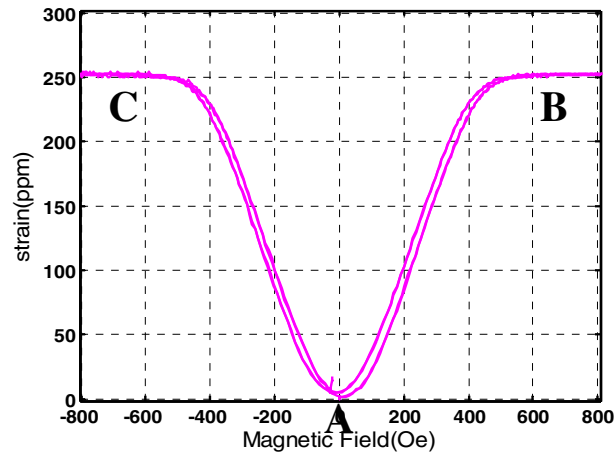


**Figure 1.5** Representative  $\lambda$ -H curve.

A, B and C refer to the different magnetization states of the material.

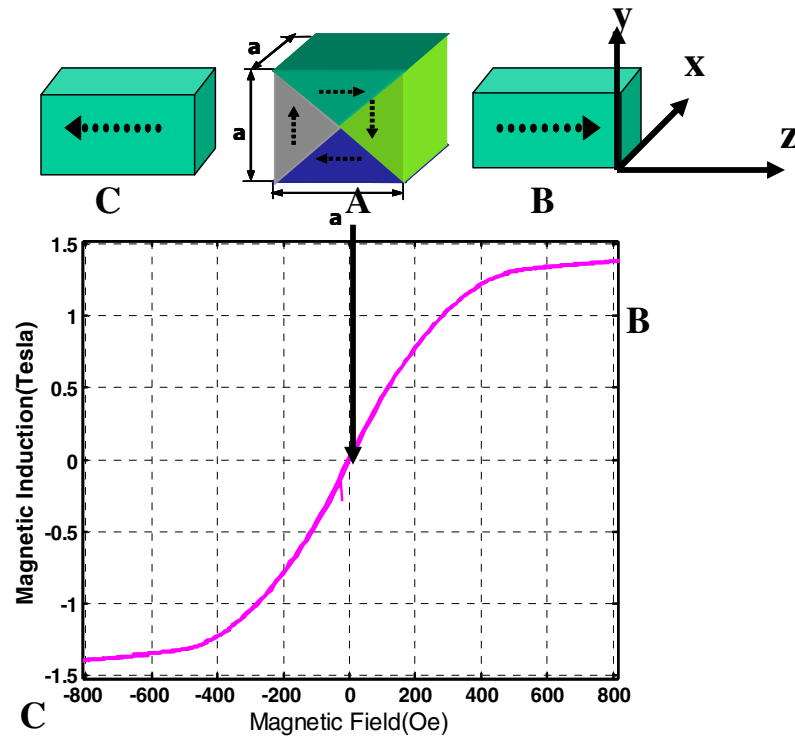


**Figure 1.6** Representative B-H curve and schematic depicting simultaneous constant volume shape change and magnetic moment reorientation with applied field.

*NOTE: for ease of illustration moments are shown in a single plane.*

*Source: Some illustrations adapted from presentation by Dai 2003.*

oriented along the [001]. Upon reversing the direction of the field, case C, all moments reorient along the [00-1] direction. Irrespective of whether the magnetic moments orient along the [001] or [00-1], i.e. positive or negative z-direction, the long axis of the material is oriented along the z-axis and leads to a net increase in length or positive magnetostriction in the z-direction.

Typically, there is a large resistance to the reorienting of magnetic moments either due to some intermediate orientations not being energetically favorable (referred to as magnetocrystalline anisotropy which is discussed at length later in this chapter) or due to pinning of these moments by defects in the material. The latter effect could lead to a large hysteresis in the B-H curves.

### **1.2.1 Actuation Under Constant Pre-load**

Compressive stress favors the orientation of the short axes along the direction in which it is applied, i.e. parallel to the rod axis. Thus on application of sufficiently high compressive stress, the long axis is oriented perpendicular to the rod axis (depicted in a cartoon in Figure 1.7(a)). On application of magnetic field (H) along the axis of the rod, magnetic moments begin to overcome the compressive stress and rotate to orient parallel to the rod axis, thus causing an increase in both magnetization and magnetostriction along the rod axis.

At sufficiently high stress, all the long axes are oriented perpendicular to the rod-axis and the sample is at its shortest length. Therefore, the total magnetostriction or change in length that can be obtained on magnetizing the sample will be higher with this level of initial stress than for the zero and low stresses cases. Increasing the initial stress beyond the lowest stress level that aligns long axes perpendicular to the rod axis requires application of greater magnetic fields to overcome this mechanical load and orient the long axis parallel to the rod. Thus, larger fields are required to obtain saturation magnetization and magnetostriction at higher values of compressive stress.

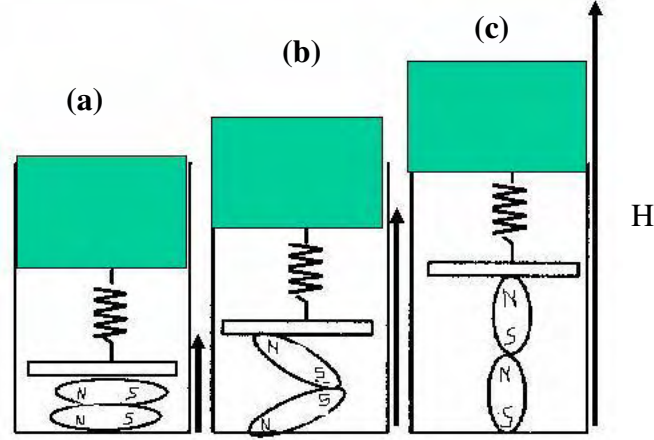


**Figure 1.7** Schematic depicting actuation behaviors in magnetostrictive materials as simple rotations of elliptical magnets. (Arrows show increasing applied field ( $H$ ) going from Figure 1.7 (a) through (b) to (c) under a constant stress state.)

This principle is useful in defining saturation magnetostriction,  $\lambda_{sat}$ , for a given sample or crystallographic direction. For example  $\lambda_{sat}$  in the  $\langle 100 \rangle$  direction is the difference between the  $\lambda_{\parallel}$  and  $\lambda_{\perp}$ . The magnetostriction obtained when all the domains (a grouping of many similarly aligned magnetic moments) are oriented parallel to one of the  $\langle 100 \rangle$  directions such as  $[100]$  is defined as  $\lambda_{\parallel} = \lambda_{100}$ . When they are all oriented perpendicular to the  $[100]$  direction, the magnetostriction along the  $[100]$  direction is  $\lambda_{\perp} = -\frac{1}{2}\lambda_{100}$  (constant-volume magnetostriction). This leads to:

$$\frac{3}{2} \lambda_{sat} = \lambda_{\parallel} - \lambda_{\perp} = \lambda_{100} - \left(-\frac{1}{2} \lambda_{100}\right) = \frac{3}{2} \lambda_{100} \quad (1.1)$$

Since the magnetization in the material is strongly influenced by the mechanical loading, the permeability (change in induction for incremental change in field) is often defined for two cases: a constant stress condition ( $\mu^{\sigma}$ ) and a constant strain condition ( $\mu^{\epsilon}$ ). To change the magnetization of a material without producing a net strain, the compressive stress has to be increased so as to compensate for the strain produced due to magnetostriction. Consequently, a greater incremental magnetic field is required to produce the same change in magnetization under constant strain than under constant stress conditions, i.e.  $\mu^{\epsilon}$  is smaller than  $\mu^{\sigma}$ .

### 1.2.2 Sensing Behavior

A magnetostrictive material in the absence of magnetic fields or stress consists of randomly oriented magnetic moments. On the application of a magnetic field along the longitudinal axis, the moments (and long axis) align with the field producing a large magnetization (Figure 1.8 (a)). However, compressive stress favors a magnetization orientation perpendicular to the sample longitudinal axis. When the compressive stress applied to the specimen reaches a certain critical value, the moments (long axes) oriented parallel to the rod axis begin to rotate through  $90^\circ$  and orient perpendicular to the rod axis (Figure 1.8 (b)). This leads to a decrease in magnetization with increasing compressive stress. When the applied stress is large enough to have caused a complete rotation of all the magnetic moments, any further increase in stress causes no further change in magnetization (Figure 1.8 (c)).

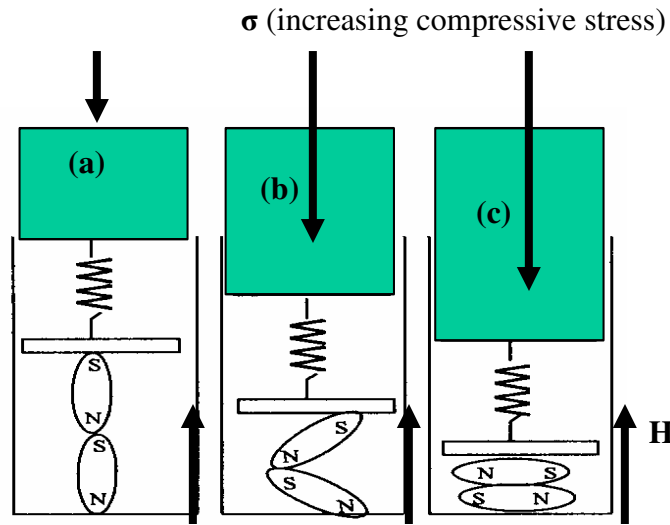


**Figure 1.8** Schematic depicting sensing behaviors in magnetostrictive materials as simple rotations of elliptical magnets. (Arrows show increasing compressive stress ( $\sigma$ ) going from 1.8 (a) through (b) to (c), under a fixed applied magnetic field.)

The compressive strain produced in a magnetostrictive material is comprised of the sum of elastic strain due to compressive stress and decrease in longitudinal dimension due to reorientation of magnetic moments. At low stress values, in the presence of a longitudinal magnetic field (before moments begin to reorient), the

strain due to the elastic effect dominates. In the *critical stress* range, moment reorientation occurs, producing a decrease in magnetostrictive strain which adds to the elastic compressive strain. This results in an increased compliance (lowering of Young's Modulus). However, at large stresses, when all the moments have reoriented, strain is predominantly elastic and the compliance asymptotically approaches a constant value.

Since, the strain in the material is strongly influenced by the material's magnetic state, the Young's modulus can be defined for two cases: constant magnetic-field conditions ( $E^H$ ) and constant magnetic induction conditions ( $E^B$ ). In the case of strain under constant magnetic induction, there is no decrease in strain due to re-orientation of the magnetic moment. Consequently, a greater incremental stress is required to produce the same change in strain under constant magnetic induction than under constant magnetic field condition, i.e.  $E^B$  is larger than  $E^H$ .

### **1.3 Physics of Ferromagnetic and Magnetostrictive Materials**

This section starts with the atomic basis of magnetism, followed by a discussion of magnetism in solids, the origin of magnetocrystalline anisotropy and magnetostriction in crystals. A short discussion on domains and domain wall motion is presented as it serves to bridge the gap between microscopic origin of magnetostriction and magnetomechanical behavior of bulk materials. These topics lay the groundwork for energy based models for bulk materials.

#### **1.3.1 Atomic Magnetism**

Considering the classical Bohr model of an atom as depicted in Figure 1.9, an electron of charge  $e^-$  in an orbit of radius  $r$  moving around a path enclosing an area ( $A=\pi r^2$ ) with an angular velocity of  $\omega$  (rad/s), constitutes a current ( $I$ )

$$I = \frac{-e\omega}{2\pi} \quad (1.2)$$

and a magnetic moment (M)

$$M = \mu_0 (I) A \quad (1.3)$$

Substituting I from Equation 1.2 and  $A=\pi r^2$  in Equation 1.3, the magnetic moment can be expressed in terms of the radius, angular velocity and electron charge:

$$M = -\mu_0 \left( \frac{e\omega}{2\pi} \right) \pi r^2 \quad (1.4)$$

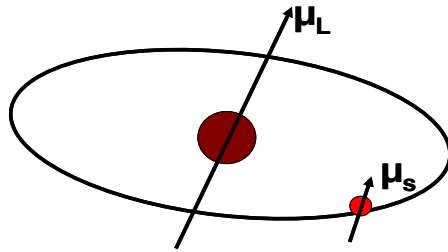


**Figure 1.9** Diagram illustrating the orbital and spin magnetic moments of an electron.

The angular momentum of the electron, P, is quantized and is an integral multiple of  $\hbar$  (where  $\hbar=h/2\pi$  and  $h= 6.63*10^{-34}$  joule-sec is the Planck's constant).  $l$  is the orbital quantum number and can take integral value 0,  $\pm 1$ ,  $\pm 2$ , etc.

$$P = m \omega r^2 = l \hbar \quad (1.5)$$

From Equations 1.4 and 1.5, the orbital magnetic moment of the electron can be written as:

$$M = \frac{-\mu_0 e \hbar}{2m} l = M_B l \quad (1.6)$$

where  $M_B=1.165*10^{-29}$  is known as the Bohr Magnetron.

Equation 1.6 describes the orbital magnetic moment. However, there is another magnetic moment which arises from the intrinsic angular momentum of an electron associated with its spin. This can be expressed as  $P=s\hbar$ , where  $s=\pm 1/2$  is the spin number for the electron.

In atoms with multiple electrons, the sequence of filling of different orbitals with electrons is determined by Hund's rule, which is discussed in detail in [Chikazumi1964]. This electronic configuration determines the total, i.e.

spin+orbital, magnetic moment of the atom or ion, which in turn plays a significant role in determining the magnetic properties of the species.

### **1.3.2 Paramagnetism and Ferromagnetism: Role of Exchange Coupling**

In materials with a net magnetic moment, the moments locally tend to align with an applied magnetic field. This produces a magnetization in the material in the direction of the applied magnetic field that is known as paramagnetism. In certain solids, such as iron, nickel and cobalt, at room temperature, the moments in neighboring ions are strongly coupled (exchange coupling) and tend to align with each other. This alignment can lead to spontaneous magnetization in the material even in the absence of magnetic fields and is known as ferromagnetism. At sufficiently high temperature, the thermal energy exceeds the exchange coupling energy between spins and breaks this alignment, leading to a paramagnetic state. The temperature at which this transition from ferromagnetic to paramagnetic state or vice-versa occurs is known as the Curie temperature.

### **1.3.3 Magnetocrystalline Anisotropy and Magnetostriction**

Magnetocrystalline anisotropy is the tendency of the magnetic moment in an atom to orient along a particular crystallographic direction as opposed to equiprobable distribution of moments along all directions. This is typically seen in atoms with incompletely filled inner shells that leads to both the creation of a net magnetic moment and an anisotropic shape to the electronic charge distribution (electronic charge cloud) [Engdahl2000]. In such atoms, rotation of the magnetic moment would tend to change the attraction or repulsion between the electronic charge cloud coupled (almost attached) to it and the neighboring ions, as illustrated by the schematic in Figure 1.10. This causes certain orientations of the magnetic moment with respect to the crystallographic axes to be more energetically favorable than others. Furthermore, in response to the change in orientation of the magnetic moment, neighboring ions tend to shift their positions, leading to magnetostriction.

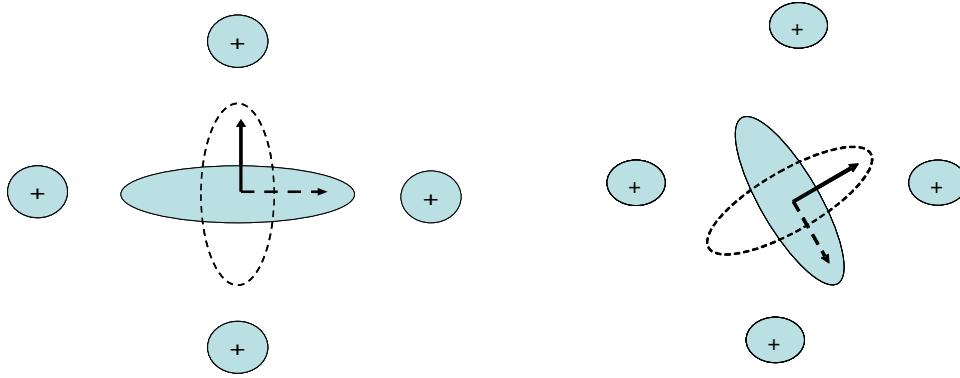


**Figure 1.10** Schematic of oblate 4f charge density of a rare earth element with + nearest neighbors, such as Tb (Terbium), rotating in a magnetic field.

Source: [Engdahl2000], contributing authors Clark and Hathaway.

A phenomenological expression for the magnetocrystalline anisotropy of a cubic lattice (Figure 1.11) may be derived from the spin-pair model as discussed in detail by Chikazumi [Chikazumi1964]. The final expression for magnetocrystalline anisotropy is:

$$E_{magnetocrystalline} = K_1 * (\alpha_1^2 \alpha_2^2 + \alpha_1^2 \alpha_3^2 + \alpha_2^2 \alpha_3^2) + K_2 * \alpha_1^2 \alpha_2^2 \alpha_3^2 \quad (1.7)$$

where  $K_1$  and  $K_2$  are the two magnetocrystalline anisotropy constants and  $(\alpha_1, \alpha_2, \alpha_3)$  are the direction cosines for the orientation of the magnetic moment. The typical value of  $K_1$  at room temperature drops from 48 kJ/m<sup>3</sup> for pure Fe through ~18 kJ/m<sup>3</sup> for ~19 at. % Ga, to nearly zero at ~20 at. % Ga in FeGa samples [Rafique2004].

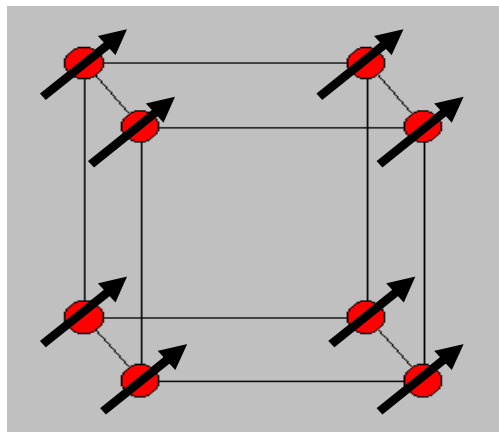


**Figure 1.11** Ferromagnetic spins in a simple cubic lattice. Source [Chikazumi1964].

An expression for magnetostriction of a cubic lattice may be derived using a spin-pair model with variable bond length (Figure 1.12 (a)) as discussed in [Chikazumi1964]. The interaction energy for spin-pairs may be expressed as:

$$w(r, \cos \varphi) = g(r) + l(r)(\cos^2 \varphi - \frac{1}{3}) + \text{higher order terms} \quad (1.8a)$$

The first term in Equation 1.8(a),  $g(r)$  is independent of the direction of magnetization and is the exchange interaction term. This plays an important role in volume magnetostriction but does not contribute to the usual magnetostriction [Chikazumi1964]. The second term represents the dipole term and plays a crucial role in determining the usual magnetostriction,  $\lambda_{100}$  and  $\lambda_{111}$ . Summing the contributions of all nearest-neighbor pairs in a cubic lattice, the total magnetoelastic energy can be expressed in terms of the strains ( $\epsilon_{xx}$ ,  $\epsilon_{yy}$ ,  $\epsilon_{zz}$ ,  $\epsilon_{xy}$ ,  $\epsilon_{yz}$ ,  $\epsilon_{zx}$ ) and orientation of magnetization ( $\alpha_1$ ,  $\alpha_2$ ,  $\alpha_3$ ) as:

$$E_{magnetoelastic} = B_1 [\epsilon_{xx} (\alpha_1^2 - \frac{1}{3}) + \epsilon_{yy} (\alpha_2^2 - \frac{1}{3}) + \epsilon_{zz} (\alpha_3^2 - \frac{1}{3})] + B_2 (\epsilon_{xy} \alpha_1 \alpha_2 + \epsilon_{yz} \alpha_2 \alpha_3 + \epsilon_{zx} \alpha_3 \alpha_1) \quad (1.8b)$$

The magnetoelastic energy is counterbalanced by the elastic energy that prevents the crystal from being deformed without limit and can be expressed as

$$E_{elastic} = \frac{1}{2} c_{11} (\epsilon_{xx}^2 + \epsilon_{yy}^2 + \epsilon_{zz}^2) + \frac{1}{2} c_{44} (\epsilon_{xy}^2 + \epsilon_{yz}^2 + \epsilon_{zx}^2) + \frac{1}{2} c_{12} (\epsilon_{yy} \epsilon_{zz} + \epsilon_{zz} \epsilon_{xx} + \epsilon_{xx} \epsilon_{yy}) \quad (1.8c)$$

Solving for minimization of the sum of the magnetoelastic and elastic energies

$$\frac{\partial (E_{elastic} + E_{magnetoelastic})}{\partial \epsilon_{ij}} = 0 \quad (1.8d)$$

the expression for the equilibrium strains  $\epsilon_{xx}$ ,  $\epsilon_{yy}$ ,  $\epsilon_{zz}$ ,  $\epsilon_{xy}$ ,  $\epsilon_{yz}$  and  $\epsilon_{zx}$  can be obtained in terms of the elastic constants, direction cosines of orientation of magnetization and  $B_1$  and  $B_2$ . The final expression for the elongation observed due to these strains in a direction ( $\beta_{1s}$ ,  $\beta_{2s}$ ,  $\beta_{3s}$ ) is:

$$\frac{3}{2} \lambda = \frac{\partial l}{l} = \frac{3}{2} \lambda_{100} (\alpha_1^2 \beta_{1R}^2 + \alpha_2^2 \beta_{2R}^2 + \alpha_3^2 \beta_{3R}^2 - \frac{1}{3}) + 3 \lambda_{111} (\alpha_1 \alpha_2 \beta_{1R} \beta_{2R} + \alpha_2 \alpha_3 \beta_{2R} \beta_{3R} + \alpha_3 \alpha_1 \beta_{3R} \beta_{1R}) \quad (1.9a)$$

where  $\lambda_{100}$  and  $\lambda_{111}$  are given by Equation 1.9(b) and illustrated in Figure 1.12

(b).

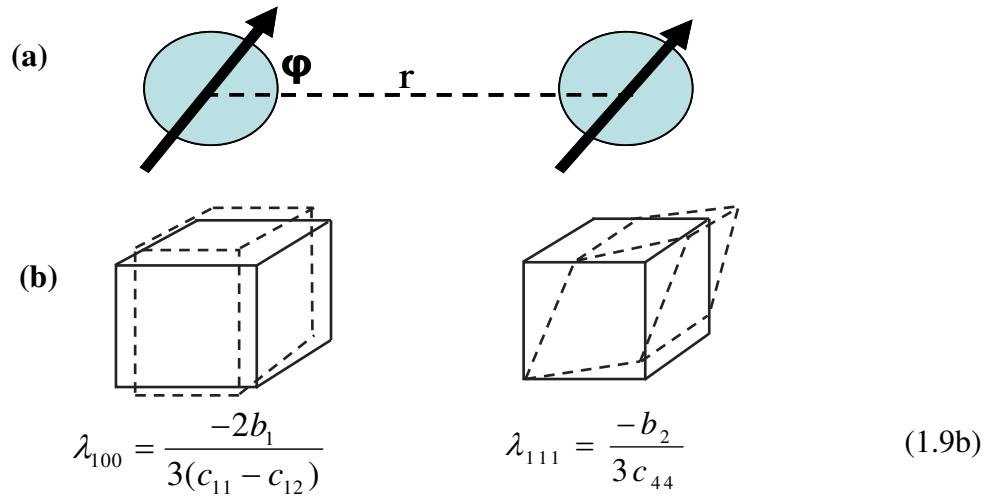


**Figure 1.12(a).** A spin pair with a variable bond length,  $r$ , and angle,  $\phi$ , between parallel spins and the bond. Source: [Chikazumi1964].

(b) Modes of elongation due to magnetostriction in cubic systems.

Source: [Clark *et al.* presentation at Galfenol Workshop, Univ. of Maryland, 2005].

### 1.3.4 Domains in Ferromagnetic Materials

The formation of domains, regions in space where the magnetic moments are strongly coupled with each other through exchange coupling and are all aligned parallel to each other, is an intermediate level between atomic magnetism and macroscopic magnetic response of a material. Formation of domains and domain walls is touched upon in this section.

#### *Formation of domains: micro-magnetics*

The formation of domains are influenced by the exchange coupling energy, magnetocrystalline anisotropy energy, magnetostriction (or magnetoelastic energy), magnetic energy and stray fields energy (due to formation of poles) in the materials as illustrated by Figures 1.13 (a) to (d).

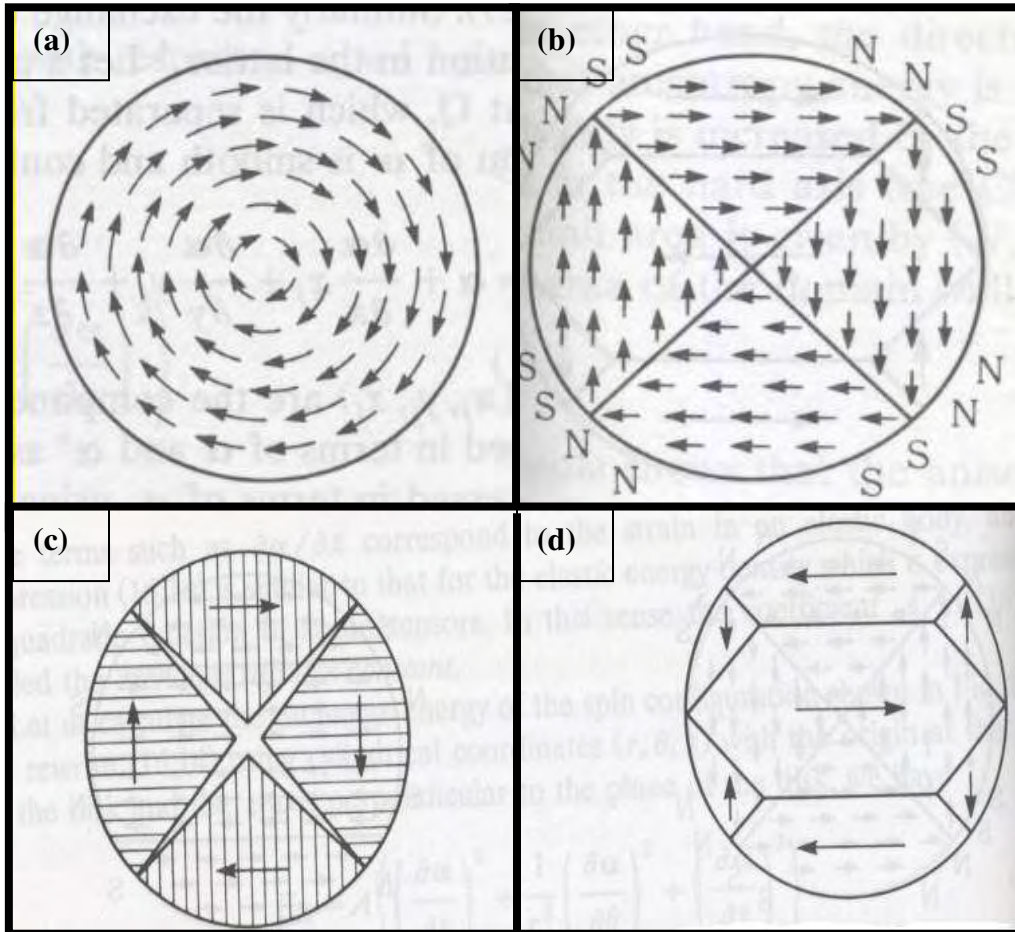


**Figure 1.13** Domain patterns in discs under different criterion.

- (a) Zero magnetocrystalline anisotropy. (b) Cubic magnetocrystalline anisotropy.  
 (c) Postulated domain structure for large positive magnetostriction.  
 (d) Expected domain structure with normal magnetostriction.

Source: [Chikazumi1964].

Consider the case of a circular disc with very small or zero external field. The magnetic moments would prefer to arrange themselves in such a manner as to prevent the occurrence of poles, thereby minimizing the stray field energy. Thus, they could form a closed flux path as shown in Figure 1.13 (a). However, this pattern is energetically feasible only if the magnetocrystalline anisotropy is extremely low. Though the expense of exchange coupling is small in this case, as the difference in orientation between two neighboring moments is small, some moments would have to

assume orientations which result in large magnetocrystalline anisotropy energy. For materials with cubic anisotropy this typically results in a domain pattern, such as the one seen in Figure 1.13 (b). The moments are oriented along the easy  $\langle 100 \rangle$  directions leading to small magnetocrystalline anisotropy energy with some expense in exchange coupling energy at the domain boundaries. The magnetostriction associated with the orientation of moments further affects the domain pattern as the material tries to avoid local stress-formations and can result in patterns such as illustrated by Figure 1.13 (c) or (d) depending on the magnetostriction of the material.

*Domain walls and domain wall motion*

Domain walls are formed due a balance between magnetocrystalline and exchange coupling energy. Large magnetocrystalline anisotropy favors the rotation of moments over fewer lattices, i.e. thin domain wall boundaries, as intermediate orientations result in a large energy penalty. In contrast, large exchange coupling favors a more gradual rotation of moments, so that the difference in orientation between neighboring spins is minimized. This results in thicker domain walls. The moments in the domain wall can rotate/re-orient more easily than the moments within a domain, in response to an applied magnetic field. This results in domain boundary motion, which is an important mechanism for magnetization.

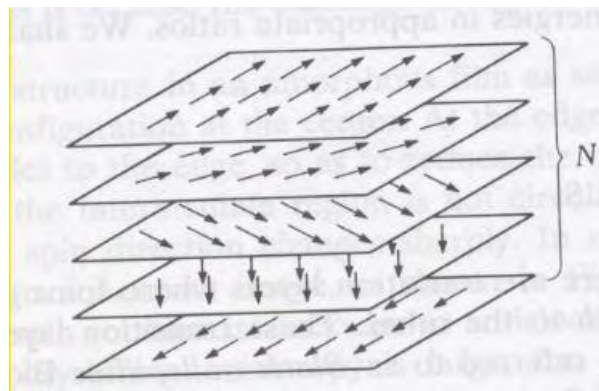


**Figure 1.14** Rotation of spins in the domain wall.

Source: [Chikazumi1964].

**1.4 Survey of Constitutive Models for Magnetomechanical Behavior**

This section surveys various constitutive models for magnetomechanical behavior of bulk materials. It starts with the Preisach model followed by a discussion

on linear piezo-magnetic equations. The constants used in these linearized equations form the basis of definitions for efficiency of transduction and figure of merit. Finally, various non-linear constitutive models for magnetomechanical behavior are discussed.

#### 1.4.1 Preisach Model: Hysteresis Operators

One of the earliest tools used to model ferromagnetic hysteresis was the Preisach model. In its rudimentary form it employs a hysteresis operator, which takes the value  $\pm 1$  depending on the current state and history based on the previous state. More recently, it has been demonstrated that the Preisach model may be modified to account for the effect of stress [Bergqvist1991, Suzuki2004] and thus model the magnetoelastic behavior of magnetostrictive materials. However, the hysteresis operator is a mathematical tool and does not address the underlying physics of the problem.

#### 1.4.2 Linear Constitutive Equations

For engineering purposes, the highly non-linear relationships between stress ( $\sigma$ ), strain ( $\epsilon$ ), magnetic field ( $H$ ) and magnetic induction ( $B$ ) are represented by a linearized set of coupled equations, which are valid for small perturbations of the above-mentioned quantities. These one-dimensional coupled linear equations are known as piezo-magnetic relations:

$$\epsilon = S^H \sigma + d_{33} H \quad (1.10a)$$

$$B = d_{33}^* \sigma + \mu^\sigma H \quad (1.10b)$$

$$\text{where } S^H = \frac{1}{E^H}$$

For the more generalized three dimensional case, the strain ( $\epsilon$ ) and stress ( $\sigma$ ) may be represented as column vectors of six components  $[\epsilon_{11} \ \epsilon_{22} \ \epsilon_{33} \ \epsilon_{23} \ \epsilon_{31} \ \epsilon_{12}]^T$  and  $[\sigma_{11} \ \sigma_{22} \ \sigma_{33} \ \sigma_{23} \ \sigma_{31} \ \sigma_{23}]^T$  and the magnetic field ( $H$ ) and induction ( $B$ ) by column vectors of three elements  $[H_1 \ H_2 \ H_3]^T$  and  $[B_1 \ B_2 \ B_3]^T$ . The compliance at constant field  $S^H$  ( $\text{Pa}^{-1}$ ) and permeability at constant stress  $\mu^\sigma$  (Tesla/Ampere) are 6\*6 and 3\*3 matrices respectively. The piezo-magnetic coefficients  $d_{33}$  (meter/Ampere) and  $d_{33}^*$  (Tesla/Pa)

are respectively 6\*3 and 3\*6 matrices. The equations can be expressed in a compact manner in tensor notation as:

$$\varepsilon_i = S_{ij}^H \sigma_j + d_{ki} H_k, \quad i=1 \text{ to } 6 \quad (1.10c)$$

$$B_m = d_{mj}^* \sigma_j + \mu_{mk}^\sigma H_k, \quad m=1 \text{ to } 3 \quad (1.10d)$$

*Figure of merit for actuators and sensors*

The constants in the piezo-magnetic equations can be used to determine the magnetomechanical coupling factor of the material ( $k_{cc}^2$ ), which is indicative of the transduction capability of the material. It is a measure of the efficiency with which magnetic energy can be transformed to mechanical energy.

$$k_{cc}^2 = \frac{d_{33} d_{33}^* E^H}{\mu^\sigma} = 1 - \frac{E^H}{E^B} \quad (1.11a)$$

where  $E^H$  and  $E^B$  are respectively Young's modulus at constant magnetic field and induction (as discussed in Section 1.2.2).

For actuators the  $\lambda_{max}$  and  $E$  are also very important factors as they determine the stroke that can be achieved per unit length of actuator and block-force that can be achieved per unit cross-section area.  $d_{33}$  determines the magnetostrictive strain (or stroke) that can be obtained per unit field applied to the magnetostrictive material.

For magnetostrictive sensors, a direct measure of the figure of merit is the  $d_{33}^*$  in Equation 1.11 (b) as it is the change in magnetic induction (B) for unit stress applied ( $\sigma$ ), at constant magnetic field (H).

$$d_{33}^* = \frac{\Delta B}{\Delta \sigma} \Big|_{H=cont} \quad (1.11b)$$

While this is an excellent measure of the sensitivity of the material, the device level details need to be included to find the charge (q) produced per unit stress applied.

$$\frac{\Delta q}{\Delta \sigma} = \frac{\Delta B}{\Delta \sigma} \Big|_{H=cont} \times \frac{\Delta q}{\Delta B} = d_{33}^* \frac{\Delta q}{\Delta B} \quad (1.11c)$$

To evaluate the right hand side of Equation 1.11 (c), the details of the sensing circuit such as the number of turns ( $N$ ), cross-section area of sample ( $A$ ) and total resistance ( $R$ ) are necessary. For large  $R$ , the sensing current developed and consequently the back-emf generated is small; therefore Equation 1.11 (c) can be expressed as

$$\frac{\Delta q}{\Delta \sigma} = \frac{NA}{R} d_{33}^* \quad (1.11d)$$

In Equation 1.11(d) the sensitivity has the units Coulomb/Pascal as it is charge developed in the sensor per unit stress.

### 1.4.3 Non-linear Constitutive Equations

The linear equations are valid only for small perturbations about a given magnetic field and stress. The constants used in the linearized piezo-magnetic equations have to be characterized or modeled as a function of both stress and field in order to generate a complete picture of the magnetomechanical behavior of the material. Furthermore, for a material that exhibits large hysteresis, the history of the material plays an important role in its behavior and needs to be accounted for. All these can only be achieved by modeling the complete non-linear behavior of the material.

The main non-linear models that have been developed so far can be broadly classified into two types: (i) Models built on the Jiles Model; (ii) Energy-based models. The Jiles-Atherton model [Jiles1983, 1984] models magnetostrictive behavior as comprising of domain rotation and domain wall pinning. The effect of stress on the magnetization vs. field curves is incorporated by introducing the concept of a stress equivalent field term  $H_\sigma$  [Jiles 1995a, 1995b]. However, some of the shortcomings of the Jiles-Atherton model and its extension are that it does not have an explicit way of handling magnetocrystalline anisotropy, making it in general a one-dimensional model.

Among the energy-based models, the Armstrong model is the most comprehensive approach, and is constructed to include the magnetocrystalline, magnetoelastic and magnetic field energy terms as expressed in Equation 1.12

$$\begin{aligned}
E(\sigma, H) &= E_{\text{magnetocrystalline}} + E_{\text{magnetoelastic}} + E_{\text{magnetic}} \\
&= K_1 * (\alpha_1^2 \alpha_2^2 + \alpha_1^2 \alpha_2^2 + \alpha_1^2 \alpha_2^2) + K_2 * \alpha_1^2 \alpha_2^2 \alpha_3^2 \\
&\quad \left\{ \begin{aligned} &-\frac{3}{2} \lambda_{100} * \sigma * (\alpha_1^2 \beta_{1s}^2 + \alpha_2^2 \beta_{2s}^2 + \alpha_3^2 \beta_{3s}^2) \\ &-3 \lambda_{111} * \sigma * (\alpha_1 \alpha_2 \beta_{1s} \beta_{2s} + \alpha_2 \alpha_3 \beta_{2s} \beta_{3s} + \alpha_3 \alpha_1 \beta_{3s} \beta_{1s}) \end{aligned} \right\} \quad (1.12) \\
&\quad -\mu_0 * M_s * H * (\alpha_1 \beta_{1F} + \alpha_2 \beta_{2F} + \alpha_3 \beta_{3F})
\end{aligned}$$

where  $(\alpha_1, \alpha_2, \alpha_3)$ ,  $(\beta_{1F}, \beta_{2F}, \beta_{3F})$  and  $(\beta_{1s}, \beta_{2s}, \beta_{3s})$  are respectively the direction cosines for orientation of magnetization, magnetic field and stress. The origin of the magnetocrystalline anisotropy and magnetomechanical energy terms is explained in Section 1.3.3.

For a given value of applied stress and magnetic field in any direction, the total energy (sum of the three above-mentioned energy terms) corresponding to the magnetization vector oriented along different directions is evaluated [Armstrong 1997, 2000]. This determines the probability that the magnetization takes that particular orientation. By performing a probability weighted summation over all the states, the average macroscopic property of this material is evaluated.

This thesis discusses the application of the Armstrong model in simulating and explaining the strikingly different actuation behavior of FeGa single crystals with different Ga content (Chapter 4) as well as attempting a more rigorous formulation to include the temperature effect and capture the paramagnetic-ferromagnetic phase transition. This model is also applied to capture the Villari-effect and coupled with a lumped parameter model for magnetic interaction between the magnetostrictive sample and biasing circuit to simulate sensing behavior accurately (Chapter 5).

### 1.5 Background on Metallurgy and Crystal Structure of Iron Gallium Alloys:

Iron-Gallium alloys present unique challenges associated with the identification of the various phases present in alloys of different Ga content and in the same alloy subjected to different heat-treatment, as well as with the fundamental understanding of the cause of magnetostriction in these alloys. These challenges are touched upon in this section. While this dissertation does not investigate the crystallography of FeGa alloys, this background proves to be essential in understanding the reason behind the choice of ~19, 24.7 and 29 at. % Ga FeGa samples for magnetomechanical characterization in Chapter 3. Some of the insights gained from this section are used to arrive at a hypothesis to explain certain the experimental trends as well as motivate the choice of certain parameters for the energy based model in Chapter 4.

#### *Iron-Gallium alloy system*

Early work showed that single-crystal BCC iron demonstrates  $\lambda_{100}$  of 21 to 23 ppm and  $\lambda_{111}$  of -25 to -20 ppm in the range of temperatures  $\pm 100^\circ\text{C}$  [Tatsumoto1959] while substituting non-magnetic aluminum upto 17 at. % Al increases magnetostriction and decreases magnetocrystalline anisotropy [Hall1959]. At 17 at. % Al,  $\lambda_{100} \approx 85$  ppm and  $\lambda_{111} \approx 0$  was observed. Building on this work, Clark *et al.* studied the magnetostriction in gallium substituted in Fe upto 34 at. % Ga, as shown in Figure 1.15. It was found that  $(3/2)\lambda_{100}$  increases monotonically with increasing Ga content to reach a peak value of ~320 ppm at 17 at. % Ga in furnace cooled samples and ~400 ppm at 19 at. % Ga in quenched samples. Further increase in Ga content resulted in a decrease in magnetostriction until it reached a “valley” of ~250 ppm at 24 at. % Ga and a subsequent increase in magnetostriction to a second peak of ~425 ppm at about 29 at. % Ga (Figure 1.15). Furthermore,  $\mu_0 M_{\text{sat}}$  decreases from ~2.1 T for pure iron, through ~1.7 T at 19 at. % Ga to ~0.5 T at 35 at. % Ga, while the nominal Young’s modulus  $E_{100}$  decreases more than two-fold from 57 GPa to 27 GPa for increase in atomic Ga content from 19% to 24% (Table 1.2).

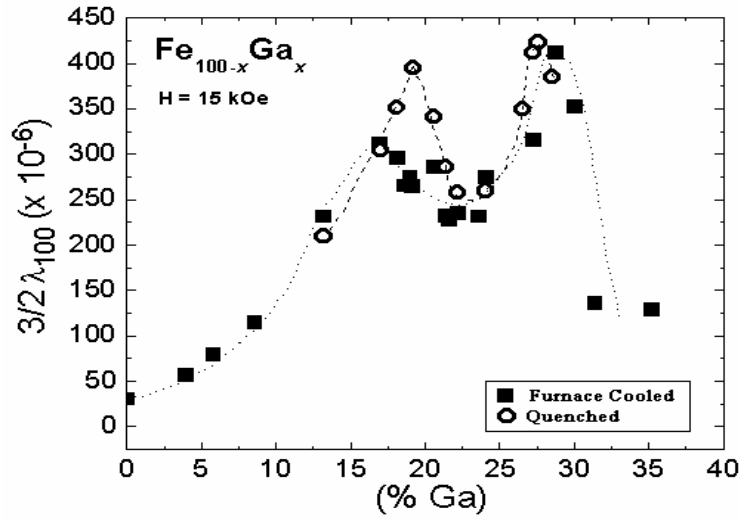


**Figure 1.15** Magnetostriction ( $3/2\lambda_{100}$ ) of FeGa vs. Ga content [Clark2000, Clark2001b].

**Table 1.2** Material properties at room temperature of single-crystal FeGa alloys of varied Ga content. Source: Compiled from [Clark2001a, b] and [Kellogg2003b].

% Ga (approx)	19	24	27	35
$E_{100}$ (GPa)	57	27	20	
$\mu_0 M_{\text{sat}}$ (Tesla)	~1.7	~1.32		~0.55

Several researchers have investigated the possible physics behind the magnetostrictive behavior of these alloys and the cause of the 2-peak curve for variation in  $\lambda_{100}$  with Ga content.

Though the exact mechanism for the magnetostriction in FeGa alloys is not completely understood, several aspects have been explained. The large  $\lambda_{100}$  exhibited at low Ga content, which increases with Ga content upto 19 at. % Ga, may be explained qualitatively using a pairing model [Cullen2001]. Though Ga atoms are large relative to Fe, they randomly substitute for Fe atoms by fitting into  $\alpha$ -Fe BCC lattice sites forming Ga-pairs along the edges of the cubic lattice as illustrated by a 2-

D schematic in Figure 1.16(a). The Ga pairs may facilitate short term order leading to anisotropic condition, resulting in magnetostriction in the  $\langle 100 \rangle$  direction. As the Ga content increases beyond 17 at. % Ga (in furnace cooled and 19 at. % Ga in quenched FeGa alloys), an increased formation of  $D0_3$  and B2 crystallographic structure (Figure 1.16 (b)) results.

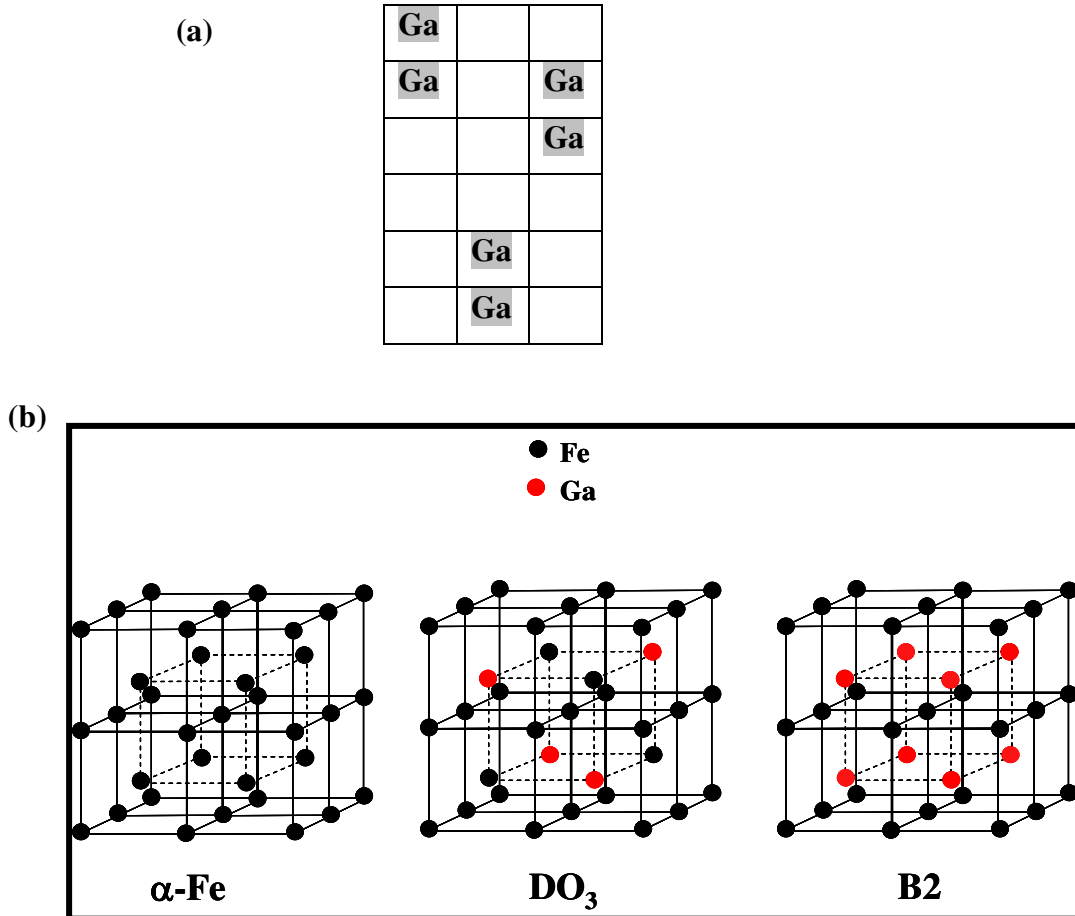


**Figure 1.16 (a)** Schematic of Ga-Ga pairs Fe-lattice randomly substituted with Ga atoms (disordered A2 phase).

**(b)** Crystallographic structure of ordered phases  $D0_3$  and B2 of FeGa.

Source: Presentation by Clark *et al.*, in Galfenol Workshop, University of Maryland, College Park, 2005.

This trend is consistent with the phase diagram shown in Figure 1.17 and may cause a decrease in magnetostriction [Kawamiya1972, Clark2001b]. The formation of  $D0_3$  at increased Ga content and the effect of slow cooling on increased formation

of  $D0_3$  have been demonstrated by Lograsso *et al.* [Lograsso2006]. It was demonstrated that 19.5 at. % Ga samples have 100% A2 (disordered) phase when quenched but 67% A2 and 33%  $D0_3$  when slow cooled. However, 22 at. % Ga samples have 40% A2 (disordered) phase and 60%  $D0_3$  phase when quenched and 100%  $D0_3$  when slow cooled. This illustrates the strong dependence of the formation of  $D0_3$  phase on heat-treatment around the first magnetostriction peak. The ordered  $D0_3$  phase is precipitated not only when Fe-Ga alloys are slow-cooled from a temperature higher than the A2/ $D0_3$  transition temperature but also when quenched samples are heated from room temperature to a certain critical temperature as demonstrated by Datta *et al.* [Datta2006]. The critical temperature depends on the material composition and heating rate and is typically  $\sim 200^\circ\text{C}$ , i.e. well below the A2/ $D0_3$  transition temperature.

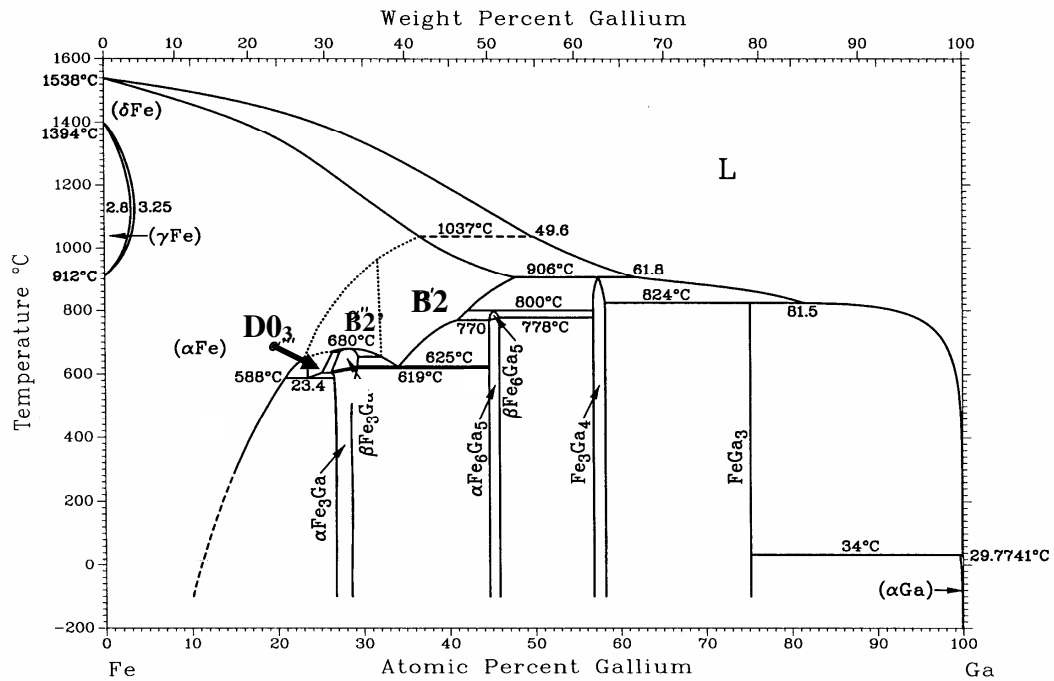


**Figure 1.17** Binary FeGa phase diagram [Kubaschewski1982, Massalaski2002].

While the formation of  $D0_3$  (and probably B2) leads to the decrease in magnetostriction with Ga content upto  $\sim 24$  at. % Ga, alloys with Ga content more than 24 at. % demonstrate significantly lower elastic shear modulus values at room

temperature  $c'=c_{11}-c_{12}$  (9.4 GPa at 24.1 % and 6.8 GPa at 27.2 %), while the corresponding magnetomechanical coupling ( $b_1$  of -5.1 and -4.8 MJ/m<sup>3</sup> respectively)

$$\frac{3}{2} \lambda_{100} = \frac{-b_1}{c_{11} - c_{12}} \quad (1.13)$$

shows a very small decrease in magnitude [Clark2003]. Thus the magnetostriction in the <100> direction (Equation 1.13), increases from 270 ppm to 350 ppm. Other researchers report the presence of DO<sub>19</sub> (ordered hexagonal) and L1<sub>2</sub> (ordered fcc) phases in the 26-29 at. % Ga range with different heat treatments [Srisukhumbowornchai2002]. Modeling of the magnetostriction produced by various structures from first principles using quantum mechanics by Wu *et al.* [Wu2002] may help resolve some of the ambiguities encountered in the current qualitative theories.

### **1.6 Organization and Contributions of this Dissertation**

The organization of this dissertation and research contributions towards a better understanding of the magnetomechanical behavior of single-crystal and polycrystalline FeGa alloys is summarized below:

#### *Chapter 2: Magnetic issues*

The distribution of magnetic field and flux along the dimensions of a magnetostrictive element and at its boundary is an important consideration in characterizing magnetostrictive samples. A 2-D axi-symmetric model of a typical transducer circuit is developed using COMSOL Multiphysics<sup>TM</sup> to simulate this distribution. Modeling and correcting for these effects can improve sample characterization accuracy. Based on this analysis, suggestions are made for a better design for a transducer to be used for magnetostrictive material characterization, which exhibits reduced variation in field and flux.

#### *Chapter 3: Characterization of single-crystal actuator and sensing behavior*

Experimental results are presented that extend the envelope of characterization of single-crystal actuation behavior beyond the first magnetostrictive

peak (~19 at. % Ga) to encompass the  $\lambda$ -H and B-H curves close to the magnetostriction valley (24.7 at. % Ga) and second magnetostriction peak (29 at. % Ga) samples. The presence of multiple phases at these compositions leads to characteristics that are considerably different from those of the 19 at. % Ga sample. So far, even for the samples around the first magnetostriction peak, the magnetomechanical behavior of FeGa alloys has been characterized solely in the  $\langle 100 \rangle$  direction. The  $\lambda$ -H and B-H of a  $\langle 110 \rangle$  oriented 18 at. % Ga sample is characterized to understand the effect of stress and behavior in the  $\langle 110 \rangle$  direction, as a first step to understand its behavior along various crystallographic directions.

Typical sensing characterizations performed by applying constant drive current to generate the magnetic field, may suffer from large variations in the magnetic bias field during testing. This is caused by the interaction between the transducer's magnetic circuit and magnetostrictive sample, which is particularly significant for alloys like FeGa which have a sufficiently high permeability to make their reluctances comparable to that of the sensor magnetic circuit. A change in the magnetomechanical state of the sample, such as increase in reluctance caused by compressive stress, can cause a large increase in the MMF dropped across the sample and consequently an increase in the magnetic field in the sample. This issue is addressed in Chapter 3, by establishing an accurate method for estimation of sensing behavior of materials that is independent of the magnetic interaction between the sample and the magnetic circuit. This is accomplished using a PID controller with a feed-back loop to vary the biasing drive current to compensate for variation in sample reluctance and keep the field through the sample constant. Using this technique, the sensing behavior ( $\epsilon$ - $\sigma$  and B- $\sigma$  curves) of a 19 at. % Ga sample in the  $\langle 100 \rangle$  direction and 18 at. % Ga sample in the  $\langle 110 \rangle$  direction are characterized.

#### *Chapter 4: Modeling of single-crystal actuation behavior*

The primary objective of this effort was to apply a model that simulates the actuation behavior of magnetostrictive materials to FeGa alloys along various crystallographic directions. An additional objective was to see if the model

formulation enables prediction of FeGa sensing behavior from parameters fit to actuation data.

With this in mind, the modeling of the magnetomechanical behavior of single-crystal magnetostrictive materials was addressed at two levels: alignment of spins (magnetization) in individual lattices within a domain and the distribution of orientation of various domains to simulate the macroscopic response of the material. The model at the lattice level is employed to predict the temperature dependence of  $M_{\text{sat}}$  and  $\lambda_{\text{sat}}$  within a domain. For modeling magnetostrictive behavior at constant temperature, the problem reduces to finding the distribution of orientation of various “domains” to a particular stress and field input, which is accomplished by the Armstrong model [Armstrong2003a]. This distribution determines macroscopic response of the material.

An attempt is made to demonstrate that the Armstrong model can be used to simulate and explain the strikingly different trends in actuation behavior of single-crystal FeGa alloys with varied Ga content as well as the behavior along various crystallographic directions, at constant temperature. Furthermore, predictions are made for behavior in tension and it is demonstrated that the model can prove to be useful for generating a database of the material properties such as  $\mu_R$  and  $d_{33}$  as a function of both stress and field.

#### *Chapter 5: Modeling of Villari-effect and interaction with magnetic circuit*

The model developed in Chapter 4 is modified to capture Villari-effect or inverse transduction behaviors and predict sensing behavior of samples under compressive loads at various applied bias fields. An attempt is made to predict the sensing behavior using model parameters obtained from the actuator behavior. The predictions are benchmarked (verified) against experimental sensing characteristics of a 19 at. % Ga sample in the  $\langle 100 \rangle$  direction and an 18 at. % Ga sample in the  $\langle 110 \rangle$  direction to demonstrate its capability to predict sensing behavior in different crystallographic directions. An attempt is made to predict tensile sensing behavior,

which is necessary to eventually model of magnetostrictive cantilever sensors and/or torque sensors that simultaneously experience both tensile and compressive loading.

Though the bias field for sensors is typically provided by a permanent magnet or a constant DC current, the bias field magnitude in the magnetostrictive sample is expected to vary with stress induced changes in permeability, as discussed in Chapter 3. To accurately model this sensing performance, a model that accounts for both the interaction between the magnetic circuit and the magnetostrictive sample in the presence of changing stresses and the constitutive Villari-effect behavior of the material is developed. The model simulates sensing characteristics at constant drive current and the variation in field through the sample due to its magnetic interaction with the circuit and is compared with experimental constant-current sensing characterization data for the  $\langle 100 \rangle$  oriented 19 at. % Ga sample.

#### *Chapter 6 Characterization and modeling of polycrystalline behavior*

While study of single-crystal FeGa alloys is a good starting point for characterizing Galfenol behavior, commercial actuators and sensors are more likely to be made of polycrystalline FeGa. This is due to greater yields produced by manufacturing process used to make polycrystals which could make FeGa commercially viable, provided the actuation and sensing properties of polycrystals are not significantly inferior to that of single-crystals. This motivates the study of the effect of the presence of various crystallographic orientations in polycrystal samples in degrading its performance relative to that found in oriented  $\langle 100 \rangle$  single crystal alloys.

The actuation and sensing behavior of 18.4% Ga polycrystalline samples produced by Etrema Products Inc., using the Free Stand Zone Melt (FSZM) manufacturing processes with a zoning rate of 350 mm/hour, is characterized. The sample texture is determined using Electron Back Scattering Diffraction of multiple sample cross-sections.

Polycrystalline actuation and sensing behavior is modeled as a volume-fraction weighted sum of the behavior along individual [100], [110], [210], [310], [211] and [311] crystallographic directions enabling a prediction of actuation and sensing data from the cross-section texture of the sample averaged over its length. The variation in magnetomechanical behavior due to variation in cross-section texture is also simulated.

## Chapter 2: Magnetic Issues

The distribution of magnetic field and flux along the dimensions of the magnetostrictive element is an important consideration in characterizing magnetostrictive samples as well as in designing magnetostrictive transducers. A 2-D axisymmetric model of the transducer circuit employed in the characterization is developed using COMSOL Multiphysics<sup>TM</sup>, a commercial FEM package to investigate this spatial variation in magnetic quantities. Modeling and correcting for these effects may lead to improved characterization and could prove to be a useful tool in designing efficient transducers.

In this chapter, the potential formulation of the magnetostatic problem is introduced first, followed by a conceptual description of the demagnetization effect, which is a factor that should not be neglected in designing magnetic circuits and characterizing magnetic materials. The next section deals with the development of the transducer model in the FEM package and benchmarking the finite-element results against known analytical results. In the third subsection, the transducer model with Galfenol sample and steel end-caps is employed to make predictions about the variation in magnetic field and flux along the dimensions of the specimen and the implications of these results for experimental characterization. The insights from this section motivated the design of experiments involving the placing of Hall-effect sensors and sense coils at 2 different positions along the length of the sample. These experimental results are described in detail in the fourth section and an attempt is made to reconcile some of the experimental observation with FEM simulation. Finally, the fifth and sixth sections summarize the implications of this study for the characterization of magnetic samples and suggestions for design of transducers, which may reduce the spatial variation in magnetic flux and field.

### **2.1 Introduction**

This section deals with the potential formulation of the magnetostatics problem and a conceptual description of the demagnetization effect.

### 2.1.1 Potential Formulation of the Magnetostatic Problem

The complete set of Maxwell's equation in a polarizable material medium is the following:

$$\nabla \cdot \mathbf{D} = q \quad \text{Gauss's law} \quad (2.1)$$

$$\nabla \cdot \mathbf{B} = 0 \quad \text{No magnetic poles} \quad (2.2)$$

$$\nabla \times \mathbf{E} = - \frac{\partial \mathbf{B}}{\partial t} \quad \text{Faraday's law of induction} \quad (2.3)$$

$$\nabla \times \mathbf{H} = \mathbf{J} + \frac{\partial \mathbf{D}}{\partial t} \quad \text{Ampere's law (modified)} \quad (2.4)$$

These laws are supplemented by a continuity equation:

$$\nabla \cdot \mathbf{J} = - \frac{\partial q}{\partial t} \quad (2.5)$$

and material properties, which are a set of linear equations describing the relationship between electric or magnetic quantities in the material medium.

$$\mathbf{B} = \mu_0(\mathbf{H} + \mathbf{M}) \quad \mathbf{D} = \epsilon_0 \mathbf{E} + \mathbf{P} \quad \mathbf{J} = \sigma \mathbf{E} \quad (2.6)$$

This application is only concerned with the static magnetic terms in these equations. For example, though there is a current flowing in the coils, the analysis of how this current is generated by the application of electric potential (voltage) is not important to this problem. However, the magnetic field and flux generated in the transducer due to this current is of utmost importance. Thus both electric terms and terms with derivatives in time can be excluded from this quasi-static analysis, reducing the set of equations describing the problem to:

$$\nabla \cdot \mathbf{B} = 0 \quad (2.7)$$

$$\nabla \times \mathbf{H} = \mathbf{J} \quad (2.8)$$

$$\mathbf{B} = \mu_0(\mathbf{H} + \mathbf{M}) \quad (2.9)$$

This problem can be reduced further in order to solve for just one variable, by constructing a magnetic vector potential ( $\mathbf{A}$ ) such that:

$$\mathbf{B} = \nabla \times \mathbf{A} \quad (2.10)$$

This formulation of the magnetic potential incorporates Equation 2.7 because the divergence of the curl of a vector is identically equal to zero

$$\nabla \cdot (\nabla \times \mathbf{A}) \equiv 0 \quad (2.11)$$

Equation 2.9 involves the magnetization of the media due to the application of the field  $H$ , which can be approximately described by the linear relationship  $\mathbf{M} = \chi H$

Thus Equation 2.9 can be restated as:

$$\mathbf{B} = \mu_0(1 + \chi)H \quad \text{or} \quad \mathbf{B} = \mu_0\mu_r H \quad (2.12)$$

From Equations (2.8), (2.10) and (2.12) we get the following vector potential formulation

$$\nabla \times \left( \frac{1}{\mu_0\mu_r} (\nabla \times \mathbf{A}) \right) \equiv \mathbf{J} \quad (2.13)$$

In this approach the space is divided into different regions according to the geometry of the magnetic transducer being studied. Each region in space is then assigned a current density ( $\mathbf{J}$ ) if it is a coil or current carrying element and a relative permeability ( $\mu_r$ ) depending on its magnetic properties. The boundary conditions are discussed in detail in Section 2.2. Finally, the solution of this equation yields the value of the vector potential  $\mathbf{A}$  as a function of spatial coordinates. Once this is known, the value of the magnetic induction  $\mathbf{B} = \nabla \times \mathbf{A}$  and the value of magnetic field

$$\mathbf{H} = \frac{1}{\mu_0\mu_r} (\nabla \times \mathbf{A}) \quad \text{can be evaluated in every region.}$$

### 2.1.2 Demagnetization Effect and its Influence on the Magnetization Curve

When a finite size magnetic sample is magnetized, free magnetic poles are induced on its ends which give rise to a magnetic field that opposes the direction of

magnetization as shown in Figure 2.1 [Chikazumi 1964]. This field, known as the demagnetization field ( $H_d$ ), depends on the geometry of the magnetic sample and the magnetization. Hence, it can be expressed as:

$H_d = N_d M$ , where  $N_d$  is known as the demagnetization factor and is geometry dependent.

Typically,  $N_d$  is small for thin, long bodies magnetized along their long axis and tends to zero for closed flux paths. In case of short thick bodies, this factor is large and tends to 1 for large flat plates magnetized perpendicular to the plane.

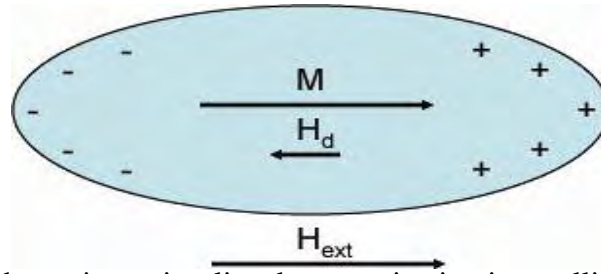


**Figure 2.1** Schematic to visualize demagnetization in an ellipsoidal body.

(+, - do not imply magnetic monopoles. This analogy from polarization in dielectrics used to better illustrate the cause of the demagnetizing field.)

The net magnetic field inside the magnetic sample is

$$H_{eff} = H_{ext} - H_d = H_{ext} - N_d M \quad (2.14)$$

The effect of demagnetization is that the net magnetic field inside the sample is smaller than the external magnetic field. This reduction in the net magnetic field is proportional to the magnetization of the sample, which leads to a shearing of the M-H or B-H curve as shown in Figure 2.2. The extent of shearing depends on the demagnetization factor  $N_d$ .

It is essential to note that the demagnetization field and consequently the effective field and magnetization are not uniform even in samples with common geometrical shapes such as cylinders and rectangular prisms [Joseph1965] and  $N_d$  thus corresponds to the average value of the demagnetizing field produced. However,

in the case of ellipsoids there is no spatial variation in the demagnetizing field, making it a valuable shape for both evaluating the B-H curves of specimens as well as benchmarking numerical simulations.

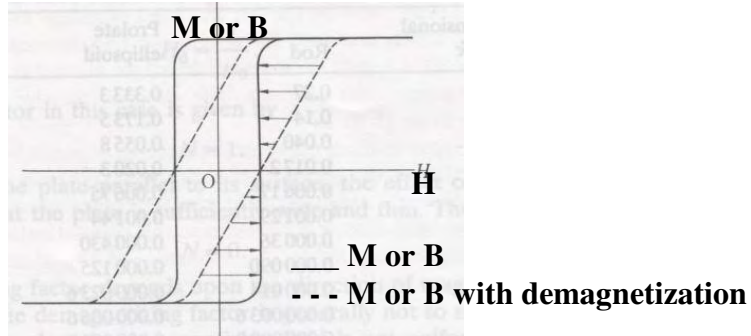


**Figure 2.2** Effect of demagnetization on shearing of B-H curve.

Source: [Chikazumi1964]. Arrows point from the larger external magnetic field required with demagnetization effect to the corresponding external magnetic field required when this effect is absent, to produce the same magnetization.

## **2. 2 Developing and Benchmarking a FEM Module**

This section deals with the development of a 2-D axisymmetric model for the magnetic transducer using commercial Finite Element software developed by COMSOL Inc. known as COMSOL Multiphysics™ [COMSOL2005]. The numerical predictions of this model are benchmarked with analytical values of demagnetization in ellipsoidal geometries with different aspect ratios.

### **2.2.1 Development of FEM Model**

The FEM analysis was developed using the static 2-D axisymmetric magnetostatic module in COMSOL Multiphysics™ with azimuthal currents (direction of current perpendicular to the plane of Figure 2.3). The boundary conditions employed in the case of boundaries between various materials was *continuity* which implies that the tangential component of the magnetic field and normal component of the magnetic induction are continuous across a boundary. The *insulation* boundary condition was employed only for a domain enclosing all the elements being modeled. This domain is about 3 times the size of the transducer and

is modeled with air around the transducer (the full extent of this region is shown in the insert on the left side of Figure 2.3). The boundary of this domain is sufficiently far away that the insulation condition, which implies that no flux can cross the boundary, is valid. The details of the different parts of the transducer are illustrated in Figure 2.3. The unit used for length along the x and y axes is meters

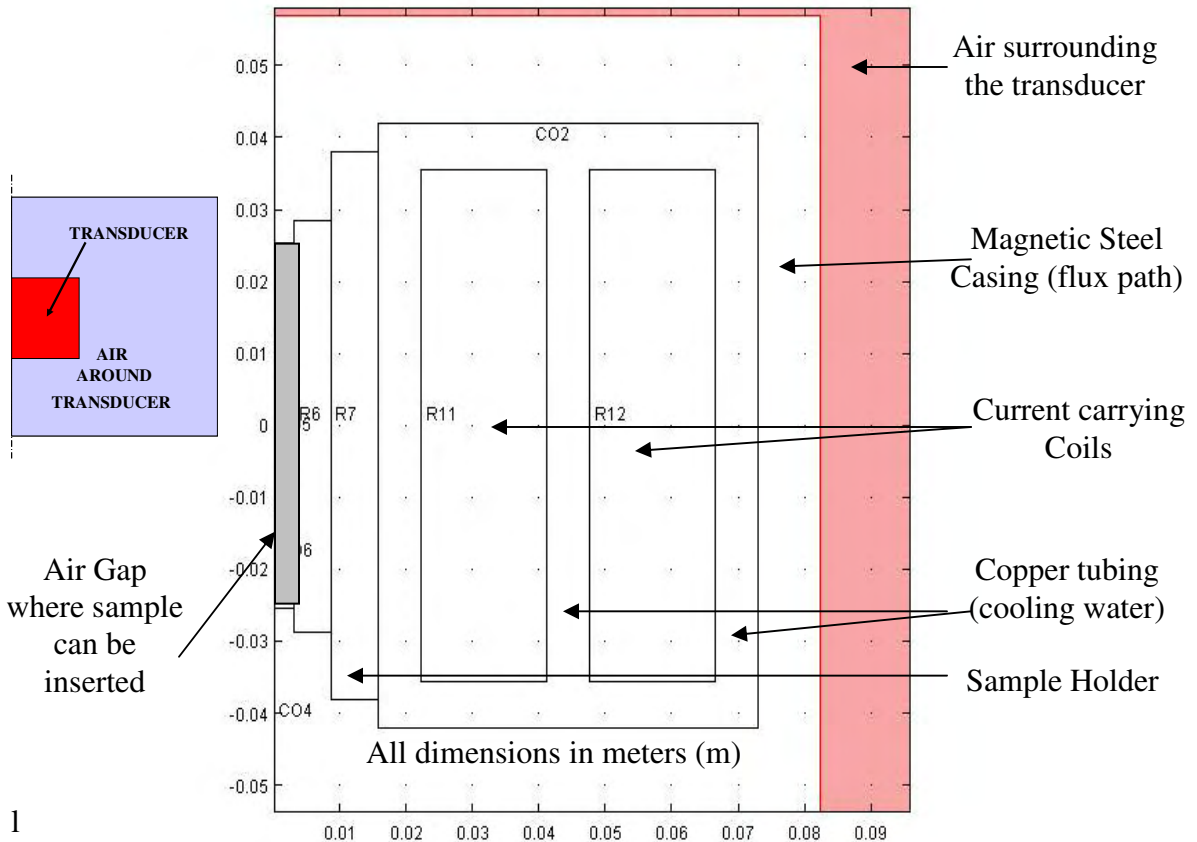


**Figure 2.3** Axisymmetric model of the transducer in COMSOL Multiphysics.<sup>TM</sup>

The transducer used for characterization in this dissertation was developed by Kellogg [Kellogg2003b].

### 2.2.2 Benchmarking the 2-D Axisymmetric FEM Model by Studying Demagnetization in an Ellipsoidal Shaped Object

The 2-D axisymmetric FEM model was bench-marked with the analytical solution for the field distribution in an ellipsoid immersed in a uniform external field. The analytical solution shows that the demagnetization factor is uniform across the

dimensions of the ellipsoid, thereby ensuring that the internal field is uniform but lower than the external field, for a uniform applied external field. The analytical formula [Chikazumi1964] for demagnetization in a prolate ellipsoid (shorter axes are equal) with ratio of length to diameter  $k$  is

$$N_d = \frac{1}{k^2 - 1} \times \left[ \frac{k}{\sqrt{k^2 - 1}} \log_e (k + \sqrt{k^2 - 1}) - 1 \right] \quad (2.15)$$

The axisymmetric model of the transducer was constructed as described in Section 2.2.1. All transducer parts except the magnetic steel flux return path and sample holder parts are made of copper or aluminum and hence were assigned a relative permeability ( $\mu_r$ ) of 1. The flux return path was assigned a relative permeability ( $\mu_r$ ) of 2000 while the ellipsoidal body inserted in the center of the air-gap was assigned a relative permeability of 60.

The azimuthal current density was set at 500 A/m<sup>2</sup>, which is very small compared to the actual current which flows through the transducer (modeled later). Since the variation of the magnetic induction  $B$  (or magnetization,  $M$ ) with the magnetic field  $H$  is modeled as a linear function ( $\mu_r = \text{constant}$ ) the actual magnitude of the field used to calculate the demagnetization factor is not important. The spatial variation of magnetic field in the transducer with a prolate ellipsoid placed at the center is shown in Figure 2.4. Note that  $H_{\text{norm}}$  refers total field.

$$( H_{\text{norm}} = \sqrt{H_R^2 + H_Z^2} )$$

The detailed picture of variation of field and flux in and around the prolate ellipsoid with ratio of long axis to short axes of four is illustrated in Figure 2.5.

The uniform dark color inside the ellipsoid in Figure 2.5 shows that the field is uniform within the sample but of lower magnitude than the surroundings (lighter color implies stronger field). This is consistent with expectation that the field inside the sample is lower due to demagnetization effect but is uniform as the demagnetization factor is uniform within the sample.

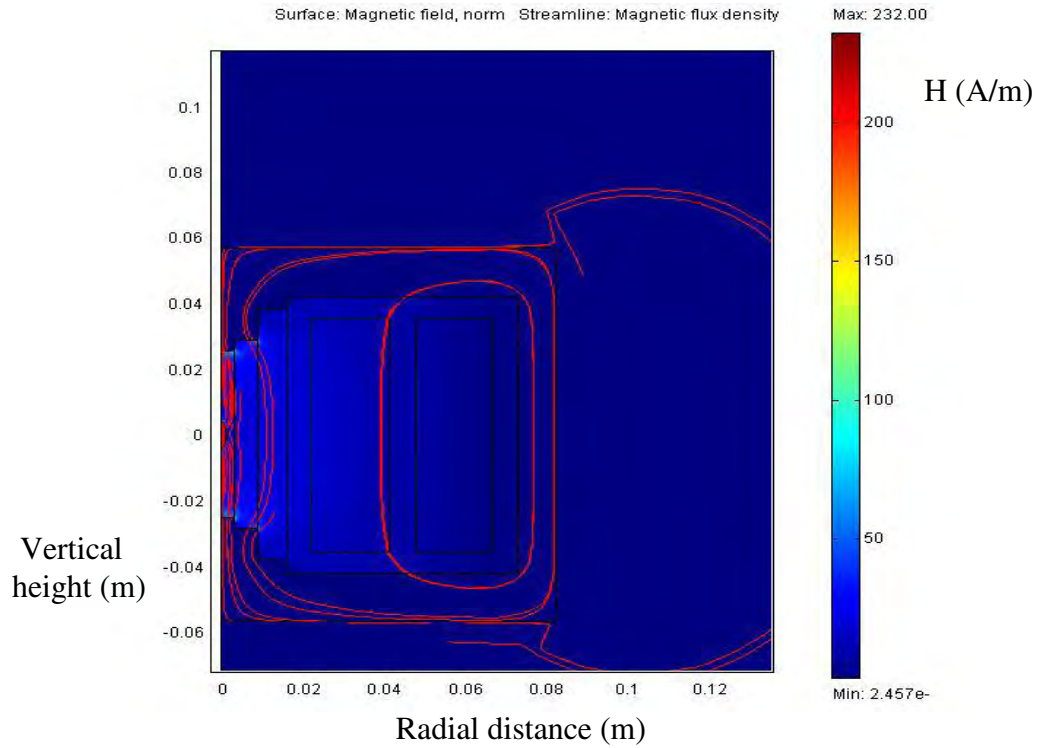


**Figure 2.4** Spatial variation of magnetic field  $H$  in the transducer.

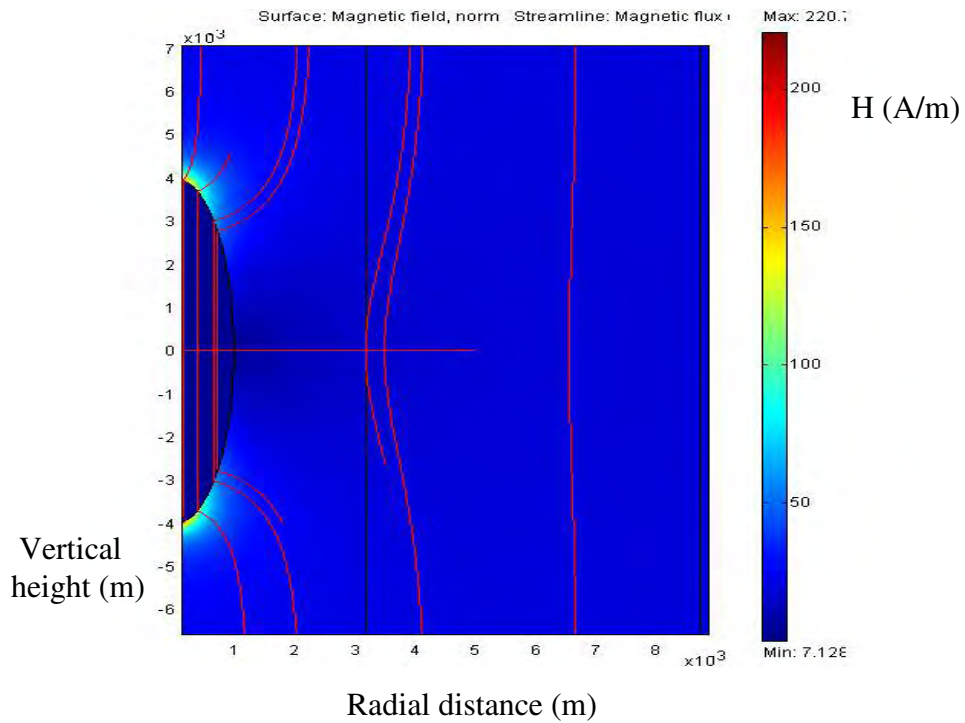


**Figure 2.5** Field distribution (color indicative of magnitude) and flux lines through an ellipsoid.

The FEM model was used to find the field inside ellipsoids with  $\mu_r = 60$  and ratio of major axis to minor axes of 2, 4 and 8 and corroborated with analytical results. Table 2.1 lists the predicted values of fields inside the ellipsoidal samples of the three different geometries for an external applied field of 19.7 (estimated from uniform field in the air gap in absence of sample).

**Table 2.1** Internal field and demagnetization factors predicted by the FEM code for prolate ellipsoids of various radius ratios.

K ( $L_{\text{major axis}}/L_{\text{minor axes}}$ )	$H_{\text{inside}}$ (A/m) Predicted by FEM	$N_d$ Predicted by FEM
2	1.78	0.1706
4	3.67	0.0740
8	7.5	0.0276

NOTE: 
$$N_d = \frac{\frac{H_{out}}{H_{in}} - 1}{\chi}$$

Figure 2.6 and 2.7 respectively show that the field in the sample and demagnetization factors predicted by the FEM model agrees very well with analytical results.

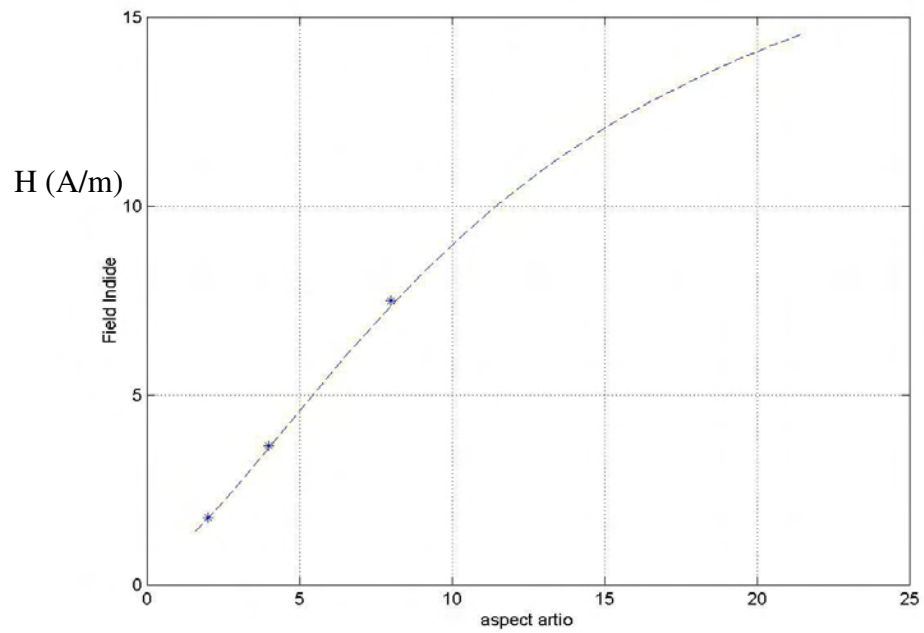


**Figure 2.6** FEM predictions (denoted by \*) with analytical value of  $H_{\text{inside}}$  (denoted by --) for  $H_{\text{ex}} = 19.7$  A/m.

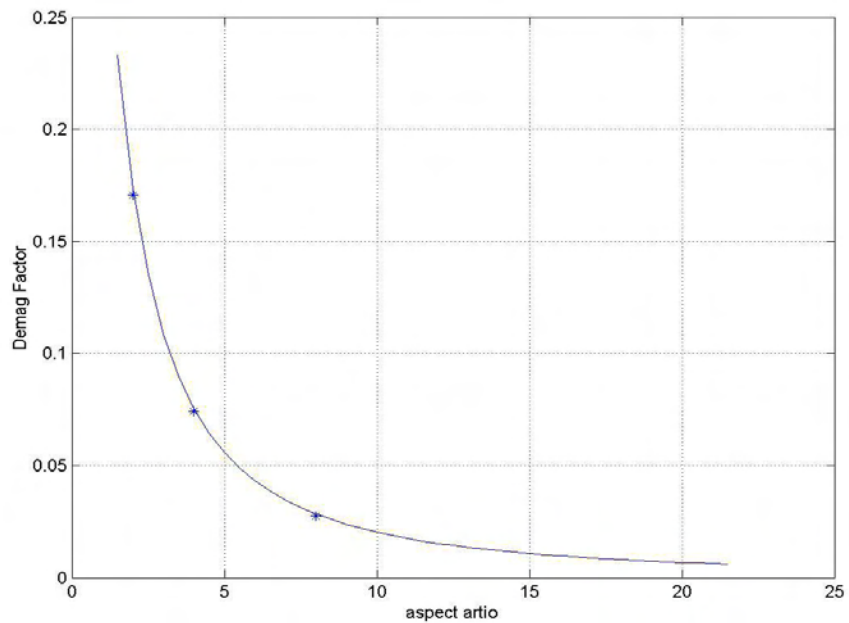


**Figure 2.7** FEM predictions (denoted by \*) superimposed on analytical value (denoted by --) of demagnetization factor.

### 2.3 Insights from Finite-Element Model of Iron-Gallium Cylinder Samples with End Caps

The FEM transducer model was successfully benchmarked with the test case of an ellipsoid. The model was then extended to a 6.35 mm (quarter inch) diameter and 25.4 mm (one inch) long Fe-Ga sample (modeled with  $\mu_r=60^*$ ) with 6.35 mm (quarter inch) diameter and 12.7 mm (half inch) long steel end caps ( $\mu_r=2000$ ) on the top and bottom. A current density of  $883460 \text{ A/m}^2$  was used to model a current of 2A flowing through the coils.

*\* NOTE: Sample relative permeability  $\mu_r$  cannot be directly measured. It is estimated from the B-H curves from the derivative  $(1/\mu_0)*(dB/dH)$  and in general varies with the stress-state and applied field.  $\mu_r=60$  is chosen as a conservative estimate, representative of most parts of the B-H curves.*

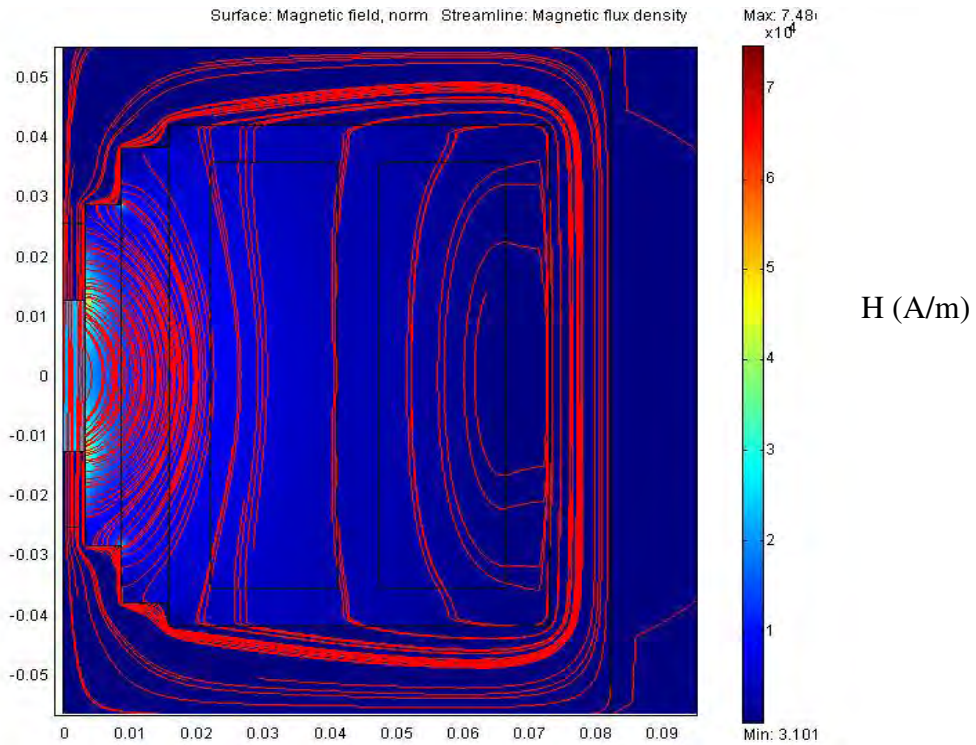


**Figure 2.8** Spatial variation of magnetic field H in the transducer with FeGa sample.

The simulation shows that a large magnetic field is dropped across the sample in comparison with the rest of the circuit. A reasonably large field is also dropped in

the region adjoining the sample. The curved flux lines around the sample indicate that there is a significant flux leakage all along the length of both the sample and the end caps which is likely to cause a variation in the magnetic induction as illustrated in Figure 2.9(a). The induction falls from 2.05T to 1.78T along the length of the end cap. There is a further decrease in flux density from 1.78 T to 1.63 T from the ends of the sample to its center due to a smaller but moderate amount of flux leakage (~8% variation of magnetic induction along the length of the sample). The field variation along the length of the sample is also restricted to about 8% in Figure 2.9(b).

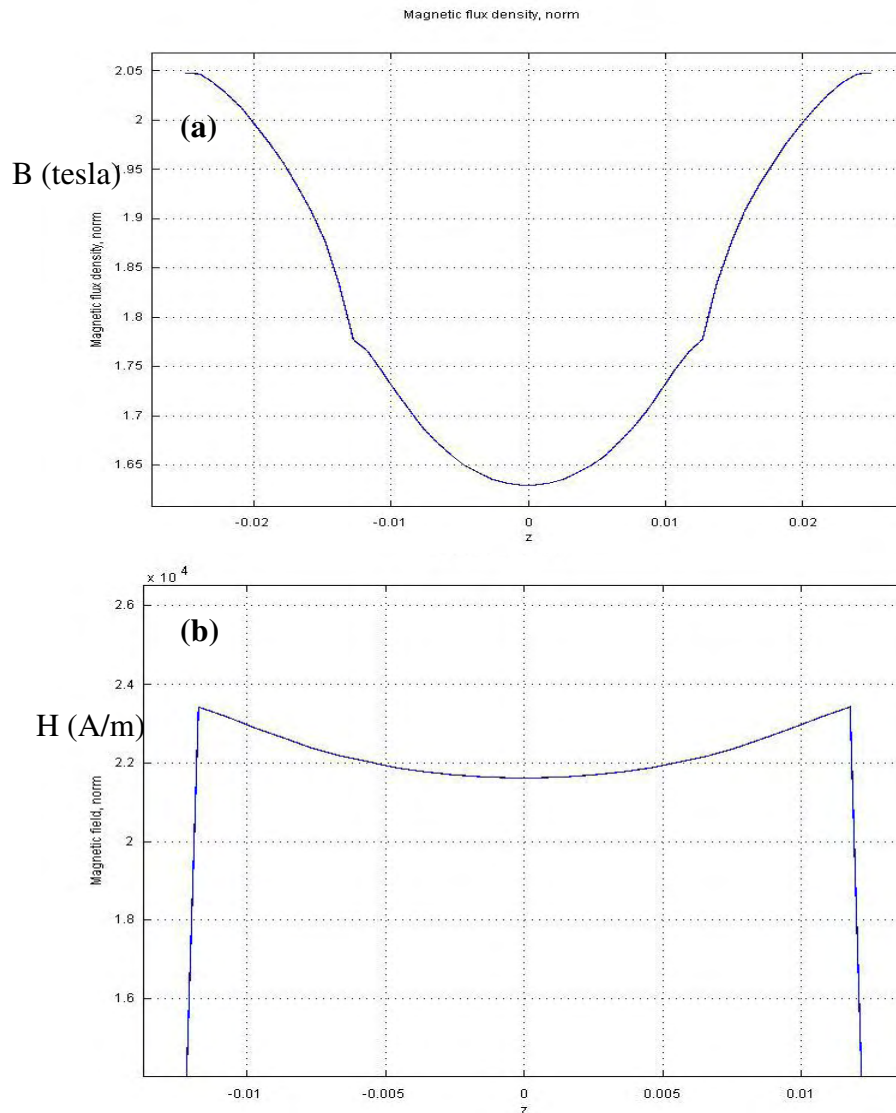


**Figure 2.9 (a)** Magnetic Induction distribution along sample length.

**(b)** Total field distribution along length of sample (vertical variation).

Since, the magnetic field within the sample is estimated by a hall-chip placed at the surface, it is important to understand the radial variation in the magnetic field, especially at the sample-air interface. The flux lines in Figure 2.8 seem to indicate that the radial variation in H at the sample-air interface is likely to be larger near the end caps than at the center as symmetry conditions at the center are likely to ensure a more radially uniform field. This lateral (radial) variation in the total, lengthwise (z-component) and radial component of the magnetic field is studied at two stations along the length: center of the sample and sample end as shown in Figure 2.10.

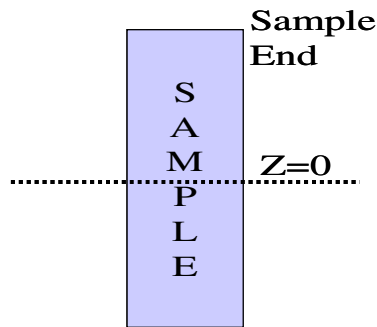


**Figure 2.10** Longitudinal stations where the radial variation in magnetic field is studied.

Figures 2.11 (a) and 2.11 (b) demonstrate that at  $z = 0$ , the total magnetic field and z-component of the magnetic field are nearly identical. This is because the radial component of the sample is negligibly small at the central station as illustrated by Figure 2.11 (c). Even this radial field, which is 3 orders of magnitude smaller than the z-component of the field, is likely to be caused by numerical errors.

Another important issue is the variation in z-component of the magnetic field within and outside the sample. In this case, the magnetic field is uniform within the sample (<1% variation) and decreases by less than 10% even at a distance of ~1 mm away from the surface of the sample, illustrating that even if the sensing element of the hall-chip is not exactly at the surface the field estimate obtained by it is a fairly accurate description of the field inside the sample.

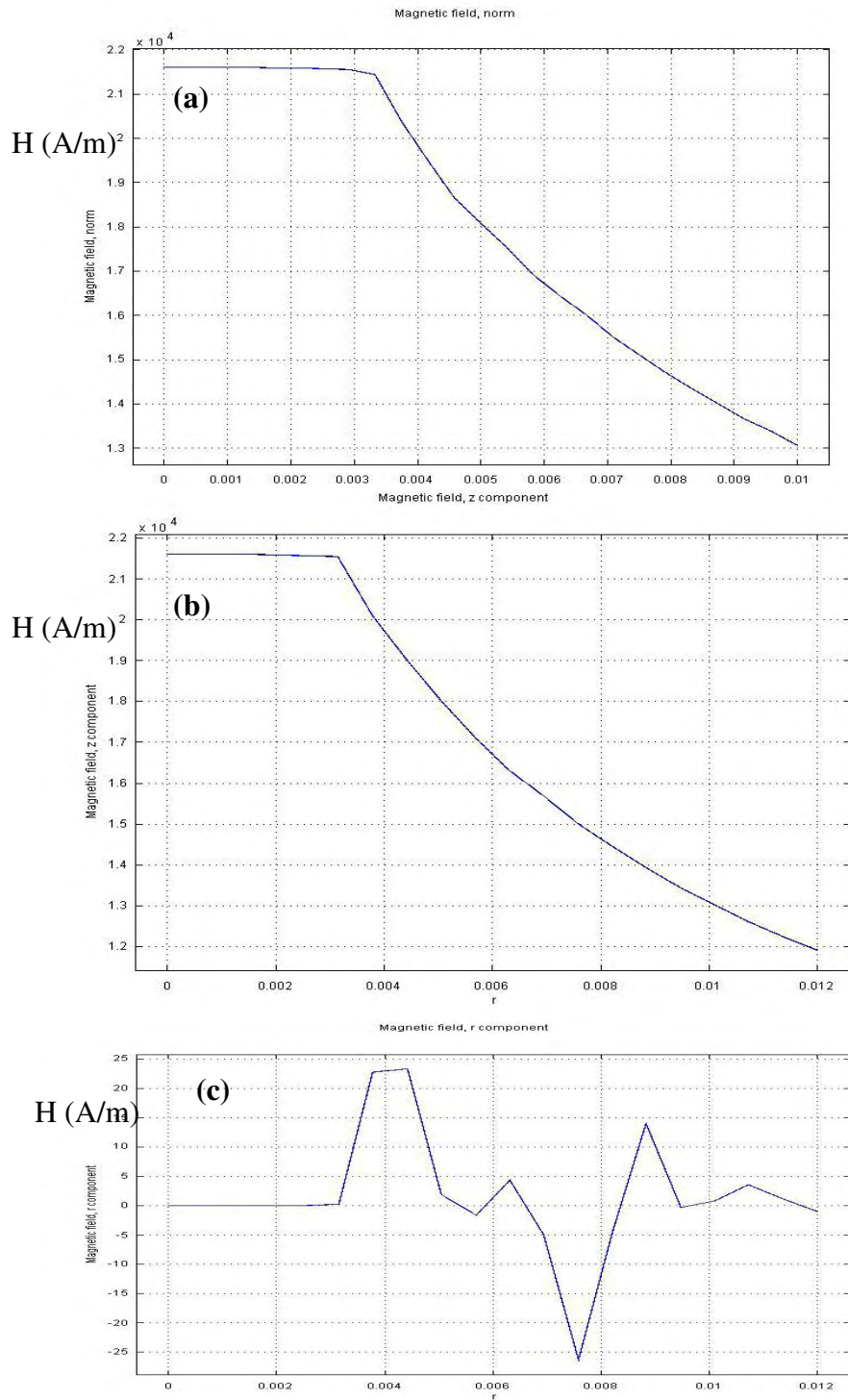
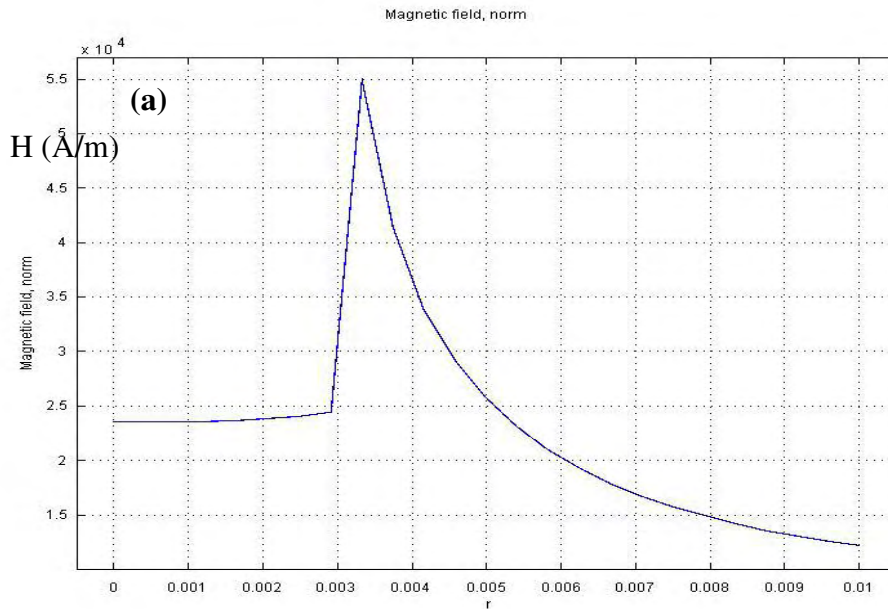


**Figure 2.11** (a) Total field distribution along radius of sample at  $z = 0$ .  
 (b) z-component of field distribution along radius of sample at  $z = 0$ .  
 (c) r-component of field distribution along radius of sample at  $z = 0$ .

In the case of choosing the length station very close to the tip of the sample, Figures 2.12 (a) and 2.12 (b) show that the total magnetic field and z-component of the magnetic field are significantly different. This is because the radial component of the magnetic field is very large (Figure 2.12(c)), especially at the boundary, due to entry of magnetic flux lines.

An important factor in this case is that there is a slight variation in the z-component of the field inside the sample (~2%) and a very steep decline in the z-component of the magnetic field just outside the sample. At a distance of ~1mm from the surface the drop in field is ~33%. Therefore, a hall-chip near the edge of the sample is likely to underestimate the magnetic field in the sample. Furthermore, a small deviation from the hall chip being exactly perpendicular to the surface can lead to its estimate of the z-component of the field being corrupted by the large radial component of the magnetic field near the surface.

While all these simulations were carried by modeling FeGa as a ferromagnetic material with  $\mu_r=60$ , some of these simulations were repeated for  $\mu_r=360$ . It was found that the qualitative trends were the same while there was a small difference in the quantitative picture of the field distribution when the permeability was increased.



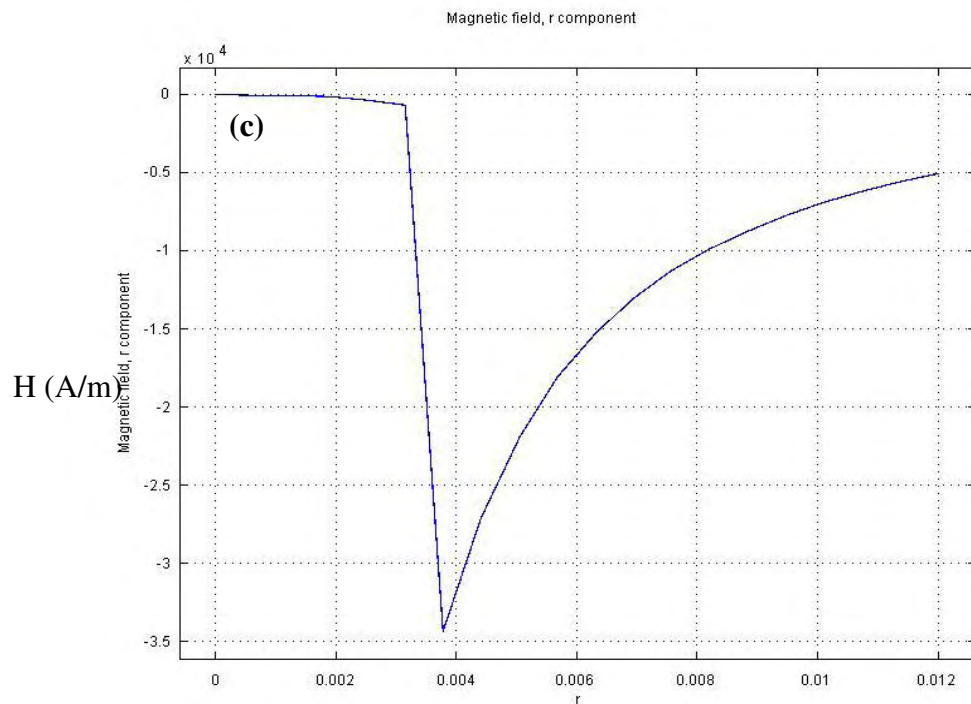
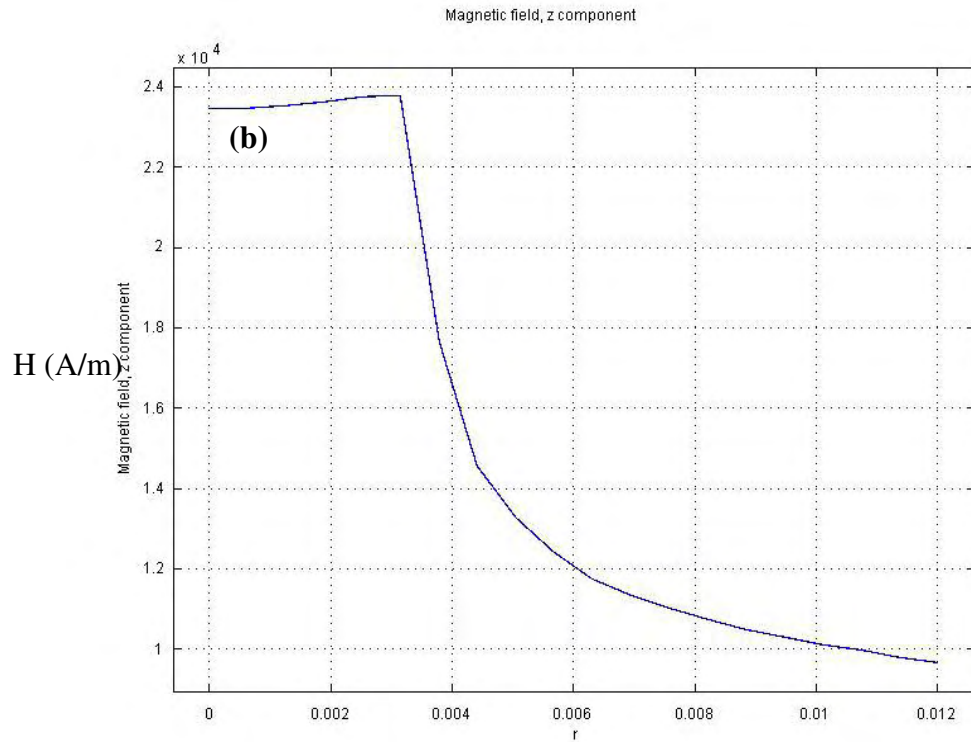


**Figure 2.12** (a) Total field distribution along radius of sample near its end.  
 (b) z-component of field distributions along radius of sample near its end.  
 (c) r-component of field distribution along radius of sample near its end.

#### 2.4. Experimental Results with Hall-Chips and Sense Coils Located at Various Places

The insights from the FEM simulations discussed in the previous section motivated the design of the following experiment (Figure 2.13). Two sense coils, one on the end cap and another on the upper half of the sample, were employed to analyze the variation in induction along the length of the sample and end caps. It is to be noted that plotting the induction measured by the sense coil around the end cap does not give the B-H curve of the end cap as the hall-chip is located on the specimen and therefore estimates the z-component of the field in the specimen and not the end-cap. Two hall-chips are used, one at the center of the sample and one at the bottom-end of the sample, to compare the magnetic field estimated at these two places.

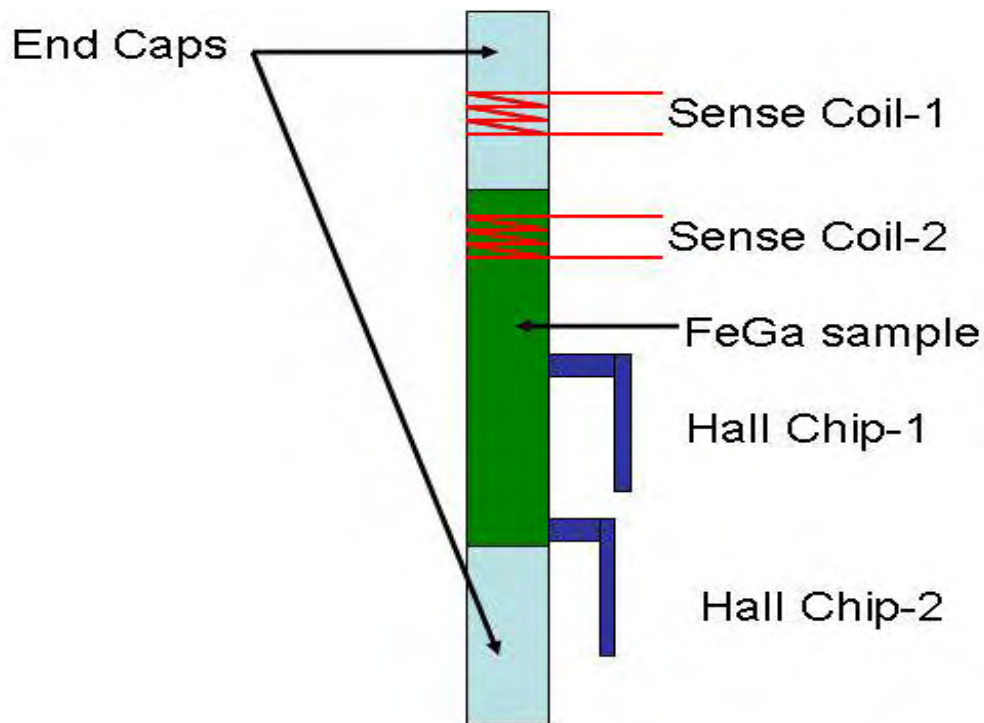


**Figure 2.13** Schematic of positioning of sense coils and hall chips on the sample.

However, when the experiment was carried out all 4 devices did not work simultaneously. In the first case the two sense coils and one hall chip (the one at the end) worked well. These results are shown in Figure 2.14 and they clearly indicate

that the magnetic induction in the end caps is higher than in the sample, as predicted by the FEM simulation. Furthermore, the end caps reach saturation magnetization ( $M_{sat}$ ) after the sample and have a larger value of  $M_{sat}$  than the sample, proving that they do not limit the flux which can pass through the sample.

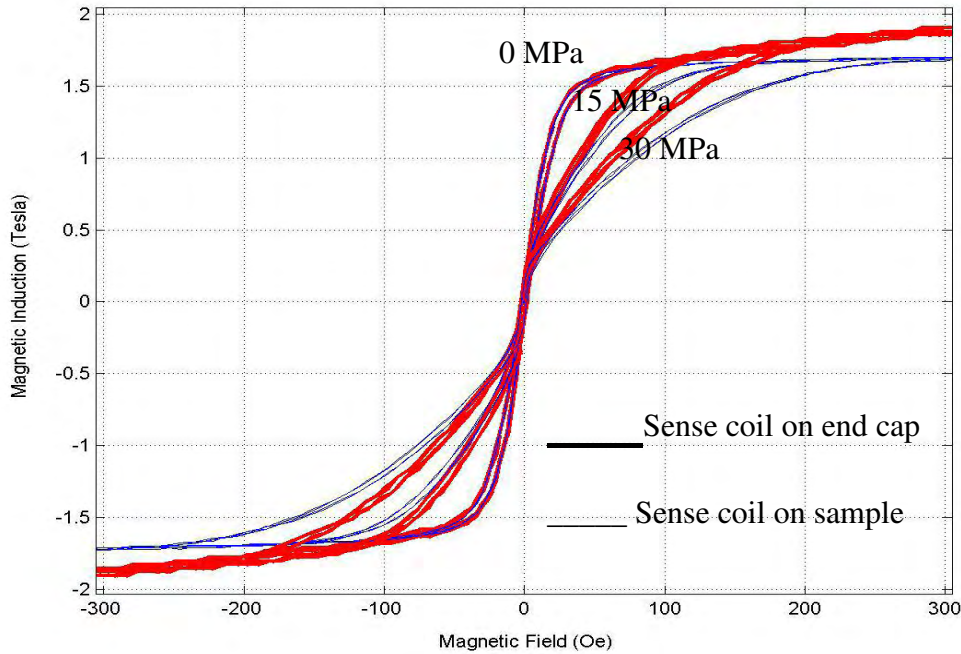


**Figure 2.14** Comparison of B-H curves with one hall-chip at the end of the sample and two sense-coils, one on the end cap (exhibit higher  $M_{sat}$  and B) and the other on the sample (exhibit lower  $M_{sat}$  and B).

Another important issue is the difference in the field estimated by hall chip placed at the center and at the end of the sample. This was carried out with a second set of experiments with one sense coil (placed on the sample) and two hall chips, one each located at the center and extremity of the sample. The results of these tests are shown in Figure 2.15 (a) and (b). The general trend demonstrated is explained in terms of the B-H curve at 15 MPa compressive stresses, as shown in Figure 2.15 (b). At lower values of field/magnetic induction, the magnetic field estimated by the hall chip at the end of the sample appears to be much smaller than that estimated by the hall chip at the center which agrees well with the FEM simulations (assuming that both hall-chips were reasonably perpendicular to the sample surface).

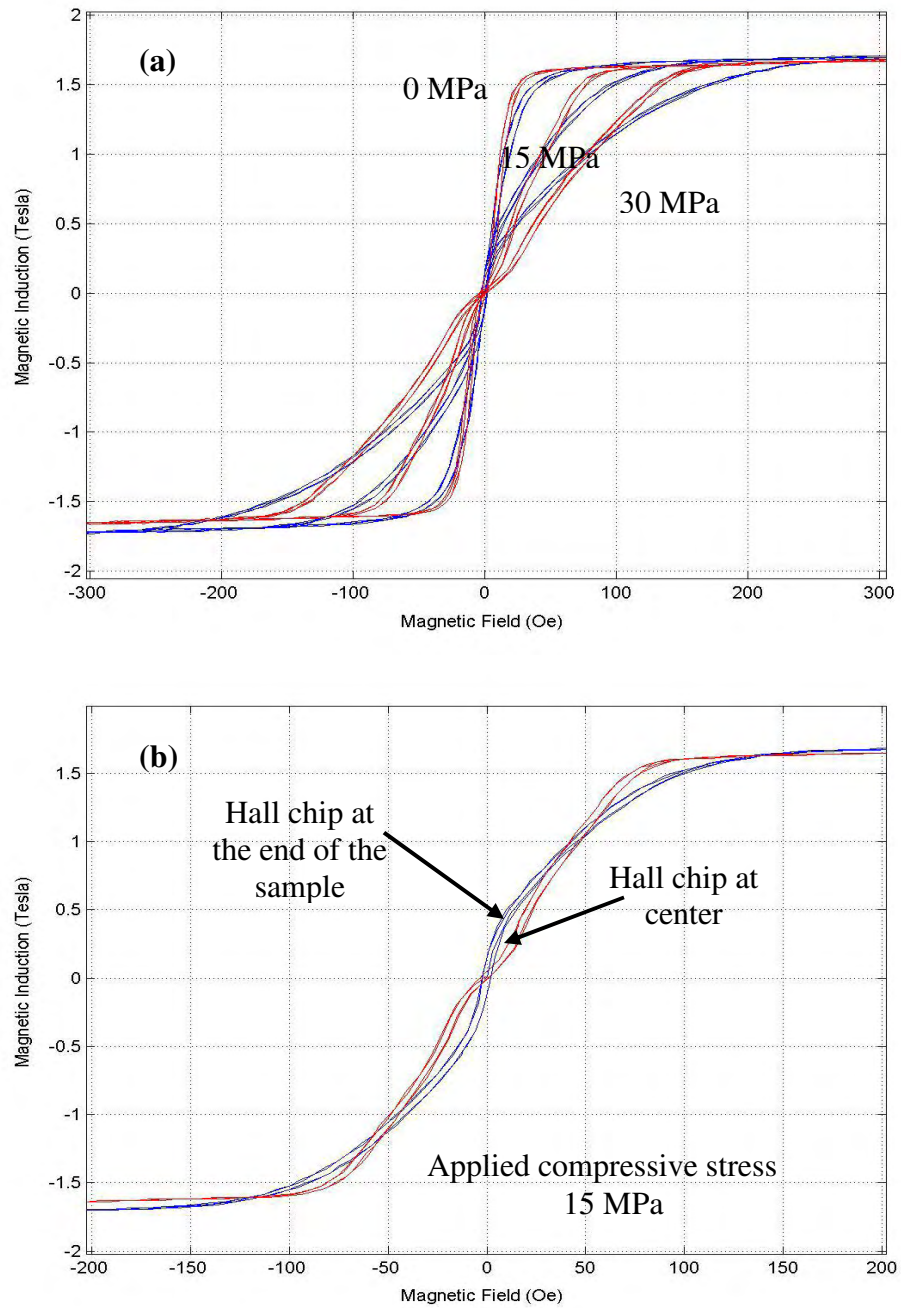


**Figure 2.15 (a)** Comparison of B-H curves with sense-coils on the end cap and hall-chip on sample center (curves low permeability at low fields) and hall-chip at the end of the sample (shows large variation in B with H at small fields).  
**(b)** The 15 MPa case of Figure 2.15 (a), shown here for greater clarity.

However, at higher values of fields/magnetic induction the field estimated by the hall-chip at the ends of the sample appears to be higher than that estimated by the hall-chip at the center. This difference in predictions was due to a different field distribution at reduced permeability as material approaches magnetic saturation and was verified by repeating the simulation by modeling the FeGa rod close to saturation, as  $\mu_r=2$ . The results illustrated in Figures 2.16(a) and (b) clearly show that

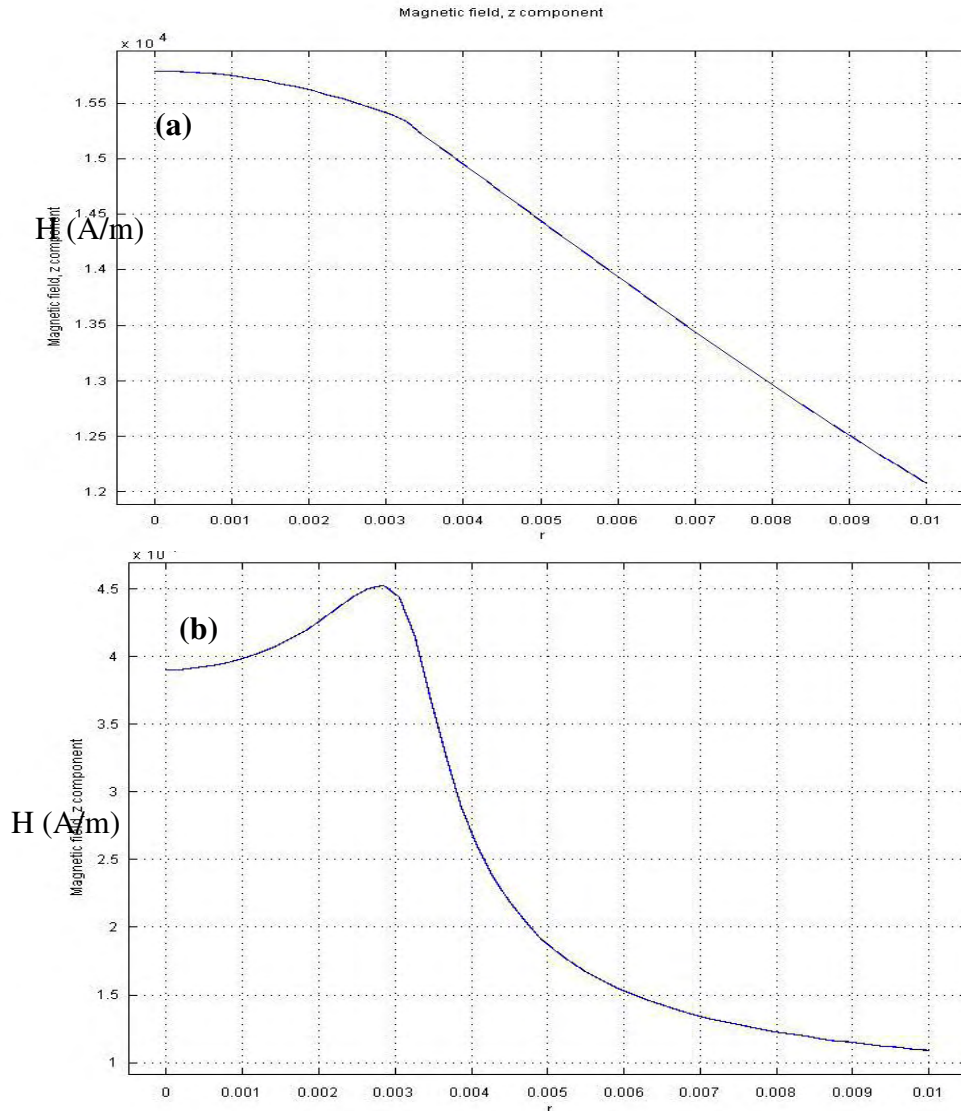


**Figure 2.16 (a)** Z-component of field distribution along radius of sample ( $\mu_r=2$ ) at its mid-point ( $z = 0$ ).

**(b)** Z-component of field distribution along radius of sample ( $\mu_r=2$ ) at one of its ends ( $z = L/2$ ).

the field at the end of the sample can be much larger than that at the center, when the magnetic sample approaches saturation. This also implies that there is likely to be a large variation in the field through the length of the sample as it approaches saturation.

It should be noted that only the qualitative trends observed in the experiment are explained here as a detailed quantitative simulation to completely predict the experimental variation in H estimated by the hall chips is beyond the scope of this work. Such a task is additionally complicated by the fact that some regions of the sample may saturate before others leading to varying permeability in different regions of the sample. The current work therefore focuses on understanding the basic physical picture of the field and induction distribution. This is used to suggest the ideal place to locate the sensing devices as well as provide a bound on the errors in measurement.

## **2.5 Conclusions**

A 2-D axisymmetric model of the magnetic transducer was developed using COMSOL Multiphysics<sup>TM</sup> FEM software and benchmarked for the case of prolate ellipsoidal specimens of various aspect ratios. The FEM predictions were found to be in good agreement with the analytical results.

The FEM model was then used to estimate the spatial magnetic field and induction distribution in and around a 2.54 cm (1 inch) long and 0.635 cm (¼ inch) diameter FeGa specimen (modeled with  $\mu_r = 60$ ). It was found that the longitudinal variation (at  $r=0$ ) of both the magnetic induction and field inside the sample was about 8%. Hence, a sense coil wound at an average length of half the distance from the center to end of the specimen is likely to estimate the induction within the specimen to an accuracy of  $\pm 4\%$ .

The lateral or radial variation in magnetic field is more complex and also of great importance in estimating the field inside the sample via a hall sensor placed on the surface of the sample. It was found that in the case of FeGa (modeled with  $\mu_r =$

60) the z-component of the field does not vary significantly with radial position inside the sample [variation with  $r < 1\%$  at the sample center and  $\sim 2\%$  at the end of the sample]. Outside the sample, at a distance of 1 mm outside the surface of the sample the field drops by 10% at the center but by as much as 33% at the end of the sample. These results indicate that the most accurate description of the field within the sample is obtained by placing the hall chip at the center. Furthermore, the field estimate here is less likely to be corrupted by the radial component of the field which is very large near the edge of the sample. Simulations performed assuming  $\mu_r = 360$  for the sample showed that the qualitative trends were the same though the quantitative variation was slightly different. Overall, a correctly oriented hall-chip (with an active sensing of  $\sim 0.5$  mm), placed in the range of  $\pm 3.175$  mm (0.125 inch) from the sample center is likely to estimate the magnetic field in the sample to an accuracy of  $\pm 3\%$ .

Finally, as the sample approaches  $M_{\text{sat}}$  the value of relative permeability in the sample tends to one ( $\mu_r \rightarrow 1$ ). This causes a large field variation along the length of the sample. The FEM model predicts the field at and near the interface of the sample and end cap is considerably (about 2-3 times) higher than that at the center. However, as the sample reaches saturation there is no significant difference in the induction and magnetostriction values and the estimates may be reasonably accurate if the hall-chip is placed close to the center.

*Recommendation on transducer design:*

From this study, the following observations were made:

1. As the flux passes from the high permeability transducer body and end-caps into the sample there is some flux leakage at the interface leading to a longitudinal drop in flux from the ends of the sample to the center.
2. It appears that this may also lead to flux-lines being concentrated within the sample, leading to a lateral variation in field/flux inside the sample.

A reasonably good solution to mitigate this effect is, qualitatively speaking, allow a larger amount of flux at the interface of transducer and end-caps as well as

end-caps and sample. This may be achieved by a tapered path (progressive reduction of cross-section area from say twice the cross-section of the end-caps to that of the end-cap) that focuses the flux before it enters the end-caps. This may reduce the longitudinal and to some extent lateral variation in field within the sample.

## **2.6 Summary**

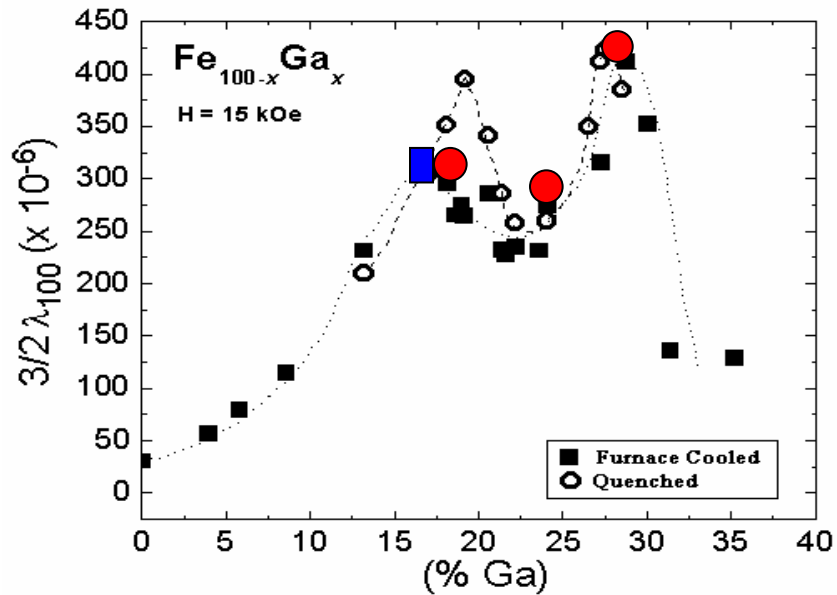
In summary, given the simulation results and the space constraint, an ideal configuration is to have the hall-chip on a point at the mid-length ( $z = 0$ ) of the sample, the sense-coil at an average length of half-the distance between the mid-length and the end (between  $z = 0$  and  $z = \pm L/4$ ) and strain-gauges centered on the sample mid-length ( $z = 0$ ). For such a configuration the sense-coil estimates are likely to be accurate to  $\pm 4\%$  and hall-chip estimates  $\pm 3\%$  for the most part. The magnetostriction estimates are likely to be more accurate than  $\pm 4\%$  as they are centered on the sample mid-length. Thus, a  $\lambda$ -H or B-H curve measured with the optimized location of strain-gauges, sense coil and hall-chip is likely to have a worst case additive error of  $\pm 7\%$ , for most parts of the  $\lambda$ -H or B-H curve.

## Chapter 3: Experimental Single-crystal Actuation and Sensing Behavior

Clark *et al.* [Clark2000, 2001a, b] have shown that  $\lambda_s$  varies significantly with Ga content (Figure 3.1) and it can be expected that the magnetomechanical behaviors also vary strongly with Ga content. An understanding of the composition-dependent magnetomechanical behavior and specifically the  $\lambda$ -H and B-H characteristics will facilitate the optimization of FeGa actuator and sensor designs. Previous research has characterized the magnetomechanical behavior of single crystal 17% and 19% Ga samples in the  $\langle 100 \rangle$  direction [Clark2001a, b, Kellogg2005]. This work focuses on characterization of slow cooled  $\langle 100 \rangle$  oriented single-crystal 19, 24.7 and 29 at. % Ga samples targeting compositions of the first peak, the first valley and the second peak in the magnetostriction curve shown in Figure 3.1 These samples capture the following important trends in behavior. Up to 19 at. % Ga (17 at. % Ga in furnace cooled and 19 at. % Ga in quenched samples), disordered substitution of Ga occurs in BCC  $\alpha$ -Fe resulting in increasing magnetostriction with % Ga. However, ordered DO<sub>3</sub> crystal structures begin to form for higher % Ga [Lograsso 2006] decreasing the magnetostriction ( $\lambda_{100}$ ) observed when Ga content is increased from 19 through ~25 at. %. As the Ga content increases from 24% to 28%, a decrease in the difference between the  $c_{11}$  and  $c_{12}$  elastic moduli is observed [Clark2003], while the magnetomechanical coupling constant,  $b_1$ , remains relatively constant in Equation 1.13. This results in the second  $\lambda_{100}$  peak [Clark2003]. Thus the behavior of slow cooled  $\langle 100 \rangle$  oriented single crystal FeGa with 19\*, 24.7 and 29 at. % Ga are all expected to differ significantly from each other.

\* NOTE: The slow-cooled 19 at. % Ga sample is likely to have some DO<sub>3</sub>, but predominantly consists of BCC  $\alpha$ -Fe randomly substituted with Ga as opposed to the slow cooled 24.7 at. % Ga sample which predominantly consists of DO<sub>3</sub> crystal structure [Lograsso 2006].

The present work aims to characterize the composition dependent variation in the  $\lambda$ (magnetostriction)-H and B-H characteristics. In view of the fact that the sensing behavior can be predicted from the actuator behavior (as discussed in Chapter 5) sensor characterization was performed for only 19 at. % Ga. Furthermore, in an attempt to understand and model the behavior along various crystallographic directions, both actuation and sensing behaviors of a  $\langle 110 \rangle$  oriented  $\sim 18$  at. % Ga, single crystal sample were characterized and are presented in this chapter.



- Expected  $\lambda_{100}$  and Ga content of  $\langle 100 \rangle$  samples characterized in this chapter
- Expected  $\lambda_{100}$  and Ga content of  $\langle 110 \rangle$  sample characterized in this chapter

**Figure 3.1** Magnetostriction ( $3/2\lambda_{100}$ ) of FeGa vs. Ga content [Ref. Clark *et al.*].

### 3.1 Magnetic Transducer

This section describes the set-up of the magnetic transducer for actuator and sensor characterization, the metallurgical process used to grow the single crystal samples and a detailed description of mounting the sample and data acquisition. An in depth description of the various components of the transducer is provided by Figure 2.3 in Chapter 2, Section 2.2.

### 3.1.1 Description of Magnetic Transducer

The experimental setup consisted of a water-cooled current coil with a flux return path that could produce a field of upto 3000 Oe, well beyond the saturation field for FeGa alloys, at a constant temperature of 23°C. Figure 3.2 (left side) shows the transducer set-up for quasi-static actuator characterization. A constant pre-stress was applied by trays with lead weights that loaded the sample through an attachment balanced on the transducer shaft as shown in the figure.

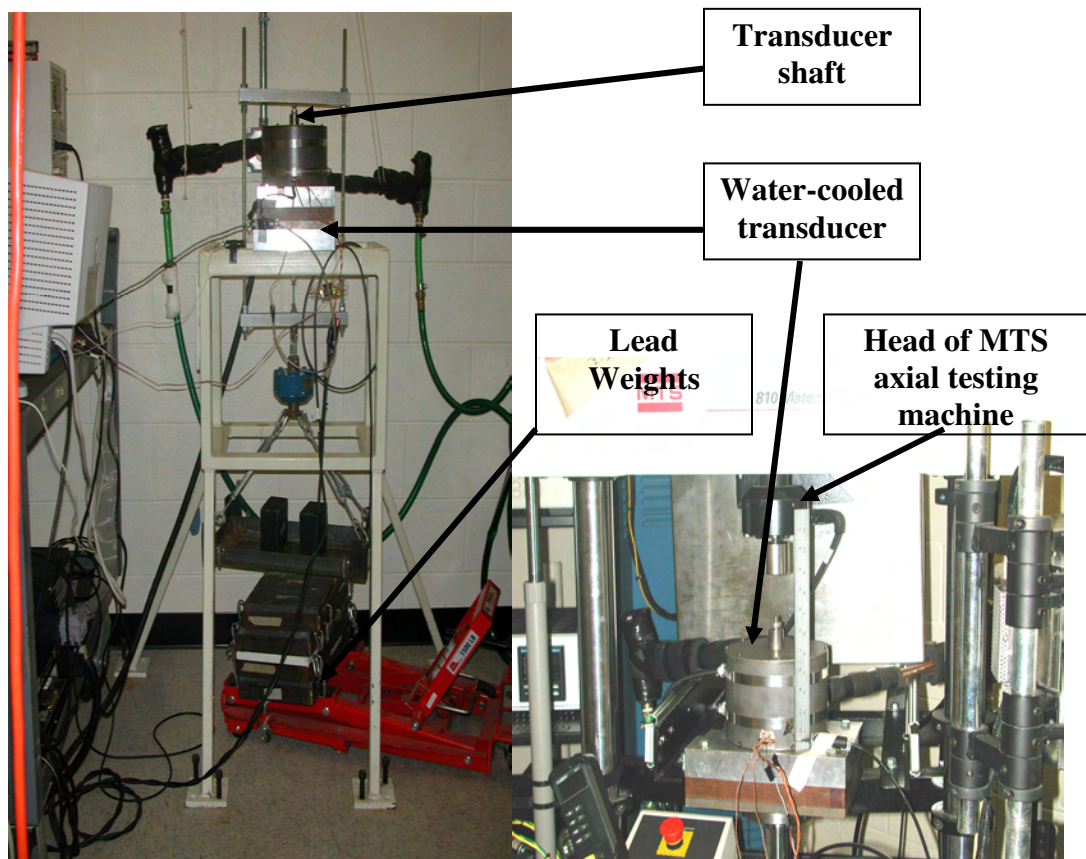


**Figure 3.2** Magnetic Transducer set up for quasi-static actuator characterization (left) and sensing characterization (right).

For sensor characterization, the transducer was mounted on the lower rod of an MTS, axial testing machine and the compressive load was applied by the head of the axial testing machine pressing down on the sample (Figure 3.2, right).

### 3.1.2 Sample Preparation and Mounting

#### *Sample preparation and heat treatment*

All single-crystal samples characterized were extracted from single-crystals produced by the Ames Lab, Iowa using the modified Bridgman technique with growth rate of ~2mm/hour. All the samples were annealed at 1000°C (except the 29 at. % Ga sample, which was annealed at 800°C) for 168 hours followed by furnace cooling to room temperature at the rate of approximately 10°C/minute.

#### *Verification of sample orientation and gallium content:*

The crystallographic orientation of all the single crystal samples was verified at the Ames Lab, Iowa using Laue X-ray back reflection analysis while the composition was determined using Energy Dispersive Spectroscopy (EDS). The orientation of the 19 at. % Ga <100> sample and 18 at. % Ga <110> sample were rechecked at the University of Maryland by performing x-ray diffraction on the small discs representative of the sample cross-sections, which were extracted from the sample by electric discharge machining (EDM).

#### *Sample mounting*

Figure 3.3 shows a close-up view of a single crystal Fe-Ga sample mounted in the transducer. The samples were typically 25.4 mm (1 inch) long with a diameter within  $\pm 2\%$  of 6.35 cm ( $\frac{1}{4}$  inch), and the longitudinal axis along a <100> direction. Steel end caps made from 1018 steel annealed at 900°C for 1 hour, about 12.7 mm ( $\frac{1}{2}$  inch) long were attached at the ends with magnetically-conducting grease (grease with fine-iron particles) coated between the contact surfaces to avoid air gaps.

### 3.1.3 Instrumentation

The following instrumentation was used to measure mechanical and magnetic characteristics of the sample. The outputs from these sensor/conditioning units were interfaced to the National Instrument data acquisition system through which the lab-view program acquired data serially from these channels.

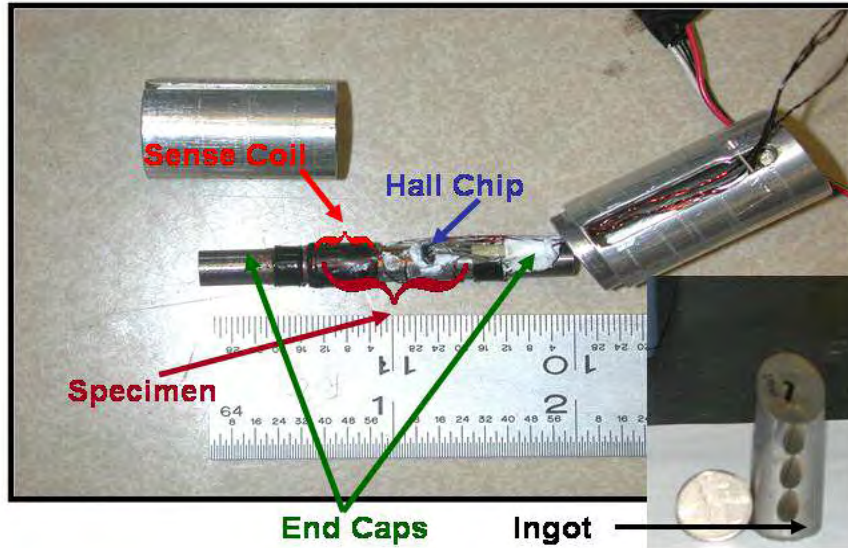


**Figure 3.3** Detailed picture of mounting of sensing elements on the sample. (Insert shows a typical single-crystal grown at Ames Lab, Iowa from which samples were extracted.)

### *Strain-gauges*

The strain produced in the sample was sensed using two CEA-06-250UN-350 strain-gauges, obtained from Vishay Micro-measurements, mounted diametrically opposite each other (to cancel the effect of bending strain). They were centered at the sample mid-point and were approximately half the length of the samples characterized. The strain limits for these gauges are ~3-5 %, so even the softest (29 at. % Ga) sample loaded at 80 MPa compressive stress was well within the operating limits. The strain-gauges were connected in series and formed one side of a quarter-bridge configuration. A 350 $\Omega$  precision resistor was added to the 350 $\Omega$  dummy resistance of the strain-conditioning unit as the resistance of the two strain-gauges connected in series amounted to 700  $\Omega$ .

### *Hall chip*

A1323EUA allegro hall-chip, attached at the sample mid-point, was used to estimate the field inside the sample. This hall-chip has a 3-pin configuration with +5V applied between input and ground. The output ranges from 0 to 5V with 0-field output corresponding to ~2.5V. With a sensitivity of 2.5mV/G it can sense a B of  $\pm 1000\text{G}$  which corresponds to  $\pm 1000\text{ Oe}$  of magnetic field inside the sample. The allowed operating temperature range was  $-40^\circ\text{C}$  to  $85^\circ\text{C}$ .

#### *Sense coil and integrating flux meter*

A sense-coil typically consisting of 125 turns was employed to estimate the average magnetic induction (B) in the sample. It was placed around the sample and its output connected to a MF-5D portable precision electronic integrating flux-meter manufactured by Walker Scientific. This instrument produced an analog output in the range of  $\pm 1\text{V}$ , proportional to the change in flux/flux-density. The proportionality constant depends on the operating range to which it was set.

#### *Principle for measurement of magnetic induction (B) using the sense coil:*

Consider a sense coil of N turns wound around a ferromagnetic sample of cross-section area A. On application of an incremental magnetic field the magnetic induction in the sample changes by  $\Delta B$  in an interval of time  $\Delta t$ . In accordance to the Lenz law, this produces an electromotive force (emf) in the coil which is proportional to the rate of change of flux through it:

$$V_{\text{sense-coil}} = \text{emf} = -N \frac{\Delta \phi}{\Delta t} = -NA \frac{\Delta B}{\Delta t} \quad (3.1)$$

The integrating flux meter senses this instantaneous voltage and integrates it over time to evaluate the change in magnetic induction. Integrating Equation 3.1 leads to:

$$\Delta B = \int_{B_1}^{B_2} dB = -\frac{1}{NA} \int_{t_1}^{t_2} V(t)_{\text{sense-coil}} dt \quad (3.2)$$

It should be noted that the integrating flux meter cannot measure the absolute value of magnetic induction (B) but can only sense the change in B with reference to its initial value at time  $t_1$ . Therefore, it is necessary to define the datum or zero-point. This is

achieved by demagnetizing the sample and zeroing the flux meter to define  $B=0$ . All subsequent measurements are made with respect to this datum.

### *Load cell*

For actuator tests, the stress was determined from the weight of the attachment, lead-blocks and trays used for loading the sample and the nominal cross-section area of each sample and is accurate to  $\pm 4\%$ . For sensor tests, the load was sensed by a 5000 lb load cell attached to the head of the MTS machine.

## **3.2 Actuator Behavior**

In this section, the procedure used to characterize the actuation behavior is discussed. This is followed by a detailed discussion of the effect of Ga content on the actuation behavior, i.e. the  $\lambda$ -H and B-H curves in the  $\langle 100 \rangle$  direction. Finally, the actuation behavior in the  $\langle 110 \rangle$  direction is discussed for a sample with 18 at. % Ga.

### **3.2.1 Actuation Characterization Procedure**

The experimental methodology for quasi-static actuator characterization, involved applying a magnetic field with maximum amplitude  $\sim 900$  Oe at a rate of about 1 cycle every 100 seconds. This was achieved by passing a current (at a frequency of 0.01 Hz) through a water-cooled transducer that maintained temperature constant within  $\pm 2^\circ\text{C}$ , while constant compressive stress state was maintained in the sample by hanging dead weights on a tray attached below a bar hanging on the top part of the housing shown in Figure 3.2 (left).

To ensure consistency of results the sample was demagnetized before every test by applying a sinusoidal current at 1 Hz with a starting amplitude of 5A (likely to correspond to a 1400 Oe field in a typical sample) which decayed geometrically at the rate of 10% between two cycles till it was less than 0.01 % of the initial amplitude.

For performing the quasi-static tests, several frequencies were experimented with before arriving at the 0.01 Hz standard that was used for all tests in this

dissertation. It was found that at higher frequencies, for example 0.05 Hz, the number of data points obtained for  $\lambda$ -H and B-H curves, especially the low-stress cases where the sample reaches saturation below 100 Oe, were insufficient to accurately capture the trends. However, going from 0.01 Hz to lower frequencies upto 0.003 Hz did not result in any change in data, even in cases where the sample saturated at fields as low as 25 Oe or as little as 2% of the cycle time. Thus, 0.01 Hz was chosen as a standard.

### 3.2.2 Effect of Gallium Content on Actuator Characteristics

The  $\lambda$ -H and B-H curves of <100> oriented single-crystal FeGa samples with 19 at. % Ga content (Figure 3.4), 24.7 at. % Ga content (Figure 3.5) and 29 at. % Ga content (Figure 3.6) are compared and discussed.

#### *General observations*

In general, on application of greater compressive stress, the magnetic field required for reaching saturation magnetization and magnetostriction is higher. For example, in the 19 at. % Ga sample,  $M_{\text{sat}}$  or  $\lambda_{\text{sat}}$  is reached at ~50 Oe for a compressive stress of 15 MPa whereas a field of ~200 Oe is required to drive the sample to  $M_{\text{sat}}$  or  $\lambda_{\text{sat}}$  for a compressive stress of 60 MPa. This can be explained on the basis of balance between magnetic and magnetoelastic energies. Larger pre-stress results in greater magnetoelastic energy, requiring the application of greater magnetic fields to rotate the magnetization parallel to the direction of the applied field.

The experimental  $\lambda$ -H and B-H curves also demonstrate that a given pre-stress has a greater effect on the higher Ga content samples as compared to the lower Ga content samples. For example, with a pre-stress of 60 MPa, a magnetic field of ~200 Oe needs to be applied to drive the 19 at. % Ga sample to saturation as compared to a field of ~600 Oe that is required for driving the 29 at. % Ga to saturation. One possible reason for the higher Ga content FeGa samples requiring greater fields to be driven to saturation, under identical stress is discussed in the chapter on modeling actuator behavior, Chapter 4.

### *Effect of compressive stress on maximum magnetostriction at different compositions*

The trends in  $\lambda$ -H curves for all Ga content show that the saturation magnetostriction reaches a maximum value in a certain range of stress that is typically about 15-30 MPa. This “optimal” compressive stress is the minimum stress required for producing the largest possible magnetostriction and can be explained as follows. When no or low stress is applied, all the long axes are not perpendicular to the rod axis in the demagnetized state. Consequently, the sample is not at its shortest length. On application of optimum compressive stress, most long axes are oriented perpendicular to the rod axis in the demagnetized state and consequently the sample is at its shortest length. Therefore the total change in sample length, when all the long axes orient parallel to the sample axis, when it is magnetized, is larger at the optimal stress than for the low-stress case.

An unexpected observation is that at higher Ga content, i.e. 24.7 at. % and 29 at. % Ga,  $\lambda_{\text{sat}}$  decreases with increasing stress. For example, in the 24.7 % Ga sample,  $\lambda_{\text{sat}}$  appears to decrease by 10 % from ~275 ppm to ~250 ppm, when the compressive pre-stress is increased from 30 MPa to 60 MPa. A similar decrease in  $\lambda_{\text{sat}}$  is observed in the 29 at. % Ga sample. However, the lower Ga content, 19 % Ga sample does not exhibit any significant decrease of  $\lambda_{\text{sat}}$  with increasing compressive stress. This trend was confirmed in both the 24.7 at. % Ga and 29 at. % Ga sample by repetition of the experiment. However, in the absence of in-situ x-ray diffraction, under stress, it is impossible to find a conclusive explanation for this behavior. It may be conjectured, that this effect is due the complex elastic interaction between the multiple phases: disordered  $\alpha$ -phase and an ordered phase  $\text{D0}_3$  [Kubaschewski1982, Lograsso2006] and several other ordered phases such as B2,  $\text{L1}_2$  and  $\text{D0}_{19}$  [Srisukhumbowornchai2002] which may be formed in FeGa samples with high Ga content, particularly in the range of 22 to 36 at. % Ga. One of the possible hypothesis that may explain this phenomenon is that one of the phases stiffens or possibly undergoes a first-order phase transition under stress, thus decreasing the over all

magnetostriction produced by the material. An investigation of this effect is beyond the scope of this thesis.

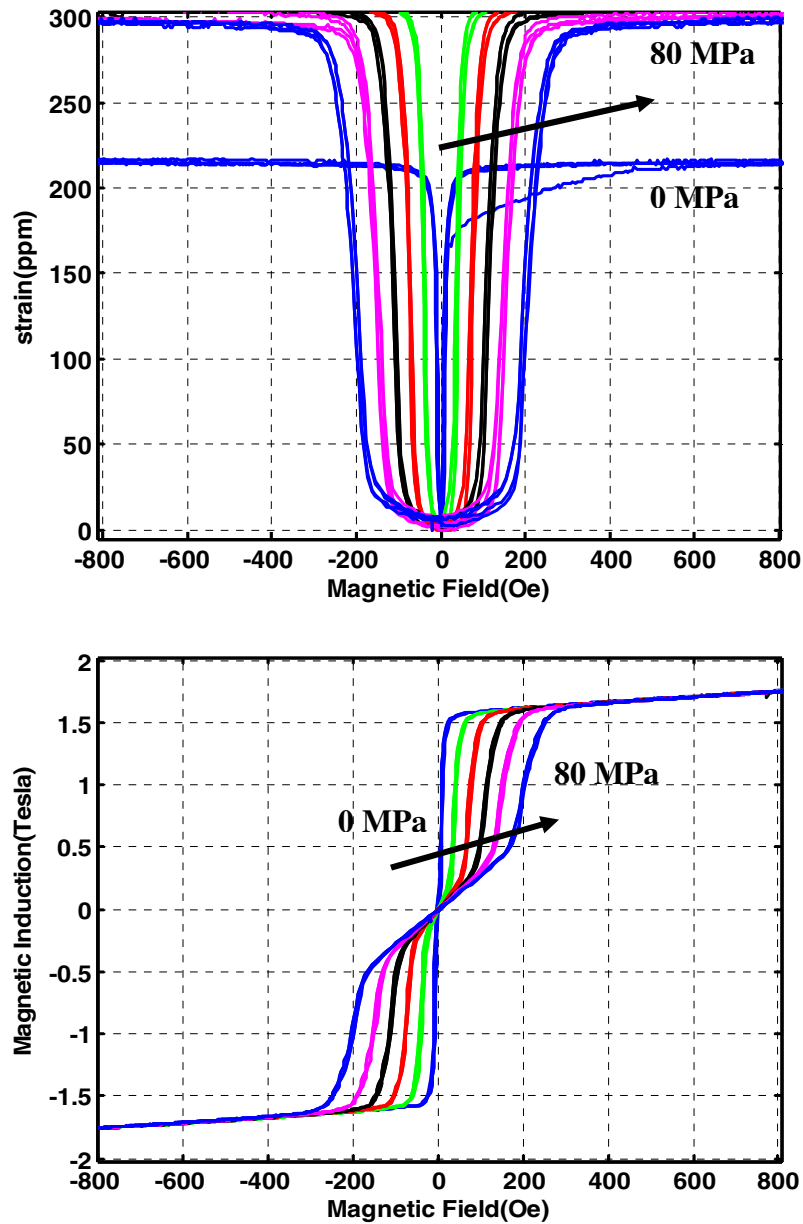


**Figure 3.4**  $\lambda$ -H (top) and B-H (below) of 19 at. % Ga, furnace cooled,  $\langle 100 \rangle$  oriented single crystal FeGa [compressive pre-stress of 0, 15, 30, 45, 60 and 80 MPa].

*NOTE: Throughout this chapter arrows indicate increasing compressive pre-stress for actuator characteristics and increasing bias field for sensor characteristics.*

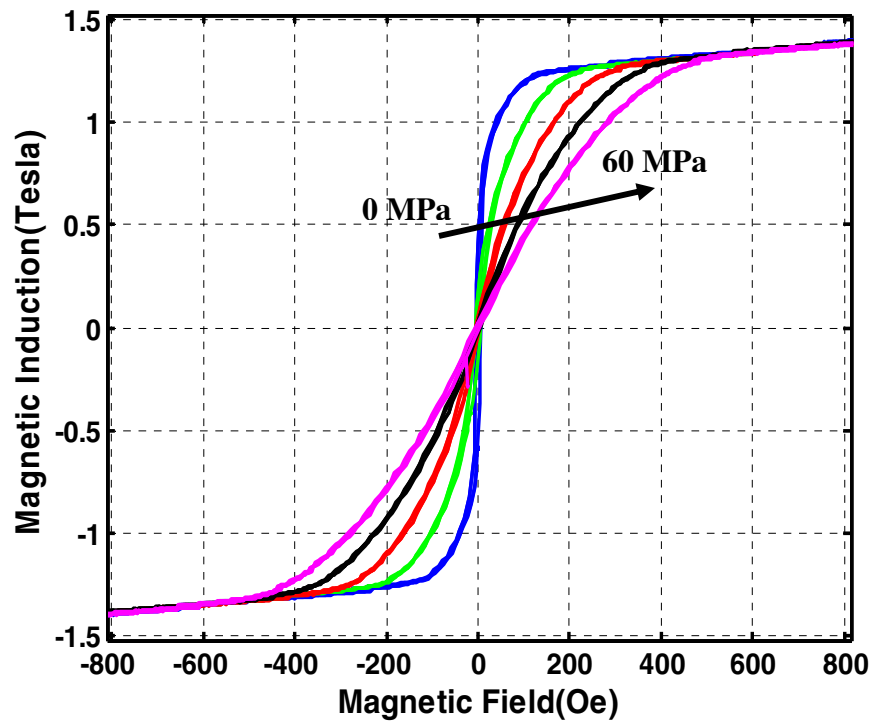
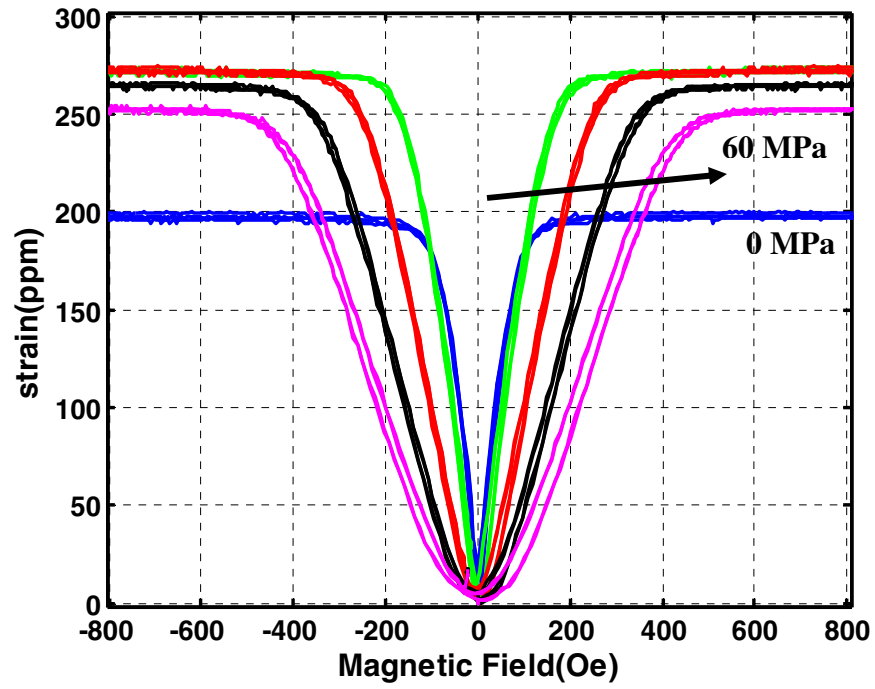


**Figure 3.5**  $\lambda$ -H (top) and B-H (below) of furnace cooled,  $\langle 100 \rangle$  oriented 24.7 at. % Ga single crystal FeGa [compressive pre-stress of 0, 15, 30, 45 and 60 MPa].

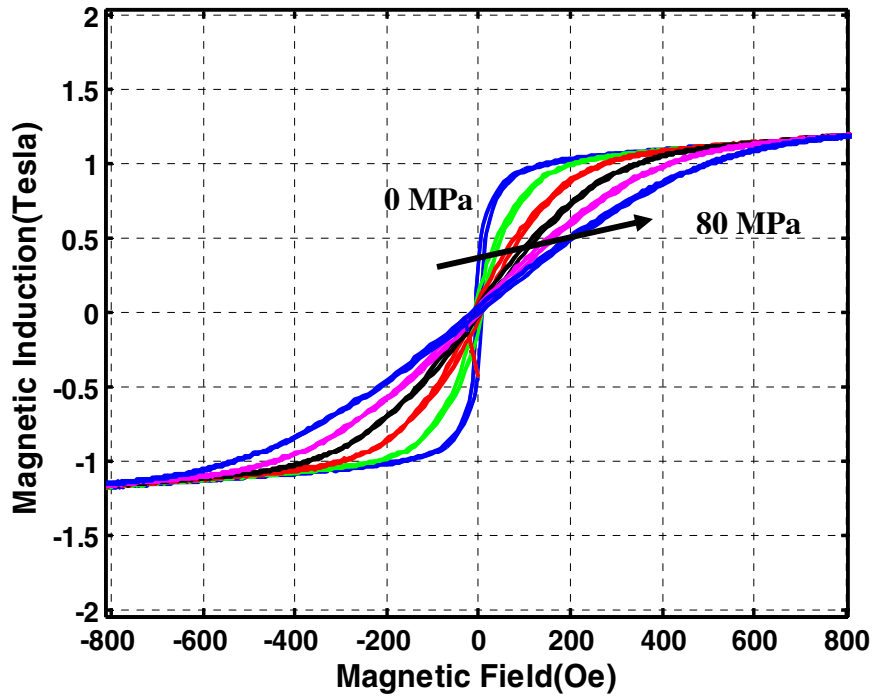
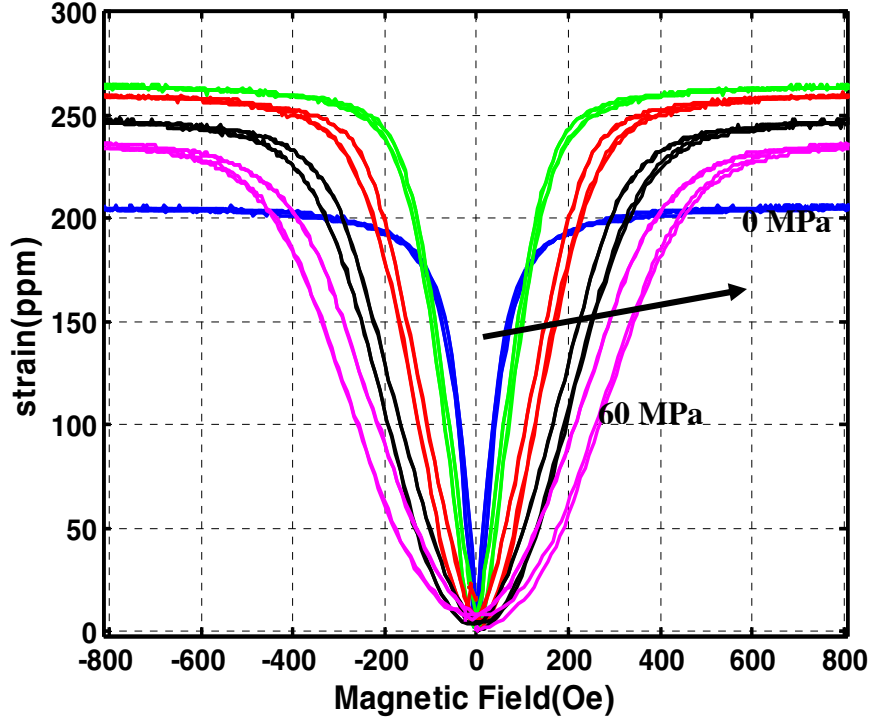


**Figure 3.6**  $\lambda$ -H (top) and B-H (below) of furnace cooled,  $\langle 100 \rangle$  oriented 29 at. % Ga single crystal FeGa [compressive pre-stress of 0, 15, 30, 45 and 60 MPa].

(Note: For 80 MPa case only the B-H curve is plotted.)

### *Effect of compressive stress on nature of B-H curves at different compositions*

The B-H curves for the 19 at. % Ga samples show a distinct kinking behavior. At low fields, the slope of the B-H curves is small (Figure 3.4) representing a regime where the magnetic permeability is low, followed by a sudden increase in slope (region of large permeability) till saturation magnetization is reached and the slope becomes nearly zero. This kinking behavior, i.e. exhibition of two distinct regimes of low and high permeability, is increased on application of a larger compressive stress. This is reflected in the  $\lambda$ -H curves as well, where the region with low permeability also corresponds to a region where change in magnetostriction with field is small. The region with large permeability also corresponds to a large change in magnetostriction with field. In the 24.7 and 29 at. % Ga samples, the B-H curves (Figures 3.5 and 3.6) are rounded and exhibit no kinking behavior.

A combination of factors, viz. the relative magnitude of the magnetocrystalline and stress anisotropy and presence of imperfection may explain this effect. The 19 at. % Ga sample having higher magnitude of magnetocrystalline anisotropy [Rafique2004] than the 24.7 and 29 at. % Ga sample is one of the possible reasons for kinking behavior. However, at large applied stress, say 60 MPa, stress anisotropy is likely to have a significant effect in the 24.7 and 29 at. % Ga. This leads to the possibility that the 24.7 and 29 at. % Ga samples may have more imperfections due to the presence of multiple phases leading to the smoothing of the B-H and  $\lambda$ -H curves at higher Ga content. This issue is addressed in more detail in Chapter 4.

#### **3.2.4 Repeatability of Data**

For each Ga content, the single-crystal characterization data presented in this chapter was obtained from only one sample as multiple samples with the same Ga content were not available. However, repeatability in the characterization data was ensured by testing each sample twice for each mounting. Furthermore, some of the samples, viz. the 19 at. % and 29 at. % Ga samples were remounted and retested after six months. The test characteristics showed repeatability within 5%, which is consistent with error bounds estimated in Chapter 2.

The repeatability of test results for the 29 at. % sample is particularly important as it confirms the decrease in magnetostriction when compressive stress higher than 30 MPa is applied and is therefore presented in this section. Figure 3.7 demonstrates that the  $\lambda$ -H curves and B-H curves are repeatable within 10 ppm strain and 0.025 T induction, with the exception of the zero-stress case where the magnetostriction is repeatable within 20 ppm.

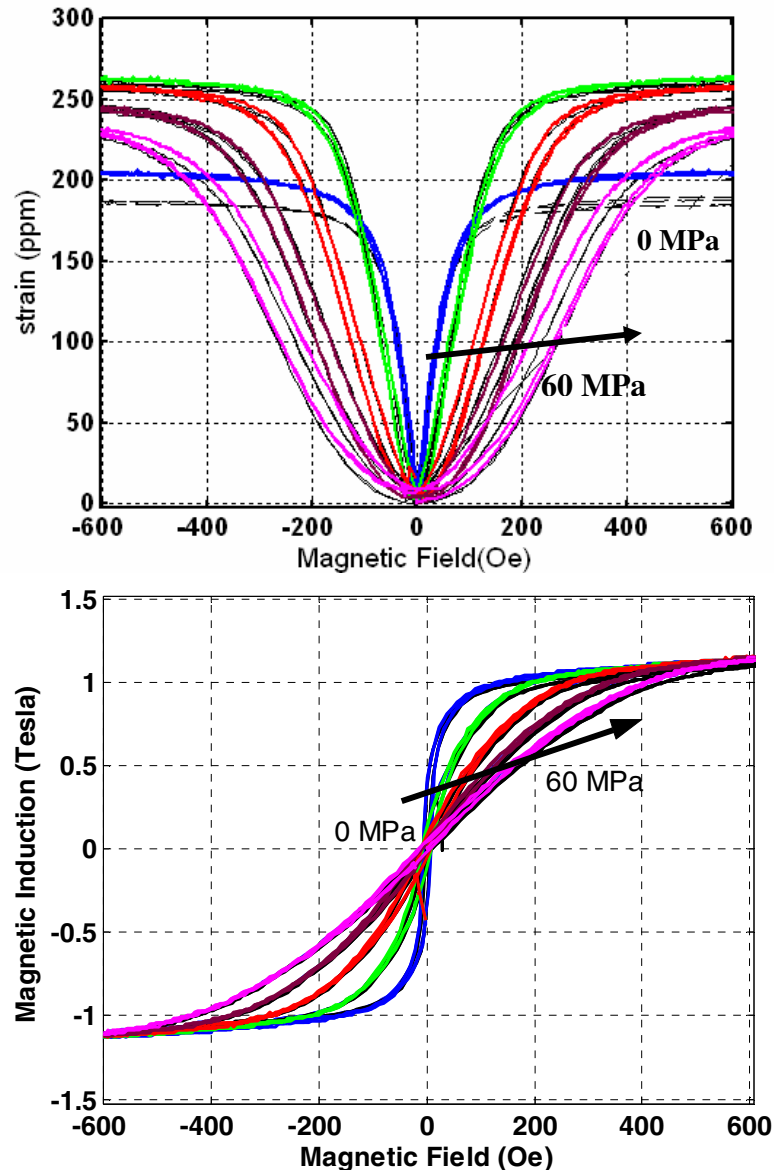


**Figure 3.7** Repeatability of  $\lambda$ -H (top) and B-H (below) of furnace cooled,  $\langle 100 \rangle$  oriented 29 at. % Ga single crystal FeGa [compressive pre-stress of 0, 15, 30, 45 and 60 MPa].

### 3.2.5 Effect of Crystallographic Direction on Actuator Characteristics

FeGa being a highly anisotropic material [Kellogg 2003], it is expected that its magnetoelastic behavior along various crystallographic directions is different. In an attempt to understand and model the behavior along various crystallographic directions, as illustrated in Figure 3.8, the actuation behavior of  $\langle 110 \rangle$  oriented  $\sim 18$  at. % Ga was characterized. It would have been preferable to have extracted a  $\langle 100 \rangle$  and  $\langle 111 \rangle$  oriented sample from the same single-crystal for comparison, but this could not be achieved due to some practical limitations. Throughout this subsection,  $\langle 100 \rangle$  sample is used to refer to the 19 at. % Ga  $\langle 100 \rangle$  oriented FeGa sample while  $\langle 110 \rangle$  sample is used to refer to the 18 at. % Ga  $\langle 110 \rangle$  oriented FeGa sample. An attempt is made to study the qualitative differences in actuation behavior along the two crystallographic directions, while some of the quantitative differences in behavior between the two samples may have been caused due to the difference in Ga content.

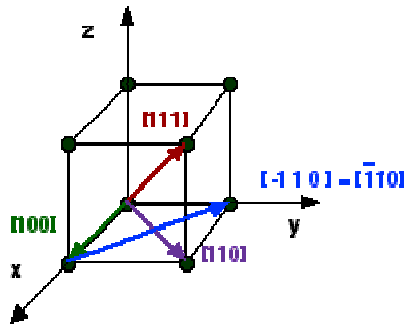


Figure 3.8 Orientations in a cubic crystal.

#### *$\lambda$ -H and B-H curves in the $\langle 110 \rangle$ direction*

It can be seen that the B-H curves in the  $\langle 110 \rangle$  direction for stresses of 30 MPa and above (Figure 3.9) exhibit four distinct regimes of magnetization. In the first regime, characterized by low permeability at low applied fields, the moments begin to rotate from an orientation perpendicular to the sample axis against the magnetocrystalline and stress anisotropy. This is followed by the second regime where large increase in magnetization and magnetostriction occurs possibly due to the flipping of moments to the  $\langle 100 \rangle$  directions nearest to the  $[110]$  sample axis. This is followed by the third regime characterized by gradual rotation to moments towards

the <110> direction. The fourth regime is characterized by permeability very close to one, where very small changes in magnetization occur due to the process of “forced magnetostriction”. This differs from the magnetization in the <100> direction (Figure 3.4) that exhibits three distinct regimes of magnetization.

The effect of stress on the B-H and  $\lambda$ -H curves is less in the <110> sample than in the <100> sample. For example, at 60 MPa compressive stress, ~150 Oe is required to reach saturation magnetization or magnetostriction in the <110> sample, compared to 200 Oe in the <100> sample. This confirms to the theory that the magnetoelastic energy is proportional to  $\lambda^*\sigma$ .  $\lambda_{110}$  being smaller than  $\lambda_{100}$ , the same level of stress has smaller effect on the <110> sample. This theory is further strengthened by the observation that by extrapolating the <110>  $\lambda$ -H, curve at 60 MPa compressive stress to a hypothetical magnetostriction value of 300 ppm, the corresponding value of field is ~200 Oe as seen in the <100> sample.

Finally considering that the typical values of magnetostriction for 18 at. % Ga are:  $3/2\lambda_{100} = 300$  ppm and  $3/2\lambda_{111} = -10$  ppm,  $\lambda_{110} = 1/4\lambda_{100} + 3/4\lambda_{111}$ , is expected to be at best 50 ppm, if the effect of pre-stress is not taken into account. However, under compressive pre-stress the magnetic moments are most likely to orient in the [001] direction perpendicular to the [110] axis producing a strain of  $-1/2\lambda_{100}$  along the [110] direction. With this as the datum a complete rotation of the moments to the [110] direction produces a net magnetostriction of  $3/4\lambda_{100} + 3/4\lambda_{111}$  i.e.  $1/2 \times (3/2\lambda_{100} + 3/2\lambda_{110})$  that is about 145 ppm as observed. This increase in magnetostriction obtained, by applying a compressive stress, is also seen in all the <100> oriented samples.

If ~145 ppm magnetostriction along <110> direction can be obtained in thin-films,  $\text{Fe}_{81}\text{Ga}_{19}$ , which was shown to be epitaxially deposited in the <110> direction on a <100> silicon substrate [Weston2002] may prove to have good actuation characteristics.

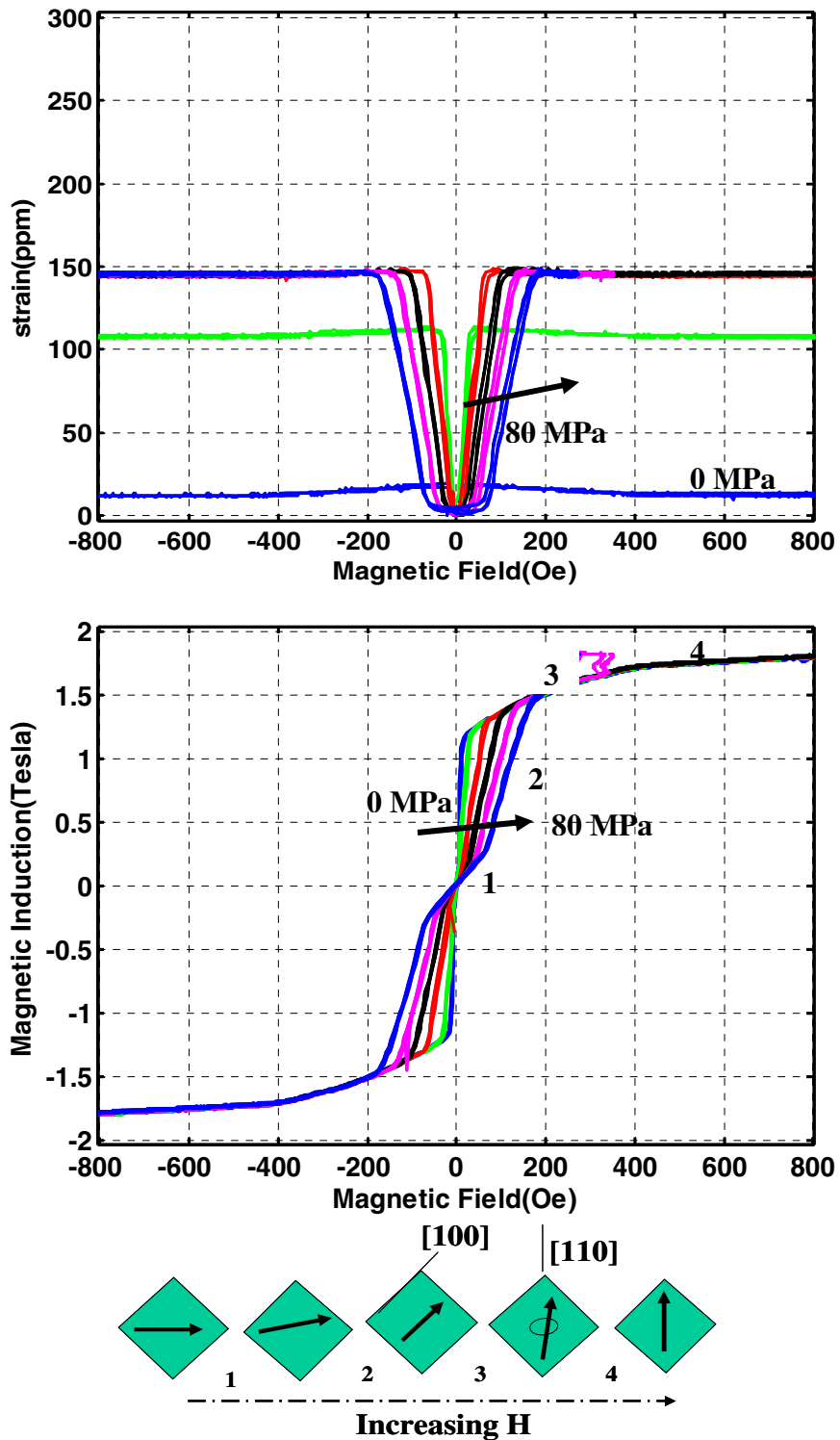


**Figure 3.9**  $\lambda$ -H (top) and B-H (middle) of furnace cooled,  $\langle 110 \rangle$  oriented ~18 at. % Ga single crystal FeGa [compressive pre-stress of 0, 15, 30, 45, 60 and 80 MPa]. Schematic of possible moment orientations (bottom) at various stages of B-H curves.

### **3.3 Sensing Behavior**

In this section, the procedure used to characterize the sensing behavior and the development of a PID (proportional, integral, differential) controller to maintain a constant field through the sample is discussed. This is followed by a detailed discussion of the sensing behavior,  $\epsilon$ - $\sigma$  (strain-stress) and B- $\sigma$  (magnetic induction-stress) characteristics, in the  $\langle 100 \rangle$  and  $\langle 110 \rangle$  direction.

#### **3.3.1 Sensing Characterization Procedure**

##### *Constant drive current tests*

A consistent test procedure was adopted to ensure that an identical demagnetized state of the specimen was achieved at the beginning of each test. The sample was demagnetized using zero-load conditions with a 1Hz sinusoidal magnetic field, with an initial amplitude of about 1400 Oe, decaying geometrically by 5% until it decreased to 0.02% of the initial amplitude. The required DC magnetic field at zero-stress was developed by gradually increasing the drive current. The specimen was then loaded to a compressive stress of 110 MPa and then unloaded to zero, at a rate of 2 MPa/s, while keeping the drive current constant. The stress (force), strain, magnetic induction and field through the sample were recorded during each experiment.

Though the drive current is maintained constant, there can be a large variation in the magnetic field through the sample. This is caused by the interaction between the transducer's magnetic circuit and magnetostrictive sample. This is particularly significant for alloys like FeGa as they have sufficiently high permeability to make their reluctances comparable to that of the magnetic circuit. In these cases, only a part of the magnetomotive force (MMF) generated by the coils is dropped across the sample (Figure 3.10). Hence, a change in the magnetomechanical state of the sample, such as an increase in reluctance caused by compressive stress, can cause a large increase in the MMF dropped across the sample and consequently an increase in the magnetic field in the sample.

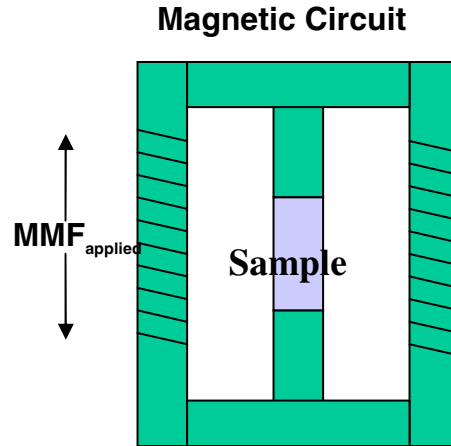


**Figure 3.10** Simplified model for interaction between sample and magnetic circuit.

### *Constant field tests*

In order to maintain a constant magnetic field through the sample, a feed-back loop was introduced to vary the drive current to compensate for variation in sample reluctance. The field through the sample was monitored by a hall sensor. The control of the drive current was implemented using a PID controller as illustrated in Figure 3.11. The proportional gain was set at 10, the integral gain at 0.01 and differential gain at zero. The voltage amplifier gain was set at 15. (With  $P=10$ , Amplifier Gain=15 and Plant Gain $\approx 0.15$ , the open loop gain  $A\approx 20$  and the designed difference between the set-point and output with feedback=  $A/(1+A)$  was estimated to be within 5%) However, the set-point voltage was offset so that the hall-chip output or field was within 1% that of the desired value. The controller response rate of 10 Hz and the proportional gain were sufficient to keep the field constant under an applied stress-ramp of 2 MPa/second. The small but non-zero integral gain of 0.01 was chosen after a few trials to make the system stable, while not affecting its response significantly.

The first step of the test procedure consisted of demagnetizing the sample as described in the previous section. During the demagnetization process the feedback loop was temporarily disconnected. Then the feedback loop was reactivated, the PID controller turned on and the  $V_{ref}$  was increased gradually from zero to a fixed value to obtain the desired value of the magnetic field. The specimen was then loaded to a compressive stress of 110 MPa and then unloaded to zero, at a rate of 2 MPa/s, while

the controller ensured that the magnetic field in the sample (estimated from the hall-chip output) was maintained constant.

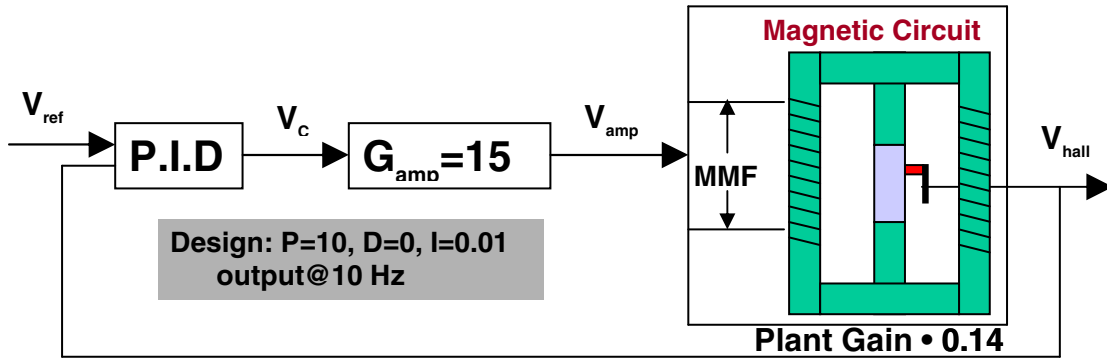


**Figure 3.11** Schematic of a proportional integral differential (PID) controller developed to maintain H constant in the sample.

### 3.3.2 Constant Drive Current vs. Constant Field Characteristics

Figure 3.12 (a) illustrates that the controller works very successfully. When the drive current is maintained constant, the variation in magnetic field through the sample on applying compressive stress can be as large as 3-4 times the initial value of field. For example, an initial field of 22.3 Oe increases to  $\sim 100$  Oe on loading to 110 MPa compressive stress (Figure 3.12 (a), left). However, with the controller on, the field was maintained at a constant value (to an accuracy of  $\pm 2$  Oe), as illustrated by (Figure 3.12 (a), right).

On application of compressive stress, magnetic induction (B) along the sample axis drops, as the magnetization (domains) rotate to a position perpendicular to the direction of application of stress. The sample permeability also drops, leading to an increase in sample reluctance which, in turn causes an increase in the magnetomotive force (MMF) dropped across the sample (if the drive current is constant). Consequently, the field increases in the sample with increased reluctance. This increase in H tends to diminish the decrease in magnetic induction (B) with compressive stress. Hence, the B- $\sigma$  curves at constant drive current are less steep than those at constant field (controller on) as shown in Figure 3.12 (b). This reflects in the sensitivity ( $d_{33}^*$ ) of constant magnetic field tests at certain bias fields, being about 4-5 times that of the sensitivity ( $d_{33}^*$ ) of constant drive current tests, which is discussed in

constant drive current (figures on left)    constant magnetic field (figures on right)

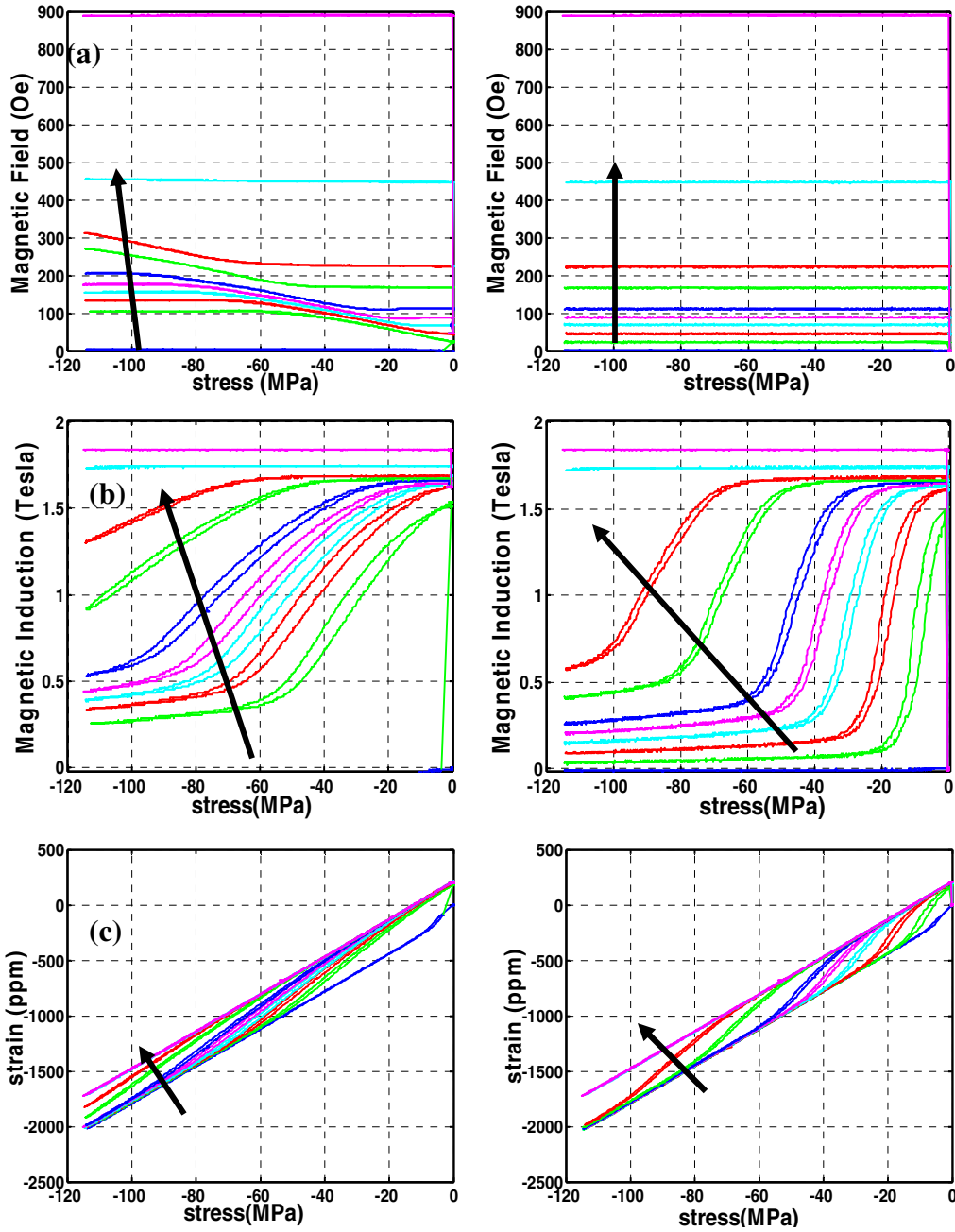


Figure 3.12 (a) Magnetic field vs. stress.

(b) Magnetic induction vs. stress.

(c) Strain vs. stress.

**NOTE:** In each of these figures the characteristics correspond to  $H= 0, 22.3, 44.6, 66.9, 89.1, 111, 167, 223, 446, 891$  Oe. In figures on left, they refer to initial field values only in figures on right they correspond to constant field values.

Chapter 5. For similar reasons the strain-stress curves at constant field show more distinct stress ranges where change in compliance occur (Figure 3.12 (c)) than their counterparts at constant drive current.

The constant field characteristics directly reflect the material properties without the need to factor out the transducer effects, as they nearly eliminate the effect of magnetic interaction between the circuit and sample and are therefore fairly independent of the transducer used to test the sample. Hence, in the rest of the thesis, only constant magnetic field characterization curves are reported.

### 3.3.3 Effect of Crystallographic Direction on Sensing Characteristics

The  $B$ - $\sigma$  and  $\varepsilon$ - $\sigma$  characteristics of  $\langle 100 \rangle$  oriented 19 at. % Ga and  $\langle 110 \rangle$  oriented 18 at. % Ga single crystal FeGa samples, both of which were annealed at  $1000^{\circ}\text{C}$  for 168 hours and furnace cooled at a rate of  $10^{\circ}\text{C}/\text{minute}$  are presented. Throughout this subsection,  $\langle 100 \rangle$  sample is used to refer to the 19 at. % Ga  $\langle 100 \rangle$  oriented FeGa sample while  $\langle 110 \rangle$  sample is used to refer to the 18 at. % Ga  $\langle 110 \rangle$  oriented FeGa sample. An attempt is made to study the qualitative differences in sensing behavior along the two crystallographic directions, while some of the quantitative difference in behavior between the two samples may have been caused due to the difference in Ga content.

The  $B$ - $\sigma$  characteristics for both bias fields and compressive stress applied in the  $\langle 100 \rangle$  and  $\langle 110 \rangle$  axis are shown in Figure 3.13 (top) and Figure 3.13 (bottom) respectively. The sensitivity (variation in  $B$  with  $\sigma$ ) is much sharper in the  $\langle 100 \rangle$  sample than the in the  $\langle 110 \rangle$  sample. This can be explained by the principle of balance between the magnetic and magnetoelastic energy. For a given bias field the magnetic energy ( $\mathbf{H} \cdot \mathbf{M}$ ), which favors an alignment of domains along the sample is slightly smaller in the  $\langle 110 \rangle$  sample than the  $\langle 100 \rangle$  sample as larger fields are required to obtain  $M_{\text{sat}}$ . However, the magnetoelastic energy, which favors a domain alignment perpendicular to the axis of application of compressive stress, is much smaller in the  $\langle 110 \rangle$  sample than in the  $\langle 100 \rangle$  sample, for a given value of stress.

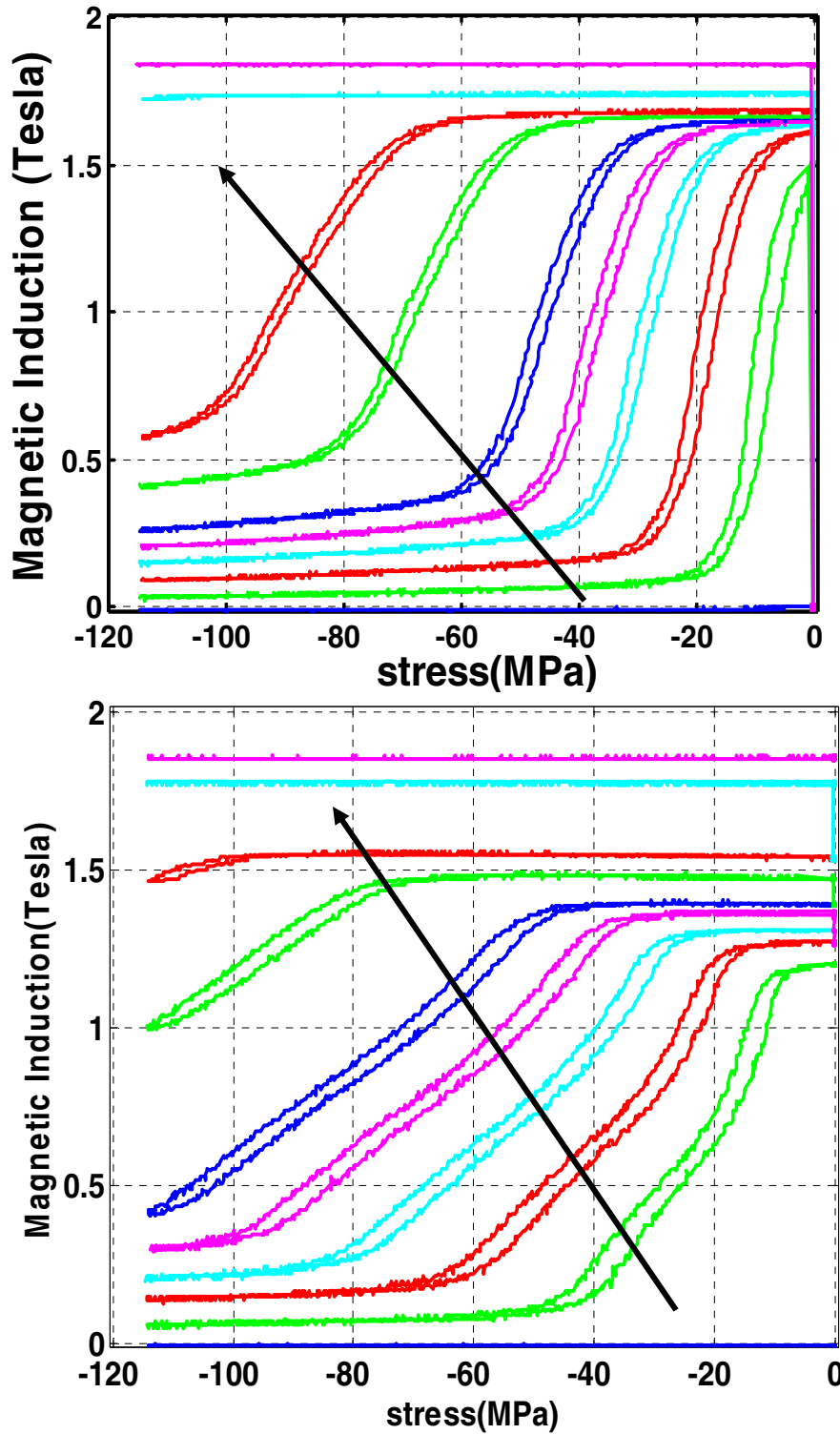


**Figure 3.13** B -  $\sigma$  characteristics of <100> oriented 19 at. % Ga (top) and <110> oriented 18 at. % Ga (below) of furnace cooled, single crystal FeGa.

H= 0, 22.3, 44.6, 66.9, 89.1, 111, 167, 223, 446, 891 Oe.

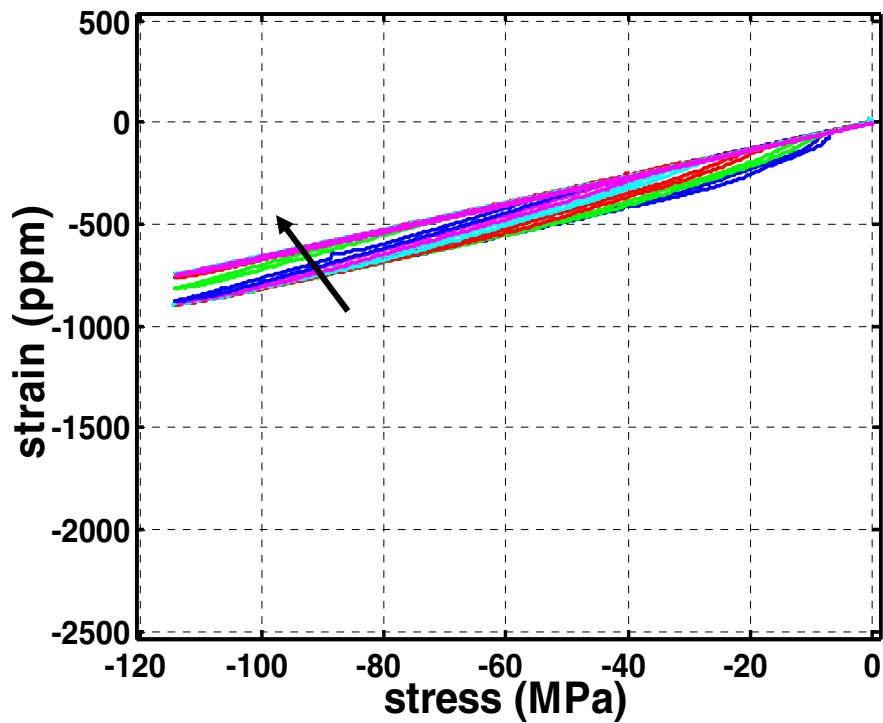
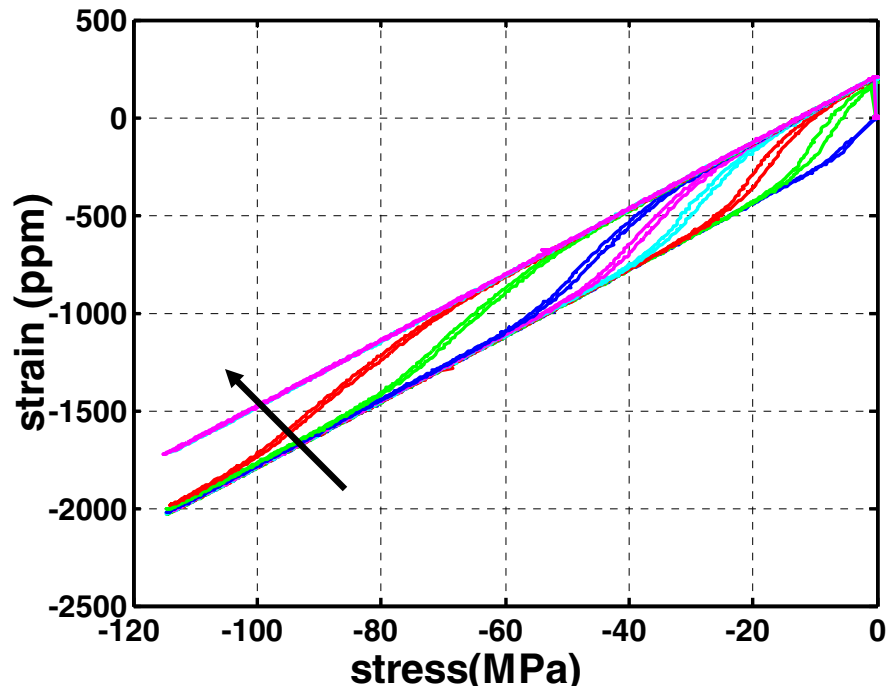


**Figure 3.14**  $\epsilon - \sigma$  characteristics of  $\langle 100 \rangle$  oriented 19 at. % Ga (top) and  $\langle 110 \rangle$  oriented 18 at. % Ga (below) of furnace cooled, single crystal FeGa.

H= 0, 22.3, 44.6, 66.9, 89.1, 111, 167, 223, 446, 891 Oe.

This is because magnetoelastic energy is proportional to  $\lambda^*\sigma$  and  $\lambda_{110}$  is less than half  $\lambda_{100}$ , as explained in Section 3.2.3. Thus a larger stress is needed in the  $\langle 110 \rangle$  sample to completely rotate the stress perpendicular to the sample axis, and therefore the sensitivity (variation in B with  $\sigma$ ) is much smaller in the  $\langle 110 \rangle$  sample.

The  $\epsilon$ - $\sigma$  characteristics show that the variation in compliance is well-demarcated for different bias fields in the 19 at. % Ga  $\langle 100 \rangle$  sample but less so in the 18 at. % Ga  $\langle 110 \rangle$  sample (Figure 3.14). This is expected as the  $\lambda_{\text{sat}}$  in the  $\langle 100 \rangle$  sample is twice that in the  $\langle 110 \rangle$  sample. Furthermore, stress has more significant effect on the magnetoelastic energy in the  $\langle 100 \rangle$  sample than in the  $\langle 110 \rangle$  sample. This leads to a smaller variation of Young's modulus with stress in the  $\langle 110 \rangle$  sample than in the  $\langle 100 \rangle$  sample.

### **3.4 Summary of Actuation and Sensing Behavior of Single Crystals**

Single crystal FeGa actuator behavior has been shown to be strongly dependent on the Ga content. Specifically, lower Ga content samples (for example 19 at. % Ga) sample exhibits a kinking behavior in B-H curves, i.e. two distinct regimes of low and high permeability, which increases on application of a larger compressive stress. In comparison, higher Ga content samples (24.7 at. % Ga and 29 at. % Ga samples) show rounded B-H curves with no kinking behavior, possibly due to a smoothing effect due to a presence of a large number of inhomogeneities/multiple phases. The  $\lambda_{\text{sat}}$  of the 19 at. % Ga sample does not decrease with increase in compressive stress, up to 80 MPa. However, in 24.7 and 29 at. % Ga samples the  $\lambda_{\text{sat}}$  reaches a peak at about 30 MPa and decreases significantly at higher stress such as 60 MPa and 80 MPa. This is an unexpected phenomenon and merits further research of the effect of stress on the crystallographic structure of these materials.

The actuator properties in  $\langle 110 \rangle$  direction have been shown to be considerably different from those in the  $\langle 100 \rangle$  direction. Larger fields are required to drive the sample to saturation in the  $\langle 110 \rangle$  at low stress due to high magnetocrystalline anisotropy in this direction. However, the effect of stress, whose

contribution to the magnetostatic energy is  $-\lambda \cdot \sigma$ , is lower in the  $\langle 110 \rangle$  direction as  $\lambda_{\text{Max}}$  is half that in the  $\langle 100 \rangle$  direction. Consequently, at higher stress, lower fields are required to drive the  $\langle 110 \rangle$  sample to saturation. This results in lower sensitivity in the sensing behavior of the  $\langle 110 \rangle$  sample i.e. variation in B with  $\sigma$  is much smaller in the  $\langle 110 \rangle$  direction. Furthermore, the E effect, or variation in modulus of the sample is much smaller in the  $\langle 110 \rangle$  direction for reasons explained in Section 3.3.3.

The possibility that a magnetostriction of  $\sim 150$  ppm can be obtained in the  $\langle 110 \rangle$  direction, if the appropriate bias compressive stress is applied has some important implications for microactuators produced by depositing FeGa thin films on Silicon substrates, which typically orient along the  $\langle 110 \rangle$  direction [Weston2002].

Finally, it has been show that a feedback-loop implemented with a PID controller varied the drive current and kept the magnetic field through the sample constant. This new testing paradigm ensured that the measured sample magnetomechanical behaviors were independent of the magnetic interaction between the sample and magnetic circuit. The constant magnetic field characteristics demonstrate about 4-5 times higher sensitivity than those at constant drive current.

## Chapter 4: Energy-based Model for Single-Crystal Quasi-static Actuation Behavior

This chapter discusses the development of the Armstrong model [Armstrong 2003 a, b] and the validation of this energy-based constitutive model for simulating the performance of magnetostrictive FeGa actuators and sensors along any of the crystallographic orientations. However, some small changes from the original Armstrong model are proposed in the formulation. Furthermore, an attempt is made to derive a more generalized model to incorporate the effect of temperature on the magnetostrictive behavior, while adhering to rigorous thermodynamic principles to the extent possible.

First, the engineering objectives of the model are discussed to guide the choice of a model. Various models developed in the past, both phenomenological and thermodynamic, are discussed and compared. The current model is then formulated as an extension of the Armstrong model that was reported in literature, to incorporate temperature effects.

The thermal predictions of this model are employed to predict the difference in actuator characteristics ( $\lambda$ -H and B-H curves) near the Curie point for a typical FeGa sample.

Next, it is shown that this generalized model reduces to the Armstrong model at constant temperature and it is attempted to use the Armstrong model to explain the behavior of single crystal FeGa alloys at various Ga content. More specifically, it is demonstrated that an appropriate combination of the following two factors: magnetocrystalline anisotropy and the Armstrong smoothing-factor  $\Omega$  (due to the presence of imperfections) may explain the varied behavior of single-crystal FeGa alloys with different Ga content.

Finally, the model is validated against experimental data of a  $\langle 110 \rangle$  oriented 18 at. % Ga, single-crystal FeGa alloy to demonstrate that it is capable of simulating actuator behavior along different crystallographic directions. Inability to procure samples oriented in other crystallographic directions (such as the  $\langle 111 \rangle$  direction), limited the validation to  $\langle 100 \rangle$  direction and the  $\langle 110 \rangle$  direction. However, model simulation is employed to predict possible magnetoelastic behavior in the  $\langle 111 \rangle$  direction.

#### **4.1 Modeling Objectives, Literature Survey and Background**

This section presents a survey of existing models, briefly describes some basic principles of statistical mechanics and provides a detailed description of the formulation of this model.

##### **4.1.1 Modeling Objectives**

The primary objective of this effort was to find a model that could simulate the behavior of magnetostrictive materials, such as FeGa alloys, along various crystallographic directions, with the smallest number of model parameters. An additional advantage would occur if the model formulation enables a prediction of sensing behavior from parameters fit to actuation data.

Furthermore, a model that could, in principle, simulate the effect of temperature, and is derived from basic principles was sought as this would prove beneficial in providing an overall structured approach to modeling magnetostrictive materials at different levels, viz. lattice, domain and macroscopic.

##### **4.1.2 Literature Survey**

One of the earliest tools used to model ferromagnetic hysteresis was the Preisach model. In its rudimentary form it employs a hysteresis operator, which takes the value  $\pm 1$  depending on the current state and history based on the previous state. More recently, it has been demonstrated that the Preisach model may be modified to account for the effect of stress [Bergqvist1991, Suzuki2004] and thus model the

magnetoelastic behavior of magnetostrictive materials. However, these models are purely mathematical tools and do not address the underlying physics of the problem.

The Jiles-Atherton model [Jiles1983, 1984] models magnetostrictive behavior as comprising of domain rotation and domain wall pinning. A modified Langevin equation is employed to model the bulk anhysteretic magnetization (magnetization-field curve without hysteresis). The motion of domain walls is modeled as impeded by the presence of pinning sites leading to hysteresis. The estimation of the model parameters from experimental data is explained in a later paper [Jiles1989]. The effect of stress on the magnetization vs. field curves is incorporated by introducing the concept of a stress equivalent field term  $H_\sigma$ , which alters the effective field  $H_{\text{eff}}$  in the Langevin term [Jiles 1995a, 1995b] thereby producing an effect of stress on the anhysteretic curves. Finally, [Li2003, Jiles2004] have shown that an extension of the original Jiles-Atherton model to incorporate the effect of stress can in principle simulate sensing behavior, i.e. variation of magnetization with stress. However, some of the shortcomings of the Jiles-Atherton model and its extension are that it does not have an explicit way of handling magnetocrystalline anisotropy. Hence, it is in general a one-dimensional model. Furthermore, it models magnetostriction using an empirical relation  $\lambda \propto M^2$  or  $\lambda \propto a_1 M^2 + a_2 M^4$ , which does not model magnetostriction under zero and low stress well, and does not, in general, hold true in all crystallographic directions.

A class of Free-Energy models has been proposed by Smith *et al.* [Smith 2003, Smith 2006] by construction of a two-well Helmholtz potential,  $\psi(M)$ , as a function of  $M$  for the uni-axial case. For a given applied field the Gibbs energy is taken to be  $G(M) = \psi(M) - HM$ . The effect of material homogeneities and non-constant effective field is incorporated through construction of a stochastic distribution to evaluate  $M$ . Stress effects may be incorporated into this model by introducing the appropriate term in the Gibbs energy. However, the drawback of this model is that like the Jiles-Atherton model this model is essentially one-dimensional, does not explicitly handle magnetic anisotropy, and uses an empirical relationship to calculate  $\lambda$  from  $M$ .

A similar approach was used by [Falk1982] wherein the Landau's phenomenological theory for second-order systems (systems where the phase transition occurs at a unique temperature that is not dependent on stress) involving the construction of a 1-D free-energy function with respect to an order parameter was used to demonstrate the hysteresis between magnetization and field in ferromagnetic systems. This model is one-dimensional and is better suited to explain the physics of hysteresis in B-H curves than for realistic simulations.

The Armstrong model was constructed to include the magnetocrystalline, magnetoelastic and magnetic field energy terms. For a given value of applied stress and magnetic field in any direction, the total energy (sum of the three above-mentioned energy terms) corresponding to the magnetization vector being oriented along different directions is evaluated [Armstrong 1997, 2000, 2002, 2003a, 2003b]. The probability that the magnetization takes a particular orientation depends on the total energy corresponding to that orientation; the lower this energy greater the probability that this state is occupied. By performing a probability weighted summation over all the states, the average macroscopic property of this material was evaluated. The Armstrong model modified for tetragonal symmetries has been used to simulate the actuation behavior of highly textured stressed-annealed FeGa alloys successfully. [Restorff2005].

So far, the Armstrong approach has been the most successful model for achieving the simulations objectives described in Section 4.1.1. Therefore the model described in this chapter builds on the Armstrong approach, attempting to include the temperature effect and possibly capture the paramagnetic-ferromagnetic phase transition.

#### **4.1.3 Background: Energy Terms and Thermodynamic Concepts**

This section discusses the various energy-terms, viz. the exchange coupling, magnetocrystalline, magnetoelastic and magnetic (magnetostatic) energy terms that determine the behavior of magnetostrictive materials, a detailed discussion of which

is presented in Chapter 1. Some concepts of statistical mechanics that are important in modeling the bulk behavior of magnetostrictive materials are also discussed here.

*Energetics of magnetostrictive materials:*

The following energy terms lead to the formation of domains, preferential orientation of magnetization vectors along certain crystallographic directions and the magnetoelastic coupling. Stray field energy is not discussed here and may be accounted for by a demagnetization factor.

(a) Exchange energy

The exchange energy between two neighboring spins  $s_i$  and  $s_j$  [Parthia1972] can be expressed as:

$$\mathcal{E}_{exchange} = const - 2J_{ij}(s_i \cdot s_j) \quad 4.1$$

(a)

If  $J_{ij} > 0$ , parallel alignment of neighboring spins is energetically favorable and may lead to ferromagnetism. On the other hand,  $J_{ij} < 0$  leads to the possibility of anti-ferromagnetism. The spin-spin interaction falls rapidly with distance and hence this interaction can be neglected for all but nearest-neighbors in a lattice. Therefore the exchange energy in the entire lattice may be expressed as:

$$E_{exchange} = const - 2J \sum_{nearest-neighbors} (s_i \cdot s_j) \quad 4.1 (b)$$

As we consider only the nearest neighbors, the interaction between any two spins is identical and  $J_{ij} = \text{constant} = J$  can be factored out of the summation.

(b) Magnetocrystalline anisotropy energy

The magnetocrystalline anisotropy energy for a cubic system [Chikazumi1964] can be expressed in terms of two constants  $K_1$  and  $K_2$  and the direction cosines for orientation of the magnetic moment ( $\alpha_1, \alpha_2, \alpha_3$ )

$$E_{magnetocrystalline} = K_1 * (\alpha_1^2 \alpha_2^2 + \alpha_1^2 \alpha_3^2 + \alpha_2^2 \alpha_3^2) + K_2 * \alpha_1^2 \alpha_2^2 \alpha_3^2 \quad (4.2)$$

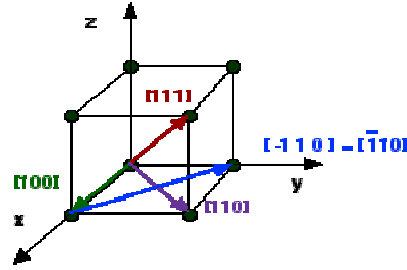


**Figure 4.1.** Crystallographic directions in a cubic system.

(c) Magnetoelastic energy

The magnetoelastic energy (coupling between mechanical and magnetic terms) of a cubic system [Chikazumi1964] can be expressed in terms of magnetostriction constants in the <100> and <111> directions ( $\lambda_{100}$  and  $\lambda_{111}$ ) and applied stress of magnitude ( $\sigma$ ) and direction cosines ( $\beta_{1s}$ ,  $\beta_{2s}$ ,  $\beta_{3s}$ ), as well as the magnetic moment direction cosines ( $\alpha_1$ ,  $\alpha_2$ ,  $\alpha_3$ ).

$$E_{magnetoelastic} = -\frac{3}{2} \lambda_{100} * \sigma * (\alpha_1^2 \beta_{1s}^2 + \alpha_2^2 \beta_{2s}^2 + \alpha_3^2 \beta_{3s}^2) - 3 \lambda_{111} * \sigma * (\alpha_1 \alpha_2 \beta_{1s} \beta_{2s} + \alpha_2 \alpha_3 \beta_{2s} \beta_{3s} + \alpha_3 \alpha_1 \beta_{3s} \beta_{1s}) \quad (4.3)$$

(d) Magnetic energy

The magnetic energy depends on the magnetic field (H), the saturation magnetization ( $M_s$ ) and the cosine of the angle between them (dot product of the direction cosines of the applied field and the magnetic moment)

$$E_{magnetic} = -\mu_0 * M_s * H * (\alpha_1 \beta_{1F} + \alpha_2 \beta_{2F} + \alpha_3 \beta_{3F}) \quad (4.4)$$

where ( $\beta_{1F}$ ,  $\beta_{2F}$ ,  $\beta_{3F}$ ) are direction cosines of the applied field.

*Some principles of statistical mechanics*

The expression for the expected value of measurable quantities in a canonical ensemble and a brief overview of methods of modeling the statistics of interacting

particles is described in this section. A detailed description of ensemble theory, statistics of interacting particles and phase transitions may be found in [Parthia1972].  
Statistics of a canonical ensemble of non-interacting particles

Consider a system A of fixed volume placed in a reservoir A' of very large heat capacity as shown in Figure 4.2. Transfer of energy takes place between the system and the reservoir but there is no flow of mass (or particles) between them. At equilibrium the system and the surrounding attain a fixed temperature T, though the energy of the system can vary between 0 and  $E_{\text{total}}$  (the energy of the composite system and reservoir). The probability ( $P_i$ ) that the system [Pathria1972] is in a state of energy  $E_i$  is proportional to  $e^{-E_i/kT}$

$$P_i = \frac{e^{-E_i/kT}}{\sum_i e^{-E_i/kT}} \quad (4.5)$$

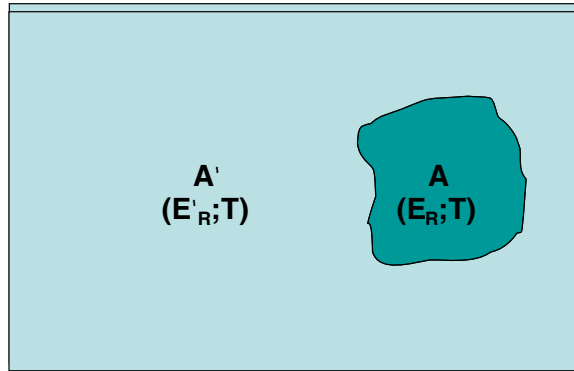


**Figure 4.2** System A placed in a reservoir of large heat capacity, in thermal equilibrium at common temperature T.

Consider a system that has  $g_i$  degenerate states, all of which have the same energy  $E_i$ , the probability ( $P_i$ ) of the system being in an energy state  $E_i$  is:

$$P_i = \frac{g_i e^{-E_i/kT}}{\sum_i g_i e^{-E_i/kT}} \quad (4.6)$$

The expected value of some property  $Q$  of the system is given by the ensemble average:

$$\langle Q \rangle = \frac{\sum_i Q_i g_i e^{-E_i/kT}}{\sum_i g_i e^{-E_i/kT}} \quad (4.7)$$

A brief note on statistics of interacting particles: phase transitions

In certain systems, the interaction between their constituents in a strong and cooperative manner leads to unique properties known as critical phenomena [Pathria1972] or phase transition. Systems with inter-particle interactions present a challenge to modeling as there is no simple way of expressing the energy levels of the total system in terms of energy levels of their individual components. For example,  $H$  for the state illustrated by the 2-D array shown in Figure 4.3, the energy of the system purely due to spin-spin interaction and the applied magnetic field would be written as:

$$E_{state-up} = -J_{i,j} \sum_{i=1:mn} \sum_{j=1:mn} (s_i \cdot s_j) - \mu H \cdot \sum_{i=1:mn} (s_i) \quad (4.8)$$

This being the energy of the system for one particular configuration (or state), the expression for the partition function which would involve a sum over all possible configurations of the system would lead to a rather complex summation!

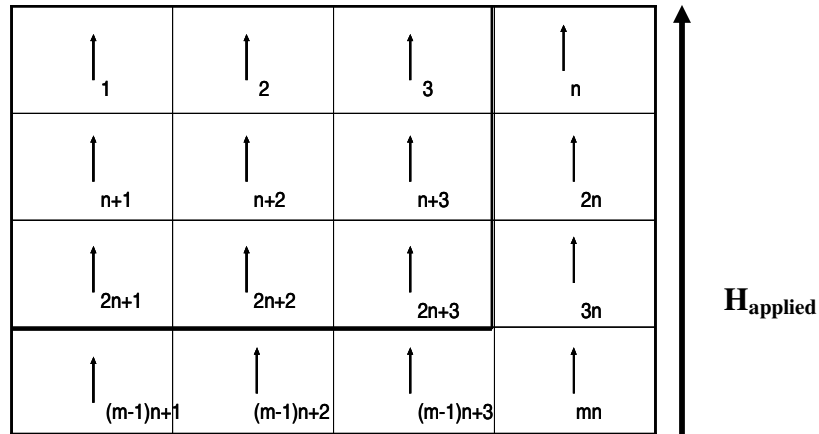


**Figure 4.3** Spins in various lattices in a 2-D array of  $m \times n$  cells.

This is one of the  $2^{mn}$  possible microstates (configurations) of the system.

A simplified way of modeling ferromagnetic systems (without inclusion of magnetocrystalline anisotropy and magnetoelastic interaction) and by limiting the interaction between spins to nearest neighbors and spin states “up” or “down” was attempted by Ising. Even this model can be solved analytically under an applied magnetic field only for a 1-D chain of spins [**Ising1925**] which yielded an analytical expression for the partition function and consequently for the free-energy, magnetization, etc. However, a short-coming of this model is that it neither displays spontaneous magnetization or discontinuity in specific-heat at any finite temperature. An analytical solution for the partition function in 2-D is possible only for the zero-field case [**Onsagar1944**] but demonstrates both spontaneous magnetization (below  $T_C$ ) and a discontinuity in specific heat at  $T_C$ , illustrating that a minimum dimensionality of two (2-D) is required to capture the essential physics of the phase-transition. For 3-D and more involved formulations numerical simulations need to be resorted to. However, such formulations are so computationally intensive that they necessitate the use of a supercomputing facility [**Zhu1988**].

In this thesis, the zero-order approximation is employed, which assumes that each spin (magnetization) in a lattice interacts with the mean-field due to all other lattices under consideration. The mean-field can be obtained from the ensemble average. Hence, there is no dimensionality involved in the formulation, greatly reducing the computational effort albeit at an expense in losing some of the physical details.

#### **4.2 Model Formulation**

An attempt is made to model the macroscopic response of the magnetostrictive sample to magnetic field, stress and temperature in terms of the distribution of the orientation of the magnetization vector (spin) in individual lattices. However, the use of a micro-magnetic numerical simulation to predict the macroscopic response is a computationally formidable task. Therefore, the modeling is performed independently at two different levels, as illustrated in Figure 4.4.

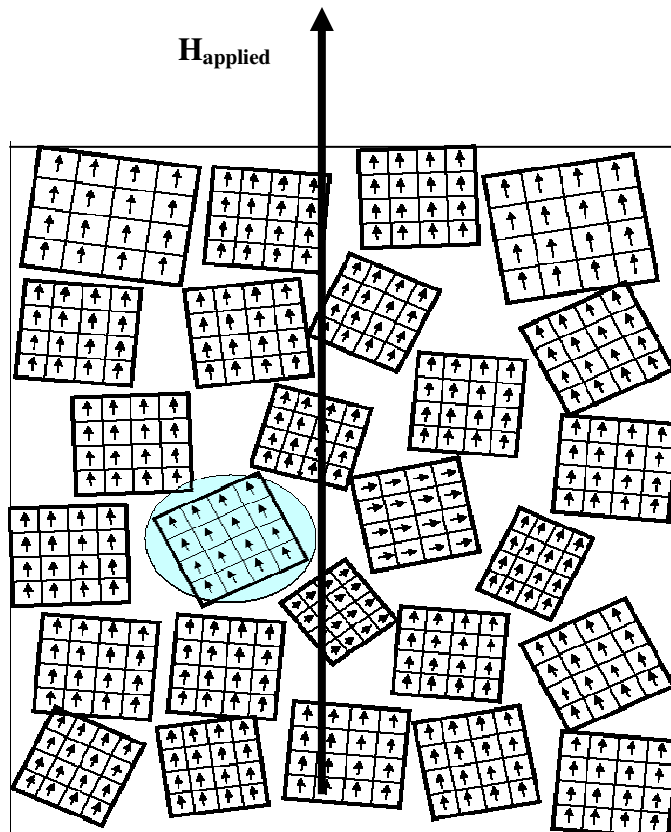


**Figure 4.4** Schematic illustration of domains in a bulk material (number of lattices making a domain, domain size, domain boundaries, etc. not properly depicted).

The Armstrong model, described in Section 4.2.1, may be interpreted as modeling the macroscopic response from the distributed orientation of various domains that constitute single-crystal samples in the presence of combinations of applied field and stress. The variation of  $M_{\text{sat}}$  due to ordering of spins within a domain is strongly affected by temperature and is described separately in Section 4.2.2.

#### **4.2.1 Armstrong Model for Cooperative Movement of Moments:**

##### **Domain Movement**

The magnetization vectors within each domain move cooperatively with no expense in exchange energy. An expense in exchange energy is encountered only at the domain boundaries, which is a small fraction of the total volume. Consequently,

the total exchange energy at the boundaries is small compared to the sum total of all the other energy terms considered over the entire system. Therefore, to predict the macroscopic behavior of the sample, without worrying about the precise description of the domain structure, the Armstrong model [Armstrong 2002], which uses only the magnetocrystalline, magnetoelastic and magnetic energies is employed. The formulation of this model is described in detail in this section.

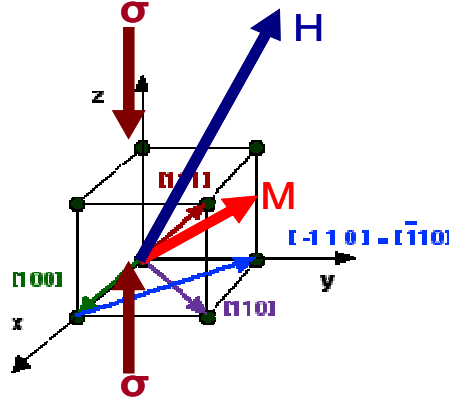


**Figure 4.5** Free-body diagram showing stress ( $\sigma$ ), magnetic field ( $H$ ) and orientation of magnetization ( $M$ ) in a single crystal sample.

Consider a magnetic field ( $H$ ) and stress ( $\sigma$ ) applied to a single crystal sample (Figure 4.5) so that the direction cosines they form with the crystallographic directions are respectively  $(\beta_{1F}, \beta_{2F}, \beta_{3F})$  and  $(\beta_{1s}, \beta_{2s}, \beta_{3s})$ . The energy corresponding to the magnetization orienting in a direction  $(\alpha_1, \alpha_2, \alpha_3)$  is given by:

$$\begin{aligned}
 E(\sigma, H) &= E_{\text{magnetocrystalline}} + \gamma_{\sigma} * E_{\text{magnetoelastic}} + E_{\text{magnetic}} \\
 &= K_1 * (\alpha_1^2 \alpha_2^2 + \alpha_1^2 \alpha_3^2 + \alpha_2^2 \alpha_3^2) + K_2 * \alpha_1^2 \alpha_2^2 \alpha_3^2 \\
 &\quad \gamma_{\sigma} \left\{ \begin{aligned} &-\frac{3}{2} \lambda_{100} * \sigma * (\alpha_1^2 \beta_{1s}^2 + \alpha_2^2 \beta_{2s}^2 + \alpha_3^2 \beta_{3s}^2) \\ &-3 \lambda_{111} * \sigma * (\alpha_1 \alpha_2 \beta_{1s} \beta_{2s} + \alpha_2 \alpha_3 \beta_{2s} \beta_{3s} + \alpha_3 \alpha_1 \beta_{3s} \beta_{1s}) \end{aligned} \right\} \\
 &\quad -\mu_0 * M_s * H * (\alpha_1 \beta_{1F} + \alpha_2 \beta_{2F} + \alpha_3 \beta_{3F})
 \end{aligned} \tag{4.9}$$

as explained in Section 4.1.3.

The probability that a magnetic domain takes a particular orientation depends on the energy corresponding to that orientation, with orientations corresponding to lower energy being preferred. The magnetostriction and magnetization are calculated as the expected value (ensemble average) due to the distribution of the orientations of these domains. The response of these domain orientations to varying field at constant stress determines actuation behavior of this material while the response to varying stress at constant field determines the sensing behavior.

### *Model implementation*

The following material constants are employed in the model: cubic magnetocrystalline anisotropy constants  $K_1$  and  $K_2$  (Joules/m<sup>3</sup>), cubic magnetostriction constants  $\lambda_{100}$  and  $\lambda_{111}$  (strain), and saturation magnetization  $M_s$  (Ampere/m). A 6<sup>th</sup> dimensionless factor  $\nu_\sigma$  had to be introduced in Equation 4.9 to slightly scale the magnetoelastic energy in order to fine-tune the variation in magnetic behavior with stress. The direction cosines  $(\beta_{1s}, \beta_{2s}, \beta_{3s})$  and  $(\beta_{1F}, \beta_{2F}, \beta_{3F})$  are respectively determined by the direction of the stress or field applied. For example, a stress and field applied along the [110] direction is represented by direction cosines  $(1/\sqrt{2}, 1/\sqrt{2}, 0)$ .

Thus, given a stress and field, the free-energy for various orientations of the magnetic moment  $(\alpha_1, \alpha_2, \alpha_3)$  are evaluated using Equation 4.9. Numerically the  $(\alpha_1, \alpha_2, \alpha_3)$  are chosen to correspond to  $\phi$  varying from 0 to 180° and  $\psi$  varying from 0 to 360° in spherical coordinates in intervals of 5°. Figure 4.6 (a) shows such a distribution of energy at 0 applied stress and 0 field while Figure 4.6 (b) illustrates the effect of compressive stress and field, both applied along the z-axis, on the energy distribution.

Assuming that the sample is comprised of a large number of domains, each of these domains is likely to have a particular orientation with a probability which depends on the energy corresponding to that orientation. It is reasonable to assume that the orientation of the domains follows a Boltzmann distribution under the

condition of non-interaction of domains (different from interaction of individual atomic moments which result in the domain formation) as well as independence of the present domain orientation on its previous state (this assumption results in an anhysteretic model).

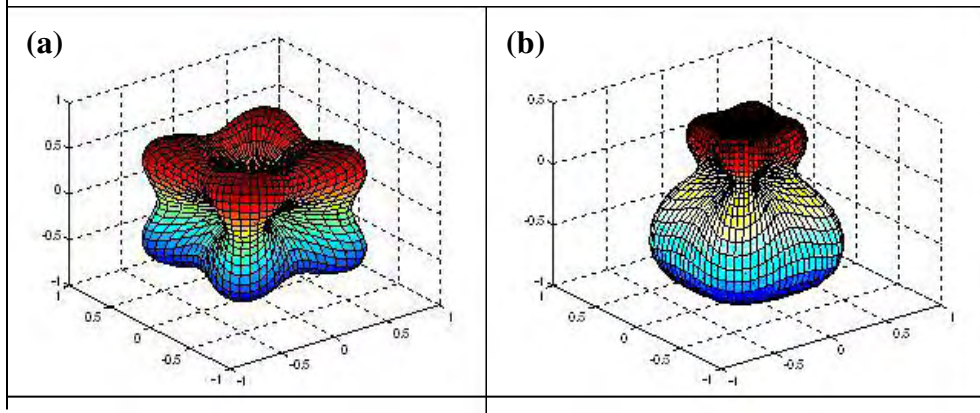


**Figure 4.6** Visualization of dependence of energy on orientation of magnetic moment generated by plotting radius proportional to the energy [normalized] in different directions. (Values for model parameters were chosen to emphasize certain effects rather than for a particular alloy.)

Energy plot at (a) 0 stress and magnetic field (b) Compressive stress and typical field at which domains flip.

The average value of a physical quantity (for example  $M_x$ ) is given by

$$M_x = \frac{\int_{\theta, \phi} (M_s \sin \theta \cos \phi) (d\theta d\phi |\sin \theta|) e^{-\frac{E(\theta, \phi)}{\Omega}}}{\int_{\theta, \phi} (d\theta d\phi |\sin \theta|) e^{-\frac{E(\theta, \phi)}{\Omega}}} \quad (4.10)$$

The 7<sup>th</sup> model parameter, a constant  $\Omega$  [Armstrong1996] is employed in Equation 4.10 to achieve the desired smoothness of the B-H and  $\lambda$ -H curves.

[NOTE:  $\Omega$  has the units  $J/m^3$  as do the  $E_{\text{magnetocrystalline}}$ ,  $E_{\text{magnetoelastic}}$  and  $E_{\text{magnetic}}$ . Physically, a low  $\Omega$  produces less smooth distributions and results in steeper gradients and sharper corners in B-H and  $\lambda$ -H curves, suggesting fewer imperfections in the crystalline structure. Conversely a large  $\Omega$  leads to smooth characteristics suggestive of greater imperfections in the material].

$M_y$  and  $M_z$  can be similarly evaluated.  $M_x$ ,  $M_y$  and  $M_z$  correspond to the macroscopic (average) magnetization along [100], [010] and [001] directions respectively. The magnetization along any other direction with direction cosines ( $\beta_{1R}$ ,  $\beta_{2R}$ ,  $\beta_{3R}$ ) can be expressed as:

$$\mathbf{M} = M_x \beta_{1R} + M_y \beta_{2R} + M_z \beta_{3R} \quad (4.11)$$

The change in length along any direction ( $\beta_{1R}$ ,  $\beta_{2R}$ ,  $\beta_{3R}$ ) due to the orientation of the magnetization vector in ( $\alpha_1$ ,  $\alpha_2$ ,  $\alpha_3$ ) is given by

$$\begin{aligned} \frac{3}{2} \lambda = \frac{\partial l}{l} = & \frac{3}{2} \lambda_{100} (\alpha_1^2 \beta_{1R}^2 + \alpha_2^2 \beta_{2R}^2 + \alpha_3^2 \beta_{3R}^2 - \frac{1}{3}) \\ & + 3 \lambda_{111} (\alpha_1 \alpha_2 \beta_{1R} \beta_{2R} + \alpha_2 \alpha_3 \beta_{2R} \beta_{3R} + \alpha_3 \alpha_1 \beta_{3R} \beta_{1R}) \end{aligned} \quad (4.12)$$

The magnetostriction is evaluated using Equation 4.13

$$\frac{3}{2} \lambda = \frac{\sum_{\theta, \phi} \left\{ \begin{aligned} & \frac{3}{2} \lambda_{100} (\alpha_1^2 \beta_{1R}^2 + \alpha_2^2 \beta_{2R}^2 + \alpha_3^2 \beta_{3R}^2 - \frac{1}{3}) \\ & + 3 \lambda_{111} (\alpha_1 \alpha_2 \beta_{1R} \beta_{2R} + \alpha_2 \alpha_3 \beta_{2R} \beta_{3R} + \alpha_3 \alpha_1 \beta_{3R} \beta_{1R}) \end{aligned} \right\} (d\theta d\phi |\sin \theta|) e^{\frac{-E(\theta, \phi)}{\Omega}}}{\sum_{\theta, \phi} (d\theta d\phi |\sin \theta|) e^{\frac{-E(\theta, \phi)}{\Omega}}} \quad (4.13)$$

## 4.2.2 Temperature Effects on Alignment of Moments within a Domain

The modeling of the ordering of magnetization vectors (spins) within each domain was performed by accounting for the exchange-energy due to the interaction between spins in lattices, together with the magnetocrystalline, magnetoelastic and magnetic energies as described in this section. The ordering is strongly affected by the temperature and determines the spontaneous magnetization in a domain. This spontaneous magnetization serves as an input for the simulation in Section 4.1.1, thus introducing the dependence of the magnetomechanical response on the thermal state.

Within the domain, the exchange coupling favors the ordered orientation of individual spins (magnetization vectors in a lattice), while temperature contributes to the disorder as illustrated in Figure 4.7(a). The application of a strong magnetic field can lead to an increased ordering and larger magnetization (forced magnetization) within a domain at the same temperature Figure 4.7(b).

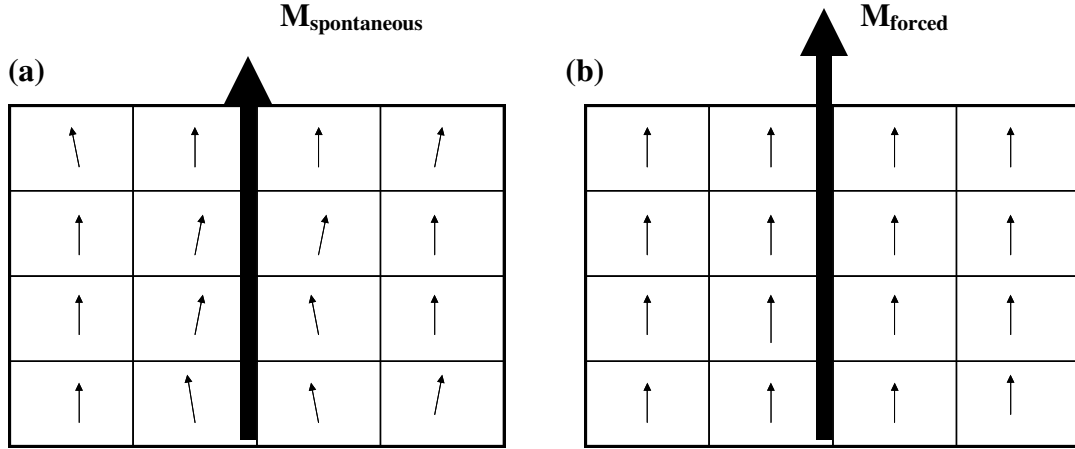


**Figure 4.7** Schematic of magnetization within a domain at room temperature.

(a) Spontaneous magnetization.

(b) Forced magnetization (high applied field).

The magnetization is estimated by modeling the domain (“unit”) as a canonical ensemble of interacting spins (magnetization vectors). The exchange energy is calculated using a zero-order approximation, to avoid the dimensionality of the problem, and the magnetization in each lattice interacts with the magnetization calculated from the ensemble average. Thus the exchange energy term looks like

$$E_{\text{exchange}} = -J (m_i \cdot \overline{M}) \quad (4.14a)$$

that is different from a typical magnetostatic energy term  $\mu_0 M^2$ .

**NOTE:**  $m_i = \mu_0 M_{\text{sat}} (\alpha_1 \hat{i} + \alpha_2 \hat{j} + \alpha_3 \hat{k})$  (4.14b)

so that the unit of  $E_{\text{exchange}}$  is Joules/ $m^3$  as with other energy terms, with a non-dimensional  $J$ .

*Model formulation:*

For a given value of stress and applied field, the energy corresponding to the magnetization in a lattice along any direction ( $\alpha_1, \alpha_2, \alpha_3$ ) is evaluated as:

$$E(\sigma, H) = E_{\text{magnetocrystalline}} + \gamma_{\sigma} E_{\text{magnetoelastic}} + E_{\text{magnetic}} + E_{\text{exchange}} \quad (4.15)$$

The expected  $M$  (calculated by the ensemble average of this system),  $\overline{M}$  is evaluated using spherical coordinates as:

$$M_x = \frac{\sum_{\theta, \phi} \{ (M_s \sin \theta \cos \phi) (d\theta d\phi \sin \theta) e^{\frac{-E(\theta, \phi)}{kT/a^3}} \}}{\sum_{\theta, \phi} \{ (d\theta d\phi \sin \theta) e^{\frac{-E(\theta, \phi)}{kT/a^3}} \}} \quad (4.16)$$

$$M = M_x \beta_{1R} + M_y \beta_{2R} + M_z \beta_{3R} \quad (4.17)$$

For the first iteration  $\overline{M} = 0$ , hence  $E_{\text{exchange}} = 0$ . Once,  $\overline{M}$  is evaluated from the first iteration it is employed in calculating  $E_{\text{exchange}}$  in the second iteration corresponding to various orientations of magnetization ( $\alpha_1, \alpha_2, \alpha_3$ ) in the lattice. This is repeated until the value of  $\overline{M}$  converges to a value with less than 1% variation between consecutive iterations. Since, ordering of spins within domains should also have an effect on the magnetostriction, the empirical relationship used is:

$$\lambda = \left( \frac{\overline{M}}{M_{\text{sat}}} \right)^2 \lambda_{\text{sat}} \quad (4.18)$$

The  $\overline{M}$  obtained from Equations 4.16 and 4.17 and  $\lambda_{100}$  and  $\lambda_{111}$  scaled using (18) may be used in the model described in Section 4.2.1 to incorporate the effect of temperature on alignment within domains on the net macroscopic behavior. Thus, this model successfully includes all the energy terms, viz. magnetocrystalline, magnetoelastic, magnetic and *exchange* energies, where the exchange energy was evaluated using the mean field (or 0<sup>th</sup> order approximation).

Another important aspect of this model is that Equation (4.16) differs from (4.10) as it employs the  $\exp[-E/(kT/a^3)]$  factor to scale the relative contributions of each term, instead of the empirical  $\exp(-E/\Omega)$  employed by the Armstrong model.

This is because the system is rigorously modeled as a canonical ensemble. The energy terms in the numerator were multiplied by  $a^3$  to represent the energy in one unit cell of the lattice, rather than an energy density. This is consistent with  $\frac{1}{2}kT$  being the energy associated with one degree of freedom. [ $k$  is the Boltzmann constant,  $T$  is the temperature in Kelvin,  $a$  is the lattice constant. It must be noted that one unit cell may possess three or more degrees of freedom, however the use of  $a^3$  and  $kT$  gives a correct order of magnitude estimate]. The value of  $J$  in Equation 4.14 (a) is chosen so that  $E_{\text{exchange}} \approx kT_{\text{curie}}/a^3$ , i.e. in the vicinity of the Curie temperature the thermal energy is comparable to the exchange energy thus ensuring that the ordering of spins breaks down near this point. At typical stress and field levels used in characterizing the FeGa samples (Chapter 3),  $E_{\text{exchange}}$  turns out to be two orders of magnitude higher than  $E_{\text{magnetocrystalline}}$ ,  $E_{\text{magnetoelastic}}$  and  $E_{\text{magnetic}}$ . Thus, stress ( $\sim 100$  MPa) and field ( $\sim 1000$  Oe) have practically no effect on ordering of spins. A field of  $\sim 100,000$  Oe is required to make the  $E_{\text{magnetic}} \approx E_{\text{exchange}}$  and have any significant influence on ordering spins by competing with the  $kT/a^3$  term.

#### **4.3 Model Simulation of Thermal Effects**

The model described in the previous section is used to simulate the effect of high temperatures on the  $\lambda$ -H and B-H curves of a typical 18-19 at. % Ga, FeGa sample. Model parameters chosen were the same as those used in the simulation of 19 at. % Ga sample (Figure 4.10), which is discussed in the next section.

The simulation in Figure 4.8 and 4.9 respectively show the  $\lambda$ -H and B-H curves at 300 K, 600 K and 900 K for a sample whose Curie temperature is  $\sim 900$  K. At room temperature ( $\sim 300$  K) the value of  $J=255$  ensures that the exchange coupling ( $\sim 5.6 \cdot 10^8 \text{ Jm}^{-3}$ ) produces an alignment of moments, while the magnetocrystalline ( $\sim 10^4 \text{ J/m}^3$ ), magnetoelastic ( $\sim 10^4 \text{ J/m}^3$  at 30 MPa) and magnetic energies ( $3 \cdot 10^4 \text{ J/m}^3$  at 200 Oe) are insignificant compared to the thermal energy ( $kT/a^3 \approx 1.77 \cdot 10^8 \text{ J/m}^3$  at 300 K). However, these energy terms play an important role in the cooperative rotation of these domains (Equation 4.12).

At 600 K the exchange coupling is not able produce as good an alignment of spins relative as at 300 K resulting in slightly lower saturation magnetization and magnetostriction. At 900 K ( $kT/a^3 \approx 5.31 \times 10^8 \text{ J/m}^3$ ), the exchange coupling is insufficient to produce an alignment of spins and consequently paramagnetic behavior is observed. Hence, there is no spontaneous alignment of moments and B does not increase drastically with H.

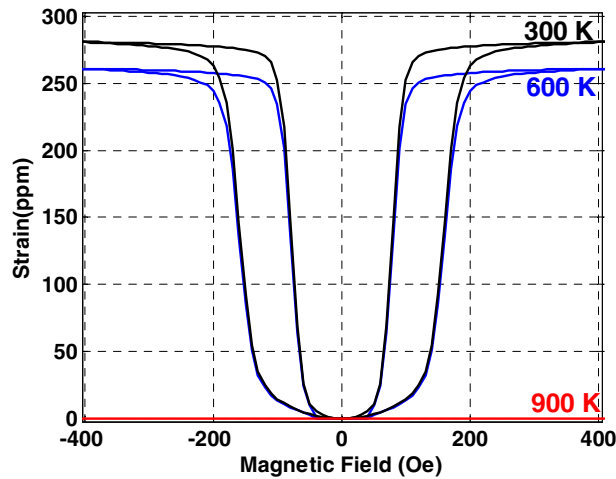


**Figure 4.8** Simulation of effect of high temperature on  $\lambda$ -H curves of typical  $\langle 100 \rangle$  single crystal 19 at. % Ga sample.

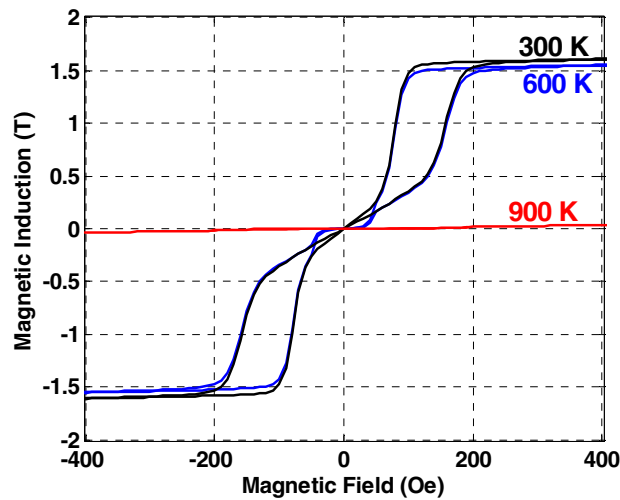


**Figure 4.9:** Simulation of effect of high temperature on B-H curves of typical  $\langle 100 \rangle$  single crystal 19 at. % Ga sample.

#### **4.4 Simulation of FeGa Single-Crystal Actuator Behavior with Varied Ga Content**

This section attempts to model the actuator behavior, i.e. the  $\lambda$ -H and B-H curves of 19, 24.7 and 29 at. % Ga single-crystals. The modeled behavior is compared with experimental characteristics presented in Chapter 3. The Armstrong-model at constant temperature discussed in Section 4.2.1 is employed for this simulation. In Subsection 4.4.4, an analysis of the sensitivity of the actuator characteristics to the variation of the magnetocrystalline anisotropy constants together with the Armstrong parameter  $\Omega$  is performed. It is demonstrated that the strikingly different nature of the actuator characteristics with increasing Ga content are reflected in the values assigned to these parameters.

##### **4.4.1 Magneto Mechanical Behavior of 19 at. % Ga Sample**

The following procedure was applied to estimate the model-parameters to simulate the behavior of 19 at. % Ga. This method was consistently employed for modeling all other samples.

###### *Procedure for estimation of parameters*

The magnetostriction (3/2)  $\lambda_{100}$  and saturation magnetization  $M_S$  were respectively estimated from the measured  $\lambda$ -H and B-H curves in Figure 4.10. The (3/2)  $\lambda_{111}$  is not critical to the [100] simulation and is chosen merely to be consistent with the trends reported in literature for variation of  $\lambda_{111}$  with Ga content, cited in [Kellogg2003b] based on the work of Clark *et al.*

$K_1$  and  $K_2$  are chosen to be consistent with values reported in previous work [Rafique2004] and to obtain a good-fit to the B-H curves at low stress. The  $\Omega$  and  $\gamma_\sigma$  were respectively chosen to achieve the desired smoothness and variation of  $\lambda$ -H and B-H characteristics with stress.  $K_1$  and  $K_2$  were iteratively modified within permissible limits (i.e. being consistent with literature) to achieve a better correlation with experimental data. However, the process of estimating parameters was *not* based on an algorithm, but was performed empirically.

Finally, a slightly higher value of  $(3/2)\lambda_{100}$  than observed in Figure 4.10 had to be chosen to account for the small loss in magnetostriction owing to the randomization of orientation caused by  $\Omega$ . This was followed by fine-tuning  $\gamma_\sigma$  to obtain better correlation between simulation and experiment at high stress. All the parameter variations were performed manually; no parameter identification algorithm was employed. The final parameters used for the simulation were:

$$\begin{aligned} K_1 &= 1.75 \cdot 10^4 \text{ Jm}^{-3}, K_2 = 0 \cdot 10^4 \text{ Jm}^{-3}, \\ (3/2)\lambda_{100} &= 318 \cdot 10^{-6}, (3/2)\lambda_{111} = -20 \cdot 10^{-6}, \\ M_S &= 1.66/\mu_0 \text{ A/m}, \\ \Omega &= 707 \text{ Jm}^{-3} \quad \gamma_\sigma = 0.9 \end{aligned}$$

There is excellent correlation between the model and experimental  $\lambda$ -H and B-H characteristics, with less than 5% normalized root mean square error. *Throughout this thesis the following procedure is employed to define the error. Corresponding to ten different equi-spaced values of magnetic field from 50 to 500 Oe, the values of experimental ( $x_i$ ) and model ( $y_i$ ) magnetostriction/magnetization are evaluated at a given pre-stress. The normalized root mean square error is defined as:*

$$\text{error} = \frac{1}{x_{\text{max}}} \sqrt{\frac{1}{N} \sum_{i=1}^N (y_i - x_i)^2} \quad (4.19)$$

The zero pre-stress  $\lambda$ -H curve is also well predicted, indicating that the magnetostriction simulation accounts for the difference in initial condition (magnetostriction) between zero-stress and 15 MPa or higher compressive pre-stress. At zero-stress and zero-field most of the moments are randomly distributed between the six  $\langle 100 \rangle$  directions. However, at 15 MPa and higher pre-stress levels most domains are oriented perpendicular to the [100] axis along which the compression is applied i.e. they are most probably oriented randomly between the [0-10], [010], [00-1] and [001] directions. Therefore, when all  $\lambda$ -H curves are plotted from the same datum, i.e. change in length is calculated from the zero-field length, the curves with pre-stress demonstrate a maximum strain that is  $1/2\lambda_{100}$  larger than the zero-stress case.

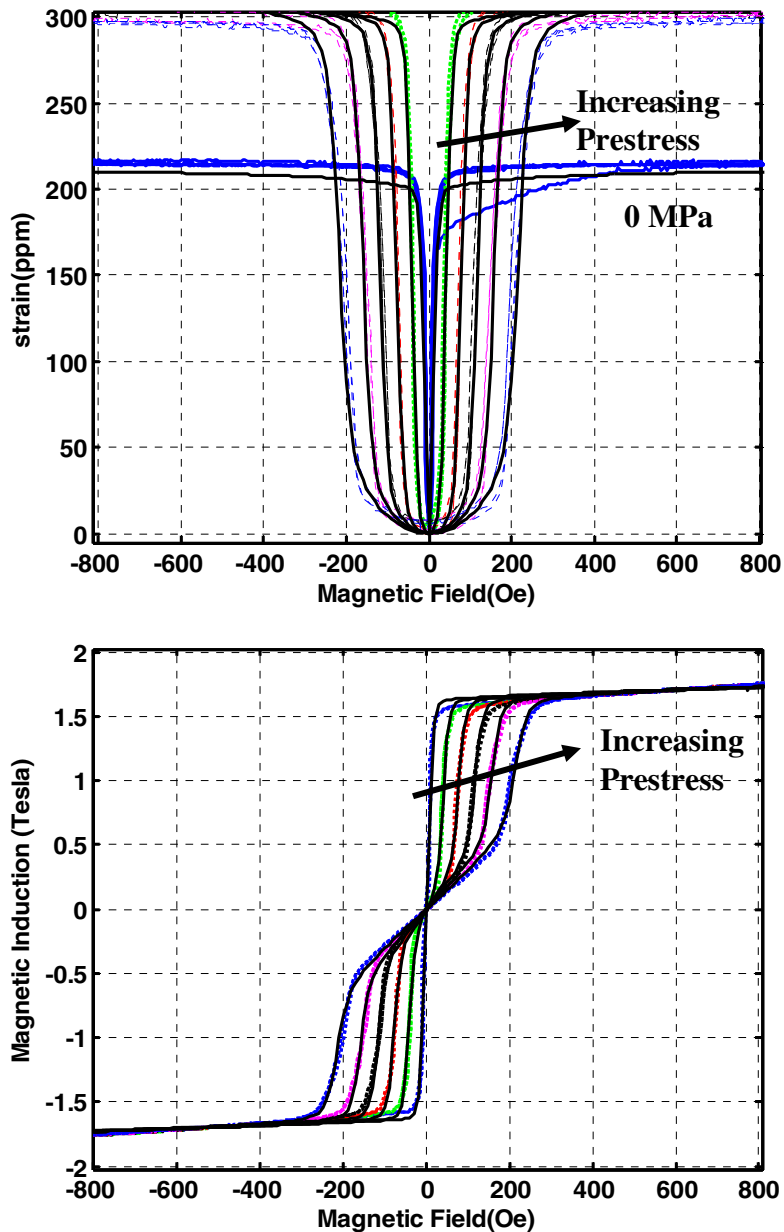


**Figure 4.10** Comparison between simulated (thin lines) and experimental (dotted lines)  $\lambda$ -H (above) and B-H (below) characteristics of [100], 19 at. % Ga single crystal FeGa alloy sample at compressive prestress: 0, 15, 30, 45, 60, 80 MPa.  
*NOTE: Arrow indicates increasing compressive pre-stress in all figures in this chapter.*

A moderately large and positive  $K_1$  indicates that the  $\langle 100 \rangle$  are the easy axes. This combined with the relative magnitude of the stress-anisotropy term due to the magnetoelastic effect may allow the model to first simulate domain rotation, indicated by the small variation of B with H. This is possibly followed by flipping of domains at intermediate applied field levels, which is indicated by a large variation of B with H. This leads to two distinct permeability regions as demonstrated by the kinking behavior in B-H curves. The small  $\Omega$  chosen to model the sharp characteristics of the 19 at. % Ga sample, compared to larger  $\Omega$  chosen for higher Ga content samples, also accentuates the kinking behavior.

#### 4.4.2 Magnetomechanical Behavior of 24.7 at. % Ga Sample

The following parameters used for the simulation of the actuator behavior, i.e. parameters that minimize the error between model simulation and experiment, are:

$$K_1 = -1.2 \cdot 10^3 \text{ Jm}^{-3}, K_2 = 0.5 \cdot 10^4 \text{ Jm}^{-3},$$

$$(3/2)\lambda_{100} = 310 \text{ ppm @ 0 to 30 MPa stress}$$

$$295, 280 \text{ and } 265 \text{ ppm @ 45, 60 and 80 MPa respectively}$$

*(approximately modeled as linearly decreasing at 1ppm/MPa from 30 to 75 MPa)*

$$(3/2)\lambda_{111} = 55 \cdot 10^{-6},$$

$$M_s = 1.32/\mu_0 \text{ A/m},$$

$$\Omega = 950 \text{ Jm}^{-3}, \gamma_\sigma = 1.05$$

The actuator characteristics of the 24.7% single crystal sample show two unique trends: absence of kinks in B-H characteristics and decrease in saturation magnetostriction with compressive stress beyond 30 MPa. An attempt is made to model these effects with a choice of magnetocrystalline anisotropies, consistent with the trends reported in literature [Rafique2004] and a higher  $\Omega$  to simulate the smoother B-H and  $\lambda$ -H curves.

Negative  $K_1$  and  $K_2 > -9K_1/4$  indicate that  $\langle 110 \rangle$  directions are the easy axes. On application of fields parallel to the sample [100] axis, the domains are likely to *first* flip to the  $\langle 110 \rangle$  directions closest to the [100] direction followed by gradual

rotation to aligning parallel to the [100] direction, producing a smooth high permeability to low permeability transition. Furthermore,  $K_1$  is an order of magnitude smaller and  $K_2$  about five times smaller than  $K_1$  of the 19 at. % Ga sample indicating that overall, magnetocrystalline anisotropy has less significant effect on the behavior of the 24.7 at. % Ga sample. The higher  $\Omega$  also contributes to the smoothness of the B-H and  $\lambda$ -H curves. All these factors possibly lead to the absence of a kink in the B-H curves of the 24.7 at. % Ga samples. With the choice of the appropriate model parameters, based on the rationale mentioned above, an excellent correlation between simulation and experimental B-H curves was obtained. The normalized root mean square error in simulation of the B-H curves, *as defined in Section 4.4.1*, is well within 5% as shown in Figure 4.11

The 24.7 at. % Ga, FeGa samples show an unexpected trend: decrease in magnetostriction with an increase in compressive stress beyond 30 MPa. This trend was confirmed by repetition of the experiment. However, in the absence of in-situ x-ray diffraction under stress, it is impossible to find a conclusive explanation for this behavior. It may be conjectured, that this effect is due the complex elastic interaction between the multiple phases as explained in Chapter 3.

For the purposes of simulation,  $3/2\lambda_{100}$  is approximately modeled as linearly decreasing at 1ppm/MPa from 30 to 75 MPa. With this correction, the  $\lambda$ -H curves are modeled very well for stress in the range of 30 and 80 MPa, within 10% normalized root-mean square error. However, low pre-stress magnetostrictive simulation demonstrates larger errors.

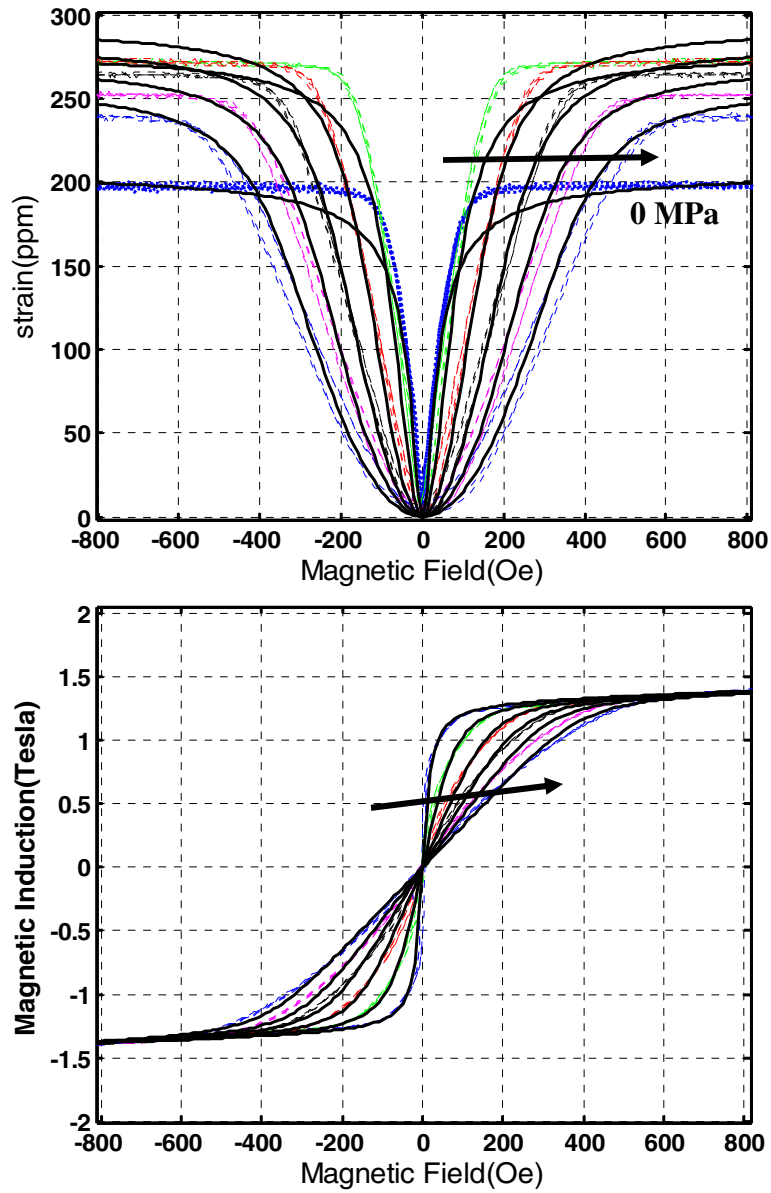


**Figure 4.11** Comparison between simulated (thin lines) and experimental (dotted lines)  $\lambda$ -H (above) and B-H (below) characteristics of [100], 24.7 at. % Ga single crystal FeGa alloy sample at compressive prestress: 0, 15, 30, 45, 60, 80 MPa.

*(Arrow indicates increasing compressive pre-stress.)*

#### 4.4.3 Magnetomechanical Behavior of 29 at. %Ga Sample

The characteristics of the 29 at. % Ga sample were simulated with the following parameters to minimize the error between model simulation and experiment:

$$K_1 = -2 \times 10^3 \text{ Jm}^{-3}, K_2 = 0.5 \times 10^4 \text{ Jm}^{-3},$$

$$(3/2) \lambda_{100} = 300 \text{ ppm @ 0 to 30 MPa stress}$$

$$282.5 \text{ and } 265 \text{ @ 45 and 60 MPa respectively}$$

$$(3/2) \lambda_{111} = 55 \times 10^{-6},$$

$$M_S = 1.11 / \mu_0 \text{ A/m},$$

$$\Omega = 1150 \text{ Jm}^{-3}, \gamma_\sigma = 1.00$$

The actuator characteristics of the 29 at. % Ga Iron-Gallium sample demonstrates trends similar to the 24.7 at. % Ga sample, exhibiting relatively larger drop in magnetostriction with stress and greater smoothness. A larger  $\Omega$  than that of 24.7% and a drop in magnetostriction of 1.17 ppm/MPa between 30 and 60 MPa were chosen to model the behavior of this sample.

It must be noted that  $K_1$  was chosen as  $-2 \text{ kJ/m}^3$  by extrapolating trends seen between 19 and 24.7 at. % Ga samples and to model zero-stress B-H curves well, while Clark *et al.* [Clark2005] have reported that  $K_1$  of a furnace cooled 28.5% sample was  $\sim 1 \text{ kJ/m}^3$ . Since, the magnitude of  $K_1$  is such that its contribution to the total energy is an order of magnitude smaller than that of the magnetoelastic energy even at 15-30 MPa compressive stress, its effect on most of the 29 at. % Ga sample characteristics are negligibly small.

A good correlation between simulation and experimental B-H curves was obtained with normalized root mean square error, *as defined in Section 4.4.1*, within 5% as shown in Figure 4.12. The normalized root mean square error in simulated  $\lambda$ -H curves at stresses of 30 MPa and higher was within 10%. However, low pre-stress magnetostrictive simulation, i.e. 0 and 15 MPa, do not show very good correlation with the experiment.

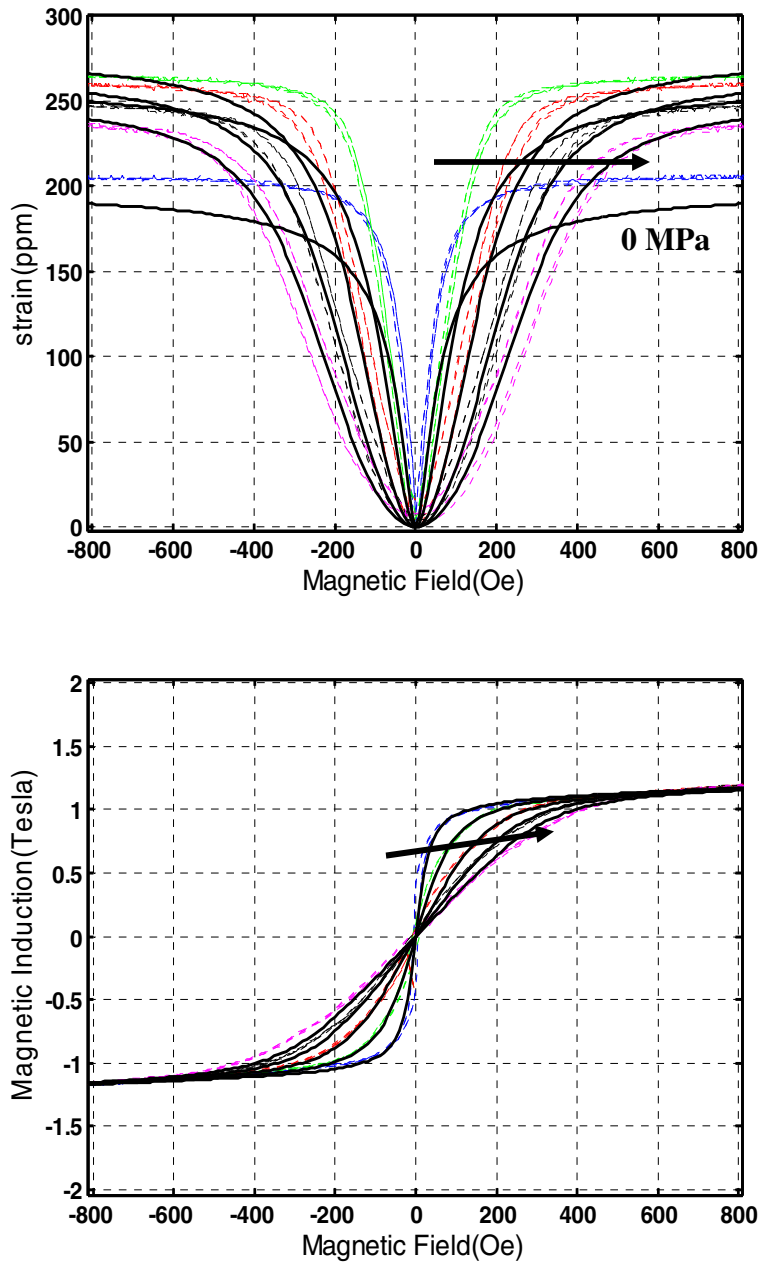


**Figure 4.12** Comparison between simulated (thin lines) and experimental (dotted lines)  $\lambda$ -H (above) and B-H (below) characteristics of [100], 29 at. % Ga single crystal FeGa alloy sample at compressive prestress: 0, 15, 30, 45, 60 MPa.  
(Arrow indicates increasing compressive pre-stress.)

Notwithstanding the poor correlation in  $\lambda$ -H simulations at low-stresses there is very good correlation between the B-H simulation and experiment. The probable

reason for this effect is the complex initial condition in the multi-phase samples which may lead to strain states that deviate significantly from expected trends.

#### 4.4.4 Discussion of Effect of Ga Content

The previous section discussed the modeling of different trends shown by single crystal FeGa alloys when the atomic percentage of gallium was increased from 19% to 24.7% and finally 29%. It was also demonstrated that the choice of parameters (Table 4.1) were able to capture those trends. In this section, we analyze the effect of Ga content both on the model parameters, and on the derivative quantities, viz. relative permeability and  $d_{33}$ .

**Table 4.1.** Variation in model parameters with increasing gallium content.

		Ga 19	Ga 24	Ga 29
$K_1, K_2$		1.75e4, 0	-1.2*e3, 0.5*1e4	-2e3, 0.5*1e4
$\lambda_{100}^* \cdot \lambda_{111}$ (ppm)		318, -20	310, 55	300, 55
$\mu_0 M_s$		1.66	1.32	1.11
$\Omega$		707	950	1150
$\gamma_\sigma$		0.9	1.05	1
$^* \lambda_{100}$ ( $\sigma$ )		318	[310 310 310 295 280 265]	[300 300 300 282.5 265 245]

The cubic magnetocrystalline energy constant  $K_1$  is moderately high and positive (17.5 kJ/m<sup>3</sup>) at 19 at. % Ga, drops steeply to 0 around 20% [Rafique2004] and goes small but negative (~-1 kJ/m<sup>3</sup>) for Ga content of 21% and beyond. The relatively high magnetocrystalline anisotropy, due to moderately high and positive  $K_1$ , must be overcome before the magnetic moment in the domain can flip: this is one of the main reasons for a kink being demonstrated only in the 19 at. % Ga sample. This is also a reason for the relative permeability of the 19 at. % Ga sample showing a double peak (one each at moderate positive and negative fields) and a valley at low fields in Figure 4.13 (a). At low fields, both positive and negative, the domains begin to rotate and have low permeability. At a critical field, they overcome the magnetocrystalline and stress anisotropies and flip to the [100] direction along which

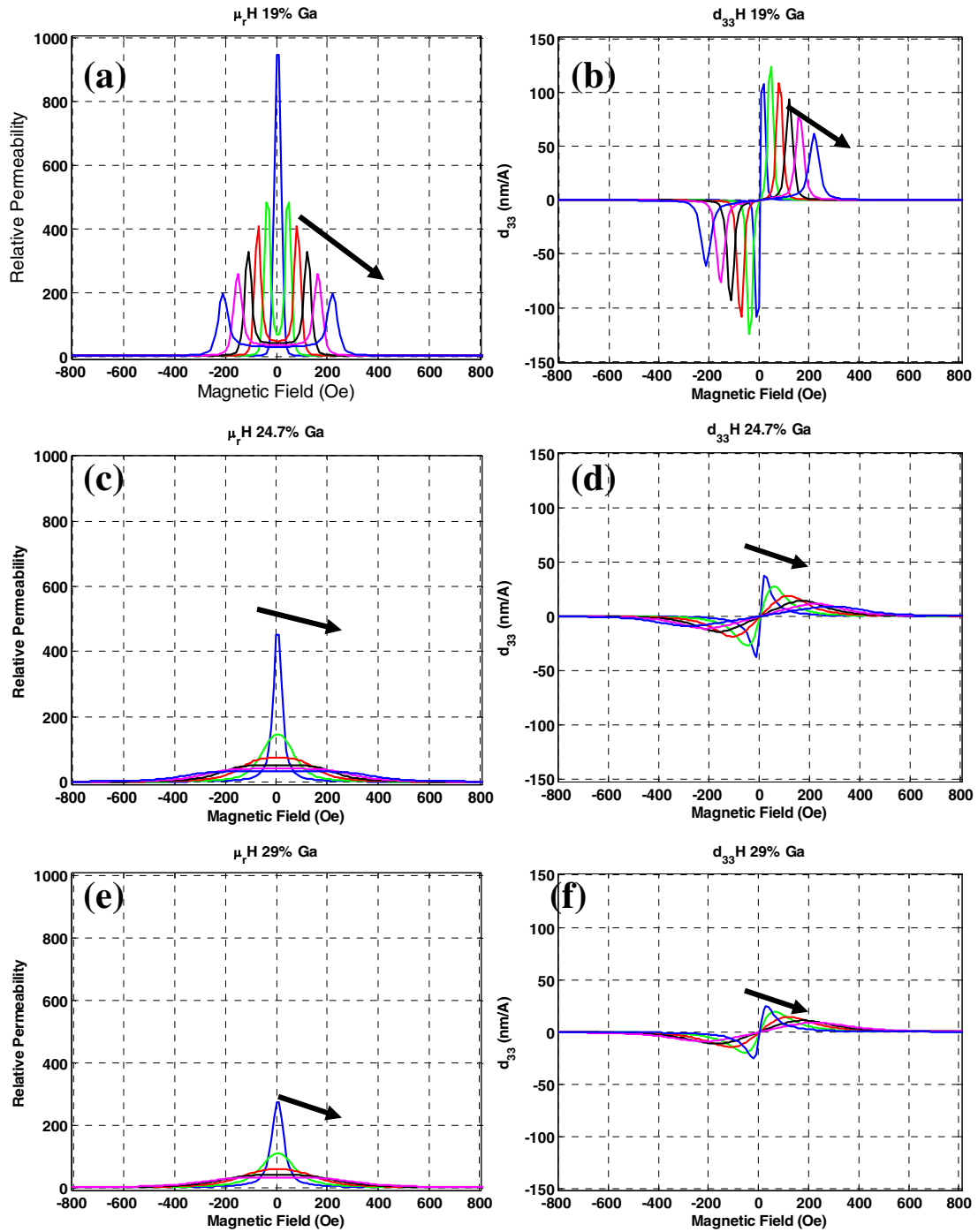


**Figure 4.13** Simulated  $\mu_R$ -H and  $d_{33}$ -H characteristics of [100], 19, 24.7 and 29 at. % Ga single crystal FeGa alloy sample at compressive prestress: 0, 15, 30, 45, 60, 80

MPa. (Arrow indicates increasing compressive pre-stress.)

(a)  $\mu_R$ -H and (b)  $d_{33}$ -H of 19 at. % Ga [100] oriented sample.

(c)  $\mu_R$ -H and (d)  $d_{33}$ -H of 24.7 at. % Ga [100] oriented sample.

(e)  $\mu_R$ -H and (f)  $d_{33}$ -H of 29 at. % Ga [100] oriented sample.

the field is applied, exhibiting a peak in relative permeability. Corresponding to this, there is also a very large change in magnetostriction with a small change in field that shows as a positive/negative peak in the  $d_{33}$ -H curves shown in Figure 4.13 (b). The magnitude of the field at which these peaks occur increases with increasing compressive stress as more field is needed to overcome the stress anisotropy.

For the 24.7 and 29 at. % Ga,  $K_1$  is very small, indicating that the magnetocrystalline anisotropy does not have much effect on the sample's magnetomechanical behavior. Furthermore, the negative  $K_1$  (and  $K_2 > -9K_1/4$ ) ensures that the  $\langle 110 \rangle$  axes are the preferred or easy axes. Thus, the domains are likely to flip first to the  $\langle 110 \rangle$  axes nearest to the [100] direction along which the field is applied, followed by rotation to the [100] direction with increasing field. Hence, the 24.7 and 29 at. % Ga exhibit a single high-permeability peak (Figures 4.13 (c) and (e)) and two  $d_{33}$  peaks near zero-field (Figures 4.13 (d) and (f)).

The increase in  $\Omega$  from  $707 \text{ J/m}^3$  for the 19 at. % Ga simulation to  $1150 \text{ J/m}^3$  for the 29 at. % Ga simulation, while  $\mu_0 M_s$  falls from 1.66 T to 1.11 T and  $|K_1|$  decreases by an order of magnitude from  $1.75 \times 10^4$  to  $2 \times 10^3 \text{ J/m}^3$  causes a decrease in the ratio between the magnetic-energy term  $\mu_0 BH$  and magnetocrystalline anisotropy terms in the numerator and the smoothing term  $\Omega$  in the denominator in Equation 4.10 and 4.13. This produces a significant smoothing effect on the B-H and  $\lambda$ -H curves. Thus, an increase in Ga content results in a decrease in both  $d_{33}$  and relative permeability for all pre-stress cases. For example, with an increase in gallium content from 19% to 29%, the zero-stress  $d_{33}$  drops from 100nm/A to 25nm/A as illustrated by Figure 4.13 (b) and (f), while the relative permeability drops from  $\sim 1000$  to 250, as illustrated by Figure 4.13 (a) and (e). Physically,  $\Omega$  signifies the extent of imperfections in the sample, i.e. a sample closer to being a single-phase; single-crystal with very few defects is likely to have small  $\Omega$  and exhibit sharper characteristics. The formation of multiple phases with increasing Ga content may have contributed to the increase in  $\Omega$  with Ga content. Large inhomogeneity in the sample results in greater probability of moments orienting in energetically less

favorable directions which can lead to smaller gradients in the macroscopic  $\lambda$ -H and B-H curves.

$\gamma_\sigma$  does not show any particular trend with Ga content. However,  $\gamma_\sigma$  was introduced to scale the magnetoelastic energy term  $\sigma^* \lambda_{100}$ , for uni-axial loading in the [100] direction, relative to other terms, especially the magnetic-energy term  $\mu_0 BH$ . This factor serves to fine tune the model to correct for error in the estimation of value of the magnetic field and stress in the sample due to spatial variation in these quantities, such as field variation discussed in Chapter 3. Thus, in single-crystal samples, this factor is likely to be influenced by specific mounting conditions, such as variations in the length of samples and interface with end caps, in addition to the choice of the model parameter  $\lambda_{100}$ . Based on the limited data available, it is not possible to hypothesize any deeper physical explanation for this observation.

The variation in  $d_{33}$  and permeability with magnetic field and stress at various compositions (Ga content), documented in Figure 4.13, provides a database of properties of these single-crystal materials. These curves are generated by taking appropriate derivatives of simulated characteristics in Figures 4.10 through 4.12. The fact that this vast amount of detail of material properties can be generated from merely 7-parameters, for each composition and heat treatment, could prove to be important factor in using this model as a design tool.

#### **4.4.5 Analysis of Sensitivity to Model Parameters: Introduction of a Non-Dimensional Parameter for Smoothing**

For given experimental  $\lambda$ -H and B-H characteristics the model parameters  $\lambda_{100}$ ,  $\lambda_{110}$  and  $M_s$  are fixed and there is no flexibility in the choice of these parameters. The parameter  $\gamma_\sigma$ , used to scale the effect of stress determined by  $\sigma^* \lambda$ , does not vary by more than 10% for single crystal samples. However, there is greater flexibility in the choice of the other three parameters  $K_1$ ,  $K_2$  and  $\Omega$ , which significantly influence the nature of the  $\lambda$ -H and B-H curves as explained in the previous section. Therefore,

the sensitivity of  $\lambda$ -H and B-H curves to these parameters, viz.  $K_1$ ,  $K_2$  and  $\Omega$  is studied in this section.

The magnitude and signs of  $K_1$  and  $K_2$  determine the easy axis of the sample. By evaluating the magnetocrystalline anisotropy energy (Equation 4.2), along the  $\langle 100 \rangle$ ,  $\langle 110 \rangle$  and  $\langle 111 \rangle$  directions for different values of  $K_1$  and  $K_2$  the Figure 4.14 is obtained. For  $K_1 > 0$  and  $K_2 > -9K_1$  the  $\langle 100 \rangle$  direction is the easy axis whereas for  $K_1 < 0$  and  $K_2 > -(9/4)K_1$  the  $\langle 110 \rangle$  direction is easy. For all other cases  $\langle 111 \rangle$  direction is the easy axis. Thus, for a given value of  $K_1$  and  $K_2$  the easy direction can be determined and this strongly influences the nature of  $\lambda$ -H and B-H curves along a given crystallographic direction.

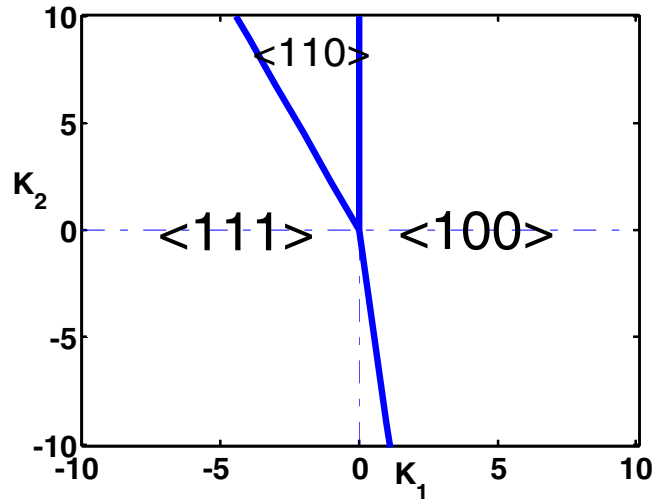


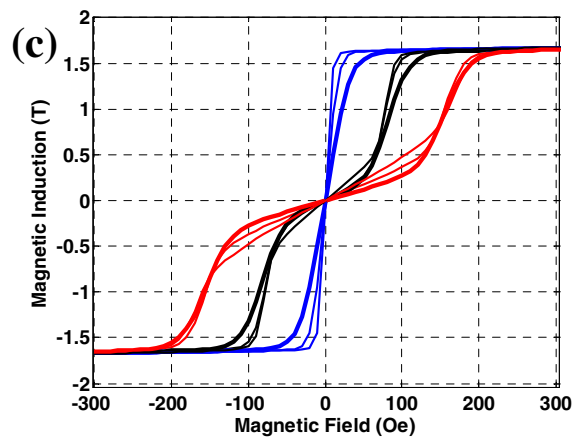
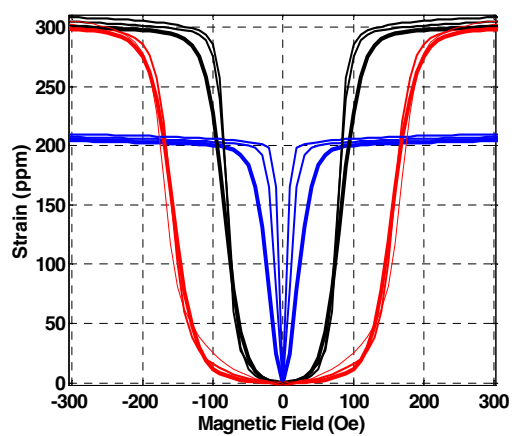
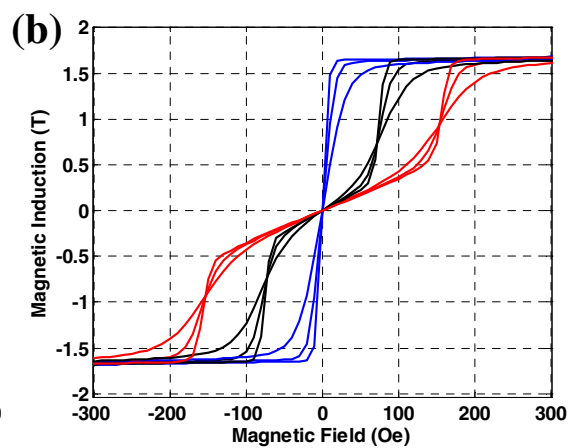
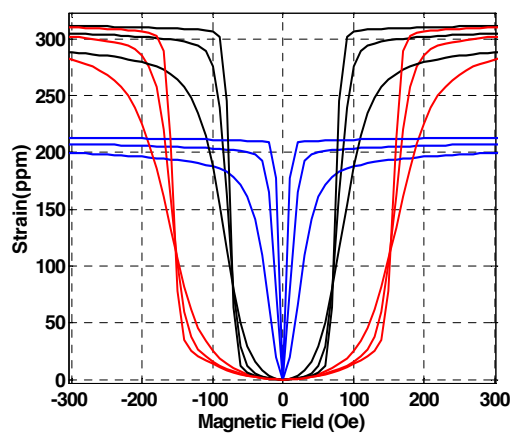
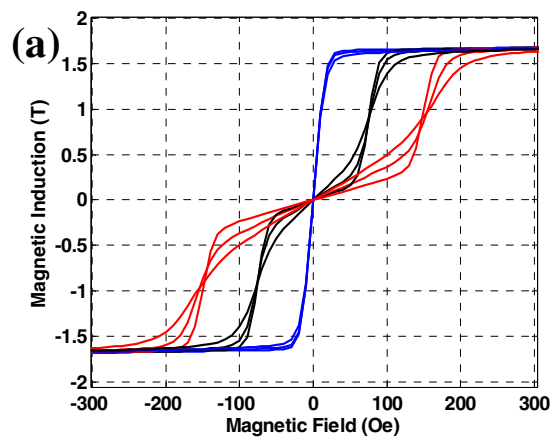
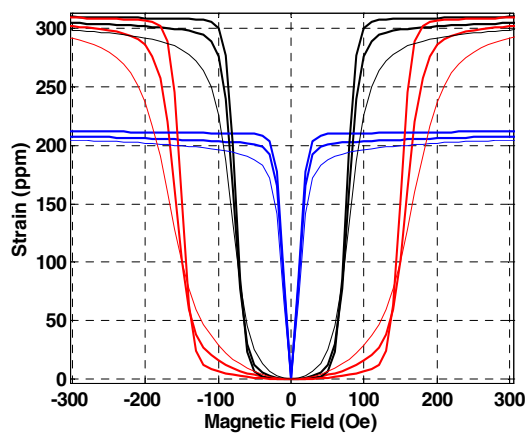
**Figure 4.14** Easy axes for different values of cubic magnetocrystalline anisotropy constants  $K_1$  and  $K_2$ .

Based on the simulation in the previous section, the interplay between the magnitude of magnetocrystalline anisotropy and the Armstrong smoothing factor  $\Omega$ , appears to play a key role in determining the nature of the  $\lambda$ -H and B-H curves. Therefore a sensitivity analysis is performed with respect to these parameters. Further, to reduce the number of cases, the value of  $K_1$  and  $\Omega$  are varied taking  $K_2=0$ . The baseline model parameters used for this analysis are those of the 19 at. % Ga sample as this is an ideal case of a sample with  $\langle 100 \rangle$  as easy axis and sufficient

magnetocrystalline anisotropy to produce distinct region of low permeability at low H followed by a region of high permeability. The sensitivity analysis is performed for compressive pre-stress of 0, 30 and 60 MPa.

Figure 4.15 (a) shows that doubling the magnetocrystalline anisotropy ( $K_1$  term) results in larger kinking effect (distinct low and high permeability region at low H) and larger gradients in  $\lambda$ -H and B-H curves. This could lead to higher peak values of  $d_{33}$  and  $\mu_r$ . Conversely, halving  $K_1$  results in smaller kinking effect and smoother  $\lambda$ -H and B-H curves. Figure 4.15 (b) shows that  $\Omega$  has the opposite effect of  $K_1$ , halving  $\Omega$  increases the gradient in the  $\lambda$ -H and B-H curves while decreasing  $\Omega$  makes them smoother. This is confirmed by Figure 4.15 (c) as simultaneously halving or doubling both  $K_1$  and  $\Omega$  nearly compensate for each other, producing very little change in the nature of the  $\lambda$ -H and B-H curves. (The reason that there is a small change in the curves is that the sensitivity to changes in  $\Omega$  appears to be more than that to changes in  $K_1$ ). Finally, halving one and doubling the other produces a large difference in the  $\lambda$ -H and B-H curves (Figure 4.15 (d)).

This sensitivity analysis suggests that the ratio between  $\Omega$  and magnetocrystalline energy plays an important role in the shape of the  $\lambda$ -H and B-H curves. Therefore a dimensionless parameter  $\Phi = \Omega / \max\_contribution (K_1 \text{ or } K_2)$  is defined, which is an indication of the smoothness of the characteristics. The maximum contribution to magnetocrystalline anisotropy energy of  $K_1$  is  $K_1/3$  and that of  $K_2$  is  $K_2/27$  as per Equation 4.2. Thus the  $\Phi$  for the 19, 24.7 and 29 at. % Ga samples are respectively 0.1212, 2.375 and 1.725. This taken together with Figure 4.15 (d) in sensitivity analysis demonstrates that  $\Phi < 0.5$  can be expected to produce the “kinking behavior” while  $\Phi > 1$  produces smooth characteristics.



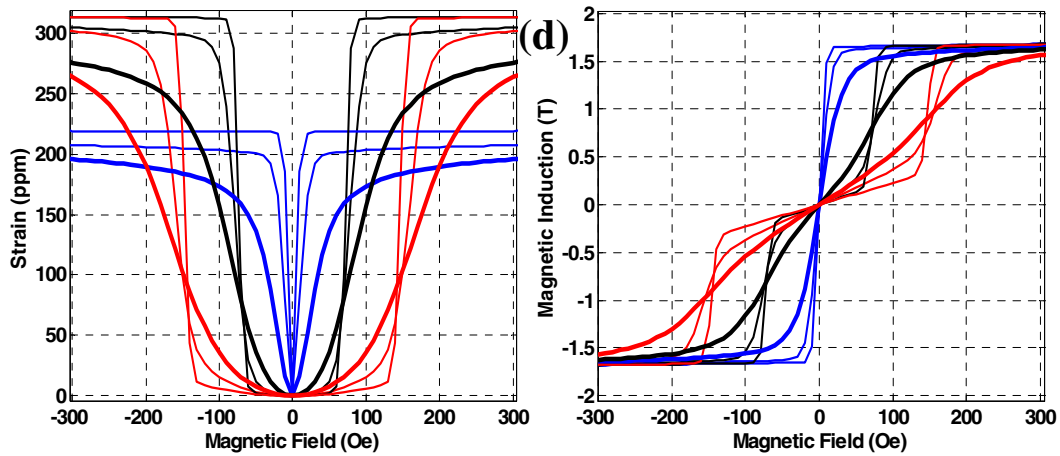


**Figure 4.15** Parametric studies of  $K_1$  and  $\Omega$

on  $\lambda$ -H (left) and B-H (right) characteristics.

(a) Effect of halving and doubling  $K_1$  at constant  $\Omega$ .

(b) Effect of halving and doubling  $\Omega$  at constant  $K_1$ .

(c) Effect of (i) halving both  $\Omega$  and  $K_1$

(ii) doubling both  $\Omega$  and  $K_1$ .

(d) Effect of (i) halving  $\Omega$  and doubling  $K_1$

(ii) doubling  $\Omega$  and halving  $K_1$ .

#### **4.5 Simulation of Actuator Behavior in Various Crystallographic Directions**

The model simulation was validated against experimental data of a  $\langle 110 \rangle$  oriented 18 at. % Ga, single-crystal FeGa alloy to demonstrate its capability in simulating actuator behavior along different crystallographic directions. Using model parameters of the 18 at. % Ga sample, predictions of the magnetoelastic behavior in the  $\langle 111 \rangle$  are reported, although a  $\langle 111 \rangle$  oriented sample could not be procured for the purpose of experimental validation.

##### **4.5.1 Magnetomechanical Behavior in $\langle 110 \rangle$ Direction**

The model parameters chosen to simulate the  $\lambda$ -H and B-H curves, illustrated by Figure 4.16, of the 18 at. % Ga sample are:

$$K_1 = 2 \cdot 10^4 \text{ Jm}^{-3}, K_2 = -4 \cdot 10^4 \text{ Jm}^{-3},$$

$$(3/2)\lambda_{100} = 320 \cdot 10^{-6}, (3/2)\lambda_{111} = -10 \cdot 10^{-6},$$

$$M_S = 1.73/\mu_0 \text{ A/m},$$

$$\Omega = 650 \text{ Jm}^{-3} \quad \gamma_\sigma = 0.9$$

The B-H curve at zero-stress in the  $\langle 110 \rangle$  direction takes large fields to saturate and exhibits distinct regimes of magnetization which are caused by the rotation/flipping of magnetization to the nearest set of easy  $\langle 100 \rangle$  direction followed by gradual rotation to the  $[110]$  direction. The requirement of a moderately large field at low-stress is indicative of moderately high magnetocrystalline anisotropy  $K_1$  and is consistent with the value reported in literature [Rafique2004].

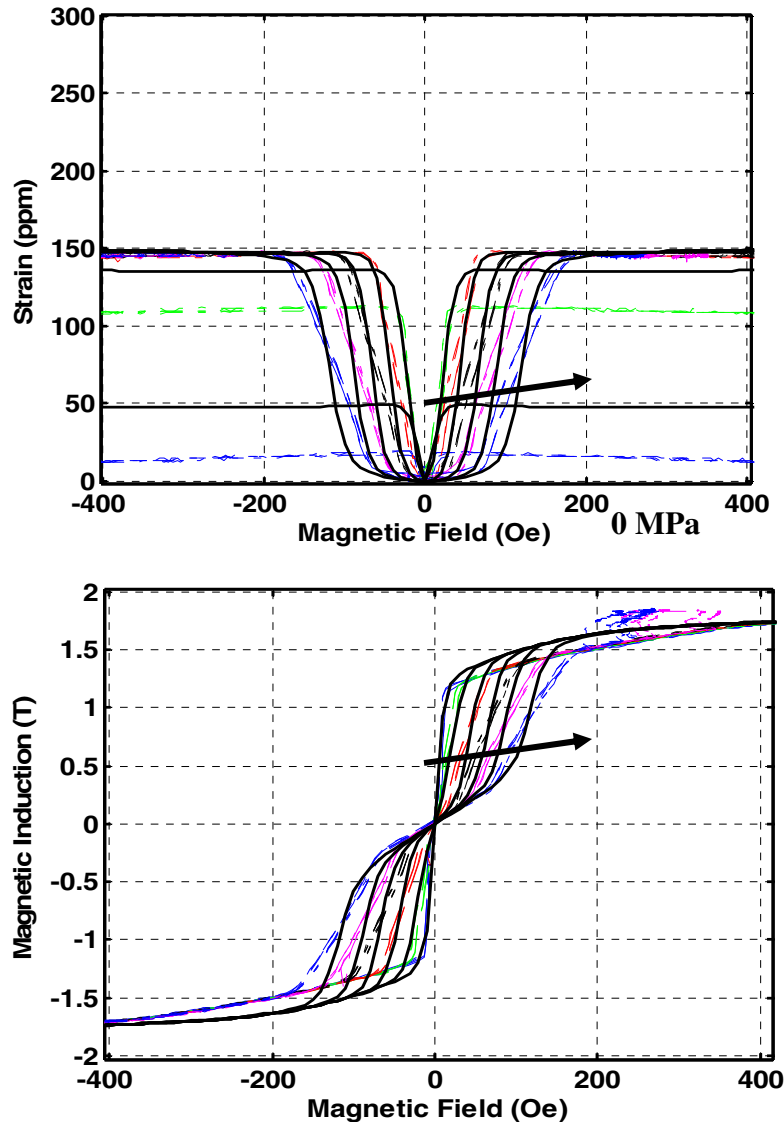


**Figure 4.16** Comparison between simulated (thin lines) and experimental (dotted lines)  $\lambda$ -H (above) and B-H (below) characteristics of  $[110]$ , 18 at. % Ga single crystal FeGa alloy sample at compressive prestress: 0, 15, 30, 45, 60, 80 MPa.

*(Arrow indicates increasing compressive pre-stress.)*

Overall, it appears that this model simulates the trends in the  $\langle 110 \rangle$  behavior fairly well, predicting the saturation magnetostriction,  $3/2\lambda_{110} = 145$  ppm. The model captures certain trends in the B-H curves, such as low permeability followed by high permeability region at high pre-stresses, which leads to a small kink, although not as pronounced as the  $\langle 100 \rangle$  19 at. % Ga sample. While the model predicts the trends well, it is unable to model specific  $\lambda$ -H and B-H curves at certain stresses well.

The simulated permeability and  $d_{33}$  (Figure 4.17) show some similarities to those in the 19 at. % Ga [100] sample, except the magnitude of the  $d_{33}$  of this sample is about half that of the 19 at. % sample in the [100] direction, primarily because  $3/2\lambda_{110} \approx 1/2 (3/2\lambda_{100})$  as explained in Chapter 3. The permeability curves show two peaks at moderate fields and a valley at the center similar to the 19 at. % Ga [100] sample, although the peaks are less sharp owing to the smaller kinking effect in the B-H curves. Physically, the application of compressive stress produces stress anisotropy, against which the moments have to rotate before flipping to the  $\langle 100 \rangle$  directions close to the [110] direction along which the field is applied. The  $\langle 110 \rangle$  sample permeability peaks are less pronounced owing to the fact that the magnetoelastic energy is smaller in the  $\langle 110 \rangle$  direction than in the  $\langle 100 \rangle$  direction for comparable levels of applied stress.

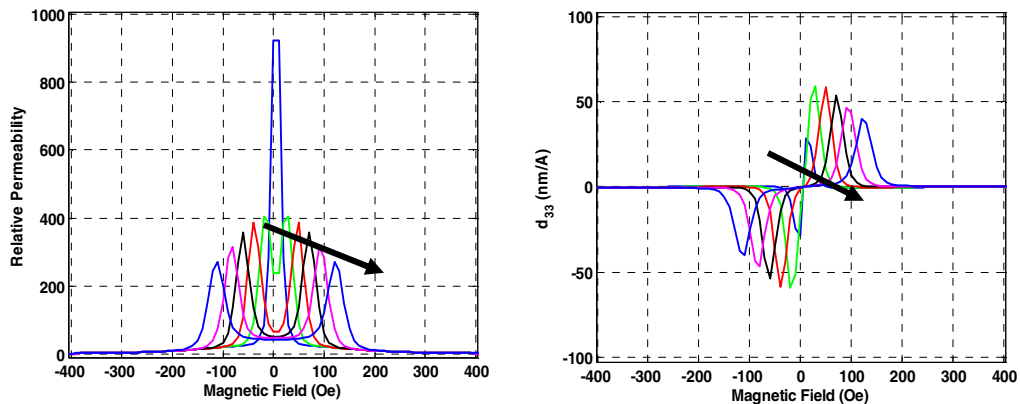


**Figure 4.17** Simulated  $\mu_r$ -H (left) and  $d_{33}$ -H (right) characteristics of [110], 18 at. % Ga single crystal FeGa alloy sample at compressive prestress: 0, 15, 30, 45, 60, 80 MPa. (Arrow indicates increasing compressive pre-stress.)

#### 4.5.2 Predicted Behavior in <111> Direction

The predicted magnetomechanical behavior for the application of pre-stress and field in the <111> direction is shown in Figure 4.18. The model parameters employed were that of the 18 at. % Ga sample.

The dominant feature of the predicted behavior is that it does not vary significantly with the level of pre-stress; the  $\lambda$ -H, B-H,  $\mu_r$ -H and  $d_{33}$ -H curves for 0-stress to 80 MPa compressive stress almost lie on top of each other. This is expected as the magnetoelastic energy, which is proportional to  $\lambda_{111} \cdot \sigma$ , is about 30 times smaller than that for comparable stress in the [100] direction. This is because  $\lambda_{100} \approx 30 \lambda_{111}$ . This estimate was based on magnetostriction values in [Kellogg2003b].

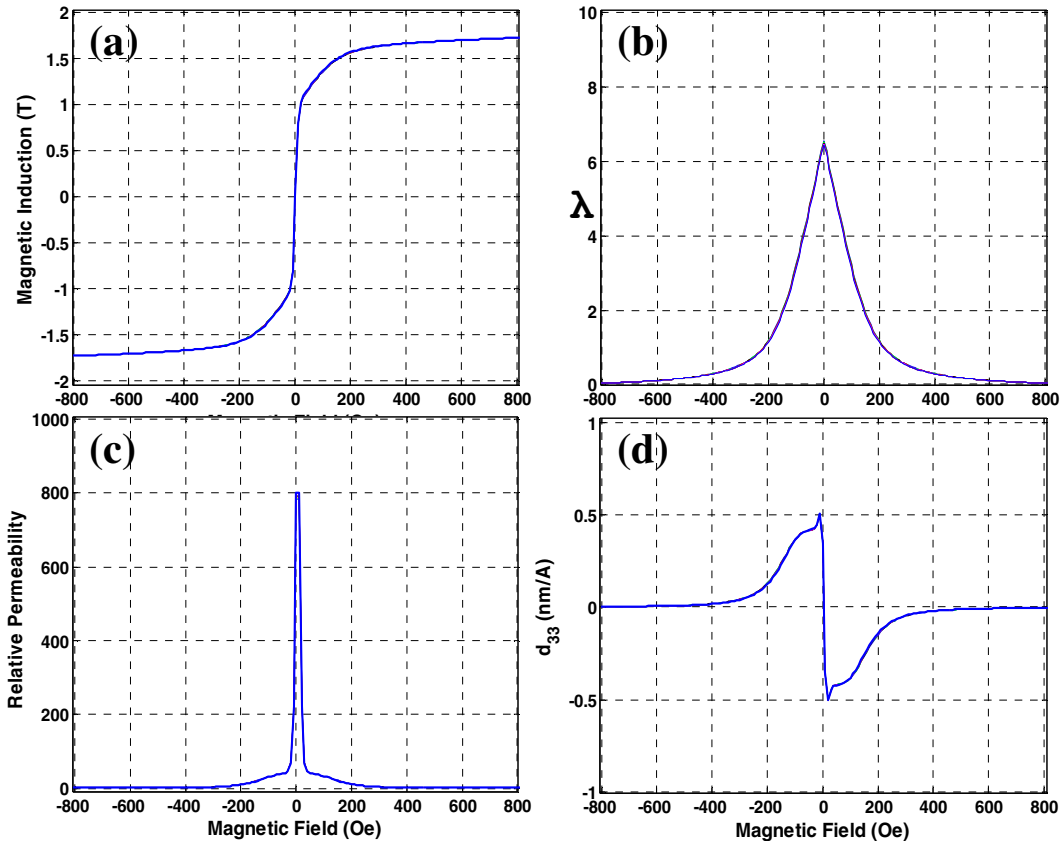


**Figure 4.18** Simulated (a) B-H, (b)  $\lambda$ -H, (c)  $\mu_r$ -H and (d)  $d_{33}$ -H characteristics of [111], 18 at. % Ga single crystal FeGa alloy at compressive prestress: 0, 15, 30, 45, 60, 80 MPa.

The B-H curve demonstrates a large change in magnetization, and consequently magnetic induction B, with field  $\sim 20$  Oe due to the orientation of domains in the  $\langle 100 \rangle$  easy directions, closest to the  $\langle 111 \rangle$  direction along which the field is applied. This is followed by a gradual increase in magnetization with field from  $\sim 20$  Oe to  $\sim 300$  Oe due to the rotation of domains from the  $\langle 100 \rangle$  directions to the magnetically hard  $[111]$  direction. Beyond 300 Oe, saturation is reached and B does not increase significantly with H. The  $\mu_R$ -H curve correspondingly exhibits a relative permeability  $\mu_R \approx 800$  at low fields,  $\mu_R \approx 30$  between 20 and 300 Oe and  $\mu_R = 1$  beyond that.

There is a small decrease in magnetostriction with increasing field as  $\lambda_{111}$  is small and negative. Correspondingly the  $d_{33}$  is less than  $-0.5$  nm/A.

#### **4.6 Predicted Behavior Under Tension**

The magnetomechanical behavior in the  $[100]$  direction under tension is simulated and compared with bench-marked simulation of behavior under compression. The model parameters employed were that of the 19 at. % Ga sample, discussed in Section 4.4.1.

Application of tension in the  $[100]$  direction favors an orientation of domains in the  $[100]$  or  $[-100]$  directions. On application of a small magnetic field in the  $[100]$  directions the domains immediately align along that direction. Therefore, under a relatively small tensile stress of 15 MPa, the magnetic field to obtain a magnetic induction of 1.5 T is  $\sim 10$  Oe as shown in Figure 4.19. This is half the field of  $\sim 20$  Oe required under zero-stress. Consequently the peak value of relative permeability with 15 MPa tension is  $\mu_R \approx 3000$  compared to  $\mu_R \approx 1000$  at zero-stress.

The magnetostriction that can be achieved at 15 MPa tension is smaller than 5 ppm. The preferential orientation of domains along  $[100]$  or  $[-100]$  at zero-field produce a large initial magnetostriction in the  $[100]$  direction. Further, domains changing from  $[-100]$  to  $[100]$  do not change the magnetostriction. Thus, the

magnetostriction under 15 MPa tension, at zero-field (initial condition) is already near saturation. Very low magnetostriction results in a very low  $d_{33}$ . This may be overcome by stress-annealing the sample as has been demonstrated in research at the Naval Surface Warfare Center [Wun-Fogle2006].

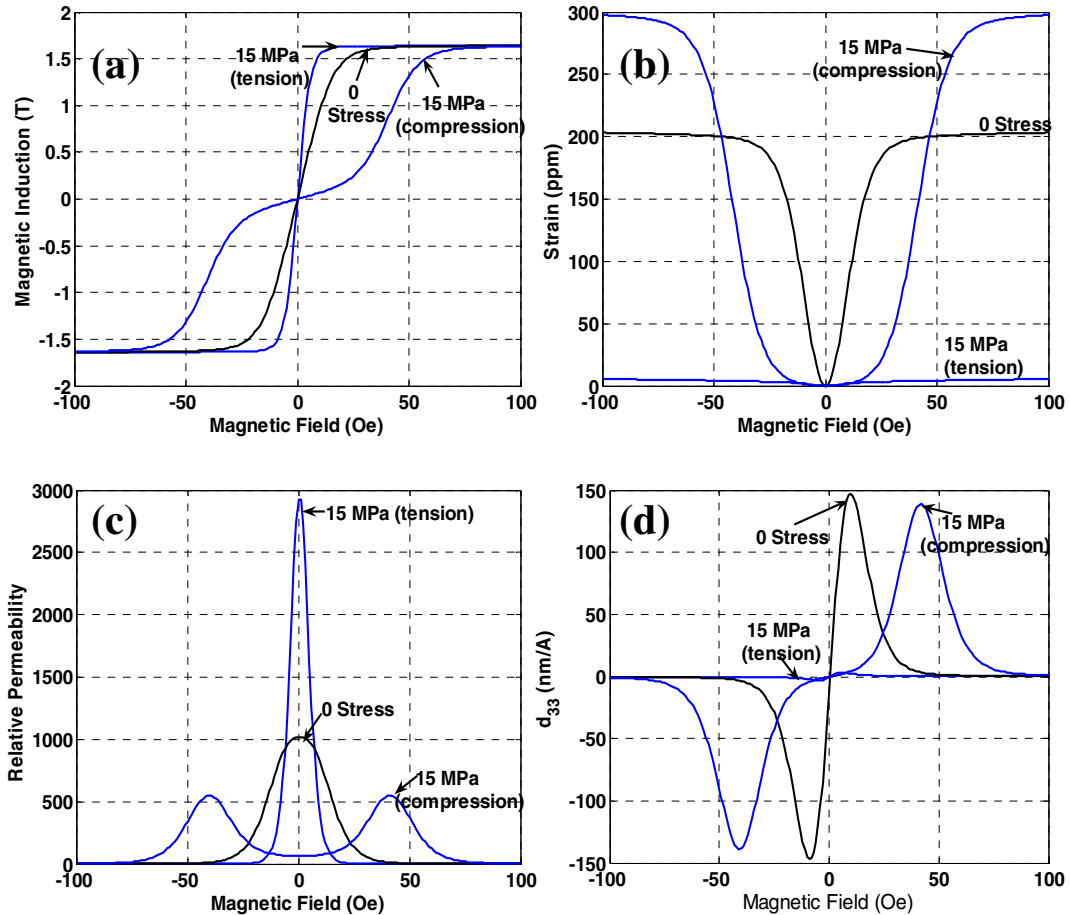


**Figure 4.19** Simulated (a) B-H, (b)  $\lambda$ -H, (c)  $\mu_r$ -H and (d)  $d_{33}$ -H characteristics to demonstrate tensile characteristics of [100], 19 at. % Ga single crystal FeGa alloy sample. Pre-stress values: 15 MPa (tension) 0 MPa and 15 MPa (compression).

#### 4.7 Summary

1. The modeling of the magnetomechanical behavior of single-crystal magnetostrictive materials was addressed at two levels: alignment of spins (magnetization) in individual lattices within a domain and the

distribution of orientation of various domains to simulate the macroscopic response of the material.

2. The alignment of spins in a domain was treated as a canonical ensemble of interacting particles and modeled using 0<sup>th</sup> order approximation (mean-field theory) to predict the temperature dependence of  $M_{\text{sat}}$  and  $\lambda_{\text{sat}}$  within a domain. This was used to demonstrate behavior of a typical magnetostrictive material close to Curie temperature.
3. For modeling magnetostrictive behavior at constant temperature, the problem reduces to finding the distribution of orientation of various “domains” to a particular stress and field input, which is accomplished by the Armstrong model. This distribution determines the macroscopic response of the material.
4. The different trends observed in the magnetomechanical behavior of samples with different Ga content, i.e. 19, 24.7 and 29 at. % Ga single crystal samples were simulated using the model. It was demonstrated that the choice of certain parameters: magnetocrystalline anisotropy  $K_1$  and  $K_2$  as well as Armstrong smoothing parameter was able simulate the strikingly different trends in the B-H curves. A linear dependence of  $\lambda_{100}$  on compressive stress beyond 30 MPa had to be introduced to capture the experimental observation of decrease in saturation magnetostriction in the 24.7 and 29 at. % Ga samples at higher stress.
5. It was demonstrated that it is possible to create a database or map of variation in material properties such as  $\mu_R$  and  $d_{33}$  with both stress and field, which could prove to be useful design tools, using just 7-parameters for each single-crystal material.

6. Finally, it was demonstrated that this model could predict  $\lambda$ -H and B-H curves along various crystallographic directions, viz.  $\langle 110 \rangle$  and  $\langle 111 \rangle$ , other than the  $\langle 100 \rangle$  direction. However, bench-marking the model simulation with  $\langle 110 \rangle$  experimental data showed that while the trends predicted are correct, the model may not be able to simulate some of the experimental curves well.
  
7. Predictions of material behavior in tension are in general agreement with work by other researchers.

## Chapter 5: Modeling the Sensing Behavior (Villari-Effect) & Interaction with Magnetic Circuit

This chapter discusses the application of the Armstrong free-energy model, formulated and validated against actuator data in Chapter 4, in simulating the sensing behavior of single crystal FeGa alloys. The model is validated against experimental sensing data for furnace cooled 19 at. %  $\langle 100 \rangle$  oriented single crystal FeGa alloys and 18 at. %  $\langle 110 \rangle$  oriented single crystal FeGa alloys, demonstrating its potential to simulate sensing behavior along various crystallographic directions. Inability to procure samples oriented in other crystallographic directions, such as the  $\langle 111 \rangle$  direction, limited the validation to the two above mentioned cases. However, model simulation is employed to predict possible sensing behavior in the  $\langle 111 \rangle$  direction.

Furthermore, it is demonstrated that the sensing behavior can be accurately predicted from model-parameters obtained from simulating actuator behavior. Based on this corroboration, predictions for sensing behavior of 24.7 and 29 at. % Ga single-crystal FeGa alloys are made.

An attempt is made to couple the free-energy sensing model with a lumped-parameter model that simulates the magnetic interaction between the magnetostrictive specimen and the magnetic circuit comprising the transducer. This enables a prediction of the variation in field through the sample due to changes in reluctance of the magnetostrictive sample with stress.

### *Literature survey*

Advances in fabrication and modeling of magnetostrictive materials, coupled with the necessity of non-contact sensors have resulted in an increased interest in magnetostrictive sensors [Calkins 1999]. The Villari effect, in which the application of stress changes the state of magnetization of the material (or reluctance of the magnetostrictive sample), can be utilized in converting force or pressure waves to magnetic or electrical signals. This principle is employed in displacement sensors,

hearing aids, accelerometers and for force and torque sensors by suitable choice of sensing configurations [Calkins 1999]. The design of these sensors would benefit from a modeling tool that is capable of predicting the device sensitivity (variation in magnetic induction with stress), as well as material permeability and Young's modulus as a function of bias field and stress. This chapter attempts to develop such a modeling tool, which is capable of simulating sensor characteristics along various crystallographic directions.

Various models developed in the past have attempted to simulate the sensing behavior of magnetostrictive materials. Bergqvist and Engdahl [Bergqvist1991] have generalized the Preisach model to handle stress-effects by treating the combination of field and stress as an effective field  $H_e$ , thus extending this model to both handle effect of stress on actuator behavior as well as simulate sensing behavior. The effect of stress on the magnetization vs. field curves was also modeled by [Jiles 1995a] by introducing the concept of a stress equivalent field term  $H_\sigma$ , which alters the effective field  $H_{eff}$  in the Langevin term. This model was also able to simulate the sensing behavior, viz. the variation in magnetization with applied stress, under constant magnetic field. The sensing behavior was simulated and validated against experimental data for nickel by Jiles [Jiles2004].

However, the Armstrong model was found best suited to simulate single-crystal sensing behavior as it is capable of predicting magnetomechanical behavior along any crystallographic direction and incorporates the magnetocrystalline and stress anisotropies on the basis of physical principles. Furthermore, the model can be formulated to predict sensing behavior from model parameters estimated from actuator characteristics.

### **5.1 Energy Model Application to Sensing Behavior**

This section discusses the formulation of the energy model to predict sensing behavior, validates it by benchmarking against experimental data for furnace cooled 19 at. % <100> oriented and 18 at. % <110> oriented single crystal FeGa alloys and

makes predictions of the possible sensing behavior in typical <111> oriented 18 at. % as well as <100> oriented 24.7 and 29 at. % Ga single-crystal FeGa alloys.

It must be noted that the experimental data was obtained under constant field conditions, by varying the drive current to compensate for changes in reluctance of the sample, as discussed in Chapter 3.

### 5.1.1 Formulation

The model formulation and implementation are very similar to that discussed in Section 4.2.1. Whereas, in Section 4.2.1., the stress is a constant and H is varied, the sensing behavior in this section is modeled by keeping the field constant, designated as bias field  $H_{\text{bias}}$  and varying the stress from 20 MPa tension to -110 MPa compression. For each value of stress, with magnitude  $\sigma$  and direction cosines ( $\beta_{1s}$ ,  $\beta_{2s}$ ,  $\beta_{3s}$ ) with respect to the crystallographic axes, and each value of bias field,  $H_{\text{bias}}$  with magnitude H and direction cosine ( $\beta_{1F}$ ,  $\beta_{2F}$ ,  $\beta_{3F}$ ), the energy for the magnetization orienting in a direction ( $\alpha_1$ ,  $\alpha_2$ ,  $\alpha_3$ ) is given by [Chikazumi1964]:

$$\begin{aligned}
 E(\sigma, H) &= E_{\text{magnetocrystalline}} + \gamma_{\sigma} E_{\text{magnetoelastic}} + E_{\text{magnetic}} \\
 &= K_1 * (\alpha_1^2 \alpha_2^2 + \alpha_1^2 \alpha_3^2 + \alpha_2^2 \alpha_3^2) + K_2 * \alpha_1^2 \alpha_2^2 \alpha_3^2 \\
 &\quad \gamma_{\sigma} \left\{ -\frac{3}{2} \lambda_{100} * \sigma * (\alpha_1^2 \beta_{1s}^2 + \alpha_2^2 \beta_{2s}^2 + \alpha_3^2 \beta_{3s}^2) \right. \\
 &\quad \left. -3 \lambda_{111} * \sigma * (\alpha_1 \alpha_2 \beta_{1s} \beta_{2s} + \alpha_2 \alpha_3 \beta_{2s} \beta_{3s} + \alpha_3 \alpha_1 \beta_{3s} \beta_{1s}) \right\} \\
 &\quad -\mu_0 * M_s * H * (\alpha_1 \beta_{1F} + \alpha_2 \beta_{2F} + \alpha_3 \beta_{3F})
 \end{aligned} \tag{5.1}$$

The distribution of orientations of the magnetization vector may be assumed to follow a Boltzmann distribution as discussed in Chapter 4, Section 4.2.1. Hence, the average value of a physical quantity (for example  $M_x$ ) is given by:

$$M_x = \frac{\int \Sigma_{\theta, \phi} [(M_s \sin \theta \cos \phi) (d\theta d\phi | \sin \theta |) e^{-\frac{E(\theta, \phi)}{\Omega}}]}{\int \Sigma_{\theta, \phi} [(d\theta d\phi | \sin \theta |) e^{-\frac{E(\theta, \phi)}{\Omega}}]} \tag{5.2a}$$

$M_y$  and  $M_z$  are likewise evaluated. The magnetization in a direction ( $\beta_{1R}$ ,  $\beta_{2R}$ ,  $\beta_{3R}$ ) is given by:  $M = M_x \beta_{1R} + M_y \beta_{2R} + M_z \beta_{3R}$  (5.2b)

The magnetostriction may be calculated as:

$$\Sigma_{\theta,\phi} \left[ \frac{\left\{ \begin{array}{l} \frac{3}{2} \lambda_{100} (\alpha_1^2 \beta_{1R}^2 + \alpha_2^2 \beta_{2R}^2 + \alpha_3^2 \beta_{3R}^2 - 1/3) \\ + 3 \lambda_{111} (\alpha_1 \alpha_2 \beta_{1R} \beta_{2R} + \alpha_2 \alpha_3 \beta_{2R} \beta_{3R} + \alpha_3 \alpha_1 \beta_{3R} \beta_{1R}) \end{array} \right\} (d\theta d\phi |\sin \theta|) e^{\frac{-E(\theta,\phi)}{\Omega}}}{\Sigma_{\theta,\phi} \left[ (d\theta d\phi |\sin \theta|) e^{\frac{-E(\theta,\phi)}{\Omega}} \right]} \right] \quad (5.3)$$

The sensing response is calculated by evaluating the magnetic induction B:

$$B = \mu_0 (H_{\text{bias}} + M) \quad (5.4)$$

The total strain is evaluated as:

$$\varepsilon^{\text{total}} = \lambda + \frac{\sigma}{E_0} \quad (5.5)$$

where  $E_0$  is the nominal Young's modulus, obtained under high bias field, where the applied stress is insufficient to rotate the domains to an orientation perpendicular to the direction of applied field. Equation 5.5 evaluates the total strain response by adding the magnetostrictive strain to the elastic strain.

The sensitivity  $d_{33}^*$  was evaluated as

$$d_{33}^* = \frac{B_{i+1} - B_i}{\sigma_{i+1} - \sigma_i} \quad (5.6)$$

The Young's Modulus  $E_H$  was evaluated as

$$E_H = \frac{\sigma_{i+1} - \sigma_i}{\varepsilon_{i+1}^{\text{total}} - \varepsilon_i^{\text{total}}} \quad (5.7)$$

where  $i$  and  $i+1$  are indices to represent successive values of stress, strain and magnetic induction. In this numerical calculation, successive values of stress differed by 1 MPa.

### 5.1.2 Simulation of Behavior Along <100>

The simulation of sensing behavior was performed with the model parameters which were obtained from modeling the actuator behavior as described in Chapter 4.

The only extra parameter required was  $E_0$ , nominal Young's modulus, which was obtained from the experimental  $\varepsilon$ - $\sigma$  curve at 891 Oe bias field. The model parameters are:

$$K_1 = 1.75 \cdot 10^4 \text{ Jm}^{-3}, K_2 = 0 \cdot 10^4 \text{ Jm}^{-3},$$

$$(3/2)\lambda_{100} = 318 \cdot 10^{-6}, (3/2)\lambda_{111} = -20 \cdot 10^{-6},$$

$$M_S = 1.66/\mu_0 \text{ A/m}, \Omega = 707 \text{ Jm}^{-3}$$

$$\gamma_\sigma = 0.9, E_0 = 59 \text{ GPa}$$

**NOTE:** *Though experimental data for sensing was obtained for compressive stresses only, simulation of sensing behavior for both compressive and tensile loads is presented with an objective of developing a tool that can eventually predict sensing in structures that simultaneously experience both tensile and compressive loading, such as in bending and shear.*

Overall, there is an excellent correlation between the simulated and experimental  $\varepsilon$ - $\sigma$  and  $B$ - $\sigma$  characteristics, with less than 5% error at bias fields from 0 to 89 Oe as illustrated by Figure 5.1. However, there is a larger error in the simulation for bias fields of 111 Oe and higher, probably due to lower  $M_{\text{sat}}$  considered in the model, compared to experimental results. The correlation obtained between simulation, based on model parameters obtained from actuator data, and experimental results for sensing behavior proves that sensing behavior can be predicted from actuator characteristics very precisely using this model.

The simulation for the tensile stress in Figure 5.2 demonstrates that for the bias fields shown, the material has a useful sensitivity ( $d_{33}^* \approx 30 \text{ T/GPa}$ ) only for 22.3 Oe bias. This sensitivity is exhibited at very low tensile stress but drops rapidly to zero by about 10 MPa tension. Smaller bias fields may result in better sensitivity under tension. In the compressive stress regime, the material demonstrates a peak sensitivity of  $\sim 140 \text{ T/GPa}$  at the 22.3 Oe bias field which drops to  $\sim 75 \text{ T/GPa}$  at 223

Oe bias field. This demonstrates that at higher bias fields although the material is sensitive to a higher range of stress, its peak sensitivity decreases.

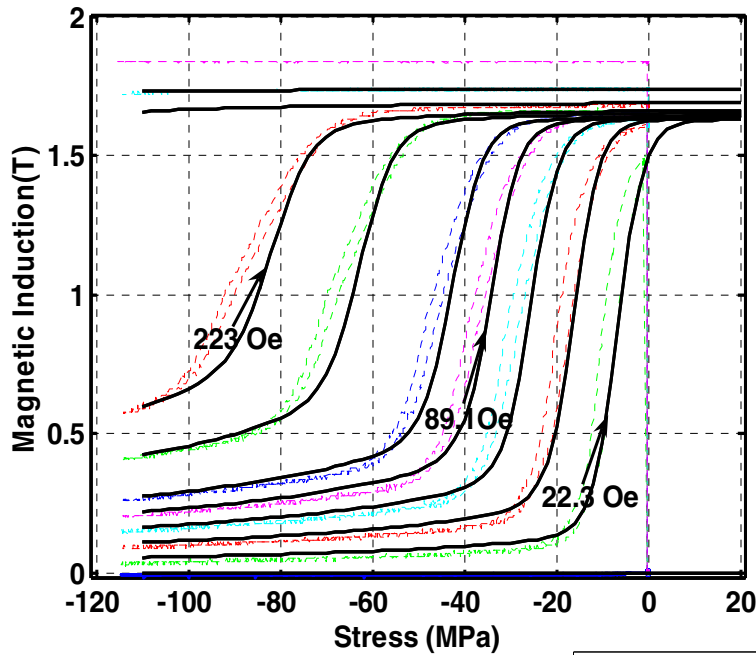
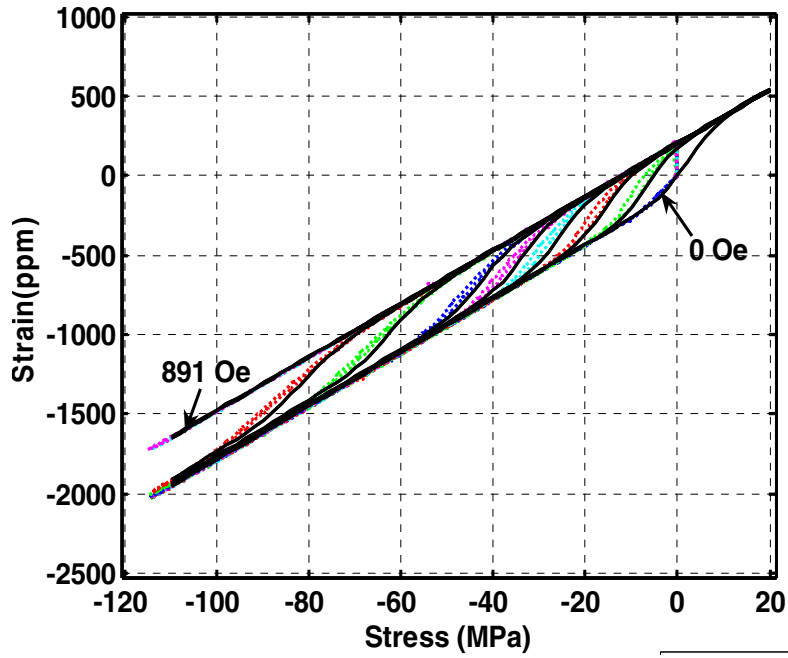


**Figure 5.1** Comparison between simulated (solid lines) and experimental (dashed lines)  $\epsilon$ - $\sigma$  (above) and  $B$ - $\sigma$  (below) characteristics of [100], furnace cooled, 19 at. % Ga single crystal FeGa alloy sample at bias fields: 0, 22.3, 44.6, 66.9, 89.1, 111, 167, 223, 446, 891 Oe.

The material shows a large softening due to  $\Delta E$  effect, with the Young's modulus,  $E^H$ , falling to  $\sim 25$  GPa, which is less than half the nominal Young's modulus, at bias fields upto 111 Oe (Figure 5.2).

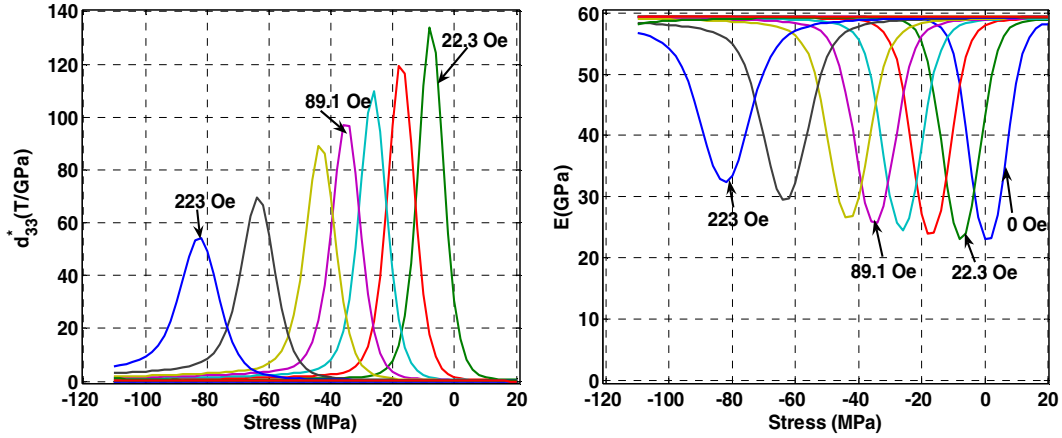


**Figure 5.2** Simulated  $d^*_{33-\sigma}$  (left) and  $E^H-\sigma$  (right) characteristics of [100], 19 at. % Ga single crystal FeGa alloy sample at bias fields: 0, 22.3, 44.6, 66.9, 89.1, 111, 167, 223, 446, 891 Oe.

### 5.1.3 Simulation of Behavior Along $\langle 110 \rangle$

The sensing behavior along the  $\langle 110 \rangle$  direction was also simulated with the model parameters obtained from actuator behavior as described in Chapter 4. The model parameters are:

$$K_1 = 2 \cdot 10^4 \text{ Jm}^{-3}, K_2 = -4 \cdot 10^4 \text{ Jm}^{-3},$$

$$(3/2)\lambda_{100} = 320 \cdot 10^{-6}, (3/2)\lambda_{111} = -10 \cdot 10^{-6},$$

$$M_S = 1.73/\mu_0 \text{ A/m},$$

$$\Omega = 650 \text{ Jm}^{-3}$$

$$\gamma_\sigma = 0.9, E_0 = 150 \text{ GPa}$$

$E_0$  was estimated as 150 GPa from Figure 5.3 (top),  $H_{\text{bias}}$  of 891 Oe.

Overall, only the trends in the experimental  $\epsilon$ - $\sigma$  and B- $\sigma$  characteristics are well predicted. However, the model is unable to simulate the sensing behavior in the  $\langle 110 \rangle$  direction very precisely. This is understandable, considering that the simulation of actuator characteristics did not match experiment very well.

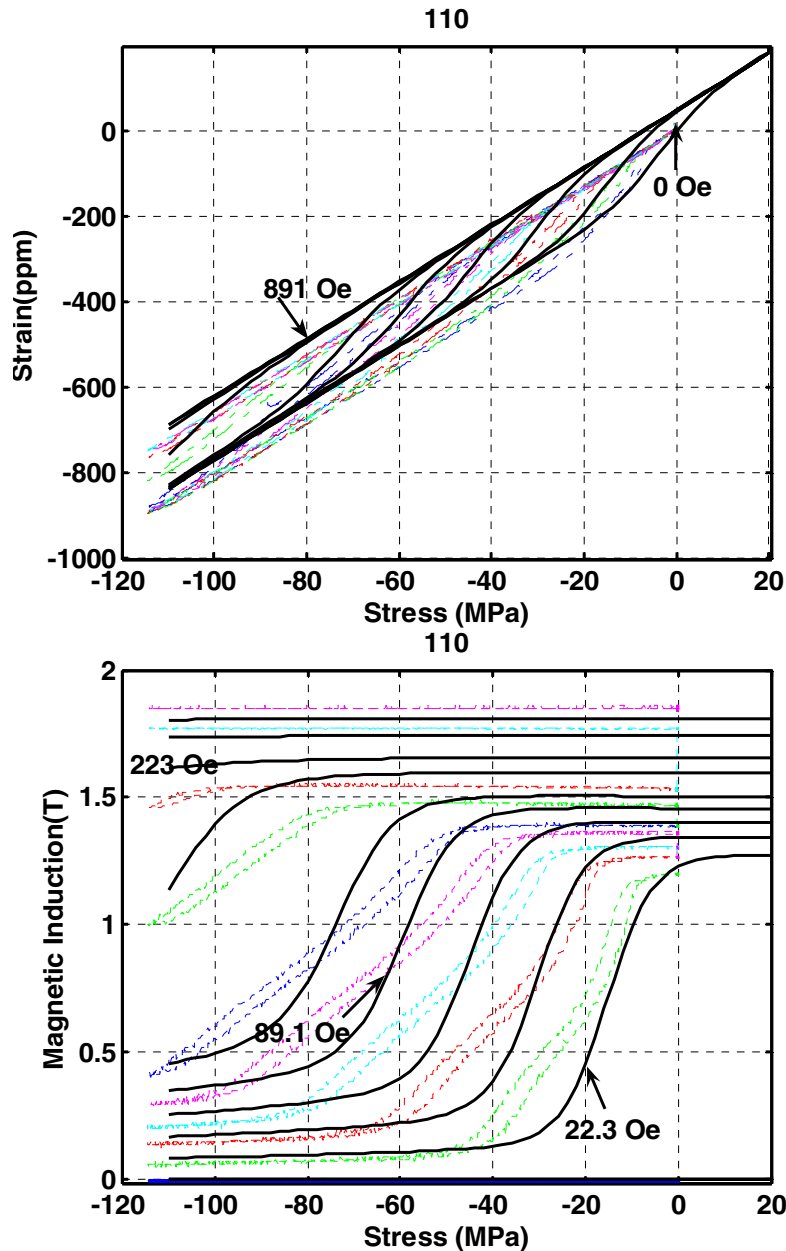


**Figure 5.3** Comparison between simulated (solid lines) and experimental (dashed lines)  $\epsilon$ - $\sigma$  (above) and B- $\sigma$  (below) characteristics of [110], furnace cooled, 18 at. % Ga single crystal FeGa alloy sample at bias fields: 0, 22.3, 44.6, 66.9, 89.1, 111, 167, 223, 446, 891 Oe.

The simulation for the tensile stress in Figure 5.4 demonstrates that even under a 22.3 Oe bias, the material has very low sensitivity ( $d_{33}^* \approx 10$  T/GPa) at very low tensile stress that drops rapidly to zero by about 20 MPa tension. In the compressive stress regime, the material demonstrates moderate peak sensitivity  $\sim 50$  T/GPa (as compared to 140 T/GPa in  $\langle 100 \rangle$  oriented 19 at. % Ga sample) under a 22.3 Oe bias field, which drops to  $\sim 20$  T/GPa at 111 Oe bias field. While the  $\langle 110 \rangle$  oriented 18 at. % Ga sample has lower sensitivity peaks, compared to the  $\langle 100 \rangle$  oriented 19 at. % Ga sample, it is sensitive over a larger range of stress.

Though the trends in the  $-\sigma$  are well predicted, the simulation curves show an offset from the experimental data. This is because the simulated magnetostrictive strain, at zero stress is much larger than the experimental value, as can be confirmed from Section 4.5.1 in Chapter 4. The simulated Young's modulus shows a large softening due to  $\Delta E$  effect, with the Young's modulus,  $E^H$ , falling to  $\sim 75$  GPa, which is less than half the nominal Young's modulus, at low bias fields (Figure 5.4). At higher bias fields, such as 111 Oe, the Young's modulus falls by about a third to  $\sim 100$  GPa.

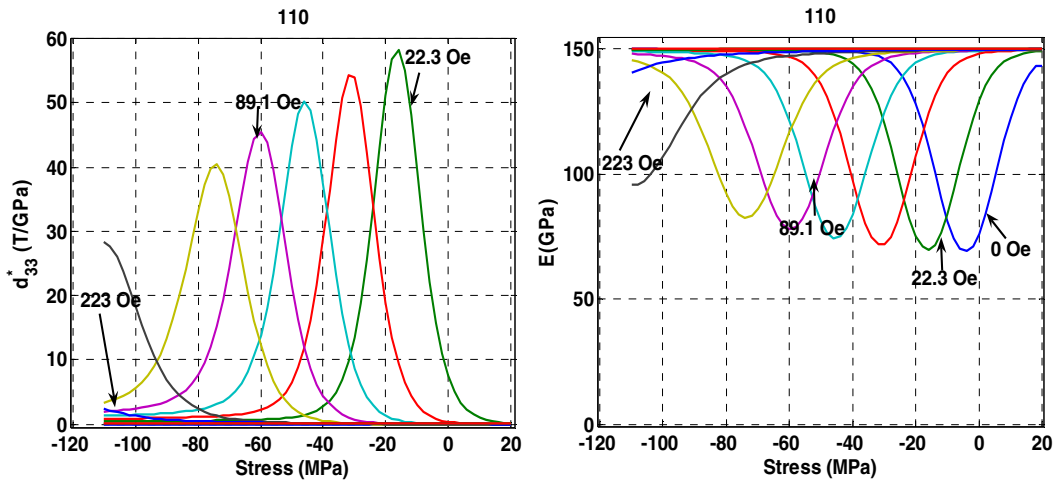


**Figure 5.4** Simulated  $d_{33}^*-\sigma$  (left) and  $E^H-\sigma$  (right) characteristics of  $[110]$ , 18 at. % Ga single crystal FeGa alloy sample at bias fields: 0, 22.3, 44.6, 66.9, 89.1, 111, 167, 223, 446, 891 Oe.

#### 5.1.4 Prediction of Behavior Along <111>

The sensing behavior along the <111> direction of a typical 18 at. % Ga, FeGa sample is shown in Figure 5.5. Inability to procure samples oriented in this direction leaves us with no experimental data to corroborate this prediction. Further, the simulation has been confined to B- $\sigma$  curves. The other model parameters employed were that of the 18 at. % Ga sample in the previous section.

The dominant feature of the predicted B- $\sigma$  curves is that the B does not vary significantly with applied stress. This is expected as the magnetoelastic energy, which is proportional to  $\lambda_{111} \cdot \sigma$ , is about 30 times smaller than that for comparable stress in the <100> direction as  $\lambda_{100} \approx 30 \lambda_{111}$  for the 18 at. % Ga sample [Kellogg2003b]. Hence, the model predicts that even compressive stresses upto 100 MPa are likely to be insufficient to change the orientation of the magnetization vector significantly. Furthermore,  $\lambda_{111}$ , being negative, an increase in compressive stress favors a rotation of magnetization parallel to the applied stress producing a small increase in magnetization and consequently induction with stress.

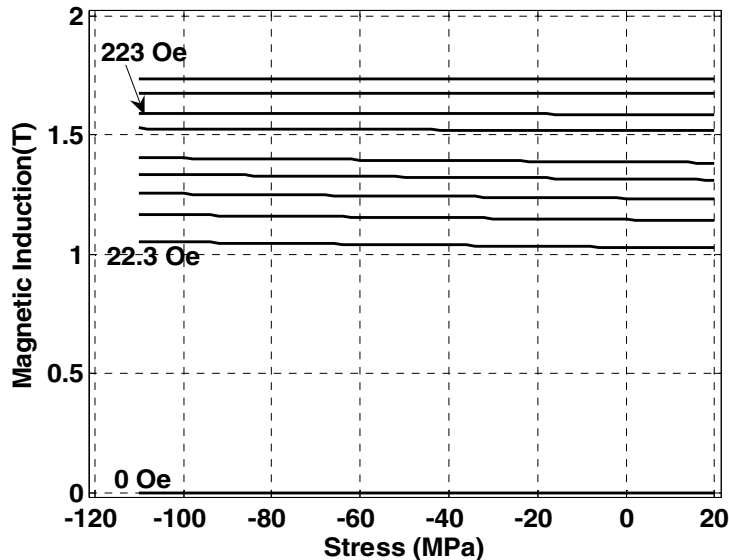


**Figure 5.5** Simulated characteristics of [111], furnace cooled, 18 at. % Ga single crystal FeGa alloy sample at bias fields: 0, 22.3, 44.6, 66.9, 89.1, 111, 167, 223, 446, 891 Oe.

### 5.1.5 Prediction of Behavior of 24.7 and 29 % at. % Ga <100> FeGa Samples

It was demonstrated in Section 5.1.4 that there is excellent correlation between simulated sensing behavior, based on model parameters obtained from actuator data, and experimental results for the <100> direction. Therefore, predictions of sensing behavior in the <100> direction for the 24.7 and 29 at. % Ga, FeGa samples were attempted using parameters obtained from simulation of actuator behavior in Chapter 4.

The parameters used for the simulation of the actuator behavior are:

#### ***24.7 at. % Ga <100> oriented, furnace cooled FeGa sample***

$$K_1 = -1.2 \cdot 10^3 \text{ Jm}^{-3}, K_2 = 0.5 \cdot 10^4 \text{ Jm}^{-3},$$

$$(3/2)\lambda_{100} = 310 \text{ ppm @ 0 to 30 MPa stress}$$

$$295, 280 \text{ and } 265 \text{ ppm @ 45, 60 and 80 MPa respectively}$$

*(approximately modeled as linearly decreasing at 1ppm/MPa from 30 to 75 MPa)*

$$(3/2)\lambda_{111} = 55 \cdot 10^{-6},$$

$$M_S = 1.32/\mu_0 \text{ A/m},$$

$$\Omega = 950 \text{ Jm}^{-3}, \gamma_\sigma = 1.05$$

#### ***29 at. % Ga <100> oriented, furnace cooled FeGa sample***

$$K_1 = -2 \cdot 10^3 \text{ Jm}^{-3}, K_2 = 0.5 \cdot 10^4 \text{ Jm}^{-3},$$

$$(3/2)\lambda_{100} = 300 \text{ ppm @ 0 to 30 MPa stress}$$

$$282.5 \text{ and } 265 \text{ @ 45 and 60 MPa respectively}$$

$$(3/2)\lambda_{111} = 55 \cdot 10^{-6},$$

$$M_S = 1.11/\mu_0 \text{ A/m},$$

$$\Omega = 1150 \text{ Jm}^{-3}, \gamma_\sigma = 1.00$$

*(Decrease in  $(3/2)\lambda_{100}$  with stress is not extrapolated beyond 80 MPa due to lack of experimental data)*

The peak sensitivity  $d_{33}^*$  predicted for the 24.7 and 29 at. % Ga samples is respectively  $\sim 40$  T/GPa and 25 T/GPa (Figure 5.6), which is much smaller than the  $d_{33}^* \sim 140$  T/GPa of the 19 at. % Ga sample. As in the case of actuation behavior, low magnetocrystalline anisotropy and higher  $\Omega$  in the higher Ga content samples (viz. 24.7 and 29 at. % Ga) could possibly result in a more gradual rotation in magnetization on application of stress, resulting in smaller sensitivities than the 19 at. % Ga sample.

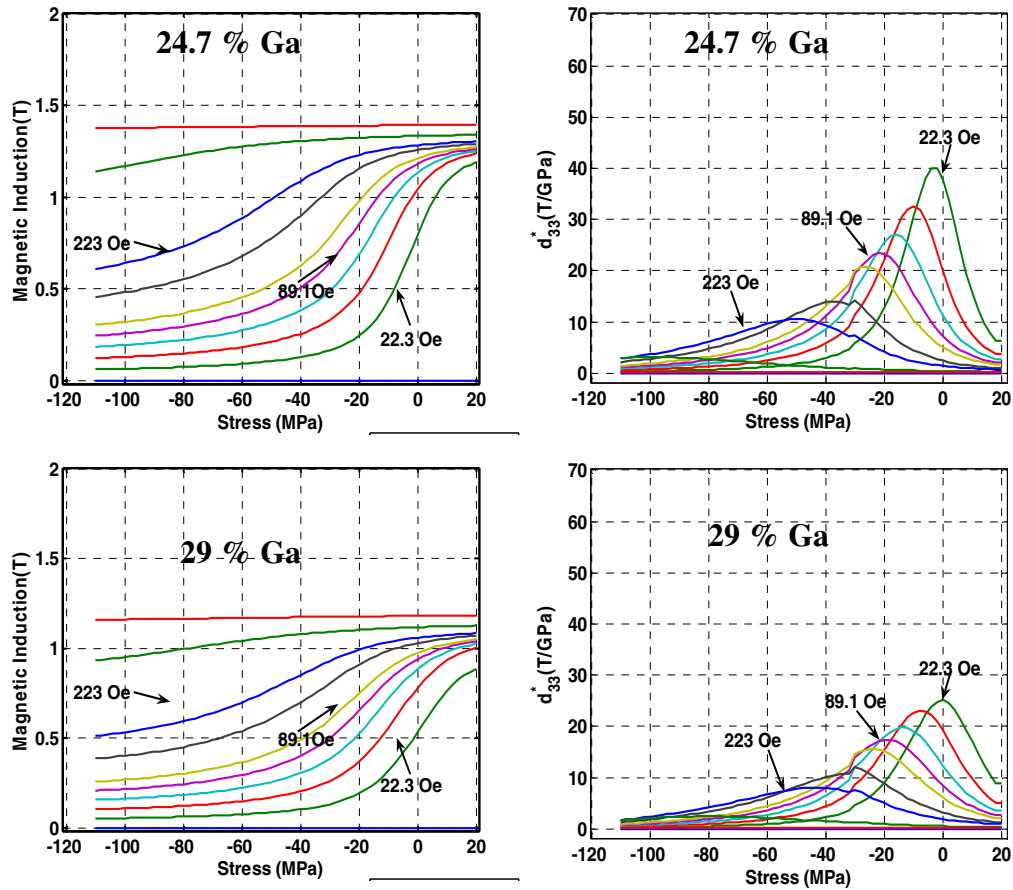


**Figure 5.6** Simulated  $B$ - $\sigma$  (left) and  $d_{33}^*$ - $\sigma$  (right) characteristics of [100], 24.7 (above) and 29 at. % Ga (below) single crystal FeGa alloy sample at bias fields: 0, 22.3, 44.6, 66.9, 89.1, 111, 167, 223, 446, 891 Oe.

## **5.2 Coupling Magnetic Energy-based Model with Lumped Parameter Model for Interaction with Magnetic Circuit**

Though the bias field for sensors or sensing characterization is typically provided by a permanent magnet or a constant DC current, the bias field magnitude in the magnetostrictive sample is expected to vary with stress induced changes in permeability. To accurately model this sensing performance, a model that accounts for both the interaction between the magnetic circuit and the magnetostrictive sample in the presence of changing stresses and the constitutive Villari-effect behavior of the material was developed. The model is used to simulate sensing characteristics and the variation in field through the sample due to its magnetic interaction with the circuit and compared with experimental sensing characterization data obtained by maintaining the drive current constant. This model may prove useful in designing non-contact sensors that are based on measuring field changes in magnetostrictive materials due to variation of their reluctance with stress.

### **5.2.1 Formulation of Coupled Model**

The first step towards developing a coupled model is to understand the magnetic interaction between the magnetostrictive sample and the magnetic circuit. This is achieved by treating the sample and circuit as “lumped parameters” with reluctance  $\mathfrak{R}_s$  and  $\mathfrak{R}_c$  respectively and developing an analogy with the electric circuit shown in Figure 5.7.

The total magnetomotive force (MMF) generated by the current through the drive coil is divided between the magnetic circuit and FeGa sample, analogous to a voltage divider circuit. Hence, the MMF drop across the sample is:

$$\text{MMF}_{\text{sample}} = \text{MMF}_{\text{generated}} \frac{\mathfrak{R}_s}{(\mathfrak{R}_s + \mathfrak{R}_c)} \quad (5.8)$$

where  $\text{MMF}_{\text{generated}}$  is given by:

$$\text{MMF}_{\text{generated}} = N \times I \quad (5.9)$$

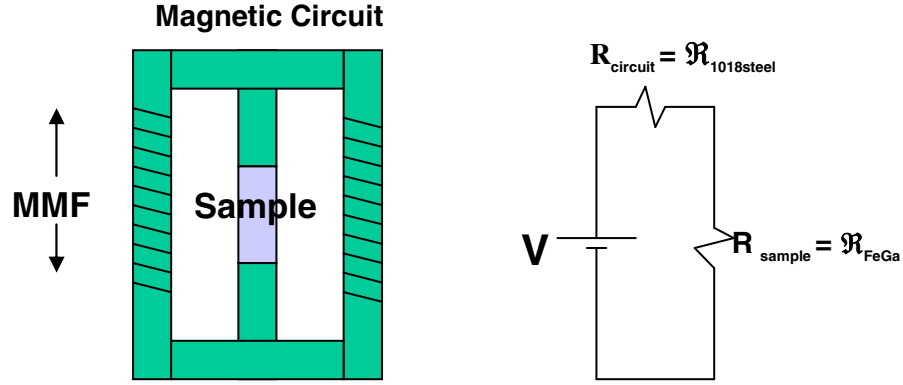


**Figure 5.7:** Magnetic Circuit Model.

<b>MMF</b> : Magnetomotive force	$\mathfrak{R}_{\text{circuit}}$ : Circuit Reluctance
$\mathbf{H}_{\text{sample}}$ : Magnetic field through sample	$\mathfrak{R}_{\text{sample}}$ : Fe-Ga Sample Reluctance
$L_{\text{sample}}$ : Length of the sample	$\mu_{\text{R}}$ : relative permeability
<b>A</b> : area of sample cross-section	$\mu_0$ : permeability of free space
$\mathbf{N} \times \mathbf{I}$ : product of number of turns and current	

Using Equations (5.8) and (5.9) the field in the sample can be expressed in terms of drive current and reluctances of the sample and circuit as:

$$H_{\text{sample}} = \frac{MMF_{\text{sample}}}{L_{\text{sample}}} = \frac{N \times I}{L_{\text{sample}}} \times \frac{\mathfrak{R}_{\text{sample}(\sigma=0)}}{\mathfrak{R}_{\text{sample}(\sigma=0)} + \mathfrak{R}_{\text{circuit}}} \quad (5.10)$$

Application of a compressive stress changes the magnetic state of the Galfenol sample, causing a change in  $\mathfrak{R}_{\text{sample}}$ , while  $\mathfrak{R}_{\text{circuit}}$  remains constant. This leads to a change in MMF drop across the sample and consequently the field through the sample which can be modeled as follows.

Initially, the  $H_{\text{sample}} = H_{\text{bias}}$  corresponding to a known value of drive current  $I$  is used to evaluate  $\mathfrak{R}_{\text{sample}} / \mathfrak{R}_{\text{sample} + \mathfrak{R}_{\text{circuit}}}$ , using Equation (5.10). It should be noted

that the actual values of these reluctances are not important. However, the ratio  $\mathfrak{R}_{\text{sample}} / (\mathfrak{R}_{\text{sample}} + \mathfrak{R}_{\text{circuit}})$  and its change with increase in stress determine the interaction between the sample and circuit. Therefore, we can arbitrarily assign  $\mathfrak{R}_{\text{sample}(\sigma=0)} + \mathfrak{R}_{\text{circuit}} = 1$  and directly obtain  $\mathfrak{R}_{\text{sample}(\sigma=0)}$  from Equation 5.10.

Corresponding to this no-stress initial condition we can evaluate  $\mu_{\text{Rsample}0}$ , initial permeability of the sample as

$$\mu_{\text{Rsample}(\sigma=0)} = B(0) / \mu_0 H_{\text{bias}} \quad (5.11)$$

At this stage the lumped parameter value for  $\mu_{\text{sample}}$  is coupled to the constitutive model for Villari-effect. On application of a stress  $\sigma$  and  $H_{\text{bias}}$ , the new magnetic induction  $B(\sigma)$  is evaluated by the constitutive model. The new value of relative permeability is:

$$\mu_{\text{Rsample}}(\sigma) = B(\sigma) / \mu_0 H \quad (5.12)$$

Since, the reluctance is inversely proportional to the relative permeability ( $\mathfrak{R} = L / \mu_0 \mu_{\text{R}} A$ ) we estimate the new sample reluctance as

$$\mathfrak{R}_{\text{sample}}(\sigma) = \left( \mu_{\text{Rsample}(\sigma=0)} / \mu_{\text{Rsample}}(\sigma) \right) \mathfrak{R}_{\text{sample}(\sigma=0)} \quad (5.13)$$

while the circuit reluctance remains constant at  $1 - \mathfrak{R}_{\text{sample}(\sigma=0)}$

Thus the new ratio of reluctance of sample to total reluctance can be evaluated and substituted in Equation (5.10) to obtain  $H_{\text{sample}}$ . This new value of  $H_{\text{sample}}$  can be substituted into the constitutive model to further refine  $B$  and reluctance and in turn  $H_{\text{sample}}$ . This process can be iterated until a satisfactory degree of convergence is achieved. Another technique is to stop at  $H_{\text{sample}}$  evaluated from the first iteration and substitute this value of  $H$  at the next (successive)  $\sigma$ . Either way, both variation of  $H_{\text{sample}}$  with  $\sigma$  and its impact on the  $\lambda$  and  $B$  can be calculated.

## 5.2.2 Comparison of Coupled Model with Experimental Data

The  $\sigma$  and  $B$ - $\sigma$  characteristics (Figure 5.8) were simulated by coupling the constitutive Villari-effect model discussed in Section 5.1.1 with a lumped parameter model for magnetic interaction between the magnetostrictive sample and the remaining magnetic circuit, as discussed in Section 5.2.1. The model parameters for the 19 at. % Ga, FeGa alloy were obtained from modeling the actuator characteristics as described in Chapter 4. Using these parameters, the coupled sensing model was used to predict the constant drive-current characteristics. There is good correlation between the simulated and experimental constant drive-current  $\sigma$  and  $B$ - $\sigma$  characteristics, as illustrated by Figure 5.8.

However, the error in prediction was  $\sim 15\%$  at some places and the large hysteresis in experimental data was not predicted by the model. This was probably caused by non-linear interaction between the magnetostrictive sample and magnetic circuit that could not be captured well by the linear lumped-parameter model.

Thus, the coupled constitutive model for Villari-effect and lumped parameter model for magnetic interaction captures the trends in increase in magnetic field in the sample with stress well, though actual predictions of  $B$ - $\sigma$  curves are not very accurate, possibly due to the reasons discussed above.

The simulated plots for the variation in the derivatives, viz. sensitivity  $d_{33}^*$  and Young's modulus  $E^H$  with stress are not likely to be very accurate. Nevertheless, the magnitude of the quantities predicted provide an understanding of the large difference in properties characterized when the magnetic interaction with the circuit is not accounted for or a controller is not employed to maintain the field through the sample constant.

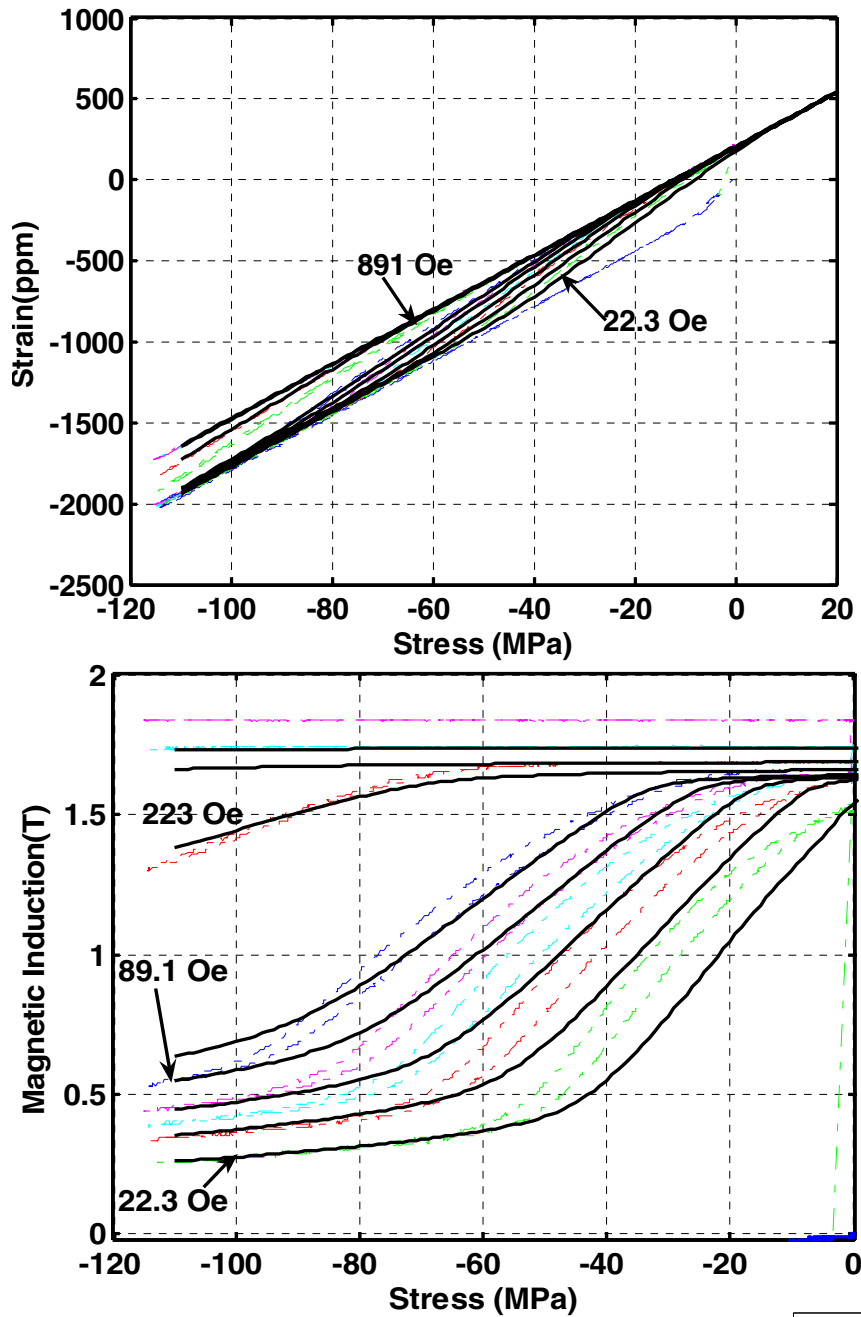


**Figure 5.8** Comparison between simulated (solid lines) and experimental (dashed lines)  $\epsilon$ - $\sigma$  (above) and  $B$ - $\sigma$  (below) characteristics of [100], furnace cooled, 19 at. % Ga single crystal FeGa alloy sample with constant drive current and magnetic interaction with circuit.

Initial bias fields: 0, 22.3, 44.6, 66.9, 89.1, 111, 223, 446 891 Oe.

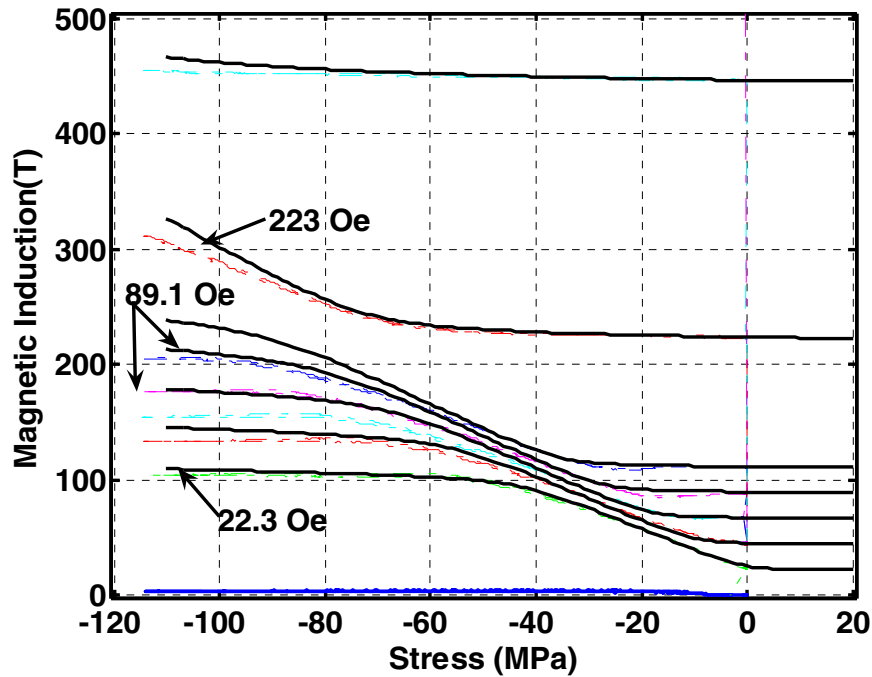


**Figure 5.9** Comparison between simulated (solid lines) and experimental (dashed lines) variation in magnetic field through a [100], furnace cooled, 19 at. % Ga single crystal FeGa alloy sample with constant drive current and magnetic interaction with circuit.

Initial bias fields: 0, 22.3, 44.6, 66.9, 89.1, 111, 223, 446 891 Oe.

The material demonstrates peak sensitivity  $\sim 25$  T/GPa when the field is allowed to vary, compared to  $\sim 140$  T/GPa at constant field. The material shows a smaller softening due to  $\Delta E$  effect, with the Young's modulus,  $E^H$ , falling to  $\sim 45$  GPa, which is about 25% drop in modulus, compared to the constant field case where the Young's modulus drops by about 50% (Figure 5.10).

This demonstrates that both the sensitivity  $d_{33}^*$  and drop in modulus are greatly suppressed due to the increase in field in the sample as a consequence of the

increase in sample reluctance with stress. Not accounting for this interaction can lead to an underestimation of the sensitivity and variation in the modulus of the material.

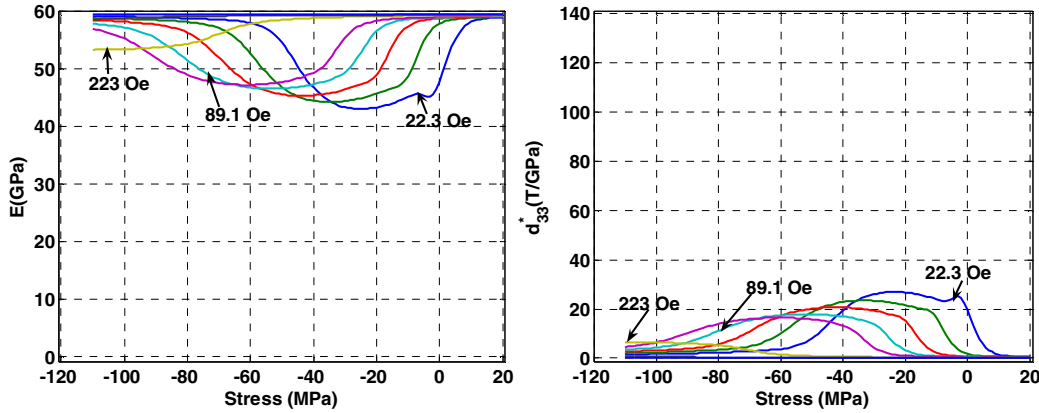


**Figure 5.10** Simulated  $E$ - $\sigma$  (left) and  $d_{33}^*$ - $\sigma$  (right) characteristics of [100], furnace cooled, 19 at. % Ga single crystal FeGa alloy sample with constant drive current and magnetic interaction with circuit.

Initial bias fields: 0, 22.3, 44.6, 66.9, 89.1, 111, 223, 446, 891 Oe.

### 5.3 Conclusions

1. The correlation obtained between sensor simulation, based on model parameters obtained from actuator data, and experimental results for sensing behavior proves that it can be predicted from actuator characteristics, very precisely using this model. This correlation is shown to be excellent in the  $\langle 100 \rangle$  oriented furnace cooled 19 at. % Ga sample and reasonably good in the case of  $\langle 110 \rangle$  oriented furnace cooled 18 at. % Ga sample.
2. In the compressive stress regime, the  $\langle 110 \rangle$  oriented 18 at. % Ga sample demonstrates moderate peak sensitivity  $\sim 50$  T/GPa as compared to a high peak sensitivity  $\sim 140$  T/GPa in  $\langle 100 \rangle$  oriented 19 at. % Ga sample. While the  $\langle 110 \rangle$  oriented 18 at. % Ga sample has lower sensitivity peaks, compared to the  $\langle 100 \rangle$  oriented 19 at. % Ga sample, it is sensitive over a larger range of stress.

3. The dominant feature of the simulated B- $\sigma$  curves in the <111> direction of a typical 18 at. % Ga furnace cooled sample is that the B does not vary significantly with applied stress. This is expected as the magnetoelastic energy, which is proportional to  $\lambda_{111}^* \sigma$ , is about 30 times smaller than that for comparable stress in the <100> direction as  $\lambda_{100} \approx 30 \lambda_{111}$ .
4. Peak sensitivity  $d_{33}^*$  of the 24.7 and 29 at. % Ga samples is respectively  $\sim 40$  T/GPa and 25 T/GPa, which is much smaller than the  $d_{33}^* \approx 140$  T/GPa of the 19 at. % Ga sample. The low magnetocrystalline anisotropy and higher  $\lambda_{111}$  in the higher Ga content samples could possibly result in a more gradual rotation in magnetization on application of stress, resulting in smaller sensitivities than the 19 at. % Ga sample.
5. A coupled model that accounts for both the interaction between the magnetic circuit and the magnetostrictive sample in the presence of changing stresses and the constitutive Villari-effect behavior of the material was developed. This model simulation was validated against constant drive-current (varying field) experimental data for the <100> oriented 19 at. % Ga sample and found to show good correlation.
6. It was demonstrated that sensitivity  $d_{33}^*$  and drop in modulus are greatly suppressed due to the increase in field in the sample due to increase in sample reluctance with stress.
7. Predictions of material behavior in tension proved that the material is not well-suited as a sensor under tension in its present state.

## **Chapter 6: Characterization and Analysis of Actuation and Sensing Behavior of Polycrystals**

While study of single crystal FeGa alloys, discussed in the previous chapters, is a good starting point for characterizing and modeling Galfenol behavior, commercial actuators and sensors are more likely to be made of polycrystalline FeGa. Textured polycrystalline FeGa alloys can be produced by zone refining (FSZM) at rates  $\sim 350$  mm/hour [Etrema Products Inc.] that are two orders of magnitude faster than single crystal growth rates ( $\sim 1$  mm/hour) and thus can more readily be made commercially viable, provided the actuation and sensing properties of polycrystals are not significantly inferior to that of single-crystals. This motivates the material characterization and development of a model to predict the actuation and sensing behavior of polycrystalline FeGa alloys, which is the emphasis of this chapter.

This chapter starts with a brief discussion of previous work in characterization of polycrystalline FeGa alloys, modeling schemes used for prediction of magnetomechanical behavior of polycrystals and the contributions of this chapter. This is followed by sections on experimental characterization, analysis of cross-section texture of the sample characterized, model formulation, and comparison of the model predictions with experimental behavior.

The aim of this chapter is to attempt to predict the polycrystalline behavior from known single-crystal behavior and cross-section texture. A detailed characterization of *production grade polycrystalline* sample is performed and its magnetomechanical behavior is simulated, using the model discussed in this chapter, from the sample's cross-section texture. Thereafter, an attempt is made to explain the variability in behavior between polycrystals, in terms of the variation in cross-section texture.

*Previous work and research direction of this chapter*

Early work on characterization of actuation behavior of FeGa alloys focused on understanding the effect of Ga content on the saturation magnetostriction in single-crystals [**Clark 2001**] and characterization of single-crystal actuator behavior ( $\lambda$ -H and B-H curves) at various pre-stresses [**Clark 2001, Kellogg 2005**]. This work was augmented by the characterization of the behavior of polycrystals obtained by directional solidification, extrusion, extrusion and annealing [**Kellogg 2005**] as well as those produced using zone refining [**Summers 2004**]. However, characterization of sensing behavior of polycrystalline FeGa has not been reported to date. This chapter presents characterization results of *both* actuation and sensing behavior of a typical 18.4 at. % Ga, production grade polycrystal (produced by zone refining at a rate of ~ 350 mm/hour by Etrema Products Inc.). Since the behavior of the polycrystalline sample is dependent on its texture, a modeling tool that can predict the behavior of the polycrystalline rod from the texture of its cross-section is developed and validated in this chapter.

Previous work in modeling magnetostrictive behavior [**Buiron2001, Callen1965, Decoquer2002, Ginzburg1977, Kellogg2002b, and Park2002**] has addressed various aspects of this problem.

Broadly speaking, one set of researchers [**Callen1965, Decoquer2002, Kellogg2002b**] attempt to predict the saturation magnetostriction of polycrystalline ferromagnetic materials with cubic structure given the  $\lambda_{100}$ ,  $\lambda_{111}$  and texture.

Callen [**Callen1965**] compares analytical techniques used to estimate the magnetostriction of random polycrystalline materials. These include:

1. Akulov approximation: assumption that all grains see a constant stress
2. Voigt approximation: assumption that all grains are in state of constant strain
3. Vladimirsky approximation: the local stress at each grain is estimated by treating it as a spherical crystal surrounded by an isotropic matrix whose properties represent that of the polycrystalline aggregate.

The first two methods, viz. Akulov and Voigt approximations, represent the two extreme mechanical constraints and hence neither of them are physically reasonable [Kellogg2003b]. The Vladimirsky approach was found to estimate the saturation magnetostriction of Fe and other cubic systems better than the other two approaches [Callen1965].

A more sophisticated approach has been developed by Kellogg [Kellogg2002b] and Decoquer [Decoquer2002] using finite element method (FEM) to account for elastic interaction between grains in calculating the saturation magnetization of a sample given its texture. These could prove to be useful tools in predicting the saturation magnetostriction of polycrystals given their texture. However, none of these models simulate the actuation ( $\lambda$ -H and B-H curves) or the sensing (B- $\sigma$  and C- $\sigma$  curves) behavior, which is critical for design and simulation of device performance in engineering applications.

The modeling of actuation characteristics has been addressed by another set of researchers [Ginzburg1977, Buiron2001, Park2002]. Ginzburg [Ginzburg1977] derived a polycrystalline model by extending a simplified model of two adjacent domains accounting for both boundary motion and domain rotation under low magnetic field. Though this model handles a wide range of tensile and compressive stresses, this model is applicable only at low values of applied magnetic field.

Buiron *et al.* [Buiron2001] employs a formulation for the problem wherein the magnetization vectors in a grain are allowed to lie only in the easy directions. For example in Fe this would constitute the six  $\langle 100 \rangle$  directions. For a given field and stress, the volume fractions of moments in each of the easy directions in that grain would be chosen so as to minimize the total energy of that grain. The polycrystalline response is then calculated by accounting for the interactions between the grains using a FEM scheme.

Park *et al.* [Park2002] has shown that the actuation behavior of polycrystalline materials can be modeled as a weighted sum, determined from the sample's cross-section texture, of the behavior along various crystallographic directions. However, to model the behavior along the individual crystallographic directions an existing comprehensive 3-D model [Armstrong 1997] was employed. Park *et al.* [Park2002] have extended this model to predict the  $\lambda$ -H and B-H curves of polycrystals with known texture and validated it with experimental results from Terfenol-D samples. However, this model does not account for the elastic-interaction between various differently oriented grains.

The polycrystal model discussed in this chapter employs the formulation of Park *et al.* [Park2002] but includes a larger set of crystallographic directions, viz. [100], [110], [111], [210], [211], [310] and [311] to predict the polycrystalline behavior and a scheme to account for the longitudinal variation in cross-section texture. Furthermore, this model is formulated to predict *both* the polycrystal actuator as well as sensor behavior for a specimen whose cross-section texture was determined by electron back-scatter diffraction (EBSD) at three longitudinal stations. The model prediction is benchmarked against experimental data. The variation in permeability, piezo-magnetic coefficients ( $d_{33}$  and  $d_{33}^*$ ) and Young's modulus with stress and field were also estimated by the model.

### **6.1 Experimental Characterization**

The quasi-static actuation behavior characterized from the  $\lambda$ -H and B-H curves and sensor behavior characterized from the  $\epsilon$ - $\sigma$  and B- $\sigma$  curves of production grade polycrystals are presented in this section. The following subsections discuss the test set-up and procedure, variation in experimental data between three polycrystals manufactured by the same process and summary of actuation and sensing behavior of one of these samples (whose cross-section texture was determined by EBSD after the characterization).

### 6.1.1 Test Set-up and Procedure

#### *Actuator behavior*

The quasistatic actuation behavior  $\lambda$ (magnetostriction)-H and B-H characteristics of a 5.08 cm (2 inch) long and 0.635 cm (¼ inch) diameter production grade polycrystalline sample of composition Fe<sub>81.6</sub>Ga<sub>18.4</sub> (supplied by Etrema Products Inc.), subjected to compressive stresses from 0 to 80 MPa have been experimentally investigated in this study. The experimental methodology involved applying a magnetic field by passing a current at a frequency of 0.01 Hz, to ensure quasistatic test-rate; through a 1200 turn solenoid in a water-cooled transducer (maintains constant temperature of 23°C). A constant compressive stress state was maintained in the sample by hanging dead weights as illustrated by Figure 3.2 (left) in Chapter 3. To ensure consistency of results the sample was demagnetized before testing at each pre-stress with a 1 Hz sinusoidal magnetic field, with initial amplitude of about 1400 Oe, decaying geometrically by 5% until it decreased to 0.02% of the initial amplitude.

#### *Sensing behavior*

The water-cooled transducer was mounted on a Universal axial force testing machine to determine the quasistatic  $\epsilon$ - $\sigma$  and B- $\sigma$  characteristics as illustrated in Figure 3.2 (right), Chapter 3. The sample was demagnetized using zero-load conditions with the same procedure used for actuator characterization. The required DC magnetic field at zero-stress was developed by gradually increasing the drive current. The specimen was then loaded to a compressive stress of 110 MPa and then unloaded to zero, at a rate of 2 MPa/s while keeping the magnetic field constant. Typically, application of stress changes the sample reluctance resulting in a change in the field through the sample due to magnetic interaction between the circuit and sample. However, a feed-back loop was introduced to vary the drive current to compensate for this effect and keep the field through the sample (monitored from the hall sensor output) constant as described in Chapter 3, Section 3.3.1.

### 6.1.2 Manufacturing Process and Variability in Actuator Behavior:

The 18.4 at. % Ga production-grade polycrystalline samples were produced by Etrema Products Inc. using a free stand zone melt (FSZM) manufacturing processes with a zoning rate of 350 mm/hour. Since, the variability in magnetomechanical properties in different stocks of samples may be an issue in characterizing polycrystalline materials, seven samples, each 5.08 cm (2 inch) long and 0.635cm (¼ inch) in diameter were supplied by Etrema Products Inc. Four of the seven samples were extracted from various locations along one FSZM polycrystal while the other three were extracted from various locations along the other FSZM polycrystal. For characterization purposes, three samples were chosen: two from the stock of four samples and other one from the stock of three samples. The actuation characteristics of these three samples, shown in Figure 6.1, are analyzed for the variation in properties.

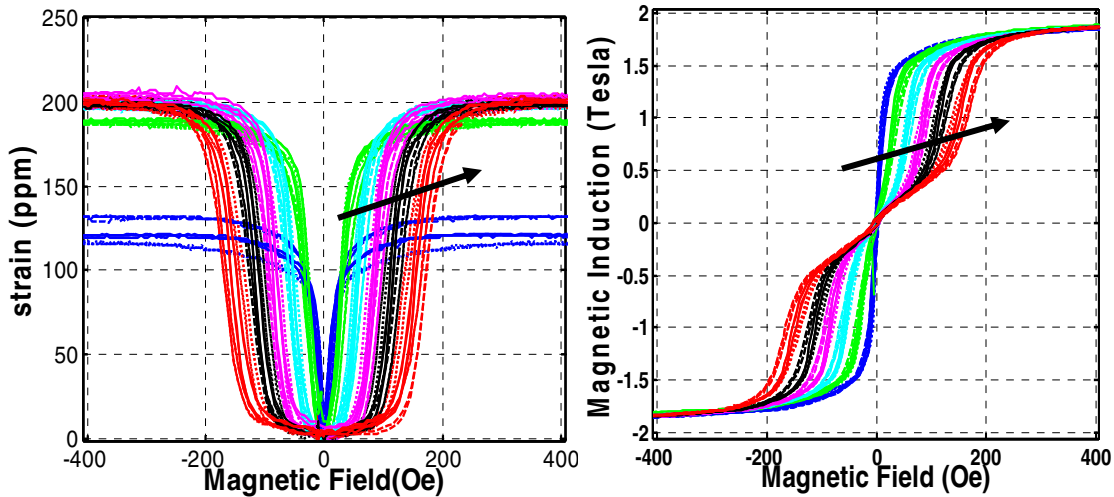


**Figure 6.1** Actuation  $\lambda$ -H (left) and B-H (right) characteristics of three different production grade sample at 0, 15, 30, 45, 60, 80 MPa compressive pre-stresses.

(Arrow indicates increasing stress.)

The saturation magnetostriction of the three samples was found to be in the range of  $200 \pm 5$  ppm (a variation of  $\pm 2.5\%$ ) and the saturation material induction ( $\mu_0 M_{\text{sat}}$ ) in the range of  $1.85 \pm 0.025$  Tesla (a variation of 1.3%). Both these variations are within the limits of experimental error and it may hence be concluded that the  $\lambda_{\text{sat}}$

and  $M_{\text{sat}}$  of all three samples are identical within the range of experimental error discussed in Chapter 2 and 3.

However, in the burst region, characterized by a large increase in magnetostriction and magnetic induction with small increases in field (i.e. regions of large permeability and  $d_{33}$ ), there is a significant variation in characteristics of the sample. For example, one of the largest variations in behavior can be observed at a field of  $\sim 120$  Oe and 60 MPa pre-stress, wherein the magnetostriction is in the range of  $120 \pm 30$  ppm (a variation of  $\pm 25\%$ ) and magnetic induction in the three samples is  $1.1 \pm 0.2$  Tesla (a variation of  $\pm 18\%$ ), excluding the effect of hysteresis. Another way of characterizing this variability is studying the slope of the  $\lambda$ -H curves. For example, with a pre-stress of 60 MPa and a field of  $\sim 150$  Oe the average  $d_{33}$  (variation in  $\lambda$  with H) varies from  $\sim 1.5$  to 3 ppm/Oe between the three samples.

In conclusion, even though the saturation magnetostriction and magnetization of the samples are similar, there is a large variation in the field at which the burst region occurs as well as the permeability (slope in B-H curve) of the burst region, possibly due to variation in texture between the samples. The effect of variation in texture on this variation in the magnetomechanical behavior is studied in detail in section 6.6 with the help of the energy-based model for polycrystals.

### 6.1.3 Final Actuator and Sensor Data and Discussion

Mechanical and magnetic responses to major loop magnetic field tests for one of the rods are shown in Figure 6.2. The maximum magnetostriction ( $\lambda_{\text{sat}}$ ) of the production grade sample is about 200 ppm. Considering that typical [100] and [111] oriented  $\sim 18$  at. % Ga single crystals show saturation magnetostriction around 310 ppm and -20 ppm respectively [Clark2000, Kellogg2003b], a polycrystalline material comprised of a large volume fractions of grains which are close to the [100] directions and a smaller but significant volume fractions which are close to the [110] and [111] is likely to exhibit a lower saturation magnetostriction, such as  $\sim 200$  ppm.

The trends shown by the  $\lambda$ -H and B-H curves of the 18.4 at. % Ga polycrystal are similar to those shown by the 19 at. % Ga single-crystals discussed in Chapter 3. However, the polycrystal characteristics are more rounded than the [100] single crystal characteristics. This is expected, as grains with different orientations are likely to undergo rotation/flipping at different fields suggesting a more gradual change in macroscopic characteristics with increasing field.

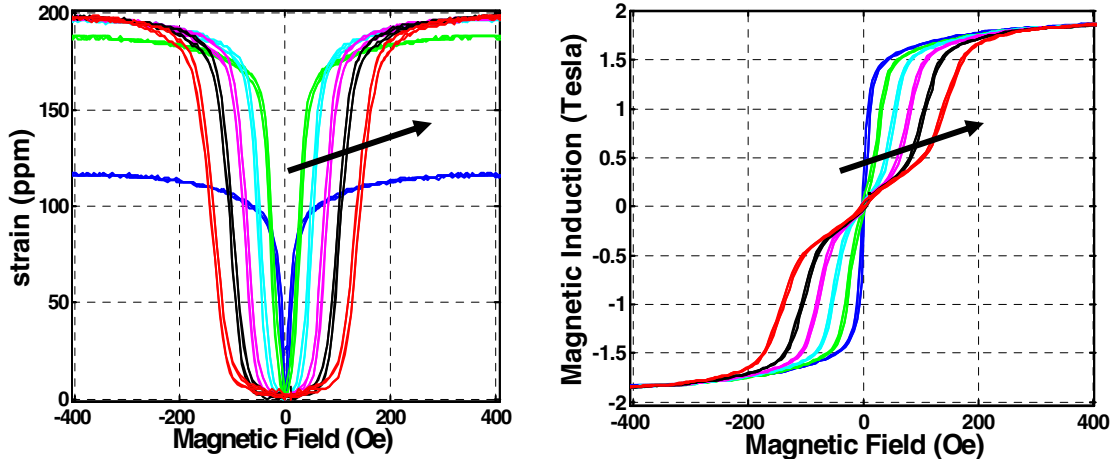


**Figure 6.2:** Actuation  $\lambda$ -H (left) and B-H (right) characteristics of 18.4 at. % Ga production grade FeGa sample at 0, 15, 30, 45, 60, 80 MPa compressive pre-stresses. *NOTE: Throughout this chapter arrows indicate increasing compressive pre-stress for actuator characteristics and increasing bias field for sensor characteristics.*

The sensing behavior of the polycrystalline sample is shown in Figure 6.3. The variation of strain with stress is not linear at most bias fields, as in the case of single crystals. At bias fields of 446 Oe and above, the stress-strain characteristics are linear, from which the nominal Young's modulus of the material under compression is calculated to be about 101 GPa. Single crystal FeGa sample with 18 at. % Ga can be expected to have Young's modulus of ~60, 150 and 300 GPa respectively in the [100], [110] and [111] directions [Kellogg2003b]. This is a possible indication that the polycrystal contains large volume fraction of grains oriented close to [100] direction, or directions close to [100] such as the [310] directions. The presence of relatively small (yet significant) percentage of volume fractions of grains close to [110] and [111] or directions between them such as [211] are likely to have

contributed to a high Young's modulus (and lower magnetostriction) of this polycrystalline sample, than observed in a pure [100] single crystal.

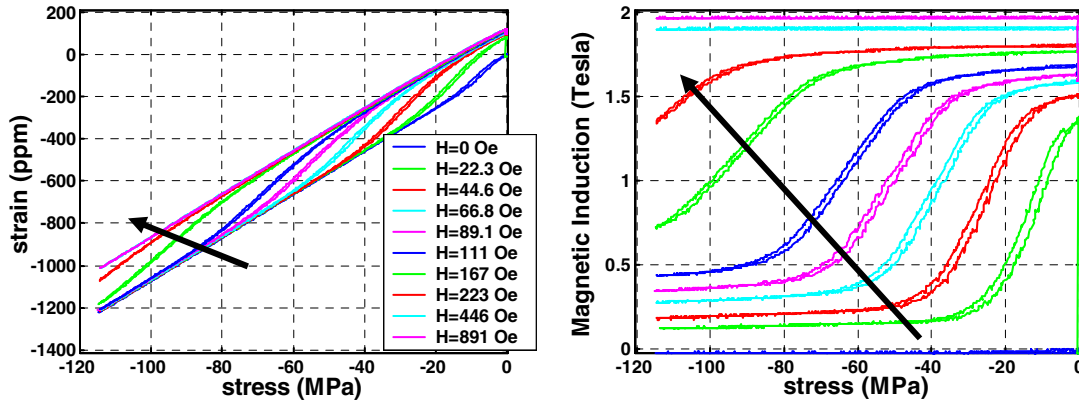


**Figure 6.3:** Sensing  $\epsilon$ - $\sigma$  (left) and  $B$ - $\sigma$  (right) characteristics of 18.4 at. % Ga production grade FeGa sample at 0, 22, 44, 66, 89, 111, 167, 223, 446, 891 Oe bias fields.

In Figure 6.4, one can observe the similarity in trends and difference in sensitivity of  $B$ - $\sigma$  curves of an 18.4 at. % Ga polycrystal and a [100], 19 at. % Ga single crystal sample. For this small a difference in Ga content, it is expected that the texture effects are the dominant cause of the difference in characteristics. As expected the polycrystal is less sensitive, i.e. the variation of magnetic induction with applied stress is smaller than for the single-crystal. This is possibly due to the presence of

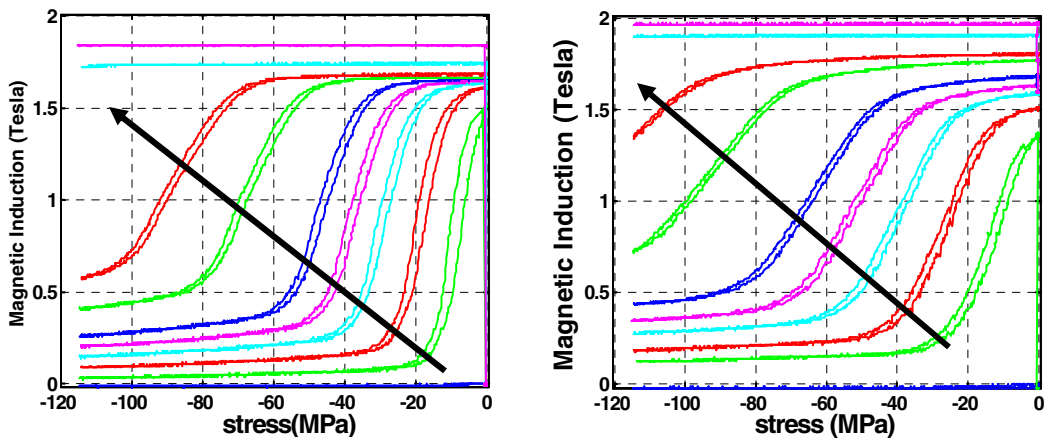


**Figure 6.4** Sensing characteristics of 19 at. % Ga single crystal (left) and 18.4 at. % Ga production grade sample (right) at 0, 22, 44, 66, 89, 111, 167, 223, 446, 891 Oe bias fields.

grains oriented closer to directions other than  $\langle 100 \rangle$ , which contribute to the reduced sensitivity relative to that of the [100] oriented single-crystal. The extent to which the presence of grains oriented in directions other than the  $\langle 100 \rangle$  directions diminish the sensing (and actuator) properties is discussed in detail in the Section 6.3.

## **6.2 Texture Analysis**

The cross-section texture at three longitudinal stations of the sample that was characterized in Section 6.1.3 was determined using Electron Back Scattering Diffraction (EBSD). The grains boundaries in each cross-section, the color-coded orientation of each grain as well as the location of the three longitudinal stations are illustrated in Figure 6.5. Most grains have a maximum linear dimension between 250  $\mu\text{m}$  and 2 mm. The table on the left indicates the volume fraction (determined by the areas) of grains that lie within  $10^\circ$  of the [100], [110], [111], [210], [211], [310] and [311] orientations. It is observed that the sum of the volume fractions in all these directions add up to greater than 100%. This is due to the overlap caused by the possibility of the same grain being counted in two directions: for example, the [311] and [211] directions are within  $10^\circ$  apart and a grain oriented say,  $5^\circ$  away from each of these directions would be counted in both directions. As a first approximation, for modeling purposes, the volume fractions in all the directions are normalized by dividing them by the sum of these volume fractions so that they add to 100%.

### *Longitudinal variation in texture*

There is large longitudinal variation in cross-section texture which may cause differences in properties along the length of the sample. For example the normalized percentage of grains (area) oriented within  $10^\circ$  of the [100] direction is about 40% at quarter length from the top, 6.5% in the middle and 16% at three-quarters of the length from the top to bottom.

Fiber orientation fraction

100	43.1%
110	1.4%
111	0.0%
210	6.4%
211	10.9%
310	28.7%
311	16.6%

107.1%

Fiber orientation fraction

100	7.3%
110	0.1%
111	0.0%
210	31.3%
211	0.2%
310	49.9%
311	23.8%

112.5%

Fiber orientation fraction

100	18.2%
110	1.2%
111	0.0%
210	20.5%
211	3.2%
310	58.8%
311	11.5%

113.5%

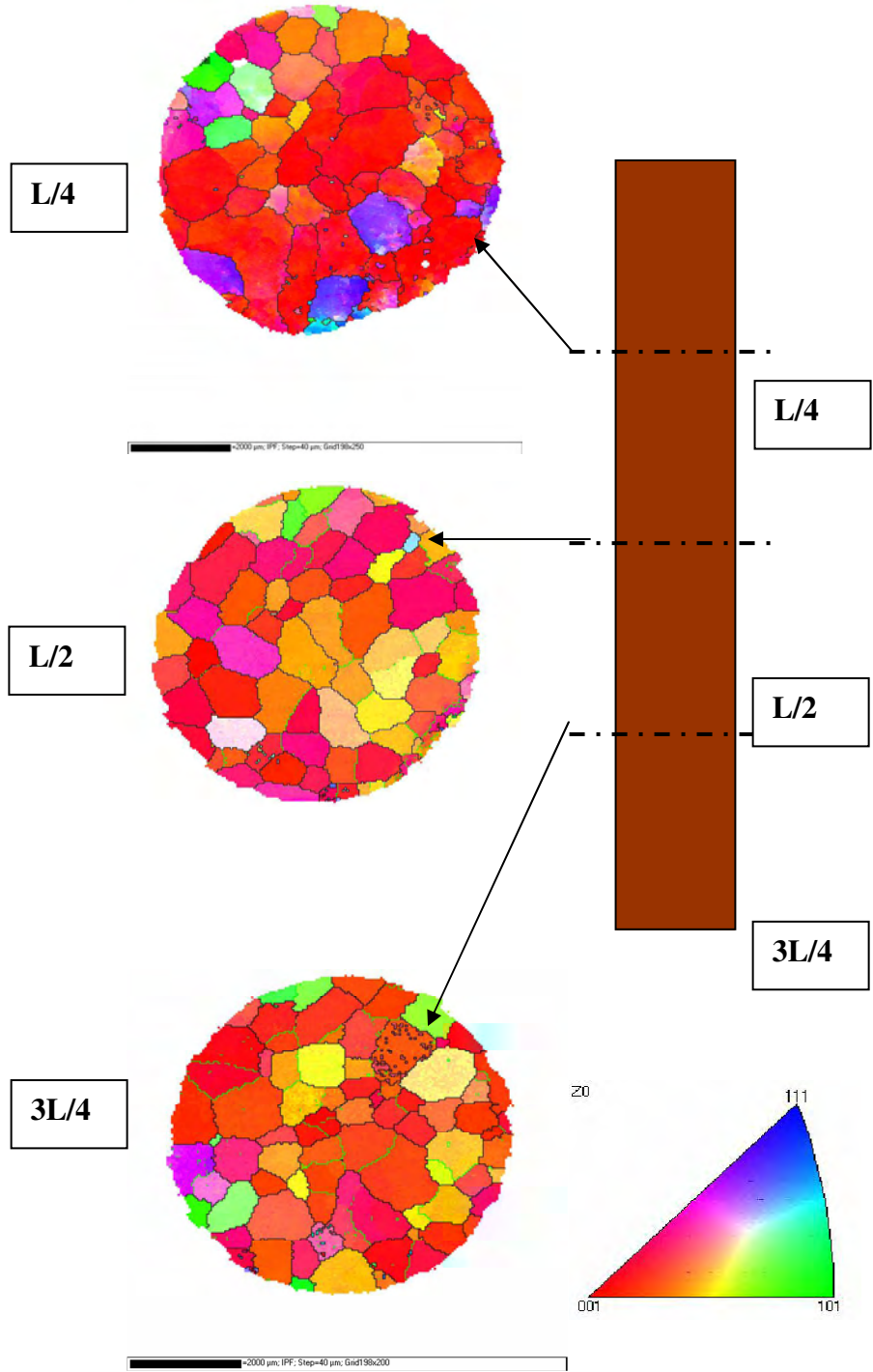


**Figure 6.5** Cross-section texture of production grade sample.  
 [Sample and EBSD analysis provided by Etrema Products Inc.]

### *Grouping of various crystallographic directions*

Based on the observation that [100] direction produces the largest magnetostriction for actuation and has largest sensitivity for sensing, we group the other directions on the basis of their angular proximity to the [100] direction. With just 3 such groups, it is much easier to interpret the texture information.

The angle subtended by the [310], [210], [311], [211], [110] and [111] directions with the [100] directions are respectively  $18.4^\circ$ ,  $26.6^\circ$ ,  $25.2^\circ$ ,  $35.3^\circ$ ,  $45.0^\circ$  and  $54.7^\circ$  and the cosines of these angles are approximately 0.95, 0.9, 0.9, 0.82, 0.71 and 0.58 and squares of the cosines 0.9, 0.81, 0.81, 0.67, 0.50 and 0.34. Based on the values of the squares of the cosines (which affects the magnetostriction as explained in Chapter 4) we classify [100] and [310] as well-oriented or desirable directions, [210] and [311] as intermediate directions and [211], [110] and [111] as undesirable directions. Based on this classification, it may be stated that at the L/4 cross-section, i.e. quarter distance from the top, approximately 70% of the grains are well-oriented, 20% intermediate and the remaining 10% are undesirably oriented. At L/2, approximately 50% are well-oriented and 50% intermediate, with almost no undesirably oriented grains, whereas at 3L/4, 68% are well-oriented, 28% intermediate and about 4% undesirable. In general this demonstrates that the sample is well oriented even though the longitudinal variation in texture (even with grouping) is significant.

### **6.3 Simple Rule of Mixture Model for Polycrystals**

The actuation and sensing behavior of the polycrystalline sample is simulated from a volume fraction weighted summation of the behavior of single crystal FeGa alloy with similar Ga-content along various crystallographic orientations. The texture information in Figure 6.5 is used to estimate the volume fractions (proportional to the area) of grains close to the  $\langle 100 \rangle$ ,  $\langle 110 \rangle$ ,  $\langle 210 \rangle$ ,  $\langle 310 \rangle$ ,  $\langle 111 \rangle$ ,  $\langle 211 \rangle$  and  $\langle 311 \rangle$  directions by normalizing the data as proposed in Section 6.2.

### *Calculation of polycrystalline response*

The model assumes that each grain sees the same value of applied macroscopic magnetic field or stress. The magnetostrictive ( $\lambda$ ) and magnetic ( $M$ ) response of a grain oriented in the [100], [110], [210], [310], [111], [211] and [311] to this field and stress is simulated using the single crystal model described in Chapter 4 and Chapter 5. Suppose, the normalized volume fractions of grains oriented within  $10^\circ$  of the [100], [110], [210], [310], [111], [211] and [311] directions are respectively  $x_{100}$ ,  $x_{110}$ ,  $x_{210}$ ,  $x_{310}$ ,  $x_{111}$ ,  $x_{211}$ ,  $x_{311}$ , then the polycrystalline response can be calculated as:

$$M_{poly} = x_{100} * M_{100} + x_{110} * M_{110} + x_{210} * M_{210} + x_{310} * M_{310} + x_{111} * M_{111} + x_{211} * M_{211} + x_{311} * M_{311} \quad (6.1)$$

$$\lambda_{poly} = x_{100} * \lambda_{100} + x_{110} * \lambda_{110} + x_{210} * \lambda_{210} + x_{310} * \lambda_{310} + x_{111} * \lambda_{111} + x_{211} * \lambda_{211} + x_{311} * \lambda_{311} \quad (6.2)$$

This technique may be used to calculate and predict the  $\lambda$ -H, B-H and B- $\sigma$  curves. In order to predict the  $\epsilon$ - $\sigma$  characteristics, the nominal Young's modulus was estimated from experimental data as  $E_0$  and the net strain response was estimated as:

$$\epsilon_{poly} = \lambda_{poly} + \sigma / E_{poly} \quad (6.3)$$

The numerical derivatives (slopes) of the  $\lambda$ -H, B-H, B- $\sigma$  and  $\epsilon$ - $\sigma$  curves are calculated to respectively estimate the  $d_{33}$ ,  $\mu$ ,  $d_{33}^*$  and E as a function of field and stress.

### *Corrections for longitudinal variation in texture*

In order to correct for the effects of longitudinal variation in texture and achieve a closer match between model prediction and experiment, an averaging scheme was introduced. This scheme is sensitive to the longitudinal location of the instrumentation on the sample for the experimentally measured quantities that are predicted by the model. We assume a constant magnetic field and stress throughout

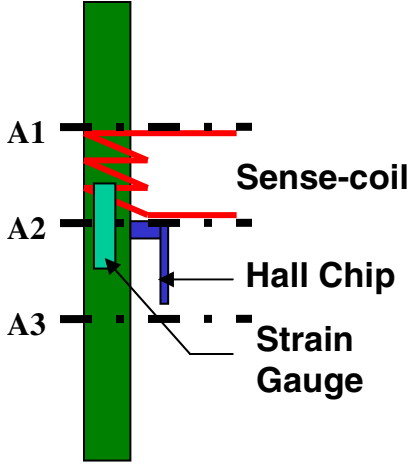


**Figure 6.6** Instrumentation location.

the sample (inputs to the model) and account for the possible longitudinal variation in magnetization and magnetostriction (model outputs). Since, the experimental data for magnetization/magnetic induction is obtained by a sense coil placed between the mid-point and quarter length from top, Equation 6.4 was employed to correct for longitudinal variations in texture by finding an “average texture”. Similarly, magnetostriction (strain) was measured by a strain-gauge centered at the mid-point of the sample and extending  $1/8^{\text{th}}$  the length on either side (i.e. half the distance from to A2 to A1 and A2 to A3). Therefore, a center weighted averaging scheme was employed to find the “average texture” (Equation 6.5).

$$x_{Mijk} = \frac{1}{2} (x_{ijk} \{A_1\} + x_{ijk} \{A_2\}) \quad (6.4)$$

$$x_{Lijk} = \frac{1}{8} (x_{ijk} \{A_1\} + 6 * x_{ijk} \{A_2\} + x_{ijk} \{A_3\}) \quad (6.5)$$

The normalized volume-fractions that have been corrected for the longitudinal variation in texture using Equations 6.4 and 6.5 are respectively used in Equation 6.6 and 6.7 to calculate the polycrystalline response.

$$M_{poly} = x_{M100} * M_{100} + x_{M110} * M_{110} + x_{M210} * M_{210} + x_{M310} * M_{310} \\ + x_{M111} * M_{111} + x_{M211} * M_{211} + x_{M311} * M_{311} \quad (6.6)$$

$$\lambda_{poly} = x_{L100} * \lambda_{100} + x_{L110} * \lambda_{110} + x_{L210} * \lambda_{210} + x_{L310} * \lambda_{310} \quad (6.7)$$

$$+ x_{L111} * \lambda_{111} + x_{L211} * \lambda_{211} + x_{L311} * \lambda_{311}$$

#### **6.4 Model Predictions and Comparison with Experimental Data**

This section discusses the method used to select model parameters and employs simulation results for various crystallographic directions to explain the effect of variation in volume fractions of different directions on the net polycrystal behavior. The predicted polycrystalline actuation and sensing behaviors are compared with experimental data. Furthermore it is demonstrated that variation in cross-section texture between samples correlates reasonably well with the observed variation in the three polycrystalline samples tested.

##### **6.4.1 Methodology of Choosing Model Parameters**

The aim of the polycrystalline modeling is to predict the actuation and sensing behavior of polycrystalline materials from texture information and knowledge of single crystal behavior. Hence, most of the parameters are either predetermined: such as the volume fractions of grains (determined by texture) or are constrained to lie in a specific range, such as  $K_1$ ,  $K_2$ , [Rafique2004],  $M_s$  and  $\Omega$  [Chapter 4 of this thesis] that have been shown to be dependent on Ga content. The magnetocrystalline anisotropy coefficients  $K_1$  and  $K_2$  were chosen to model the zero stress actuator behavior from a range of values for FeGa with Ga content between 18 and 19 at. % [Rafique2004].  $M_s$  and  $\Omega$  were chosen to be  $1.83/\mu_0$  and 625 respectively based on the trends discussed in Chapter 4, where it was demonstrated that  $M_s$  decreases and  $\Omega$  increases with increasing Ga content.

Thus,  $\lambda_{100}$ ,  $\lambda_{111}$  and  $\gamma_\sigma$  are the only parameters that were chosen without any constraint. It should be noted that while  $\lambda_{100}$  and  $\lambda_{111}$  are also dependent on Ga content [Clark 2001],  $3/2\lambda_{100}$  was chosen as 255 ppm which is lower than the typical magnetostriction for single crystal samples with 18 to 19 at. % Ga. This choice was

necessary to account for some losses in magnetostriction due to elastic interaction between grains.  $\gamma_\sigma$  was chosen as 0.8 to scale-down the magnetoelastic energy in order to fine-tune the variation in magnetic behavior with stress. The values chosen for these parameters are listed below:

$$K_1 = 3.6 \times 10^4 \text{ Jm}^{-3}, K_2 = 0 \text{ Jm}^{-3},$$

$$(3/2)\lambda_{100} = 255 \times 10^{-6}, (3/2)\lambda_{111} = -7 \times 10^{-6}$$

$$M_S = 1.83/\mu_0 \text{ A/m},$$

$$\Omega = 625 \text{ Jm}^{-3}, \gamma_\sigma = 0.8$$

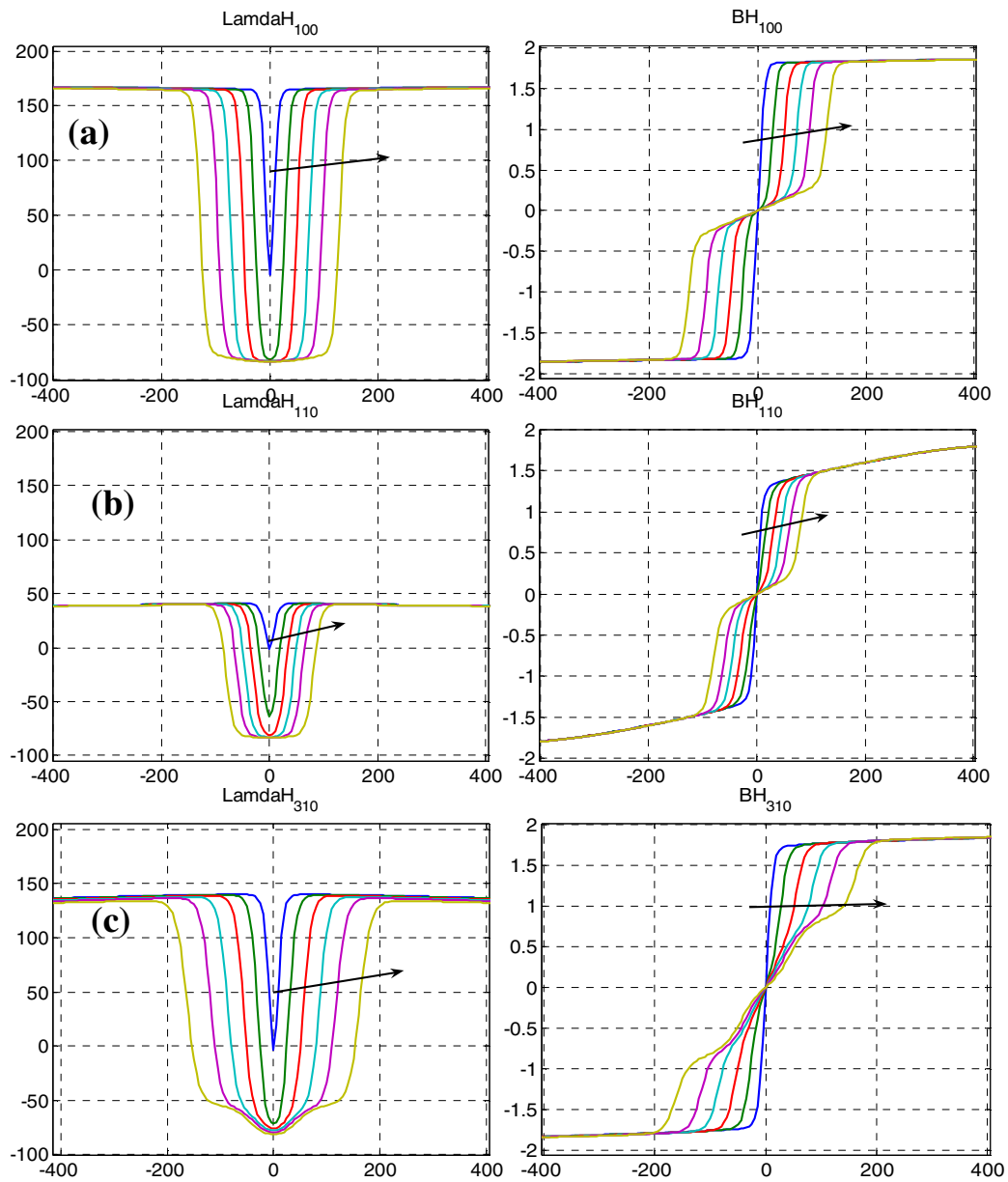
#### 6.4.2 Simulation Results for Various Crystallographic Directions

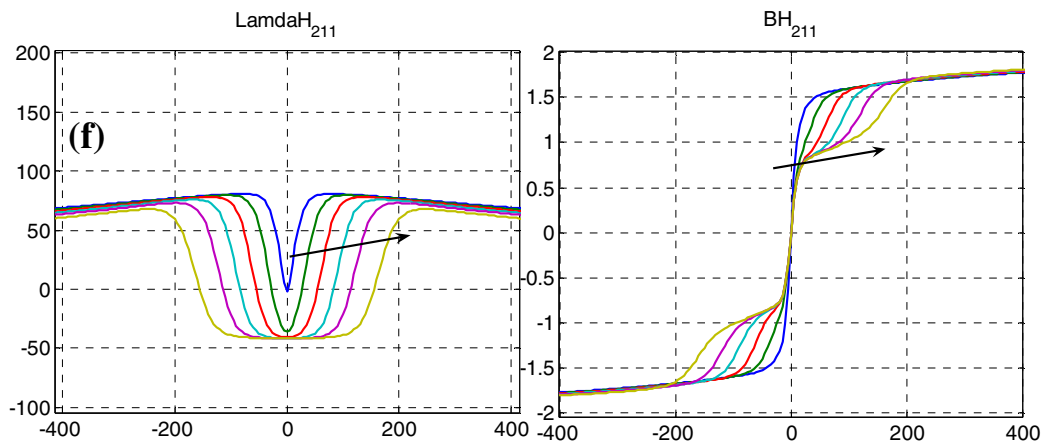
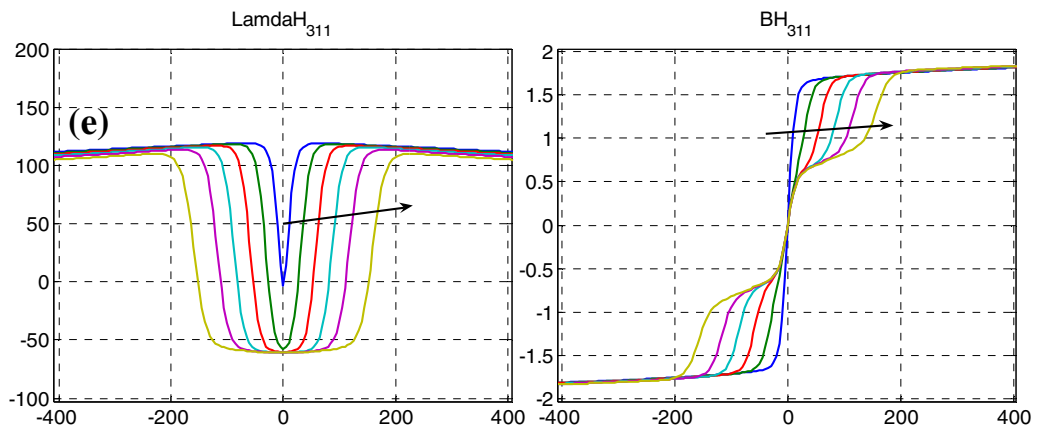
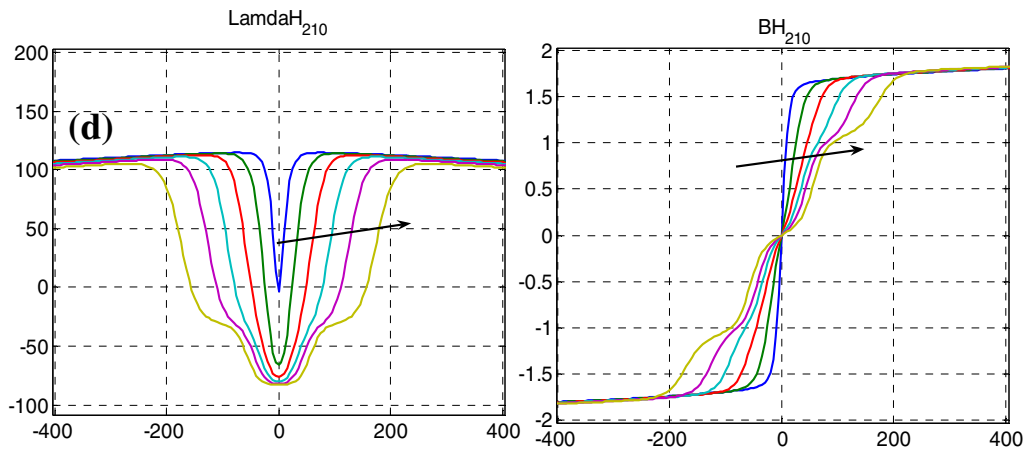
##### *Actuation behavior*

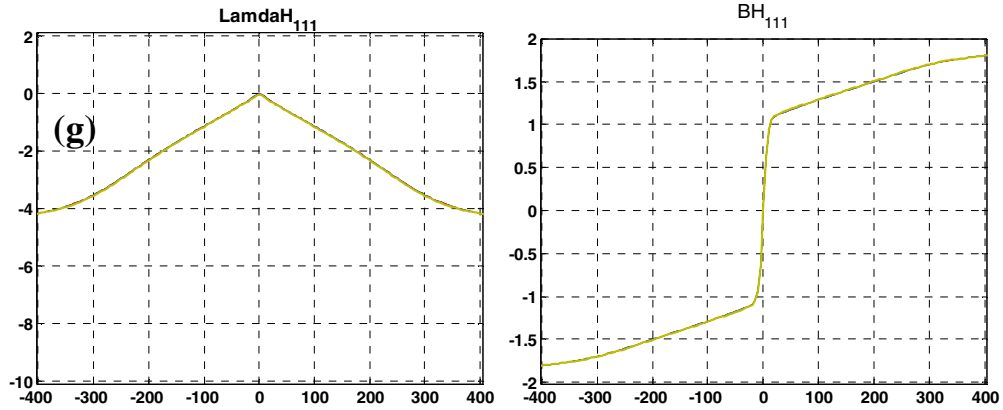
The  $\lambda$ -H, B-H and B- $\sigma$  characteristics of ~18 % Ga single crystal FeGa in the [100], [110], [210], [310], [211] and [311] directions, simulated with model parameters listed above, are shown in Figure 6.7. It can be seen that the B-H curve at zero-stress in the  $\langle 111 \rangle$  direction take a larger field to saturate and exhibits distinct regimes of magnetization which are likely to be caused by the rotation/flipping of magnetization to the nearest set of  $\langle 100 \rangle$  direction (takes very little field) followed by gradual rotation to the  $\langle 111 \rangle$  direction (requires large field). Furthermore, the effect of stress on the B-H and  $\lambda$ -H curves is most in the  $\langle 100 \rangle$  direction and least in the  $\langle 111 \rangle$  direction in agreement with the magnetoelastic energy being proportional to  $\lambda \cdot \sigma$ .  $\lambda_{111}$  being an order of magnitude smaller than  $\lambda_{100}$ , the same level of stress has very little effect on the behavior in the  $\langle 111 \rangle$  direction compared to the  $\langle 100 \rangle$  direction.

The direction closest to [100], which is [310] shows a  $\lambda_{\text{sat}}$  of ~ 220 ppm while direction farthest from [100] which is [211] shows  $\lambda_{\text{sat}} \approx 100$  ppm. (*Actually, [111] is further than [211] from [100] but is not considered in this analysis as the EBSD showed that no grain was oriented along the [111] direction.*)

In Figure 6.7 (f), the [211] direction shows an increase in  $\lambda$  at low fields followed by a small decrease in  $\lambda$  with increasing field. This is because the rotation/flipping of domains to the  $\langle 100 \rangle$  directions closest to the [211] direction is characterized by a large increase in  $\lambda$ , while the rotation of domains from  $\langle 100 \rangle$  to [211] with increasing field produce a decrease in  $\lambda$  due to the strong influence of negative  $\lambda_{111}$  on the [211] direction.



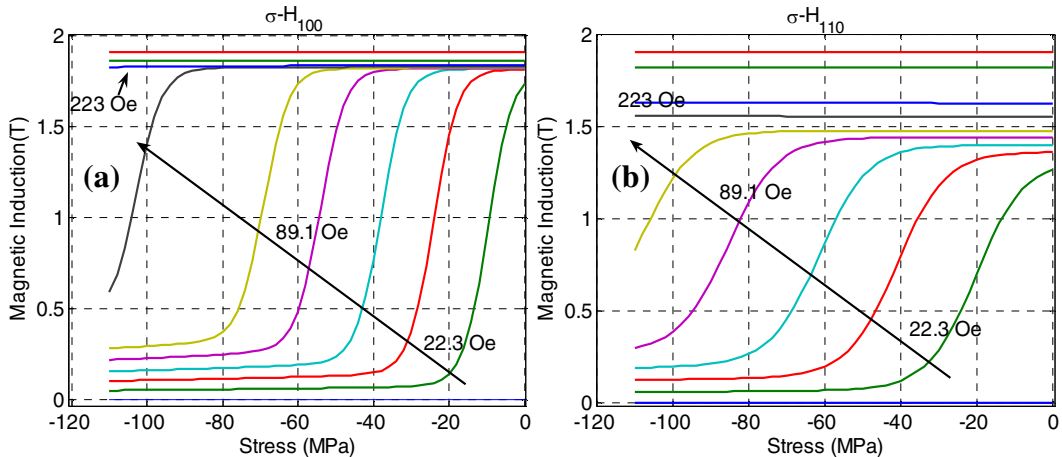




**Figure 6.7** Simulation of actuator  $\lambda$ -H (left) and B-H (right) curves at compressive pre-stress values of 0, 15, 30, 45, 60 and 80 MPa along different crystallographic directions as follows: **(a)** [100] **(b)** [110] **(c)** [310] **(d)** [210] **(e)** [311] **(f)** [211] and **(g)** [111].

### Sensor behavior

For the same reason as explained in discussion of actuation behavior, sensitivity (variation in B with  $\sigma$ ) is much larger in the  $\langle 100 \rangle$  direction than the  $\langle 111 \rangle$  direction, with sensitivity in the  $\langle 110 \rangle$  direction being moderate. The model shows a small increase in B with compressive stress in the  $\langle 111 \rangle$  direction as  $\lambda_{111}$  is negative. Directions closest to [100], such as [310] exhibit maximum sensitivity, while those farthest from [100] and close to [111] such as [211] exhibit least sensitivity (Figure 6.8).



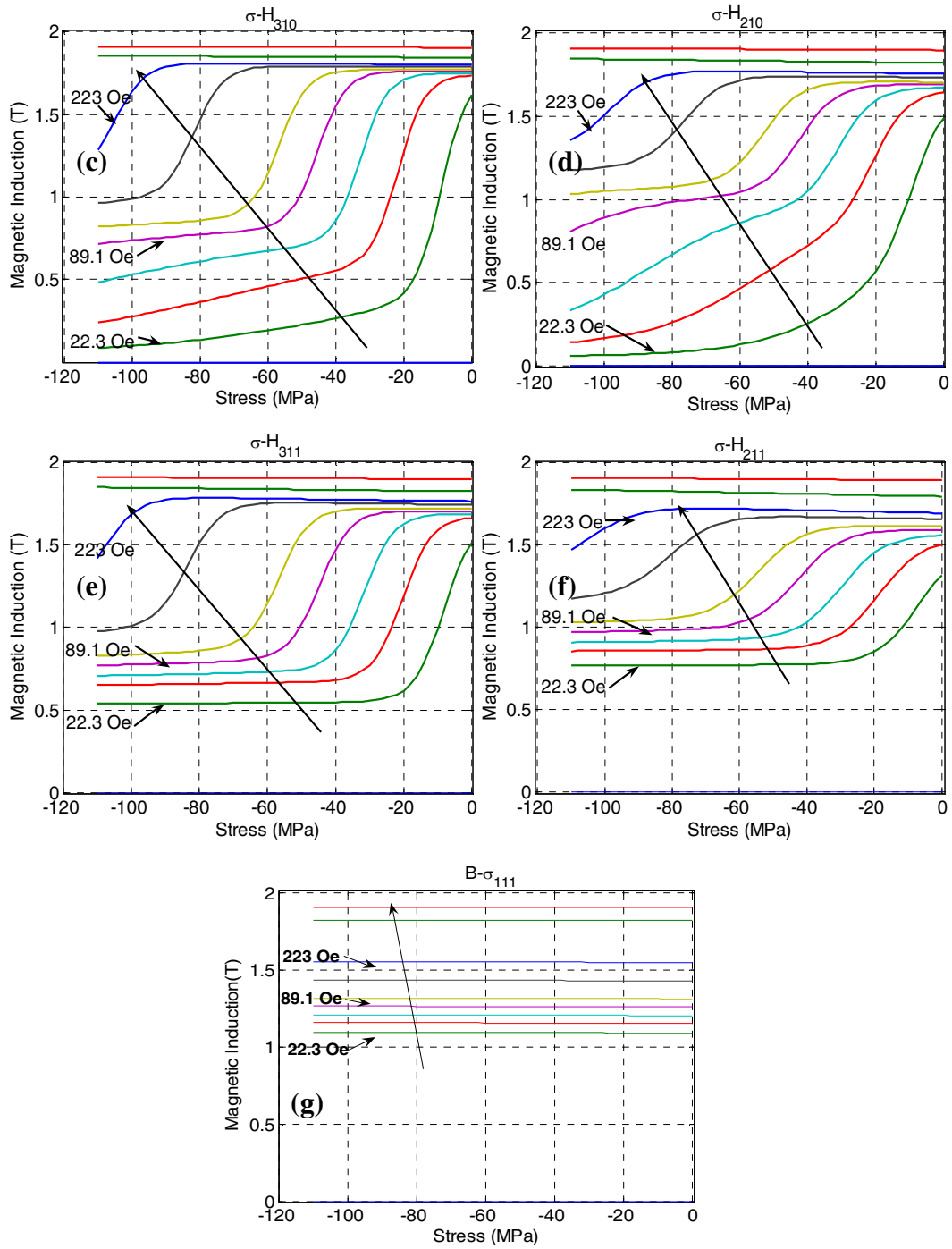


**Figure 6. 8** Simulation of sensor B- $\sigma$  behavior at bias fields of 22, 44, 66, 88, 111, 167, 222, 446, 891 Oe along different crystallographic directions as follows:

(a) [100] (b) [110] (c) [310] (d) [210] (e) [311] (f) [211] and (g) [111].

(Note: By convention, compressive stress is negative in sensor characteristics.)

### 6.4.3 Simulation of Polycrystalline Behavior and Benchmarking

The simulation of actuator and sensor response of polycrystalline FeGa alloys, shown in Figure 6.9 and 6.10 respectively, was performed by using the weighted sum of the magnetostrictive and magnetization responses in the individual crystallographic directions (Figure 6.7 and 6.8) according to Equations 6.3 and 6.4. The actuator model simulation compares well with experimental results at most stresses. There is some mismatch in magnetostriction predicted at low stress and in general the experimental polycrystal magnetostrictive response is more rounded than the simulation results. The rounded experimental characteristic may have been caused due to elastic interaction between grains which was not accounted for in this simple model. Furthermore,  $\Omega$  was chosen as  $625 \text{ J/m}^3$  as this value is in agreement with  $\Omega$  used for single crystals of this Ga content. Since an attempt was being made to simulate polycrystalline behavior from single crystal behavior along different crystallographic directions, a higher  $\Omega$  (that could have simulated smoother characteristics) was not chosen even though polycrystals are expected to have greater inhomogeneities than single crystals of similar Ga content.

The sensor behavior, which was simulated with the same parameters chosen to model the actuator characteristics, showed reasonable agreement with experimental characteristics (Figure 6.10). This proves that the model may serve as a useful tool in predicting sensing behavior from actuator data. The simulation of sensing behavior in tension (upto 20 MPa) indicates that this material does not have a large sensitivity for sensing tension except possibly at very low bias fields (smaller than 20 Oe).

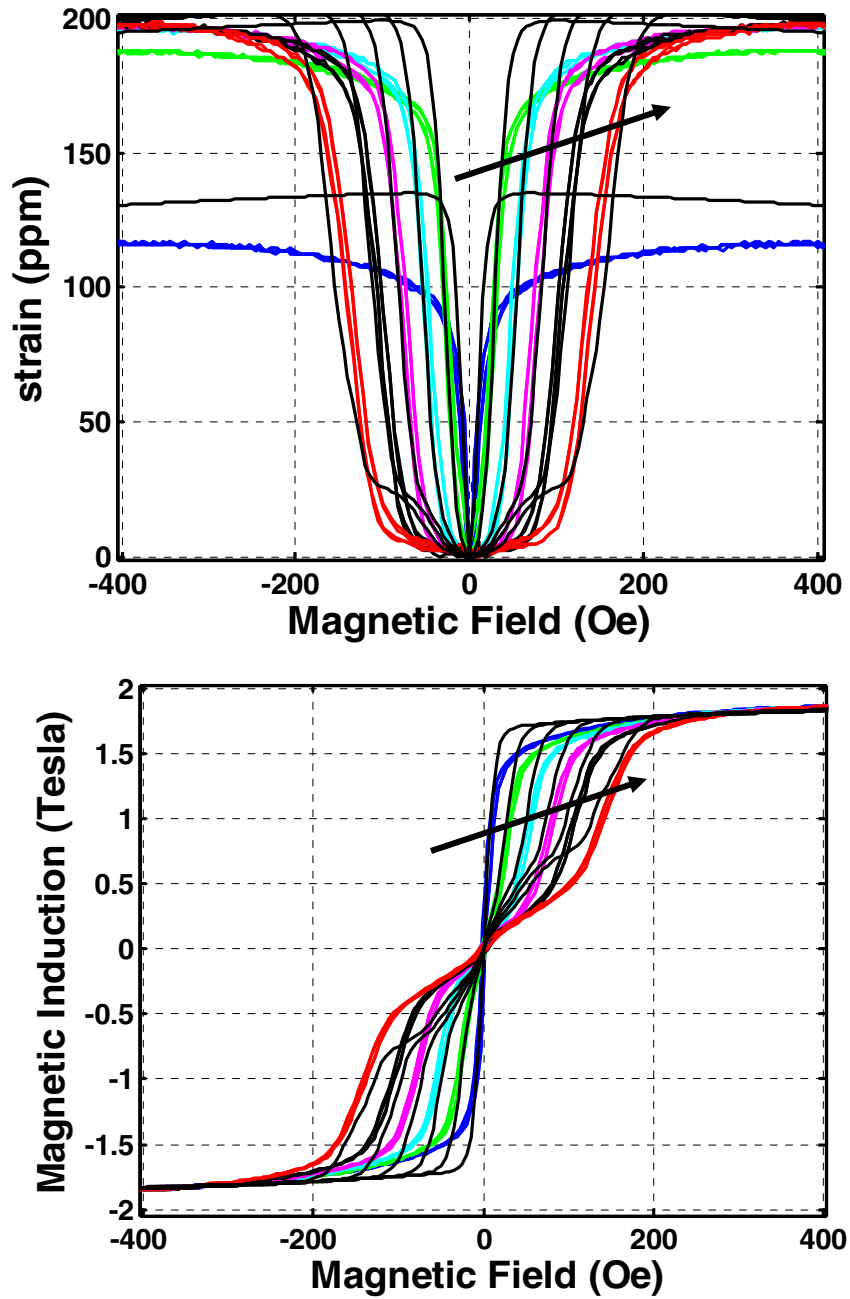


**Figure 6.9** Simulation (thin black lines) and experimental data (thick lines) of  $\lambda$ -H (top) and B-H (bottom) curves at compressive prestress of 0, 15, 30, 45, 60, 80 MPa.

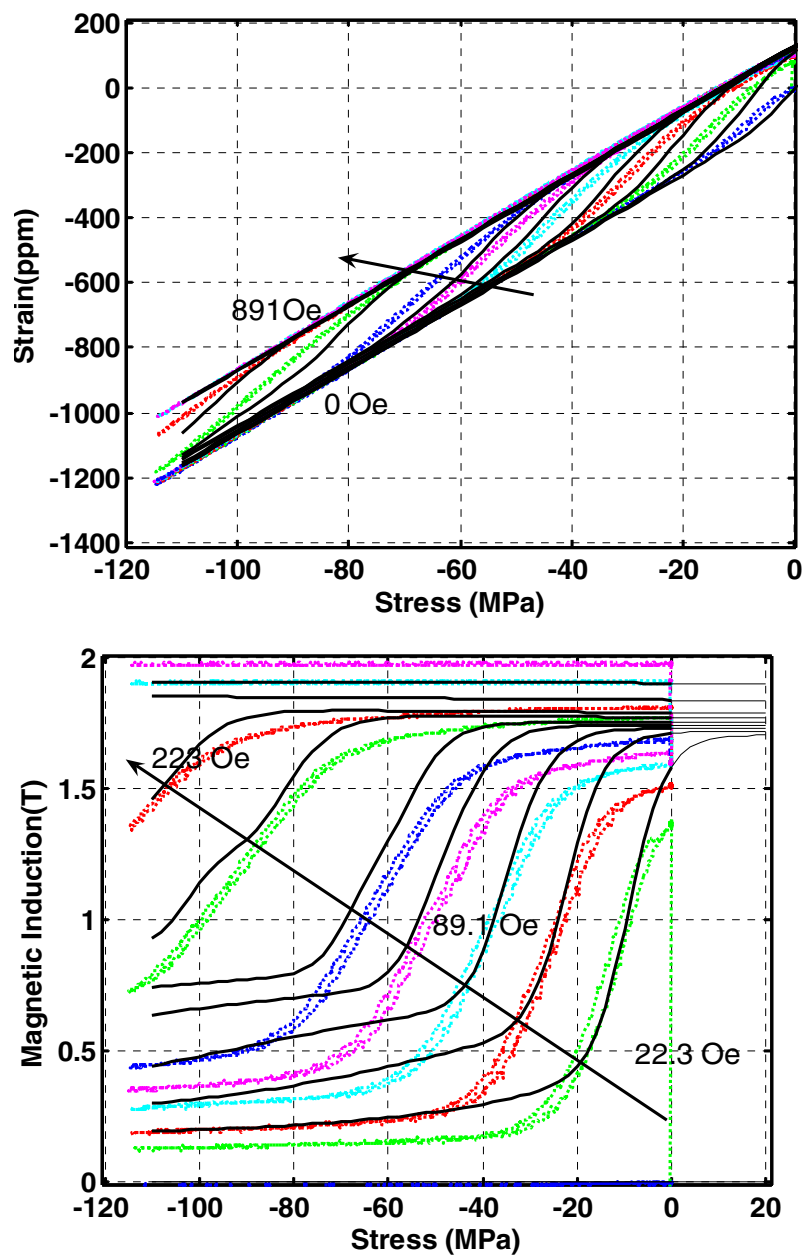


**Figure 6.10** Simulation (thin black lines) vs. experimental data (thick lines) of  $\epsilon$ - $\sigma$  (top) and  $B$ - $\sigma$  (bottom) characteristics at bias fields of 22, 44, 66, 88, 111, 167, 222, 446, 891 Oe.

### **6.5 Discussion of $\mu_r$ , $d_{33}$ , $d_{33}^*$ and $E^H$ Estimated by the Model**

The discussion of actuation and sensing behavior is not complete without analyzing the derivatives of the actuation and sensing characteristics, viz. relative permeability,  $d_{33}$ ,  $d_{33}^*$  and Young's modulus. Due to the inherent magnetoelastic coupling in magnetostrictive materials, these quantities are typically strong functions of stress and magnetic field. These quantities along the [100] (most sensitive) and [211] (among the less-sensitive, [111] being the least-sensitive) directions are compared and the ramifications of the directional effects on the polycrystalline behavior are discussed.

Figure 6.11 illustrates that the relative permeability is high in both directions under zero stress. This corresponds to flipping of domains to the nearest  $\langle 100 \rangle$  direction in both cases. At higher stresses, the [100] direction exhibits low permeability at low fields followed by increased permeability with increasing field, which possibly corresponds to a domain rotation against magnetocrystalline and stress anisotropy followed by a flip to the [100] direction. In the case of the [211] direction, at high stresses the permeability is still high at very low fields, possibly corresponding to flipping of domains to  $\langle 100 \rangle$  directions nearest to [211] followed by decreased permeability at high fields where the magnetization is gradually rotated from the nearest  $\langle 100 \rangle$  easy-axes to the relatively magnetically hard [211] direction. The combinations of these two effects results in the behavior observed in the polycrystal shown in Figure 6.12.

Both  $d_{33}$  and  $d_{33}^*$  are  $\sim 150$  (nm/ampere or Tesla/GPa) in the [100] direction as compared to  $\sim 30$  in the [211] direction, indicating that the strain/applied field in the burst regions as well as sensitivity (change in magnetic induction/stress applied) is *five* times higher in the [100] directions compared to the [211] direction. In the case

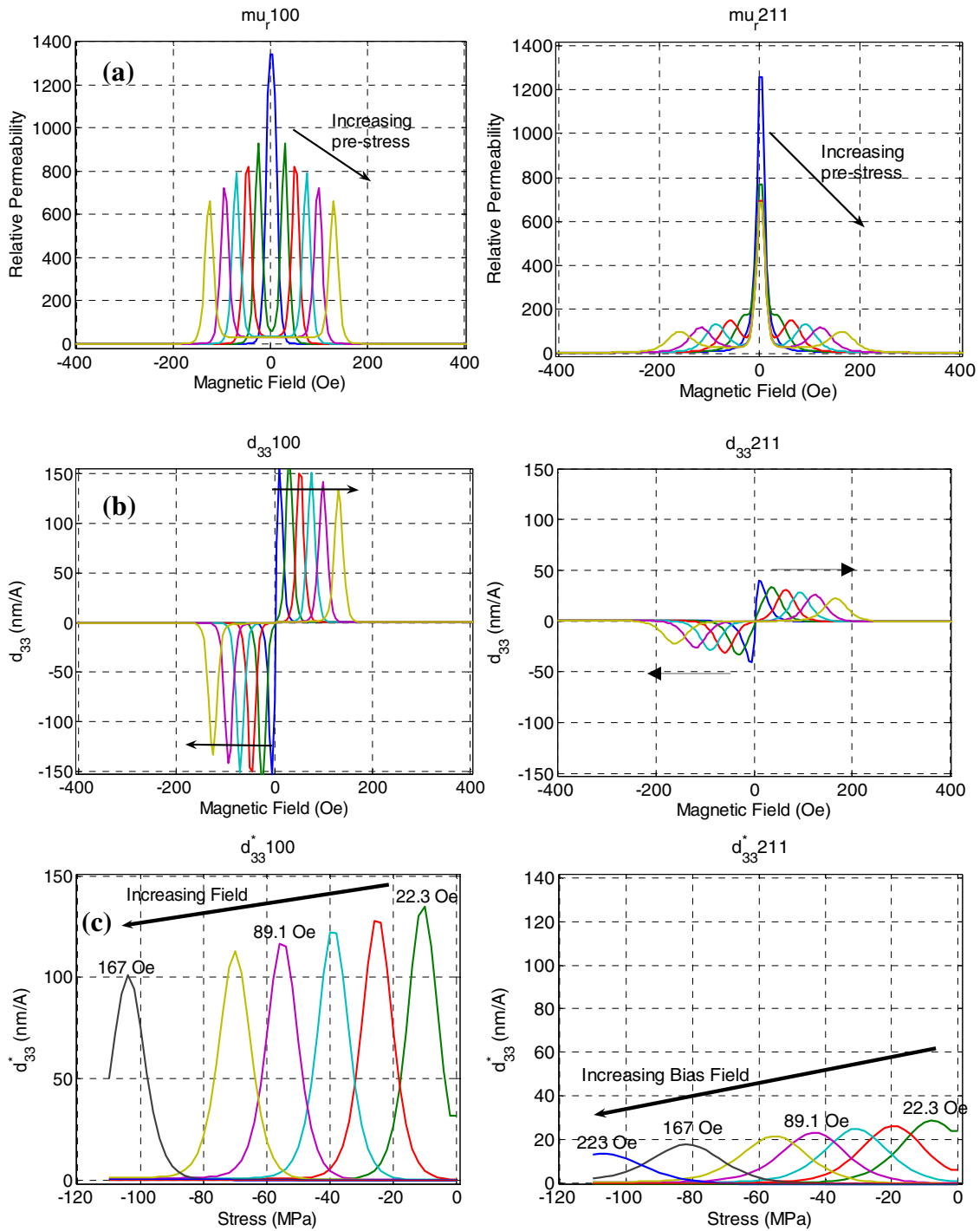


**Figure 6.11** Simulated permeability and piezomagnetic constants in the [100] (figures on left) and [211] (figures on right) directions.

**(a)**  $\mu_r$  **(b)**  $d_{33}$  and **(c)**  $d_{33}^*$ .

of polycrystal these quantities are  $\sim 100$  compared to a sensitivity  $\sim 135$  in the [100] direction which is an effect expected to be caused by the presence of grains which are not close to the [100] direction.

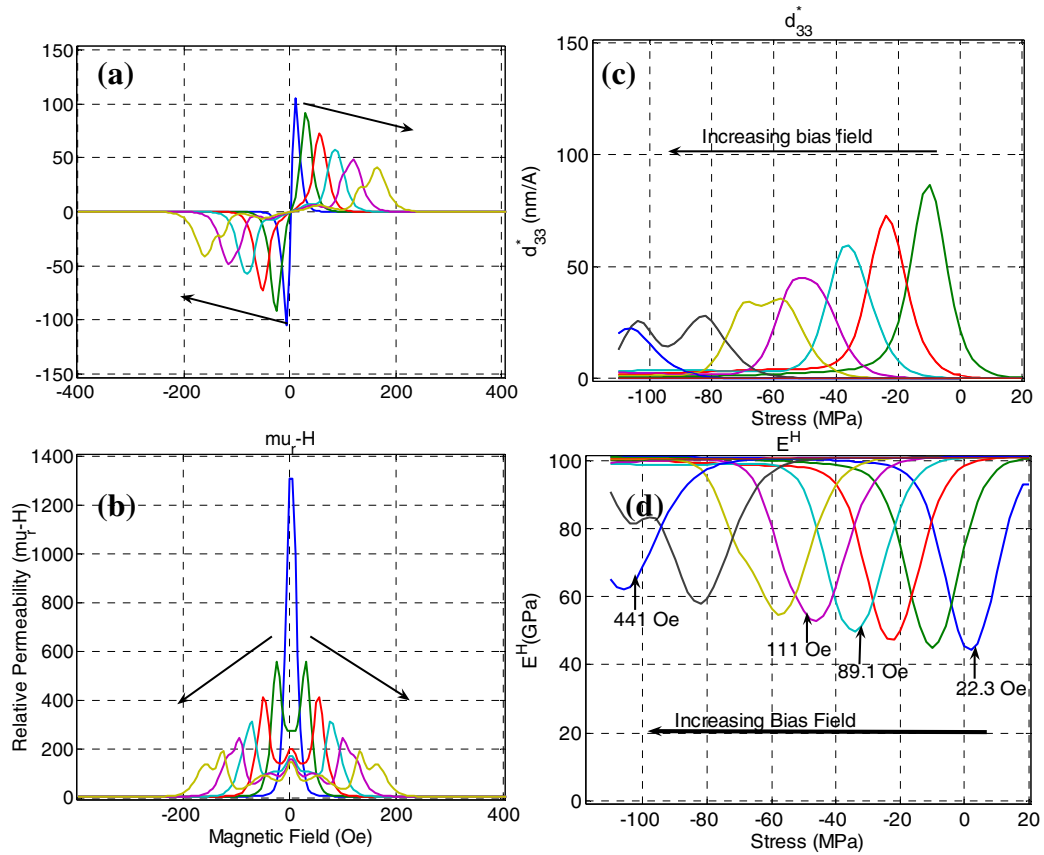


**Figure 6.12** Simulated (a)  $\mu_r$ , (b)  $d_{33}$  and (c)  $d_{33}^*$  and (d)  $E^H$  (Young's Modulus) of polycrystal.

### 6.6 Possible Cause of Variation in Data

The three different actuator responses shown in Figure 6.13 were simulated with the volume fraction corresponding to textures at the L/4, L/2 and 3L/4 longitudinal stations, obtained from EBSD measurements in Figure 6.5. The simulated saturation magnetostriction of the three samples was found to vary by about  $\pm 2.5\%$ . However, in the burst region characterized by a large increase in magnetostriction and magnetic induction with small increases in field, there was a large variation in characteristics simulated with the three different textures.

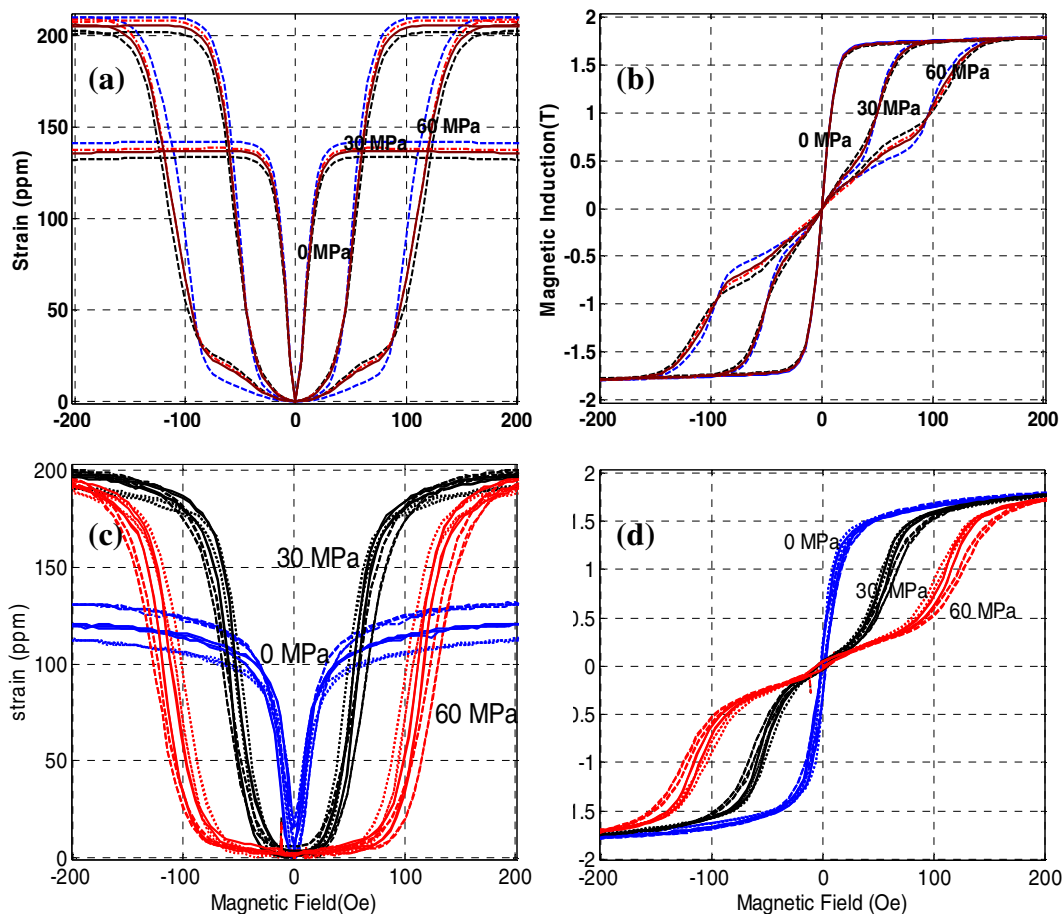


**Figure 6.13** Simulation vs. experimental data of  $\lambda$ -H and B-H curves at compressive prestress of 0, 30 and 60 MPa.

**(a) and (b)** Variation in characteristics simulated by the model from estimated variation in cross-section texture.

**(c) and (d)** Experimental data showing variation in characteristics of three polycrystals (a subset of the data shown in Figure 6.1).

These variations in the simulated actuator behavior compare well with experimentally observed variation in actuator characteristics of the three samples as can be seen in Figure 6.13. Considering that the extent of variation in texture along the length of one sample is a reasonable estimate of the variation in texture exhibited by samples extracted at different positions along the length of an FSZM polycrystal,

the simulations are able to predict the variation in actuator behavior of these samples reasonably well from the estimated variations in their texture.

## **6.6 Conclusions**

The simulated polycrystalline actuator and sensor behavior showed good agreement with experimental results. The simulation also contributed to the understanding of the effect of various crystallographic directions (differently oriented grains) on the polycrystalline behavior. Furthermore, it has been shown that the polycrystalline sensing behavior can be predicted reasonably well from the actuator characteristics using this model. It was also demonstrated that this model can predict possible variations in magnetomechanical characteristics of the polycrystalline samples from variations in the cross-section texture of these samples. The predictions made for sensing tensile stresses may prove useful in the design of bending and torsion sensors that experience both compressive and tensile loads.

Some issues which could not be handled by this model were that the polycrystalline characteristics were smoother than predicted and a lower value of  $\lambda_{100}$  had to be chosen to account for the saturation magnetostriction observed. Both these issues were possibly caused by the elastic interaction between the grains which, were not accounted for in this model. Eventually, elastic interactions between grains may need to be modeled by FEM and coupled with the single-crystal free-energy model for each grain to get very accurate models for polycrystalline actuator and sensor behavior.

## Chapter 7: Summary and Conclusions

Iron-Gallium alloys demonstrate moderate magnetostriction (~350 ppm) and saturation material induction (~1.7 T) under low magnetic fields (~400 Oe) as well as high tensile strength (~500 MPa) and limited dependence of magnetomechanical properties on temperatures between -20<sup>0</sup>C and 80<sup>0</sup>C, making them promising materials for actuation and sensing applications. With this in mind, a comprehensive characterization and modeling of varied Ga content single-crystal and 18.4 at. % Ga polycrystal FeGa alloys was attempted in this thesis, building on some of the early work of Kellogg and Flatau, and Clark *et al.* [Kellogg2003b, Clark 2001].

In the subsequent sections, a research summary and the contributions of this thesis are discussed with a focus on: characterization techniques; experimental characterization; modeling and predicting the actuation and sensing behavior of single-crystal FeGa samples of varied Ga content and along various crystallographic directions; and simulating polycrystalline magnetomechanical behavior from cross-section texture. This is followed by a brief note on some areas in which further characterization and improvements in modeling may enhance our understanding and ability to simulate the magnetomechanical behavior of this material.

### 7.1 Summary of Research

The summary is organized on the basis of research reported in each of the chapters:

#### ***Chapter 2: Magnetic issues***

A 2-D axisymmetric model of the magnetic transducer used for the material characterization studies was developed using COMSOL Multiphysics<sup>TM</sup>, a commercial finite-element software, to estimate the spatial magnetic field (H) and magnetic induction (B) distribution in and around a 2.54 cm (1 inch) long and 0.635 cm (1/4 inch) diameter FeGa specimen in a magnetic circuit representative of the transducer used for the magnetomechanical characterization in this dissertation. The specimen was modeled with  $\mu_r = 60$ , to ensure the estimates of spatial distribution in

B and H were reasonably conservative for most magnetomechanical conditions in the sample.

The simulation results, considered together with the space constraints, guided the selection of an appropriate location for the measuring elements, viz. hall-chip, sense coil and strain-gauges and the corresponding errors in estimation of H, B and magnetostriction. An ideal configuration is to have the hall-chip within  $\pm 0.3175$  cm (0.125 inch) from the center, the sense-coil wound between the center and half-the distance between the center and the top or bottom of the sample and strain-gauges centered on the sample mid-point. For such a configuration the sense-coil estimates of B are likely to be accurate to  $\pm 4\%$  and hall-chip estimates of H  $\pm 3\%$  for the most part. The magnetostriction estimates are likely to be more accurate than  $\pm 4\%$  as they are centered on the sample center. A noteworthy result from this model is that placing the *hall-chips away from the rod center*, especially close to the rod ends, can lead to large measurement errors. This can alter the very nature of the B-H and  $\lambda$ -H curves being measured as has been experimentally demonstrated.

Finally, some changes in the design of transducers are proposed to reduce the errors in estimation of the field, induction and strain by concentrating the flux to minimize lateral and longitudinal variation in field in the sample.

### ***Chapter 3: Characterization of single-crystal actuation and sensing behavior***

#### *Actuation behavior: effect of Ga content*

The characterization envelope for actuation behavior ( $\lambda$ -H and B-H curves) of single crystal FeGa in the  $\langle 100 \rangle$  direction was extended to include higher Ga content samples, viz. the 24.7 and 29 % Ga.

The nature of the  $\lambda$ -H and B-H curves was found to be strongly dependent on the Ga content. The 19 at. % Ga FeGa sample exhibits a kinking behavior in B-H curves, i.e. exhibition of two distinct regimes of low and high permeability, which

increases on application of a larger compressive stress. Higher Ga content samples (24.7 at. % Ga and 29 at. % Ga samples) show rounded B-H curves with no kinking behavior, possibly due to a smoothing effect due to a presence of a large number of in-homogeneities/multiple phases.

The  $\lambda_{\text{sat}}$  of the 19 at. % Ga sample does not decrease with compressive stress, up to 80 MPa. However, in 24.7 and 29 at. % Ga samples the  $\lambda_{\text{sat}}$  reaches a peak at about 30 MPa and decreases significantly at higher stress such as 60 MPa and 80 MPa. This is unexpected, as it has not been observed at the lower Ga content samples (21 at. % and below) tested by others, but was observed in separate tests on the 24.7 and 29 at. % Ga samples and found to be reproducible.

#### *Actuation behavior: different crystallographic directions*

The actuator properties of an 18 at. % Ga single crystal in  $\langle 110 \rangle$  direction was characterized at various compressive pre-stresses. Large fields are required to drive sample to saturation in the  $\langle 110 \rangle$  at low stress due to high magnetocrystalline anisotropy energy in this direction. However, the effect of stress, whose contribution to the magnetoelastic energy is  $-\lambda^*\sigma$ , is low in the  $\langle 110 \rangle$  direction, as  $\lambda_{110}$  is much smaller than  $\lambda_{100}$ . Consequently, at relatively high stress levels, on the order of 60 MPa, the field required to drive the  $\langle 110 \rangle$  sample to saturation are not very high.

The magnetostriction that could be obtained from the  $\langle 110 \rangle$  oriented sample was  $\sim 150$  ppm under appropriate compressive stress. This has important implications for actuation and sensing at the microscale (provided the macro-scale behavior scales down), where it has been demonstrated that FeGa films can be deposited in the  $\langle 110 \rangle$  direction on a  $\langle 100 \rangle$  silicon substrate.

#### *Sensing behavior: development of PID controller to ensure constant field*

Due to its interaction with the magnetic circuit, the bias field magnitude in the magnetostrictive sample is expected to vary with stress induced changes in permeability of the sample when the drive current, which produces the bias field, is

maintained constant. A feedback-loop implemented with a PID controller to vary the drive current to keep the magnetic field through the sample constant worked successfully. This proved to be important for ensuring that the characterization of the sample magnetomechanical behavior is independent of the magnetic interaction between the sample and magnetic circuit. This provides a technique for evaluating the true material properties without interactive effects that depend on the transducer in which the magnetomechanical characterization is being performed. In fact, the constant magnetic field characteristics have been shown to have about 4-5 times higher sensitivity than those at constant drive current, proving that material constants evaluated without this controller may not be a good indicator of the true material properties, as is not independent of the interaction with the circuit .

*Sensing behavior: <100> and <110> direction*

The sensing behavior of both 19 at. % Ga <100> oriented and 18 at. % Ga <110> oriented single crystal samples were characterized under constant magnetic field conditions. The magnetoelastic energy,  $-\lambda^*\sigma$ , being smaller in the <110> direction than in the <100> direction for same stress levels, lower sensitivity is expected. The variation in B with  $\sigma$  and variation in modulus of the sample ( $\Delta E$  effect), is also expected to be much smaller in the <110> direction. Although some of these differences in magnetomechanical behavior are possibly due the difference in Ga content in the samples, the characterization results, discussed above, appeared to be consistent with the expected trends associated with crystallographic direction.

***Chapter 4: Energy-based model for single-crystal quasi-static actuation behavior***

*Model development*

The modeling of the magnetomechanical behavior of single-crystal magnetostrictive materials was addressed at two levels: alignment of spins (magnetization) in individual lattices within a domain and the distribution of orientation of various domains to simulate the macroscopic response of the material.

The alignment of spins in a domain was treated as a canonical ensemble of interacting particles and modeled using 0<sup>th</sup> order approximation (mean-field theory) to predict the temperature dependence of  $M_{\text{sat}}$  and  $\lambda_{\text{sat}}$  within a domain. This was used to demonstrate behavior of a typical magnetostrictive material close to its Curie temperature. It was also shown that far below the Curie temperature, the exchange interaction and thermal energies are so high in comparison to the magnetocrystalline and magnetoelastic terms that orientation and stress effects have negligible effect on alignment of spins.

However, at the domain level, there is a cooperative movement of spins which does not cause an expense in exchange energy and thermal effects are less significant, thus resulting in the magnetocrystalline, magnetoelastic, magnetic energies and possibly material inhomogeneity and defects playing a key role. At this level, modeling magnetostrictive behavior at constant temperature is appropriate, and the problem reduces to finding the distribution of orientation of various “domains” to a particular stress and field input, which is accomplished by the Armstrong model. This distribution determines the macroscopic response of the material.

#### *Application of the Armstrong model for the FeGa single-crystals of varied Ga content*

The different trends observed in the magnetomechanical behavior of varied Ga content, i.e. 19, 24.7 and 29 at. % Ga single crystal samples were simulated using the model. It was demonstrated that the choice of certain parameters, viz. magnetocrystalline anisotropy  $K_1$  and  $K_2$  and Armstrong smoothing parameter  $\Omega$ , was able simulate the strikingly different trends in the B-H curves. The smoothing parameter  $\Omega$ , which is indicative of in-homogeneities, was shown to increase with Ga content. Physically, this trend is consistent with the fact that in-homogeneities such as multiple phases and are more likely to occur as the Ga content increases.

A linear dependence of  $\lambda_{100}$  on compressive stress beyond 30 MPa had to be introduced to capture the experimental observation that saturation magnetostriction decreased with compressive stress beyond 30 MPa in the 24.7 % and 29 % samples.

It was demonstrated that it is possible to create a database or map of variation in material properties such as  $\mu_R$  and  $d_{33}$  with both stress and field, which could prove to be useful design tools, using just 7-parameters for each single-crystal material. These material properties also show a large sensitivity to Ga content. For example, with an increase in gallium content from 19 % to 29 %, the zero-stress  $d_{33}$  drops from 100nm/A to 25nm/A, while the peak relative permeability drops from ~1000 to 250.

#### *Simulation of actuation in different crystallographic directions and under tension*

Finally, it was demonstrated that this model could predict  $\lambda$ -H and B-H curves along various crystallographic directions, viz.  $\langle 110 \rangle$  and  $\langle 111 \rangle$ , other than the  $\langle 100 \rangle$  direction. However, bench-marking the model simulation with  $\langle 110 \rangle$  experimental data showed that while the trends predicted are correct, the model may not be able to simulate some of the exact experimental curves well. Notwithstanding this the model accurately predicts the large increase in the  $\lambda_{100}$  observed under stress.

### ***Chapter 5: Modeling sensing behavior & interaction with magnetic circuit***

#### *Prediction of sensing behavior from actuation characteristics*

The correlation obtained between sensor simulation, based on model parameters obtained from actuator data, and experimental results for sensing behavior proves that sensing behavior can be predicted from actuator characteristics very precisely using this model. This correlation is shown to be excellent in the  $\langle 100 \rangle$  oriented furnace cooled 19 at. % Ga sample and reasonably good in the case of  $\langle 110 \rangle$  oriented furnace cooled 18 at. % Ga sample.

#### *Simulated behavior of 24.7 and 29 at. % Ga, FeGa alloys*

The behavior of 24.7 and 29 at. % Ga FeGa alloys were simulated from the respective actuator characteristics. Simulated peak sensitivity  $d_{33}^*$  of the 24.7 and 29 at. % Ga samples is respectively ~40 Tesla/GPa and 25 Tesla/GPa, which is much smaller than the  $d_{33}^* \approx 140$  Tesla/GPa of the 19 at. % Ga sample. The low

magnetocrystalline anisotropy and higher  $\Omega$  in the higher Ga content samples could possibly result in a more gradual rotation in magnetization on application of stress, resulting in smaller sensitivities than the 19 at. % Ga sample.

#### *Sensing behavior in different crystallographic directions and under tension*

In the compressive stress regime, the  $\langle 110 \rangle$  oriented 18 at. % Ga sample demonstrates moderate peak sensitivity  $\sim 50$  T/GPa as compared to a high peak sensitivity  $\sim 140$  T/GPa in  $\langle 100 \rangle$  oriented 19 at. % Ga sample. While the  $\langle 110 \rangle$  oriented 18 at. % Ga sample has lower sensitivity peaks, compared to the  $\langle 100 \rangle$  oriented 19 at. % Ga sample, it is also sensitive over a larger range of stress.

The dominant feature of the *simulated* B- $\sigma$  curves in the  $\langle 111 \rangle$  direction of a typical 18 at. % Ga furnace cooled sample is that the B does not vary significantly with applied stress. This is expected as the magnetoelastic energy, which is proportional to  $\lambda_{111} * \sigma$ , is about 30 times smaller than that for comparable stress in the  $\langle 100 \rangle$  direction. This is because  $\lambda_{100} \approx 30 \lambda_{111}$ .

#### *Coupling constitutive model for Villari effect with lumped parameter model for interaction between magnetostrictive sample and circuit*

A coupled model that accounts for both the interaction between the magnetic circuit and the magnetostrictive sample in the presence of changing stresses and the constitutive Villari-effect behavior of the material was developed. This model simulation was validated against constant drive-current (varying field) experimental data for the  $\langle 100 \rangle$  oriented 19 at. % Ga sample and found to show good correlation, significantly improving the capability to predict sensing behavior with magnetic interaction between sample and circuit.

### **Chapter 6: Characterization and analysis of behavior of polycrystals**

#### *Experimental characterization*

The saturation magnetostriction of three 18.4 at. % Ga polycrystalline FeGa samples produced by Etrema Products Inc. using a free stand zone melt (FSZM) manufacturing processes with a zoning rate of 350mm/hour was found to be in the range of  $200\pm 5$  ppm (a variation of  $\pm 2.5\%$ ) and the saturation material induction ( $\mu_0 M_{\text{sat}}$ ) in the range of  $1.85\pm 0.025$  Tesla (a variation of 1.3%). However, a significant variation in characteristics of the three samples was observed. For example, one of the largest variation in behavior can be observed at a field of  $\sim 120$  Oe and 60 MPa pre-stress, wherein the magnetostriction is in the range of  $120\pm 30$  ppm (a variation of  $\pm 25\%$ ) and magnetic induction in the three samples is  $1.1\pm 0.2$  Tesla (a variation of  $\pm 18\%$ ), excluding the effect of hysteresis. Of these three samples, the sample that demonstrated highest sensitivity was chosen for texture analysis and characterizing the sensing behavior.

#### *Texture analysis*

The cross-section texture at three longitudinal stations the sample was determined at Etrema Products Inc, using Electron Back Scattering Diffraction (EBSD). The volume fraction (determined by the areas) of grains that lie within  $10^\circ$  of the [100], [110], [111], [210], [211], [310] and [311] orientations were estimated at each longitudinal station. It was observed that there was a large longitudinal variation in texture of the sample.

#### *Simulation of polycrystalline behavior*

The polycrystal model discussed in this chapter simulated the net actuation and sensing characteristics of the sample in terms of the behavior along individual crystallographic directions, viz. [100], [110], [111], [210], [211], [310] and [311] weighted by the volume fraction of grains oriented close to these crystallographic axes.

The longitudinal variation in texture along a sample was indicative of the variation in texture between various samples as they were extracted from different places along a longer free stand zone melted (FSZM) polycrystal. This variation in

texture was employed to simulate the variation in actuator characteristics and compared with experimental data. The variation in actuator characteristics of the three samples tested is reasonably explained by the simulation incorporating the variation in cross-section texture along the length of the sample studied using EBSD.

A scheme was introduced to account for the longitudinal variation in cross-section texture and incorporate it into the model. The simulated polycrystalline actuator and sensor behavior for this sample showed good agreement with experimental results. The simulation also contributed to the understanding of the effect of various crystallographic directions (differently oriented grains) on the polycrystalline behavior. Furthermore, it has been shown that the polycrystalline sensing behavior can be predicted reasonably well from the actuator characteristics, using this model.

### **7.2 Important Contributions from this Research**

1. Error bounds for experimentally measured field, magnetostriction and magnetic induction were established using a 2-D axisymmetric model of the transducer used for magnetomechanical characterization. Changes in the design of this transducer are proposed to decrease spatial variation in field through the sample.
2. Envelope of single-crystal actuation behavior was extended beyond the first magnetostrictive peak (~19 at. % Ga) by experimental characterization of  $\lambda$ -H and B-H curves of <100> oriented single crystal samples with Ga content close to the magnetostriction valley (24.7 at. % Ga) and second magnetostriction peak (29 at. % Ga).
3. A paradigm was established for accurate estimation of sensing behavior of materials that is independent of the magnetic interaction between the sample and the magnetic circuit. This was accomplished using a PID controller with a

feed-back loop to vary the drive current to compensate for variation in sample reluctance so as to keep the field through the sample constant.

4. Characterization of actuation behavior ( $\lambda$ -H and B-H curves) and sensing behavior ( $-\sigma$  and B- $\sigma$  curves) in the  $\langle 110 \rangle$  direction of an 18 at. % Ga, single crystal sample was performed. All macroscopic single-crystal data previously reported in literature for FeGa were for the  $\langle 100 \rangle$  direction only.
5. Modeling of the magnetomechanical behavior of single-crystal magnetostrictive materials was addressed at two levels: alignment of spins (magnetization) in individual lattices within a domain and the distribution of orientation of various domains to simulate the macroscopic response of the material. The relative importance of various energy terms, viz. the exchange coupling, magnetocrystalline, magnetoelastic, magnetic and thermal energies at these two different levels was demonstrated.
6. It was demonstrated that the proper choice of certain parameters: magnetocrystalline anisotropy  $K_1$  and  $K_2$  as well as Armstrong smoothing parameter  $\Omega$  was able simulate the strikingly different trends in actuation behavior of single-crystal FeGa alloys with varied Ga content.
7. The model based on just 7-parameters can be used to generate a database of material properties such as  $\mu_R$  and  $d_{33}$  as a function of both stress and field. This should prove to be a useful design tool.
8. A paradigm was established for predicting the sensing characteristics (B- $\sigma$  curves) of a sample from its actuator behavior ( $\lambda$ -H and B-H curves). With knowledge of the nominal Young's modulus  $E_0^*$  the  $-\sigma$  (strain-stress) characteristics can also be predicted. The correlation obtained between sensor simulation, based on model parameters obtained from actuator data, and experimental results for sensing behavior proves that sensing behavior can be

predicted from actuator characteristics very precisely using this model. This correlation is shown to be excellent in the <100> oriented furnace cooled 19 at. % Ga sample and reasonably good in the case of <110> oriented furnace cooled 18 at. % Ga sample.

*\*  $E_0$  is evaluated from  $-\sigma$  characteristics at 446 or 891 Oe where the high-bias field levels ensure that the sample remains in a saturated state under the range of compressive stress applied.*

9. The constitutive model of the Villari effect was coupled with a lumped parameter model for interaction between magnetostrictive sample and the transducer magnetic circuit. Thus sensor characteristics at constant drive current can be modeled, accounting for the increase in field through the sample due to an increase in its reluctance with compressive stress. This was benchmarked against experimental data of a <100> oriented furnace cooled 19 at. % Ga sample.
  
10. Polycrystalline actuation and sensing behavior was modeled as a volume-fraction weighted sum of the behavior along individual [100], [110], [210], [310], [211] and [311] crystallographic directions enabling a prediction of actuation and sensing data from the cross-section texture of the sample. Variation in actuator properties were simulated from expected variation in cross-section texture between samples and was found to be in reasonable agreement with experimental data.

### **7.3 Future Research Directions**

While many of the issues relating to the understanding, characterization and modeling of magnetostrictive materials, particularly the FeGa alloys, were addressed in this dissertation, some issues merit further characterization and improvements in modeling. Future research in these areas may lead to a more complete understanding and predictive capability for the actuation and sensing behavior of FeGa alloys.

1. *Study of the effect of stress on crystallographic structure of 24.7 and 29 at. % Ga samples:* The 24.7 and 29 at. % Ga samples demonstrate an unexpected decrease in  $\lambda_{\text{sat}}$  at compressive stresses higher than 30 MPa. An in-situ X-ray diffraction (XRD) study of the effect of stress on the crystallographic structure of the constituent phases of these materials may provide insights into this effect.
2. *Tensile sensing:* Both actuator and sensor characterization reported in this dissertation was for compressive stress only, although model simulations were employed to simulate behavior in tension. Researchers at the Naval Surface Warfare Center (NSWC) have reported actuator characterization and modeling under tension for stress-annealed samples [**Wun-Fogle2006**] but no characterization of sensing behavior. A good direction for future research is to characterize the sensing behavior of stress-annealed samples in tension and compression, especially under low bias fields ~20-60 Oe.
3. *Sensing in bending and torsion modes:* Structures under bending or torsion experience both compression and tension. Furthermore, there is a spatial variation in stress-state and consequently magnetomechanical behavior. For example, when a beam is bent downwards, the lower half undergoes compression while the upper half undergoes tensile loading, the magnitude of both stresses increasing with distance from the neutral axes. The accurate characterization and modeling of magnetomechanical behavior under both tension and compression and capturing the spatial variation in stress and magnetomechanical behavior is essential in designing optimized bending and torsion sensors and predicting their sensitivity.
4. *Actuation and sensing at the micro-scale:* Designs of micro-scale actuators based on magnetostrictive materials have been discussed [**Quandt1995**] and methods of producing multi-layers for applying biasing fields have been

demonstrated[Quandt1997]. With specific regard to FeGa, it has been shown that  $\text{Fe}_{81}\text{Ga}_{19}$  can be epitaxially deposited in the  $\langle 110 \rangle$  direction on a [001] silicon substrate [Weston2002]. FeGa films deposited in this manner, with appropriate stress-bias introduced by mismatch in the thermal expansion coefficients of the FeGa film and the substrate may prove to be good actuators and sensors at the micro-scale for reasons discussed in Chapter 3.

5. *Predicting actuation and sensing behavior of polycrystals from cross-section texture more accurately:* Modeling elastic interactions between grains by FEM and coupling it with the single-crystal constitutive free-energy model for each grain may result in more accurate simulation/prediction of polycrystalline actuator and sensor behavior.

## Bibliography

[**Armstrong1997**] Armstrong, William D., “Magnetization and magnetostriction processes in  $Tb_{(0.27-0.30)}Dy_{(0.73-0.70)}Fe_{(1.9-2.0)}$ ”, Journal of Applied Physics, v 81, n 5, Mar 1, 1997, p 2321.

[**Armstrong2000**] Armstrong, William D., “Non-linear deformation of magnetically dilute magnetostrictive particulate composites”, Materials Science and Engineering A: Structural Materials: Properties, Microstructure and Processing, v 285, n 1, Jun, 2000, p 13-17.

[**Armstrong2002**] Armstrong, William D., “A directional magnetization potential based model of magnetoelastic hysteresis”, Journal of Applied Physics, v 91, n 4, Feb 15, 2002, p 2202.

[**Armstrong2003a**] Armstrong, William D., “Fully three-dimensional incremental model of magnetoelastic hysteresis in Terfenol-D”, Proceedings of SPIE - The International Society for Optical Engineering, v 5053, 2003, p 405-413.

[**Armstrong2003b**] Armstrong, William D., “An incremental theory of magnetoelastic hysteresis in pseudo-cubic ferro-magnetostrictive alloys”, Journal of Magnetism and Magnetic Materials, v 263, n 1-2, July, 2003, p 208-218.

[**Atulasimha2005**] Atulasimha, J. and Flatau, A.B., “Energy-based constitutive Model for Magnetostrictive Materials and its Application to Iron-Gallium Alloys”, Proceedings of the Materials Research Society Fall Conference, December 2005.

[**Atulasimha2006a**] Atulasimha, J. and Flatau, A.B., “Energy-Based Model for the magnetostrictive behavior of polycrystalline Iron-Gallium Alloys”, Proceedings of the SPIE Conference on Smart Structures and Materials, San Diego, March 2006.

**[Atulasimha2006b]** Atulasimha, Jayasimha, Flatau, Alison B. and Kellogg, Rick A. “Sensing behavior of varied stoichiometry single crystal Fe-Ga” Source: Journal of Intelligent Material Systems and Structures, v 17, n 2, February, 2006, p 97-105

**[Bergqvist1991]** Bergqvist, A. Engdahl, G., “A stress-dependent magnetic Preisach hysteresis model Source: IEEE Transactions on Magnetics”, v 27, n 6 pt 2, Nov, 1991, p 4796-4798

**[Bolshakov1996]** Bolshakov, G.V. and Lapovok, A.J. “Preisach model for magnetoelastic hysteresis” , Journal of Magnetism and Magnetic Materials, v 162, n 1, Sep 1, 1996, p 112-116

**[Buiroon2001]** Buiroon, N., Hirsinger, L. and Billardon, R., “A multiscale model of magnetostriction strain and stress effect”, Journal of Magnetism and Magnetic Materials, v 226, n SUPPL. 1, May, 2001, p 1002-1004.

**[Calkins1997]** Calkins, F.T., “Design, Analysis, and Modeling of Giant Magnetostrictive Transducers”, PhD Dissertation, Iowa State University, 1997.

**[Calkins 1999]** Calkins, F.T., Flatau, A.B., and Dapino, M.J., “Overview of Magnetostrictive Sensor Technology”, 40th AIAA/ASME/ASCE/AHS/ASC Structures, Structural Dynamics, and Materials Conference and Exhibit, St. Louis, MO, April 1999, AIAA-99-1551, Vol. 4, pp. 2763-2772.

**[Callen1965]** Callen, H. B. and Goldberg. N. “Magnetostriction of Polycrystalline Aggregates”, Journal of Applied Physics -- March 1965 -- Volume 36, Issue 3, pp. 976-977.

**[Chikazumi1964]** Chikazumi, S., “Physics of Magnetism”, © 1964 John Wiley and Sons, Inc., Library of Congress Catalog Card No 64-14985.

[Chopra2001] Chopra, I., "ENAE 651 class notes on Smart Structures", Alfred Gessow Rotorcraft Center, Department of Aerospace Engineering, University of Maryland, College Park, Fall 2001.

[Chopra2002] Chopra, I., "Review of State of Art in Smart Structures and Integrated Systems", AIAA Journal, Vol. 40, No 11, November 2002.

[Clark1980] Clark, A.E., "Ferromagnetic Materials, Vol.1", Chapter 7: Magnetostrictive Rare Earth-Fe<sub>2</sub> Compounds, North-Holland Publishing Company. 1980, pp 531-588.

[Clark2000] Clark, A.E., Restorff, J.B., Wun-Fogle, M., Lograsso, T.A., and Schlagel, D.L., "Magnetostrictive properties of body-centered cubic Fe-Ga and Fe-Ga-Al alloys", IEEE Transactions on Magnetics, vol. 36, no. 5, p.3238-3240, Sept. 2000.

[Clark2001a] Clark, A.E., Wun-Fogle, M., Restorff, J.B. and Lograsso, T.A., "Magnetic and Magnetostrictive Properties of Galfenol Alloys Under Large Compressive Stresses", International Symposium on Smart Materials-Fundamentals and System Applications, Pacific Rim Conference on Advanced Materials and Processing (PRICM-4), Honolulu, Hawaii, December 11-15, 2001.

[Clark2001b] Clark, A.E., Wun-Fogle, M., Restorff, J.B., Lograsso, T.A., and Cullen, J.R., "Effect of Quenching on the Magnetostriction of Fe<sub>1-x</sub>Ga<sub>x</sub> (0.13<x<0.21)", 8th Joint MMM-Intermag Conference, Jan. 7-11, 2001.

[Clark2003] Clark, A.E., Hathaway, K.B., Wun-Fogle, M., Restorff, J.B., Lograsso, T.A., Keppens, V.M., Petculescu, G., and Taylor, "Extraordinary magnetoelasticity and lattice softening in bcc Fe-Ga alloys ", R.A. Journal of Applied Physics, v 93, n 10 3, May 15, 2003, p 8621-8623.

[Clark2004] Clark, A.E., Wun-Fogle, M., Restorff, J.B., Lograsso, T.A., and Petculescu, G., “Magnetostriction and elasticity of body centered cubic  $\text{Fe}_{100-x}\text{Be}_x$  alloys”, Journal of Applied Physics, v 95, n 11 II, Jun 1, 2004, p 6942-6944.

[Clark2005] Clark, A.E., Wun-Fogle, M., Restorff, J.B., Dennis, K.W., Lograsso, T.A., and McCallun, R.W., “Temperature dependence of the magnetic anisotropy and magnetostriction of  $\text{Fe}_{100-x}\text{Ga}_x$  ( $x=8.6, 16.6, 28.5$ )”, Journal of Applied Physics 97, 10M316, 2005.

[Comsol2005] [www.comsol.com](http://www.comsol.com)

[Couch2002] Couch, R. N., Chopra, I. and Wuttig, M., “ Experimental characterization of NiMnGa ferromagnetic shape memory alloy bars under variable loading conditions”, Proceedings of SPIE -The International Society for Optical Engineering, v 4701, 2002, p 29-39.

[Cullen2001] Cullen, J.R., Clark, A.E., Wun-Fogle, M., Restorff, J.B. and Lograsso, T.A., Journal of Magnetism and Magnetic Materials, 226-230, 948, 2001.

[Cullen2002] Cullen, J.R., Clark, A.E., Wun-Fogle, M., Restorff, J.B. and Lograsso, T.A., “Magnetoelasticity of Fe-Ga and Fe-Al Alloys”, ICM, 2002.

[Dai2003] Dai, Liyang, Cullen, James; Wuttig, Manfred; Quandt, Eckhard and Lograsso, T., “Magnetism, elasticity, and magnetostriction of FeCoGa alloys”, Journal of Applied Physics, v 93, n 10 3, May 15, 2003, p 8627-8629

[Dapino1999] Dapino, M.J., “Nonlinear and Hysteretic Magnetomechanical Model for Magnetostrictive Transducers”, PhD Dissertation, Iowa State University, 1999.

[Dapino2002] Dapino, M. J., Smith, R. C., Calkins, F. T. and Flatau, A. B., “A coupled magnetomechanical model for magnetostrictive transducers and its

application to Villari-effect sensors”, Journal of Intelligent Material Systems and Structures, v 13, n 11, November,2002, p737-747.

**[Datta2005]** Datta, S., and Flatau, A. B., Proceedings of SPIE- The International Society for Optical Engineering, March 2005.

**[Datta2006]** Datta, S., Huang, M., Raim, J., Lograsso, T. A., and Flatau, A. B., “Effect of Thermal History and Gallium Content on Magnetomechanical Properties of Iron Gallium Alloys” Submitted to Materials Science and Engineering A, 2006.

**[Decoquer2002]** Decoquer, R., Kestens, L. and Houbaert, Y., “Modeling the Magnetostriction coefficient of Polycrystalline ferromagnetic materials with Cubic structure by means of finite element method”, Journal of Magnetism and Magnetic Materials, 2002, pp 1218-1220.

**[Downey2005]** Downey, P. R., and Flatau, A. B., “Bending behavior of iron-gallium (Galfenol) alloys for sensor applications”, Proceedings of SPIE - The International Society for Optical Engineering, v 5764, Smart Structures and Materials 2005 - Smart Structures and Integrated Systems, 2005, p 120-129

**[Engdahl2000]** Engdahl, Goran, “Handbook of Giant Magnetostrictive Materials”, Academic Press Series in Electromagnetism, Academic Press, A Harcourt Science and Technology Company © 2000, ISBN: 0-12-238640-X.

**[Falk1982]** Falk, F. , “Landau Theory and Martensitic Phase Transitions”, Journal de Physique (Paris), Colloque, v 43, n 12, Dec, 1982, p c4.

**[Garshelis1996]** Garshelis, I.J., and Conto, C.R., “A magnetoelastic torque transducer utilizing a ring divided into two oppositely polarized circumferential regions”, J. Appl. Phys. 79 (8), 15 April 1996.

**[Ginzburg1977]** Ginzburg, V., “The magnetoelastic properties of a simplified model of a ferromagnetic body in low magnetic field” IEEE Transactions on Magnetics, Sep 1977 Volume: 13, Issue: 5, pp: 1657- 1663.

**[Hall1959]** Hall, R.C., “Single crystal magnetic anisotropy and magnetostriction constants of several ferromagnetic materials including alloys of NiFe, SiFe, AlFe, CoNi, and CoFe”, Journal of Applied Physics, v 30, n 6, June 1959, p 816-819.

**[Hall1994]** Hall, D.L., “Dynamics and Vibrations of Magnetostrictive Transducers”, Ph.D. Dissertation, Iowa State University, 1994.

**[Hubert2000]** Hubert, A. and Schafer, R., “Magnetic Domains”, © 2000, Springer, ISBN 3-540-64108-4.

**[Jiles1983]** Jiles, D. C. and Atherton “Theory of Ferromagnetic Hysteresis (Invited)”, Journal of Applied Physics, v 55, n 6 pt 2B, Mar 15, 1983, p 2115-2120.

**[Jiles1984]** Jiles, D. C. and Atherton, D. L. “Theory of the Magnetization Process in Ferromagnets and its Application to the Magnetomechanical Effect”, Journal of Physics D: Applied Physics, v 17, n 6, Jun 14, 1984, p 1265-1281.

**[Jiles1989]** Jiles, D.C. and Thoelke, J.B. “Theory of ferromagnetic hysteresis: Determination of model parameters from experimental hysteresis loops”, IEEE Transactions on Magnetics, v 25, n 5, Sep, 1989, p 3928-3930.

**[Jiles1995a]** Jiles, D.C., “Theory of the magnetomechanical effect”, Journal of Physics D: Applied Physics, v 28, n 8, Aug 14, 1995, p 1537.

**[Jiles1995b]** Jiles, D.C. and Devine, M.K., “Law of approach as a means of modeling the magnetomechanical effect”, Journal of Magnetism and Magnetic Materials, v 140-144, n pt 3, Feb, 1995, p 1881-1882.

**[Jiles2004]** Jiles, D.C. and Li, L. “A new approach to modeling the magnetomechanical effect”, Journal of Applied Physics, v 95, n 11 II, Jun 1, 2004, p 7058-7060.

**[Joseph1965]** Joseph, R.I., and Schlomann E., “Demagnetizing Field in Non-ellipsoidal Bodies”, Journal of Applied Physics, v 36, n 5, May, 1965, p 1579-1593

**[Kellogg2002a]** Kellogg, R.A., Flatau, A.B., Clark, A.E., Wun-Fogle, M., and Lograsso, T.A., “Temperature and stress dependencies of the magnetic and magnetostrictive properties of  $\text{Fe}_{0.81}\text{Ga}_{0.19}$ ”, Journal of Applied Physics, v 91, n 10 II, May 15, 2002, p 7821.

**[Kellogg 2002b]** Kellogg, R.A., Flatau, A.B., Clark, A.E., Wun-Fogle, M., Lograsso, T.A., “Texture and grain morphology dependencies of saturation magnetostriction in rolled polycrystalline  $\text{Fe}_{83}\text{Ga}_{17}$ ” Journal of Applied Physics, v 93, n 10 3, May 15, 2003, p.8495-8497.

**[Kellogg2003a]** Kellogg, R. A., Flatau, A., Clark, A. E., Wun-Fogle, M., and Lograsso, T., “Quasi-static transduction characterization of Galfenol”, American Society of Mechanical Engineers, Aerospace Division (Publication) AD, v 68, Proceedings of the ASME Aerospace Division - 2003, 2003, p 273-280.

**[Kellogg2003b]** Kellogg, R.A., “Development and Modeling of Iron-Gallium alloys”, PhD Thesis, Engineering Mechanics, Iowa State University, Ames, Iowa, 2003, available online at:

[http://www.aero.umd.edu/~aflatau/TechPubs/Kellogg\\_2003\\_Dissertation.pdf](http://www.aero.umd.edu/~aflatau/TechPubs/Kellogg_2003_Dissertation.pdf)

**[Kellogg2004]** Kellogg, R.A., Russell, A.M., Lograsso, T.A., Flatau, A.B., Clark, A.E. and Wun-Fogle, M. “Tensile properties of magnetostrictive iron-gallium alloys”, Acta Materialia, v 52, n 17, Oct 4, 2004, p 5043-5050.

**[Kellogg2005]** Kellogg, Rick A., Flatau, Alison, Clark, Arthur E., Wun-Fogle, Marilyn, and Lograsso, T., “Quasi-static transduction characterization of galferol”, *Journal of Intelligent Material Systems and Structures*, v 16, n 6, June, 2005, p 471-479.

**[Kennedy2002]** Kennedy, D. K., Straub, F. K., Schetky, L. McD, Chaudry, Z. and Roznoy, R., “Development of a SMA Actuator for In-Flight Rotor Blade Tracking” *Proc. of SPIE’s symposium on Smart structures and Integrated Systems*, Newport Beach, CA, March 2002, vol3985, pp62-75.

**[Kubaschewski1982]** Kubaschewski, O., “Iron-Binary Phase Diagrams”, © 1982, Springer-Verlag, ISBN 3-540-11711-3.

**[Kudva1996]** Kudva, J., Jardine, P., Chris Martin, and Kari Appa, “Overview of the DARPA/WL ‘Smart Structures and Materials Development – Smart Wing’ Contract”, *Proc. of the SPIE North American Conference on Smart Structures and Materials*, San Diego, CA, Feb 26-29, 1996.

**[LB]** Landolt-Bornstein, New Series III/19a Vol. Data on Fe and Ni.

**[Li2003]** Li, L. and Jiles, D.C., “Modified law of approach for the magnetomechanical model: Application of the Rayleigh law to the stress domain”, *Digests of the Intermag Conference*, 2003, p AD11.

**[Liang1996]** Liang, C., Davidson, F., Schetky, L. M. and Straub, F. K., “Applications of Torsional Shape Memory Alloy Actuators for active rotor blade control-Opportunities and Limitations”, *Proc. of SPIE’s symposium on Smart structures and Integrated Systems*, San Diego, CA, 1996.

**[Lograsso2003]** Lograsso, T.A., Ross, A.R., Schlagel, D.L., Clark, A.E. and Wun-Fogle, M., “Structural transformations in quenched Fe-Ga alloys”, *Journal of Alloys and Compounds*, v 350, n 1-2, Feb 17, 2003, p 95-101.

**[Lograsso2006]** Lograsso, T.A., and Summers, E.M., “Detection and quantification of DO<sub>3</sub> chemical order in Fe-Ga alloys using high resolution X-ray diffraction”, *Materials Science and Engineering A*, v 416, n 1-2, Jan 25, 2006, p 240-245

**[Massalaski2002]** Maasalaski, T., Editor, *Binary Alloy Phase Diagrams 2<sup>nd</sup> Ed.*, ASM International, Materials Park, Ohio, 2002.

**[Park2002]** Park, W.J., Son, D.R., and Lee, Z.H., “Modeling of Magnetostriction in grain aligned Terfenol-D and preferred orientation change of Terfenol-D dendrites”, *Journal of Magnetism and Magnetic Materials*, 2002, pp 223-229.

**[Pathria1972]** Pathria, R.K., “*Statistical Mechanics*”, Butterworth-Heinemann, a division of Reed Educational and Professional Publications Ltd. ISBN 0 7506 2469 8

**[Petculescu2005]** Petculescu, G., Hathaway, K.B., Lograsso, T.A., Wun-Fogle, M. and Clark, A.E., “Magnetic field dependence of galfenol elastic properties”, *Journal of Applied Physics*, v 97, n 10, May 15, 2005, p 10M315

**[Quandt1995]** Quandt, E. and Seemann, K. “Fabrication of giant magnetostrictive thin film actuators”, *Proceedings of the IEEE Micro Electro Mechanical Systems (MEMS)*, 1995, p 273-277.

**[Quandt1997]** Quandt, E., Ludwig, A. and Seemann, K. ,“Giant magnetostrictive multilayers for thin film actuators”, *International Conference on Solid-State Sensors and Actuators, Proceedings*, v 2, 1997, p 1089-1092.

**[Rafique2004]** Rafique, S., Cullen, J. R., Wuttig, M. and Cui, J., “Magnetic anisotropy of FeGa alloys”, *Journal of Applied Physics*, v 95, n 11 II, Jun 1, 2004, p 6939-6941

**[Restorff2002]** Restorff, J.B., Wun-Fogle, M., Clark, A.E., Lograsso, T.A., Ross, A.R., and Schlagel, D.L., “Magnetostriction of ternary Fe-Ga-X alloys (X = Ni,Mo,Sn,Al)”, *Journal of Applied Physics*, v 91, n 10 III, May 15, 2002, p 8225.

**[Restorff2005]** Restorff *et al.*, Galfenol Workshop, University of Maryland, 1<sup>st</sup> February

2005.<http://www.aerosmart.umd.edu/Galfenol/2005presentations/Jimrestoff.ppt#1>

**[Sirohi2003]** Sirohi, J., Cadou, C., and Chopra, I., “Frequency domain modeling of a piezohydraulic actuator”, *Collection of Technical Papers AIAA/ASME/ASCE/AHS/ASC Structures, Structural Dynamics and Materials Conference*, v 3, 2003, p 2172-2184.

**[Smith 2003]** Smith, Ralph C, Dapino, Marcelo J., and Seelecke, Stefan, “Free energy model for hysteresis in magnetostrictive transducers”, *Journal of Applied Physics*, v 93, n 1, Jan 1, 2003, p 458-466.

**[Smith 2006]** Smith, Ralph C. Seelecke, Stefan, Dapino, Marcelo and Ounaies, Zoubeida “A unified framework for modeling hysteresis in ferroic materials”, *Journal of the Mechanics and Physics of Solids*, v 54, n 1, January, 2006, p 46-85.

**[Srisukhumbowornchai2002]** Srisukhumbowornchai, N. and Guruswamy, S., “Influence of ordering on the magnetostriction of Fe-27.5 at. % Ga alloys”, *Journal of Applied Physics*, v 92, n 9, Nov 1, 2002, p 5371

**[Stadler2005]** Presentation in Galfenol Workshop, University of Maryland, College Park, 2005.

**[Summers2004]** Summers, E., Lograsso, T.A., Snodgrass, J.D., Slaughter J., “Magnetic and Mechanical Properties of Polycrystalline Galfenol”, Proc. of SPIE conference on Smart Materials and Integrated Systems, San Diego, March 2004.

**[Suzuki2004]** Suzuki, Takaaki and Matsumoto, Eiji , “Magnetoelastic behavior of ferromagnetic materials using stress dependent Preisach model based on continuum theory”, International Journal of Applied Electromagnetics and Mechanics, v 19, n 1-4, 2004, p 485-489

**[Tatsumoto1959]** Tatsumoto, E., and Okamoto, T., “Temperature dependence of magnetostriction constants in iron and silicon iron”, Journal of the Physical Society of Japan, Vol. 14 (11), 1959, p 1588-1599.

**[Voltairas1999]** Voltairas, P.A., Fotiadis, D.I. and Massalas, C.V. “Role of material parameters and mechanical stresses on magnetic and magnetostrictive hysteresis”, Journal of Magnetism and Magnetic Materials, v 204, n 1-2, Sep, 1999, p 135-143.

**[Weston2002]** Weston, J.L., Butera, A., Lograsso, T., Shamsuzzoha, M., Zana, I., Zangari, G. and Barnard, J. “Fabrication and characterization of Fe<sub>81</sub>Ga<sub>19</sub> thin films”, IEEE Transactions on Magnetics, v 38, n 5 I, September, 2002, p 2832-2834.

**[Wu2002]** Wu, R., “Origin of large magnetostriction in FeGa alloys”, Journal of Applied Physics, v 91, n 10 II, May 15, 2002, p 7358-7360.

**[Wun-Fogle2006]** Wun-Fogle, M., Restorff, J.B. and Clark, A.E., “Magnetostriction of stress-annealed Fe-Ga and Fe-Ga-Al alloys under compressive and tensile stress”, Journal of Intelligent Material Systems and Structures, v 17, n 2, February, 2006, p 117-122.

[Yoo2005] Yoo, Jin-Hyeong; Flatau and Alison B., "Measurement of field-dependence elastic modulus of iron-gallium alloy using tensile test", *Journal of Applied Physics*, v 97, n 10, May 15, 2005, p 10M318.